UNIVERSITY OF SOUTHAMPTON

FACULTY OF ENGINEERING, SCIENCE & MATHEMATICS

School of Physics & Astronomy

DETECTION OF GAMMA-RAY POLARISATION USING THE INTEGRAL SATELLITE

By

David John Clark

Submitted for the degree of Doctor of Philosophy

October 2007

UNIVERSITY OF SOUTHAMPTON

ABSTRACT

FACULTY OF ENGINEERING, SCIENCE & MATHEMATICS

SCHOOL OF PHYSICS AND ASTRONOMY

Doctor of Philosophy

DETECTION OF GAMMA-RAY POLARISATION USING THE INTEGRAL SATELLITE

By David John Clark

Throughout the universe we observe powerful engines which accelerate particles to immense energies. The precise details of how these engines function are still poorly understood, but polarisation measurements of the high energy radiation are pivotal to gain a deeper insight into the physical environment in these systems. Interaction processes usually dominated by strong magnetic fields and highly ordered geometries are required to produce a net polarisation signal in the emission from a source. The strength and direction of a polarisation signal will lead back to an understanding of the configuration of the fields at the emission site.

There have been few attempts at measuring gamma-ray polarisation since measurements are hampered by large backgrounds and systematic effects within the detectors. However, the advent of modern fast computing clusters has made large scale simulation of an instrument's response now possible. By combining instrument data and results from detailed Monte-Carlo Mass-Model simulations using GEANT 4, it is possible to put constraints on the polarisation characteristics of the gamma-ray flux emitted by a source. Using the Compton scattered events in the SPI instrument on INTEGRAL, constraints have been put on the percentage polarisation in the prompt gamma-ray flux of GRB041219a to be 96±40% at 68% confidence and greater than 5% at 99.7% confidence. The method has also been extended to allow the summation of multiple data sets to obtain a measurement of the off-pulse polarisation of the Crab pulsar of 46% ± 10% at an angle of 123° ± 11°, showing a remarkable alignment to the rotational axis of the spinning Neutron star.

The future of polarisation measurements in the gamma-ray band relies on instruments being designed with polarimetry in mind. The detector system designed for the upcoming Laue Lens mission, GRI will be capable of polarisation measurements in the 10keV to 1MeV energy range. A Laue Lens uses transmission diffraction through crystal planes to focus the incoming gamma-rays. Diffraction is highly energy dependant and in order to recreate high resolution images, very accurate measurements of the total energy of the incident photon are necessary in order to avoid chromatic aberrations, as well as good spatial resolution. The aim is to absorb all the Compton scattered products of the incoming photons. The design uses a cavity geometry with the main germanium pixelated imaging detector embedded in a position sensitive cavity. The germanium is then enclosed in a veto to reduce background and to clean the imaging of unwanted non-photopeak events. This allows the majority of backscattered photons to be captured producing a detector with a photopeak efficiency of ~90% at 511keV and millimetric spatial resolution.

Contents

List of Figures

List of Tables

Declaration of Authorship

The work presented in this thesis has been carried out by the author, and in collaboration with others at the University of Southampton, University College Dublin in Ireland, the Max-Plank-Institut für extraterrestrische Physik in Germany, INAF-IASF Bologna in Italy and INAF-IASF Roma in Italy between October 2004 and November 2007.

Chapter 4 initially presents the Mass Modelling techniques used for the analysis. The conversion of the Mass Model from the original GEANT 3 model produced by Dr Colin Ferguson, Dr. Fan Lei and Dr. Andy Green was performed by Dr. David Willis, although substantial modification of this model was performed by the author to carry out this work including the adaption of the code to run on the Iridis 2 cluster.

The method for analysing the GRB data analysis was developed in conjunction with Professor Tony Dean and Dr. Tony Bird at the University of Southampton, Sinead McGlynn, Lorain Hanlon, Sheila McBreen and Brian McBreen at the University College Dublin. The results from GRB041219a have been published in the journal

Astronomy & Astrophysics **466:** 895-904. The analysis and interpretation of the Crab pulsar was carried out with the help and guidance of Professor Tony Dean, Dr. Tony Bird, Dr. Vanessa McBride and Dr. Adam Hill at the University of Southampton, Loredana Bassani and John Stephen at the INAF-IASF Bologna and Angela Bazzano and Pietro Ubertini at the INAF-IASF Roma. The results of the off pulse analysis are the subject of a letter submitted to the journal Science.

The work on the design of the focal plane detector for GRI was carried out with Professor Tony Dean and Dr. Tony Bird at the University of Southampton and the members of the International GRI Consortium.

Publications

Barlow, E. J., Bird, A. J., Clark, D. J., Cornelisse, R., Dean, A. J., Hill, A. B., Moran, L., Sguera, V., Shaw, S. E., Willis, D. R., Capitanio, F., del Santo, M. and Bassani, L. (2005). Detection and analysis of a new INTEGRAL hard X-ray transient, IGR J17285-2922. Astronomy and Astrophysics. **437:** L27-L30.

Barlow, E. J., Knigge, C., Bird, A. J., J Dean, A., Clark, D. J., Hill, A. B., Molina, M. and Sguera, V. (2006). 20-100 keV properties of cataclysmic variables detected in the INTEGRAL/IBIS survey. Monthly Notices of the Royal Astronomical Society. **372:** 224-232.

Bird, A. J., Barlow, E. J., Bassani, L., Bazzano, A., Bélanger, G., Bodaghee, A., Capitanio, F., Clark, D. J., Dean, A. J., Fiocchi, M., Hill, A. B., Lebrun, F., Malizia, A., Mas-Hesse, J. M., Molina, M., Moran, L., Renaud, M., Sguera, V., Shaw, S. E., Stephen, J. B., Terrier, R., Ubertini, P., Walter, R., Willis, D. R. and Winkler, C. (2006a). The Second IBIS/ISGRI Soft Gamma-Ray Survey Catalog. Astrophysical Journal. **636:** 765-776.

Bird, A. J., Malizia, A., Bazzano, A., Barlow, E. J., Bassani, L., Hill, A. B., Bélanger, G., Capitanio, F., Clark, D. J., Dean, A. J., Fiocchi, M., Götz, D., Lebrun, F.,

Molina, M., Produit, N., Renaud, M., Sguera, V., Stephen, J. B., Terrier, R., Ubertini, P., Walter, R., Winkler, C. and Zurita, J. (2007). The Third IBIS/ISGRI Soft Gamma-Ray Survey Catalog. Astrophysical Journal Supplement Series. **170:** 175-186.

Clark, D. J., Dean, A. J. and Bird, A. J. (2006). High photopeak efficiency gamma-ray detector for upcoming Laue Lens missions. High Energy, Optical, and Infrared Detectors for Astronomy II. Edited by Dorn, David A.; Holland, Andrew D.. Proceedings of the SPIE, Volume 6276, pp. 62760W (2006). **6276:** 28.

Hill, A. B., Bird, A. J., Dean, A. J., McBride, V. A., Sguera, V., Clark, D. J., Molina, M., Scaringi, S. and Shaw, S. E. (2007). An unexpected outburst from A0535+262.

Knödlseder, J. and The GRI Consortium (2007). GRI: Exploring the extremes ESA Cosmic Vision Proposal.

McGlynn, S., Clark, D. J., Dean, A. J., Hanlon, L., McBreen, S., Willis, D. R., McBreen, B., Bird, A. J. and Foley, S. (2007). Polarisation studies of the prompt gamma-ray emission from GRB 041219a using the spectrometer aboard INTEGRAL. Astronomy and Astrophysics. **466:** 895-904.

Molina, M., Malizia, A., Bassani, L., Bird, A. J., Dean, A. J., Landi, R., de Rosa, A., Walter, R., Barlow, E. J., Clark, D. J., Hill, A. B. and Sguera, V. (2006). INTEGRAL observations of active galactic nuclei obscured by the Galactic plane. Monthly Notices of the Royal Astronomical Society. **371:** 821-828.

Sguera, V., Barlow, E. J., Bird, A. J., Clark, D. J., Dean, A. J., Hill, A. B., Moran, L., Shaw, S. E., Willis, D. R., Bazzano, A., Ubertini, P. and Malizia, A. (2005). INTEGRAL observations of recurrent fast X-ray transient sources. Astronomy and Astrophysics. **444:** 221-231.

Sguera, V., Bazzano, A., Bird, A. J., Dean, A. J., Ubertini, P., Barlow, E. J., Bassani, L., Clark, D. J., Hill, A. B., Malizia, A., Molina, M. and Stephen, J. B. (2006).

Unveiling Supergiant Fast X-Ray Transient Sources with INTEGRAL. Astrophysical Journal. **646:** 452-463.

Sguera, V., Bird, A. J., Dean, A. J., Bazzano, A., Ubertini, P., Landi, R., Malizia, A., Barlow, E. J., Clark, D. J., Hill, A. B. and Molina, M. (2007a). INTEGRAL and Swift observations of the supergiant fast X-ray transient AX J1845.0-0433 = IGR J18450-0435. Astronomy and Astrophysics. **462:** 695-698.

Sguera, V., Hill, A. B., Bird, A. J., Dean, A. J., Bazzano, A., Ubertini, P., Masetti, N., Landi, R., Malizia, A., Clark, D. J. and Molina, M. (2007b). IGR J18483-0311: an accreting X-ray pulsar observed by INTEGRAL. Astronomy and Astrophysics. **467:** 249-257.

Sguera, V., Hill, A. B., Bird, A. J., Dean, A. J., Bazzano, A., Ubertini, P., Masetti, N., Landi, R., Malizia, A., Clark, D. J., Molina, M., Sguera, V., Bird, A. J., Dean, A. J., Bazzano, A., Ubertini, P., Landi, R., Malizia, A., Barlow, E. J., Clark, D. J., Hill, A. B. and Molina, M. (2007c). IGR J18483-0311: an accreting X-ray pulsar observed by INTEGRAL and Swift observations of the supergiant fast X-ray transient AX J1845.0-0433 = IGR J18450-0435. ArXiv Astrophysics e-prints. **462:** 0702477.

Willis, D. R., Barlow, E. J., Bird, A. J., Clark, D. J., Dean, A. J., McConnell, M. L., Moran, L., Shaw, S. E. and Sguera, V. (2005). Evidence of polarisation in the prompt gamma-ray emission from GRB 930131 and GRB 960924. Astronomy and Astrophysics. **439:** 245-253.

Willis, D. R., Clark, D. J., Diehl, R., Hanlon, L., Kanbach, G., McBreen, B., McGlynn, S. and Strong, A. (2006). Polarimetry with SPI. IAU Symposium. **230:** 83-84.

Dean, A. J., Clark, D. J., McBride, V. A., Bassani, L., Bazzano, A., Bird, A. J., Hill, A. B., Stephen, J. B., Ubertini, P. (2007). Polarized gamma-ray emission from the jet in the Crab nebula. Science, IN PRESS

Acknowledgements

I would like to thank everyone who has contributed or helped me during my work on this thesis. I would firstly like to thank my supervisor Professor Tony Dean for his help and guidance and ensuring I was never stuck with only one job to do, also Dr. Tony Bird and the other members of the INTEGRAL group at Southampton for their help and guidance throughout this project.

I am grateful to Chris Jordan at Jodrell Bank and Pierre Dubah at the ISDC for supplying the relevant Crab ephemeris information. I would also like to thank Ivan Wolton of Information System Services at the University of Southampton for the use of their Iridis 2 Beowulf Cluster and his help when my programming had unexpected consequences.

Thanks also go to my friends Matthew Himsworth, Samuel Birtwell, Timothy Humphreys, Julian Bailey, Kevin Martin, Daniel Summons and Gareth Lewis for many fruitful discussions and listening to my rants when things were not going so well.

Finally, I would like to thank my parents Cherry and Stephen Clark for their help in proof reading this thesis, and especially my girlfriend Emma Pretty for her help and understanding during the final stages of this work.

David Clark, 2007

Chapter 1

Introduction

Astronomy attempts to explain the universe around us. Since the earliest time people have looked up at the stars and wondered what they were. Today we use ever more sophisticated tools to look at the stars to discover their origin. By carrying out observations at different wavebands in the electro-magnetic spectrum we have discovered much about the universe, but each discovery leads to more questions. Observations in the gamma-ray regime allow us to inspect some of the most energetic emission processes related to sources. Unlike other wave bands that mainly see emission due to thermal processes within hot gasses, the majority of gamma-ray emission is non-thermal and is usually produced by electrons and other elementary particles in magnetic fields.

As more observations are taken, scientific explanations are sought to describe the emission detected. Detailed imaging and spectral information allows models of the

source of the emission to be produced. However, there can usually be more than one way to explain the emission and different observations are needed to solve this degeneracy. Linear polarisation of the emission can be used in this case, giving another parameter to measure. At gamma-ray energies linear polarisation is an important diagnostic with the potential to significantly constrain models of emission. Electrons are accelerated on ordered magnetic field lines and release gamma-rays. This emission will be polarised, with the direction and percentage of polarisation related to the emission mechanism and the geometry of the fields. Measurements of polarisation in other wavebands have been extremely valuable in determining which mechanisms and physical conditions are responsible for the emission. For example, the radio to X-ray emission from the Crab nebula was unambiguously attributed to synchrotron radiation after consistency in the polarisation was found (Weisskopf et al. 1978; Smith et al. 1988).

To date measuring gamma-ray polarisation in astronomy has always proved difficult. There have been few attempts of measuring this polarisation since measurements are hampered by small count rates, large backgrounds and systematic effects within the detectors. However, the advent of modern fast computing clusters has made large scale simulation of an instrument's response now possible. By combining instrument data and results obtained from detailed Monte-Carlo Mass-Model simulations it is possible to put constraints on the polarisation of the flux emitted by a source.

This thesis begins with a description of the physical processes and probable cosmic sources of polarised gamma-radiation. This review sets the scene for measurements of polarisation, showing how and why polarisation can be used to investigate properties of an astronomical object and as a diagnostic for models of the source emission. This section concludes with a description of some of the other missions that have in the past been used to measure gamma-ray polarisation.

The third chapter continues by explaining the instrument used for this work, INTEGRAL, and its role in modern gamma-ray astronomy. This European Space Agency satellite, although not explicitly designed for polarimetry, does include two instruments suitable for polarisation studies. These instruments are examined and their suitability for this work is discussed. In order to detect polarisation with INTEGRAL, detailed modelling of the satellite needs to be carried out using the GEANT 4 toolkit. The modelling and simulation aspect is covered in chapter 4 as well as the tests used to check the output.

Chapter 5 describes some of the better known models of Gamma-Ray Bursts and the polarisation expected to be seen in the gamma-ray flux. Chapter 6 looks at the results of using the SPI instrument on INTEGRAL to detect the polarisation in the 3 GRBs: GRB041219a, GRB060901 and GRB061122. A natural follow on from the GRB work is the attempt to measure the polarisation of a persistent source such as the Crab Pulsar. Chapter 7 covers the theory and measurement of the polarisation of the Crab off-pulse emission, along with a description of the results expected from looking at the pulsed Crab emission.

Chapter 8 looks at the future of gamma-ray astronomy detectors by documenting the work carried out with the GRI Consortium on the design of a new polarisation sensitive detector for use in an upcoming mission. This mission will use a Laue Lens to focus gamma-rays allowing for the first time an increased collecting area, without an increased background.

In the final chapter some conclusions are drawn from this work on the feasibility of polarisation studies, the future of polarisation measurements and the design of future astronomical polarimeters.

Chapter 2

Polarisation in Gamma-Ray Astronomy

2.1 Introduction

Before measuring a parameter, it is important to understand what is to be measured and why. This chapter discusses some of the justifications for gamma-ray polarimetry and the reasons why polarimetric observations can provide a unique insight into the geometries of the astronomical objects. Most of the emission mechanisms are non-thermal involving highly energetic particles in strong magnetic fields. These mechanisms can produce high degrees of linear polarisation that can reveal information on the geometry of the system.

This chapter starts by describing the principle emission mechanisms that can produce polarisation in gamma-ray astronomy. This will show how polarised emission is

produced before describing how these mechanisms are important in the astronomical objects seen in the gamma-ray sky. This chapter concludes by looking at the physics involved in detecting polarisation and some of the previous missions capable of detecting polarisation.

2.2 The Production of γ-Rays with Respect to Polarisation

There are many emission mechanisms relevant to polarisation in gamma-ray astronomy. This section will discuss in detail the mechanism showing how the polarised emission is produced and how it helps our understanding of the source. The derivations contained in this chapter are based largely of those contained in *Radiative Processes in Astrophysics* by G.B. Rybicki and A.P. Lightman (1986) and *High Energy Astrophysics, Volumes 1 and 2* by M.S. Longair (1992; 1994).

2.2.1 Bremsstrählung Radiation

Bremsstrählung, also known as free-free emission, involves a charged particle undergoing acceleration due to the electrostatic field of an ion or the nucleus of an atom. As the particle is accelerated, it emits radiation proportional to $1/m^2$, where m is the rest mass of the particle. This process is more important to lighter particles such as electrons since they experience a greater acceleration. Therefore, if there is a significant abundance of free electrons in a hot gas, we would expect to see Bremsstrählung radiation (Heristchi 1986). This process is particularly important in solar flares due to the large number of charged particles and the large number of target nuclei present during these events.

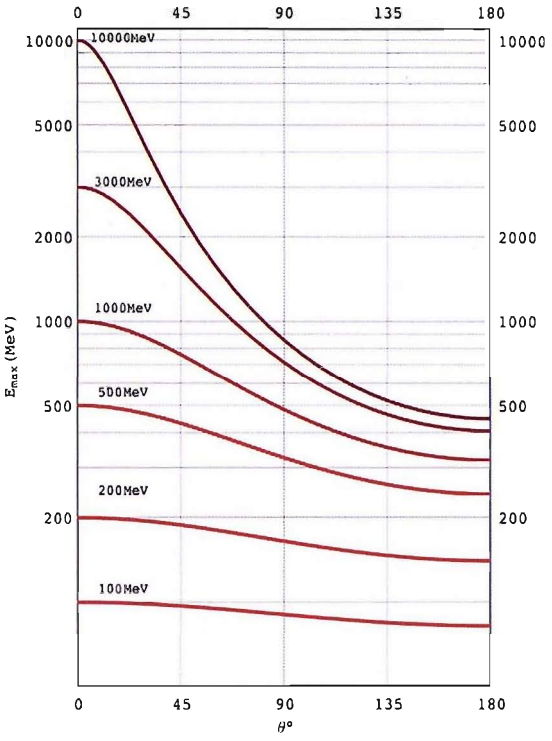

Figure 2.1: The variation of the maximum energy of emitted photons from proton-electron Bremsstrählung with the direction of emission for various incident particle energies (Heristchi 1986).

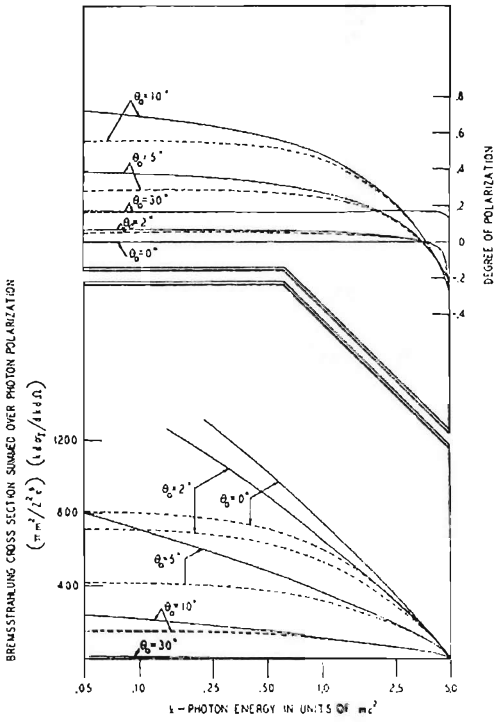

Figure 2.2: Electron-proton Bremsstrählung cross-section (lower figure) and the degree of linear polarisation (upper figure) with the emitted photon energies for $E_e=6m_ec^2$ and various photon emission angles (Gluckstern et al. 1953).

The maximum energy of a single photon emitted by an incident particle of mass, m_1, energy, E, and momentum, P, is:

$$E_{max} = \frac{m_2 \mathrm{E}}{m_1+m_2+\mathrm{E}-P\cos\theta} \qquad 2.1$$

where m_2 is the rest mass of the target particle and θ the emission angle measured from the incident particle's direction. The variation of the maximum emitted energy of a proton-electron Bremsstrählung can be seen in Figure 2.1.

At the gamma-ray energies (E > 1MeV) where the hot gas is optically thin to the emission, then the emitted power is only weakly dependant on the frequency and produces a continuous spectrum

$$P(\nu)d\nu \propto \nu^{-0.1} \quad 2.2$$

The radiation is linearly polarised in the plane of the electron's motion with the photons being emitted perpendicular to the electron's direction of travel (Gluckstern et al. 1953). The degree of polarisation for a single photon is given by,

$$\Pi = \frac{m_e c^2 E\Delta_0 - 2m_e^3 c^6}{E^2\Delta_0 - m_e c^2 E\Delta_0 + 2m_e^3 c^6} \quad 2.3$$

where E is the energy of the emitted photon, E_e is the initial total energy of the electron and

$$\Delta_0 = E_e - M\cos\theta \quad 2.4$$

Figure 2.2 shows the variation of the degree of linear polarisation with the emitted photon energy for an initial electron energy of $E_e=6m_ec^2$ for various emission angles. The degree of linear polarisation reaches a maximum of ~80%.

On a large scale, where many particles are releasing Bremsstrählung radiation it is unlikely that any polarisation will be seen in the overall flux. Without some mechanism to force all the particles to be accelerated in the same direction, the random directions of acceleration caused in a hot gas will wash out the polarisation from one particle. The force to accelerate all the electrons in a single direction is usually provided by magnetic fields and gives an ordered system in which polarisation can be detected.

2.2.2 Magneto-Bremsstrählung Radiation

In order for polarisation to be seen in Bremsstrählung emission, the system needs to be ordered. Instead of the radiation being caused by a particle accelerating due to an electrostatic field, the charged particle is accelerating due to a magnetic field. As with the other forms of Bremsstrählung, this process is most important for the lighter particles.

If the charged particle is moving with a velocity, **v**, in a constant magnetic field, $\boldsymbol{B}$, then it experiences a force given by

$$\boldsymbol{F} = \frac{Ze}{c}(\mathrm{v} \times \boldsymbol{B}) \qquad 2.5$$

The force acts orthogonally to both **v** and $\boldsymbol{B}$ so the particle will circle the magnetic field lines. If **v** and $\boldsymbol{B}$ are not orthogonal to each other, then the angle between them, known

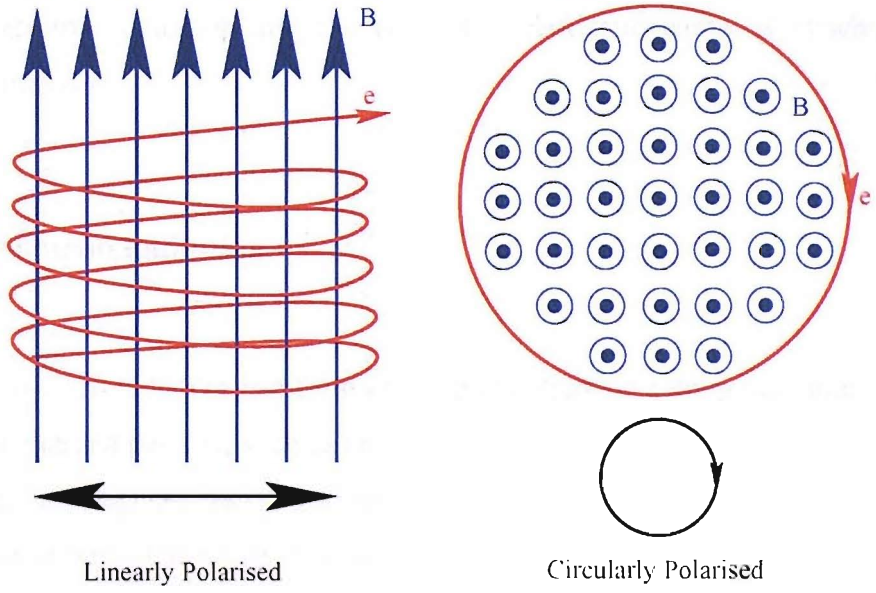

Figure 2.3: Diagram showing the motion of electrons on magnetic field lines. Below, the polarisation seen when observing the system at this angle.

as the pitch angle (χ), will force the particle to precess along a helical path in the direction of the magnetic field line. The particle experiences a constant acceleration and so emits radiation at a rate of

$$-\frac{dE}{dt} = \frac{\sigma_T}{4\pi}\left(\frac{v}{c}\right)^2 c\gamma^2 B^2 \sin^2\chi \qquad 2.6$$

where σ_T is the Thompson cross-section,

$$\sigma_T = \frac{8\pi(Ze)^4}{3m_e^2c^4} \qquad 2.7$$

and γ is the Lorentz factor,

$$\gamma = \frac{1}{\sqrt{1-\frac{v^2}{c^2}}} \qquad 2.8$$

There are three special cases of Magneto-Bremsstrählung radiation, the non-relativistic case of cyclotron emission and the two ultra-relativistic cases of synchrotron and curvature emission.

2.2.2.1 Cyclotron Radiation

Cyclotron or Gyro radiation is a form of Magneto-Bremsstrählung radiation. The force acting on a charged particle, such as an electron, will cause the particle to have a helical path along the magnetic field lines (Figure 2.3). The electron emits radiation in a dipolar distribution. The power radiated per unit solid angle varies as $\sin^2\theta$ with respect to the acceleration vector of the electron (Figure 2.4). This will give a maximum intensity perpendicular to the acceleration vector and a minimum parallel to the vector.

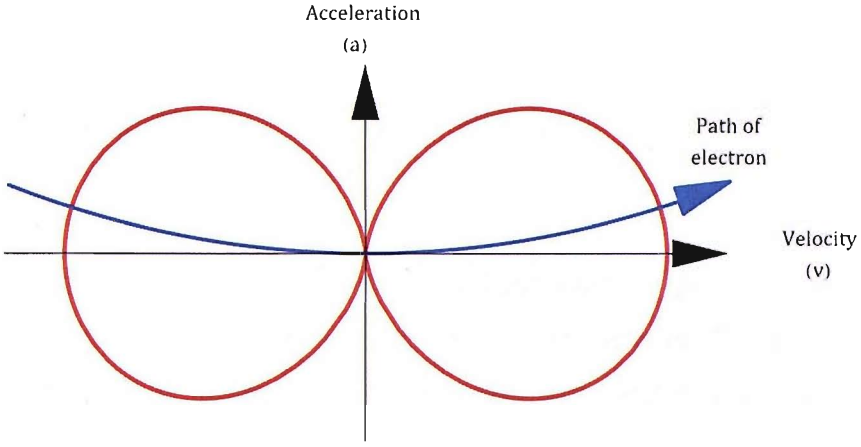

Figure 2.4: Polar diagram showing the dipole radiation distribution (red) emitted by an accelerated electron travelling along a path (blue).

The polarisation of the emission is aligned in the plane of the acceleration and direction of the electron.

Depending on the angle of the motion with respect to the observer, a different polarisation can be seen in cyclotron emission. If the observer is looking down the field lines then the radiation will be circularly polarised. However, if the observer is perpendicular to the magnetic field lines then the radiation will be linearly polarised (Figure 2.3) (Longair 1992). For an arbitrary angle the polarisation will be seen to be a combination of the two and observed to be elliptically polarised.

2.2.2.2 Synchrotron Radiation

Synchrotron radiation is the relativistic case of cyclotron radiation, where relativistic electrons radiate as they change their direction. This relativistic motion causes the emitted radiation to be beamed in the direction of motion of the electron. This creates a pulsing signal with linear or slightly elliptical polarisation depending on the pitch angle of the electron path, much like in the cyclotron case.

The polarisation is also energy dependent, since as the electron energy increases, the emitted radiation forms a narrower beam. With a narrower beam the acceleration vector has rotated less and so the polarisation appears more linear (Lei et al. 1997).

For the case of many electrons there will be a distribution of pitch angles. Electrons with beams within γ^{-1} of the line of sight will contribute to the overall intensity. Elliptical components of the polarisation on either side will cancel producing a net linear polarisation.

The observed spectrum can be approximated at MeV energies by the power-law distribution,

$$\boldsymbol{P(v)dv \propto v^{-(\alpha-1)/2}} \qquad \textbf{2.9}$$

where α is the slope of the power-law. The fractional polarisation can be shown to be (Rybicki and Lightman 1986)

$$\Pi = \frac{\alpha+1}{\alpha+\frac{7}{3}} \qquad \textbf{2.10}$$

The observed range of power-law indices for synchrotron radiation sources range from 1.5 to 5.0, leading to a degree of polarisation of 65% to 80%.

2.2.2.3 Curvature Radiation

Another form of magneto-Bremsstrählung is curvature radiation. If an electron moves in a non-uniform magnetic field, it will tend to drift in the direction of the field lines. If the field lines bend then the electron will emit photons the same as in other forms of

Bremsstrählung. This becomes important near the poles of a dipolar field where the field lines curve sharply. In synchrotron emission, the polarised photons are polarised orthogonal to the magnetic field lines. In curvature radiation, the photons emitted are polarised parallel to the field lines. This can be a useful diagnostic, if polarised synchrotron emission is seen in the radio wavelengths and the gamma-ray emission is seen to be polarised perpendicular to this, it is likely to be from curvature radiation.

2.2.3 Inverse Compton Scattering

In this process, the photon gains energy by scattering off an electron. If the electron is moving at speed, it can impart energy to the photon and if the electron energy greatly exceeds the photon energy, it is possible for a relativistic electron to up-scatter an optical photon to gamma-ray energies. For the general case, the average energy of a scattered photon is given by

$$E_{ave} = \frac{4}{3}\gamma^2 \left(\frac{v}{c}\right)^2 E_0 \qquad 2.11$$

where E_0 is the incident photon energy. If the Lorentz factor γ is around 1000 then the photon can be scattered from optical to gamma-ray energies in the MeV range. In practice the relativistic case is usually considered where $v \approx c$, equation 2.11 becomes

$$E_{ave} = \frac{4}{3}\gamma^2 E_0 \qquad 2.12$$

In an astronomical source Inverse Compton scattering leads to a power-law distribution at MeV energies of the form (Ginzburg 1979)

$$P(v)dv = v^{-(\alpha-1)/2} \qquad 2.13$$

where α is the electron power-law index. This is the same as the distribution for synchrotron radiation given in equation 2.9. This could lead to some confusion of which mechanism is producing the gamma-ray emission. This ambiguity can be solved by looking at the polarisation properties of the flux.

Inverse Compton scattering and Compton scattering can both create a polarised flux from an unpolarised flux and depolarise an initially polarised flux. The polarisation or depolarisation of the emission is dependent on the alignment of the individual photons. For an isotropic distribution the scattered radiation will be comprised of polarised photons from every direction and so the components will cancel, leaving no net polarisation being seen.

The probability that a photon will be scattered by an angle θ, is given by the Klein-Nishina differential cross-section. For unpolarised photons this is

$$\frac{d\sigma_{KN,U}}{d\Omega} = \frac{1}{2} r_0^2 \varepsilon^2 [\varepsilon + \varepsilon^{-1} - sin^2\theta] \qquad 2.14$$

Where r_0 is the classical electron radius, ε is the ratio between the energies of the scattered photon, E', and the incident photon, E_0 (Fernandez et al. 1993)

$$\varepsilon = \frac{E'}{E_0} = \frac{1}{1+\left(\frac{E_0}{m_e c^2}\right)(1-\cos\theta)} \qquad 2.15$$

The degree of linear polarisation of the scattered photons from an initially unpolarised beam is given by

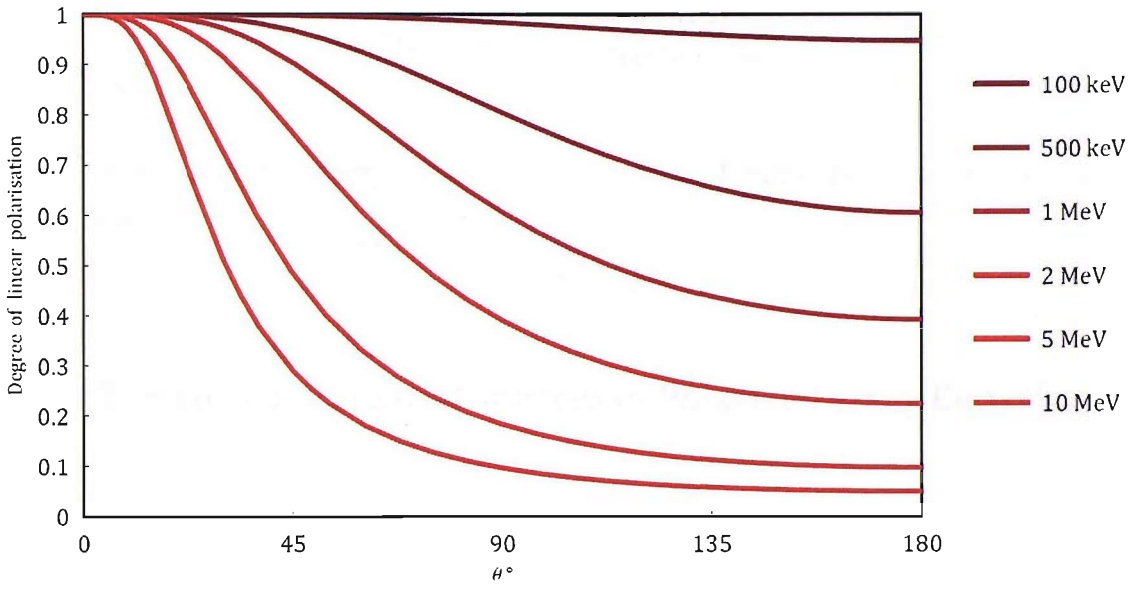

Figure 2.5: Degree of linear polarisation of scattered photons from a beam initially 100% polarised to 90 degrees.

$$\Pi_U = \frac{sin^2\theta}{\varepsilon+\varepsilon^{-1}-sin^2\theta} \qquad 2.16$$

The maximum polarisation is obtained for an angle of 90 degrees at 100 keV. For higher energies the maximum polarisation occurs at smaller angles reaching 40 degrees at 10 MeV. This happens because of the forward scattering nature of the higher energy photons.

If the initial radiation is polarised then the scatter distribution is no longer isotropic. The Klein-Nishina differential cross-section for a polarised photon is

$$\frac{d\sigma_{KN,P}}{d\Omega} = \frac{1}{2}r_0^2\varepsilon^2[\varepsilon + \varepsilon^{-1} - 2sin^2\theta cos^2\eta] \qquad 2.17$$

where the azimuthal scattering angle η, is the polarisation angle of the scattered photon. This produces a degree of linear polarisation of

$$\Pi_p = 2\frac{1-sin^2\theta\, cos^2\eta}{\varepsilon+\varepsilon^{-1}-2sin^2\theta\, cos^2\eta} \quad 2.18$$

This shows that as the energy increases the degree of linear polarisation also drops (Figure 2.5).

2.3 Overview of Potential Sources of Polarised γ-ray Emission

Many astronomical sources could produce a polarised flux. They will all, however, tend to rely on the same groups of processes, as to produce a polarised flux requires a highly ordered system, usually provided by strong magnetic fields. This section will form an overview of the astronomical objects of interest in the gamma-ray sky and what information polarisation can give us for understanding these objects. A detailed explanation of the sources examined in this thesis will occur later with along the analysis.

2.3.1 Gamma-Ray Bursts

In the late 1960s a cluster of satellites was launched called Vela. These satellites had been designed to monitor nuclear weapons testing. However, between 1969 and 1972 they witnessed 16 short bursts of gamma-rays which did not come from either the Earth or the Sun. Due to the classified nature of the mission the existence of these bursts did not reach the public domain until 1973 (Klebesadel et al. 1973). These bursts created a great deal of discussion in the community. The biggest leap forward in explaining them came with the launch of the Compton Gamma-Ray Observatory (CGRO) (Neal et al. 1990) in 1991.

The bursts observed by Vela were lasting of the order of milliseconds to tens of seconds, appearing randomly across the sky. This made determination of the location very difficult. The bursts were obviously energetic, but without accurate distance information it was difficult to know how energetic. If the burst were localised within the Milky Way then they required much less energy to create. The Burst and Transient Source Experiment, BATSE (Fishman et al. 1985), on CGRO was designed to record the positions of as many GRBs as possible. Optimised to measure brightness variations of GRBs on microsecond timescales, over the energy range 30keV to 1.9MeV, BATSE used 8 large area NaI detectors to provide all sky monitoring.

The distribution of the GRBs seen by BATSE show that the bursts must come from either very close to the earth, or more likely, outside our galaxy. Otherwise, the distribution would match the distribution of our galaxy and the burst would be seen more often in the galactic plane. This however, does create a problem for the energies involved. If the bursts are extragalactic then the energies required are much greater, briefly making them the most luminous objects in the universe.

The information collected by the CGRO has allowed two classes of GRBs to be determined, short bursts with a duration of less than 2 seconds, and long bursts with durations of longer than 2 seconds. With the short bursts being so short it has been very difficult to gain much information about them. The leading theory for the production of short bursts is the merger of a binary neutron star (Narayan et al. 1992; Katz 1997). The binary will lose its energy by gravitational radiation and spiral inward, eventually coalescing. The final merged state is too massive to form a single neutron star, but spinning too rapidly to form a black hole immediately. A black hole surrounded by a torus of debris is produced (Rees 1999).

The favoured model to explain long GRBs is the collapsar model (Aloy et al. 2000; MacFadyen et al. 2001). The supernova of a star too massive to form a neutron star, and rotating too fast to immediately collapse into a black hole will release the large amount of angular momentum before creating a black hole accreting from a large torus of debris. Both these models solve the problem of the large energies needed to produce a gamma-ray burst by having the energy emitted in a beam. It is the jetted radiation that is most likely to create polarisation in the gamma-ray flux. Jetted emission implies that there is an anisotropy in the emission, usually due to the geometry of the magnetic fields. This has been backed up by the observation of afterglows (Costa et al. 1997; Frail et al. 1997; van Paradijs et al. 1997) and "jet breaks" in the afterglow light curves of GRBs (Fruchter et al. 1999; Harrison et al. 1999; Kulkarni et al. 1999; Stanek et al. 1999; Berger et al. 2000; Halpern et al. 2000; Jensen et al. 2001; Price et al. 2001; Sagar et al. 2001; Stanek et al. 2001). The actual source of this polarised emission will be discussed in detail in Chapter 5.

There is a useful empirical model derived from an extensive study of the BATSE GRBs (Band et al. 1993). The non-thermal emission is modelled by a broken power-law of the form

$$N(E) = \begin{cases} A\left(\frac{E}{100\ keV}\right)^{\alpha} e^{\left(\frac{E}{E_{break}}\right)} & (\alpha-\beta)E_{break} \geq E \\ A\left(\frac{(\alpha-\beta)E_{break}}{100\ keV}\right)^{\alpha-\beta} e^{(\alpha-\beta)}\left(\frac{E}{100\ keV}\right)^{\beta} & (\alpha-\beta)E_{break} < E \end{cases} \quad 2.19$$

where E_{break} is the energy at which the spectrum turns over; α and β are the slopes below and above the break and A is the amplitude, measured in photons cm^{-2} s^{-1} keV^{-1}. Although it has no physical meaning, this model will be useful later when simulating the GRB flux.

GRBs become an ideal candidate when searching for polarisation. Their high flux over a very short period of time becomes very useful. Over a shorter interval there is a much lower chance that the instrument, background and polarisation properties of the source are likely to change, making modelling and analysis easier. Being so bright also means that the signal to noise ratio is also going to be much higher, increasing the significance of any detection.

2.3.2 Gamma-Ray Pulsars

Pulsars fall into two categories, accreting and rotation-powered. Rotation-powered pulsars are usually detected via their radio emission and derive their luminosity from their rotational energy. The rotational energy decreases as the pulsar radiates, observed as the spinning down of the pulse period. In contrast accreting x-ray pulsars derive most of their luminosity from the gravitational accretion of in-falling gas, resulting in the pulse period increasing over time. Historically, rotation-powered pulsars were the first to be discovered (Hewish et al. 1968). Often visualised as lighthouses in space, their pulsating nature has proved very useful in testing general relativity by using the timing of the first double pulsar seen, PSR J0737-3039 (Lyne et al. 2004).

The pulsations are caused by a rapidly rotating neutron star where the magnetic field axis is misaligned with the rotational axis by a large angle. The emission occurs from the two magnetic poles in a conical beam (Figure 2.6). As these beams sweep across our line of sight we see the pulsar, pulse. This emission is thought to be caused by synchrotron radiation (Cheng et al. 1986) or curvature radiation (Daugherty and Harding 1982) from the particles trapped on the magnetic field lines at these points. Here, a detection of polarisation at gamma-ray wavelengths could help determine the nature of the pulsar emission.

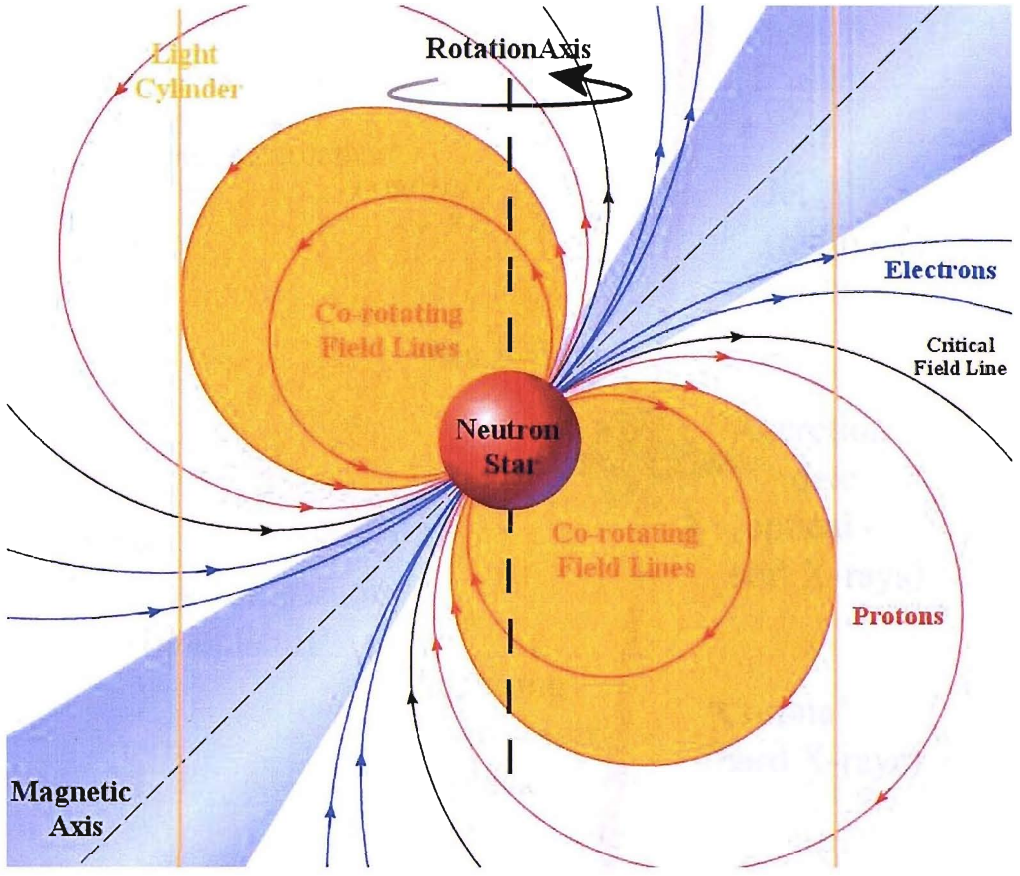

Figure 2.6: Schematic of a Pulsar. The star's magnetic and rotational axes are misaligned and collimated radiation emitted along the magnetic axis will only be seen when the axis is aligned with the observer's line of sight. The light cylinder describes the point at which the magnetic field is no longer co-rotating with the neutron star.

The Crab is a particularly good example of a well studied pulsar. It is one of the brightest gamma-ray sources and in the case of many instruments used as a calibration source. In the case of the INTEGRAL mission this means that there is a lot of archive data available, spanning many years, for use in the search for polarisation.

2.3.3 Micro-Quasars

Micro-Quasars are X-ray black hole binary systems with emission collimated into jets (Figure 2.7), perpendicularly either side of an accretion disc (Mirabel et al. 1992). These jets are thought to be a good source of polarised gamma-ray flux as they are

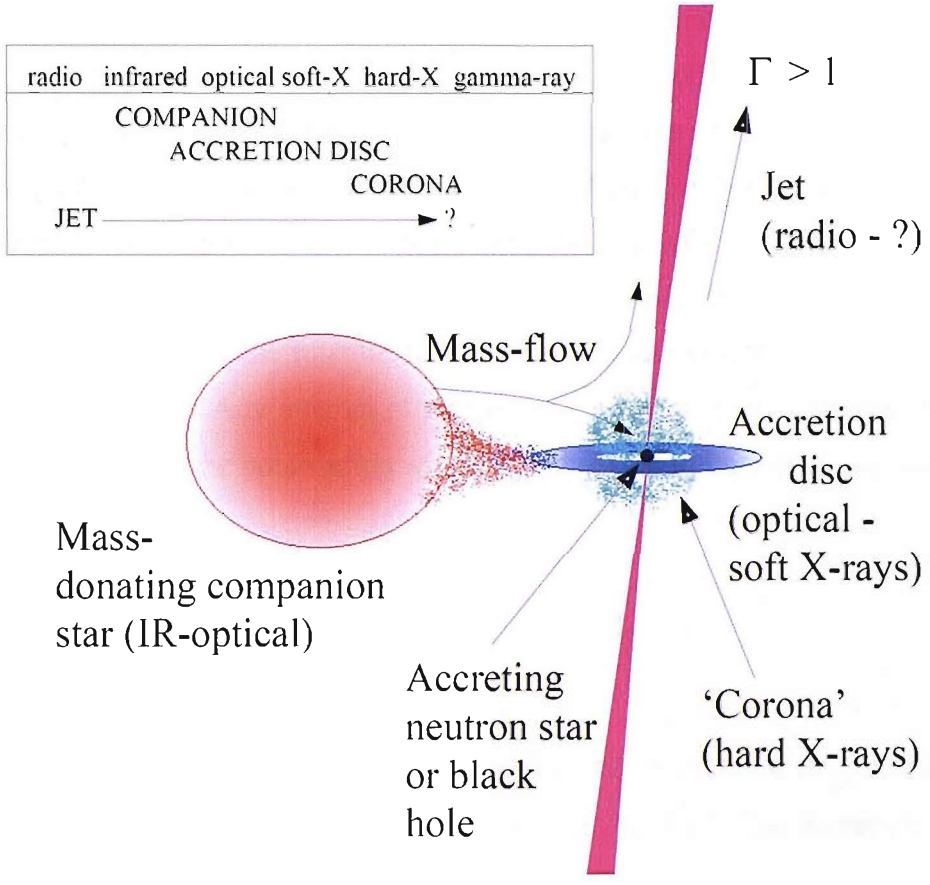

Figure 2.7: Sketch illustrating the current understanding of the physical components and sites of emission in an X-ray binary system. A compact object (neutron star or black hole) accretes material from a binary companion, and the potential accretion energy is released in the form of a combination of high-energy emission (UV/X-ray/gamma-rays) and mechanical energy in an outflow (which itself may be the site of some high-energy emission) (Fender and Maccarone 2004).

likely to be collimated by the magnetic field of the compact object (Meier et al. 2001). A small amount of linear polarisation may also be seen from the accretion disc (Connors and Stark 1977).

The emission from the relativistically beamed jet in the Micro-Quasar GRS1915+105 has been shown to be circularly polarised at radio wavelengths (Fender 2003), thought to be due to synchrotron emission. Although there is no direct evidence of X-ray and gamma-ray emission from the jet, there is evidence of a strong coupling between the observed radio and X-ray luminosities (Gallo et al. 2003). If the gamma-ray emission is

also synchrotron emission, it should be possible to detect polarisation from a source such as GRS1915+105. However, Fender et al (2003) showed that the linear polarisation GRS1915+105 rotated by ~50 degrees over ~6 hours. The rotation was shown not to be due to Faraday rotation as the polarisation produced the same rotation at different wavelengths. It is possible that the rotation of the polarisation is due to the rotation of the jet or a change in the projected position of the magnetic field in the emission regions since the rotation rate does not match with the other known rotation rates in the system. Any attempt at gamma-ray polarisation will require much longer observations and so the polarisation will be averaged, out reducing the signal.

2.3.4 Active Galactic Nuclei

Active Galactic Nuclei (AGN) are the large black holes ($M \approx 10^7 M_\odot$) at the centres of galaxies that emit large amounts of high-energy radiation by the accretion of material from the surrounding galaxy. These often show jetted emission similar to Micro-Quasars. AGN come in many different types. The different types of AGN can be unified by considering the geometry and inclination angle of the system to the observer (Figure 2.8)(Urry and Padovani 1995). The orientation dictates whether the central broad-line emission regions can be seen producing a Seyfert 1 galaxy, or if this region is obscured by the optically thick torus with only the outer narrow-line regions of a Seyfert 2 galaxy being seen. If a jet is seen then the object is classified as a Quasar. However, if the jet is orientated towards the observer then a Blazar is seen. These jets are relativistic and create large-scale structures emitting in radio wavelengths as the jet plows into the surrounding medium.

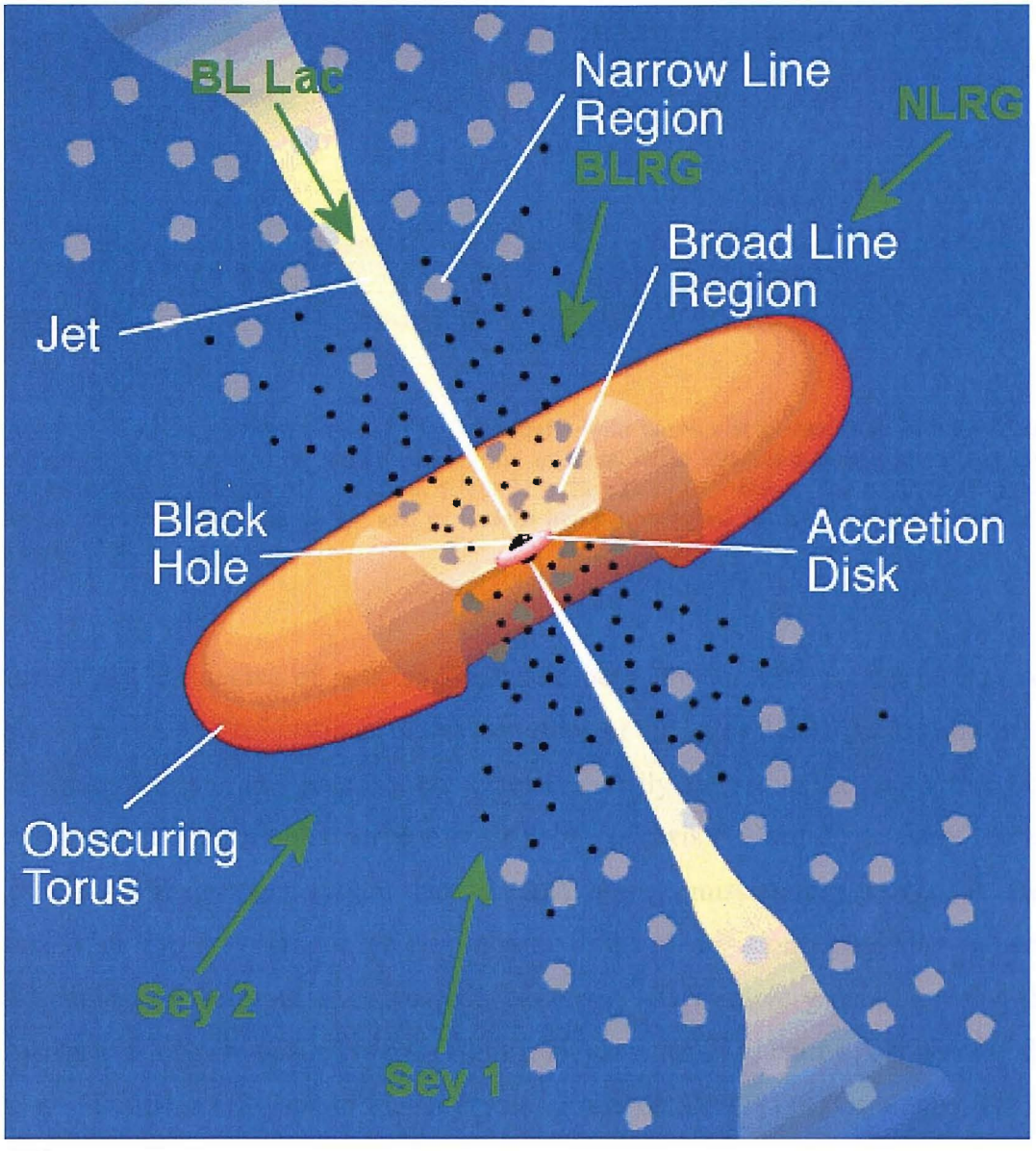

Figure 2.8: Unification model of AGN (Courtesy of M. Polletto, adapted from (Urry and Padovani 1995))

Observations in the radio and optical bands have revealed that most of the emission at these wavelengths is highly polarised, an expected result as both radiations are likely to be due to synchrotron emission. The higher energy emission is thought to be associated with electrons in either the accretion disk or the jet. If the emission comes from the accretion disk this would lead to the percentage of polarisation being dependant on the viewing angle of the disk (Sunyaev and Titarchuk 1985). For Centaurus A it is

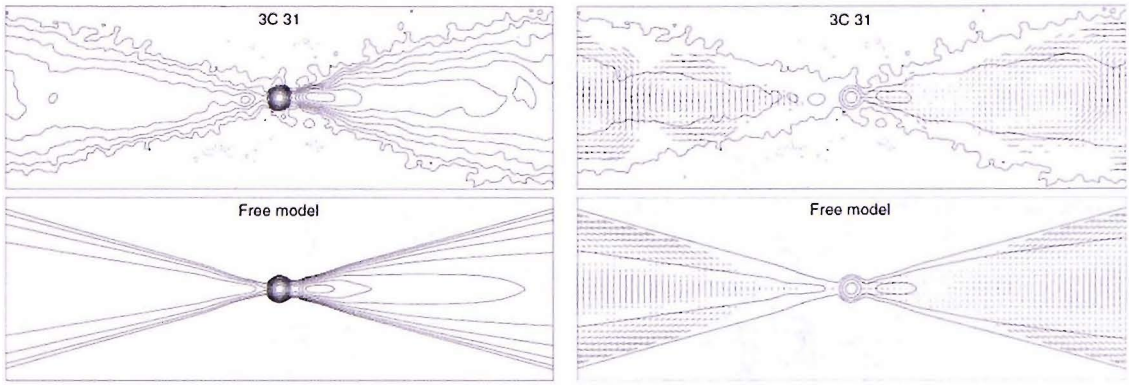

Figure 2.9: Contours of total intensity and magnetic-field vectors at a resolution of 0.75 arcsec. The plots cover 27 arcsec on either side of the nucleus. The left-hand panels show the total intensity contours at levels of -1, 1, 2, 4, 8, 16, 32 × 20 μJy beam^{-1} area. The right-hand panels show the vectors whose magnitude and directions are proportional to the magnetic-field (Laing and Bridle 2002).

predicted that the degree of polarisation should be ~60% for energies below 300 keV (Skibo et al. 1994). Simulations and observations of the jet of 3C 31 (Laing and Bridle 2002) show that the radio polarisation vector is initially aligned to the jet; further from the centre the polarisation is perpendicular to the jet axis (Figure 2.9). Since the life times of high energy electrons are short, the gamma-ray emission they produce is likely to occur closer to the origin of the jet. Measuring the polarisation would allow a better understanding of the processes involved. However, AGN are very faint, meaning that many observations are needed to gain significant statistics. Centaurus A appears with a flux of ~38 mCrab (38/1000 of the Crab flux) in the IBIS/ISGRI 3rd Catalogue (Bird et al. 2007).

2.3.5 Solar Flares

Solar flares are caused by complex magnetic field fluctuations in the sun's chromosphere and are closely related to sunspots. The emission from solar flares is seen at most wavelengths and is thought to be produced by Bremsstrählung radiation from the many low mass particles travelling along the field lines (Petrosian et al. 1994).

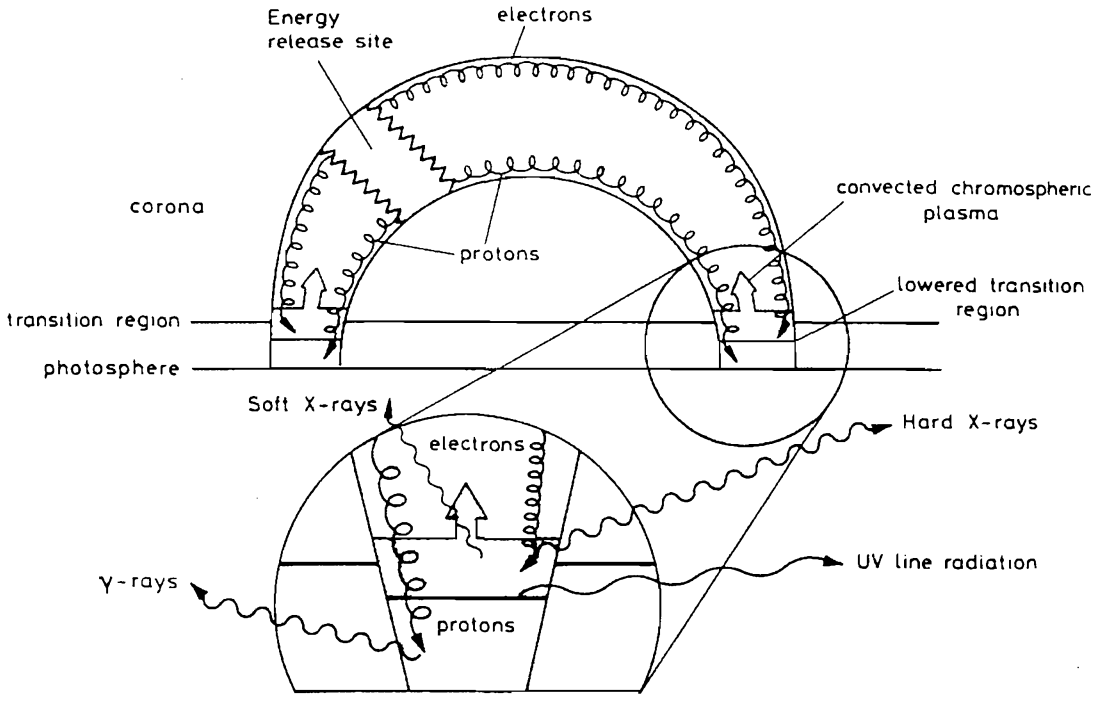

Figure 2.10: A simplified diagram of the magnetic structure and radiation emission sites of a solar flare (Lei et al. 1997).

The loops of magnetic fields on the surface of the sun produce very ordered systems of a local scale and so the emission from these regions is likely to be polarised (Figure 2.10).

The polarisation has been measured at other wavelengths (Erjushev and Tsvetkov 1970; Tindo et al. 1970; Kundu and McCullough 1972; Henoux et al. 1983; Henoux and Chambe 1990; Xu et al. 2005) and more recently McConnell et al has attempted to measure the polarisation of a flare in the 20-100keV energy band using the RHESSI satellite (McConnell et al. 2007).

2.4 Gamma-Ray Interaction Mechanisms and the Detection of Polarisation

Three mechanisms are important in the detection of gamma-rays: photoelectric effect, Compton scattering and pair production. Each can be the dominant process involved in a material depending on the energy of the gamma-rays and the atomic number of the material (Figure 2.11).

In practice the probability of a gamma-ray interacting is the sum of the probabilities for each of these interactions, defined by the linear attenuation coefficient μ. The total linear attenuation is the sum of the attenuation coefficients for each of the interaction mechanisms. The attenuation of flux through a material can be defined by:

$$\frac{I}{I_0} = e^{-\mu x} \qquad 2.20$$

where I is the intensity left at the original energy after a distance x, of the original intensity I_0.

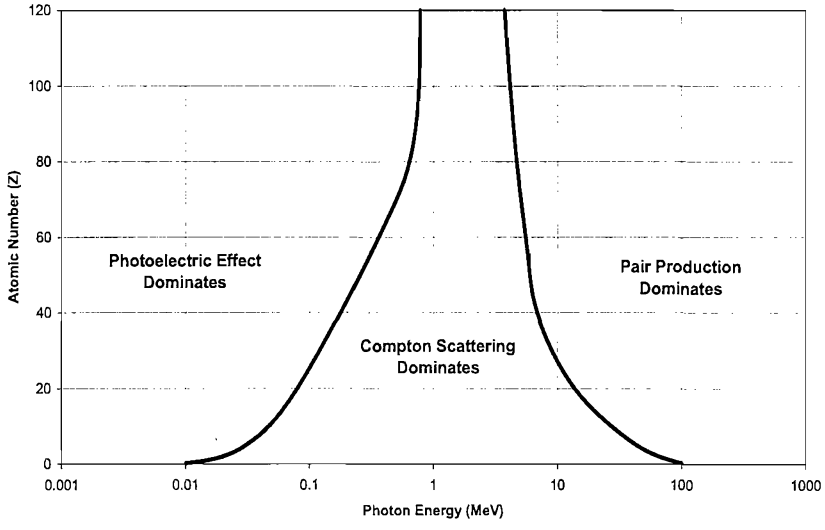

Figure 2.11: Different interactions dominate in different regions defined by the atomic number of the absorbing material and the photon energy.

2.4.1 Photoelectric Absorption

The photoelectric effect involves the incoming photon interacting with a bound electron. Free electrons cannot absorb the photon and recoil since energy and momentum are not conserved (Krane 1988). The photon's energy allows the electron to break from the atom and travel away with the energy of the photon minus the binding energy. The ionised atom can gain a new electron, emitting a photon in the process.

For an unpolarised photon, the electron will be emitted in a random direction. If the incoming photon is polarised then the probability distribution of the photon's direction is modified and becomes proportional to $\cos^2\theta$. This means the electron is most likely to be ejected in the direction of polarisation (Hall 1936). This effect can be seen in the simulations shown in Figure 2.12, where on the smallest scale the electrons are emitted in a non-isotropic fashion. On larger scales the random scatter of the electrons blurs out the initial distribution. However, with a suitably fine resolution detector, such as the Micro Pattern Gas Detector planned for XEUS and HXMT, the pattern can still be seen (Bellazzini et al. 2006; Costa et al. 2007).

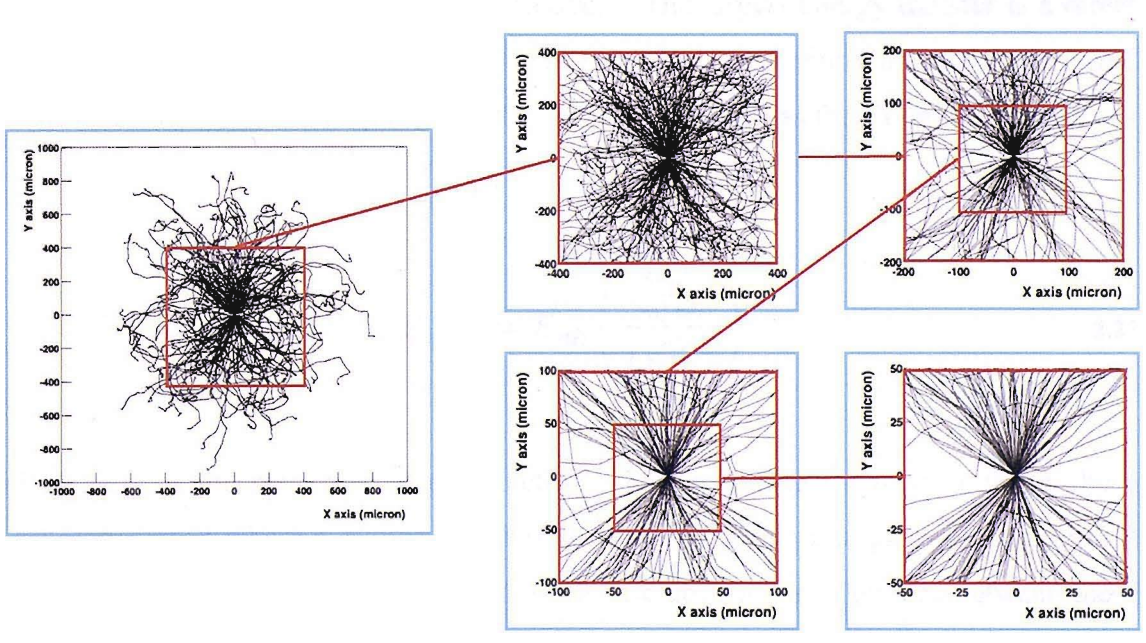

Figure 2.12: 50 keV photoelectron tracks in Neon (100% linearly polarised, collimated photon beam). (Credit: R. Bellazzini).

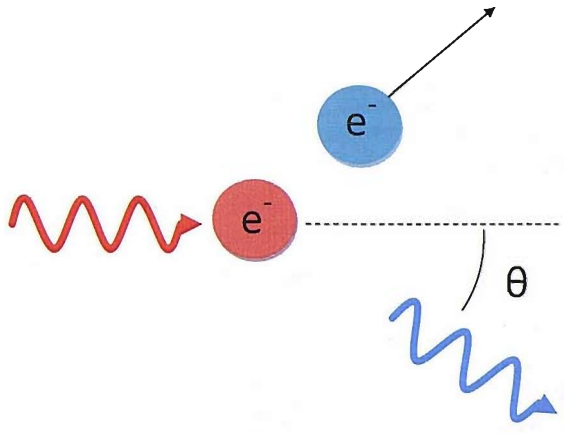

Figure 2.13: Illustration of the Compton scattering process. An incoming photon is scattered off a free electron. The electron will recoil and the photon will be scattered by an angle θ.

2.4.2 Compton Scattering

As mentioned previously, if an incoming photon meets a free electron it will scatter at an angle of θ to the photons direction and a fraction of its energy will be transferred to the electron (Figure 2.13). This energy transferred to the electron is what is measured in a detector. Unlike the photoelectric effect, the photon can never lose all its energy to the electron. The minimum transfer is a glancing impact on the electron ($\theta \approx 0°$) where little or no energy is transferred to the electron. The largest energy transfer is a direct collision between the photon and electron ($\theta \approx 180°$). The maximum energy transferred to the electron, E_{max}, from a photon with energy, E_{ph}, known as the Compton edge is

$$E_{max} = E_{ph}\left(\frac{\frac{2E_{ph}}{m_e c^2}}{1+\frac{2E_{ph}}{m_e c^2}}\right) \qquad 2.21$$

where $m_e c^2$ is the rest mass of the electron. In a real detector there will also be a backscatter peak where a photon that has already undergone a large angle scatter will deposit the rest of its energy through photoelectric absorption. The area between these two peaks forms a saddle shape and is known as the Compton continuum.

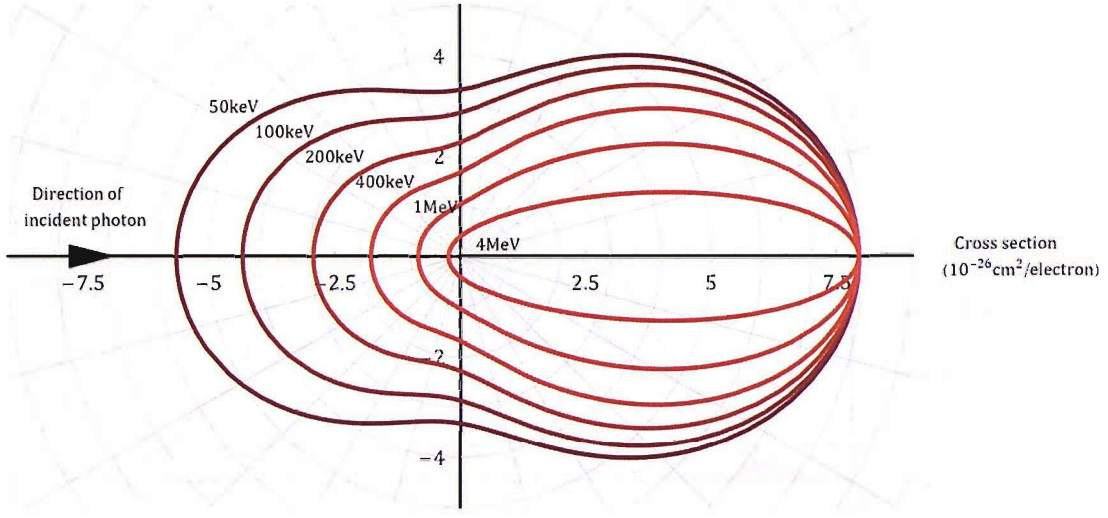

Figure 2.15: The Klein-Nishina differential cross-section seen from the side. As the photon energy increases the photon is more likely to be forward scattered (Davisson and Evans 1952).

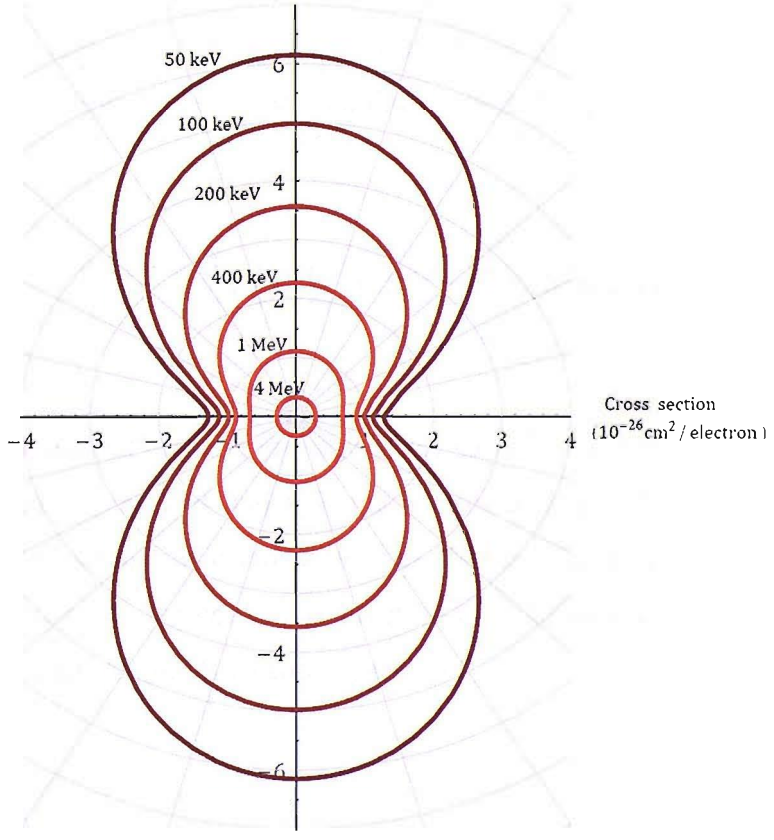

Figure 2.14: The Klein-Nishina differential cross-section for a polarised photon, seen from the direction of incidence. As the energy increases the photon is more likely to be forward scattered and the distribution becomes more isotropic.

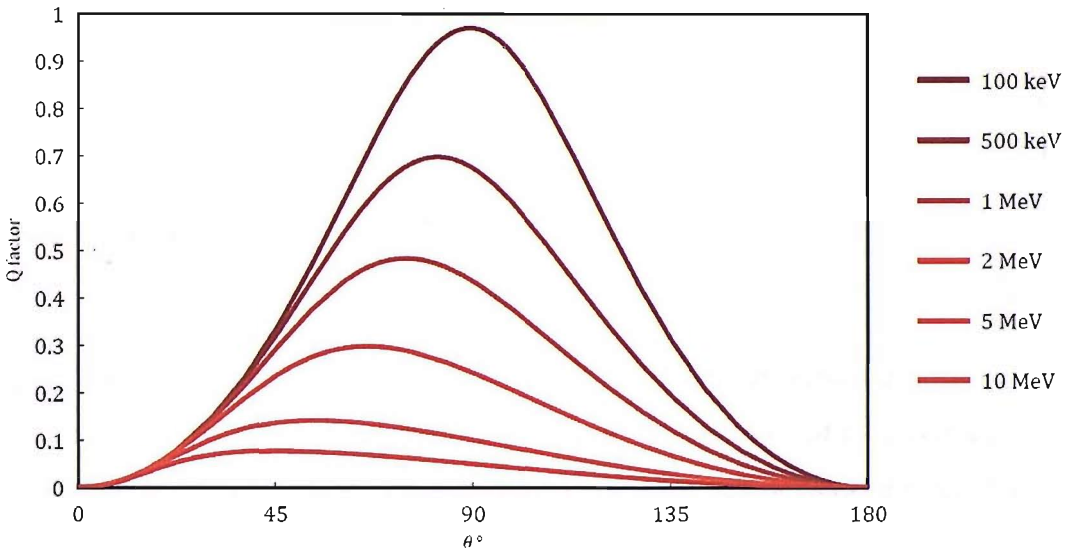

Figure 2.16: Q factor (the ratio of parallel to perpendicular scattering probability) vs scatter angle for a point scatter and detection of various incident photons.

The probability that the photon will scatter by θ is given by the Klein-Nishina differential cross-section. In the case of a linearly polarised photon, this is given by

$$\frac{d\sigma_{KN,P}}{d\Omega} = \frac{1}{2} r_0^2 \varepsilon^2 [\varepsilon + \varepsilon^{-1} - 2sin^2\theta cos^2\eta] \qquad 2.22$$

Where r_0 is the classical electron radius, ε is the ratio between the scattered photon and the incident photon energies and η is the azimuthal scattering angle, defined as the angle to the polarisation unit vector (Lei et al. 1997). This means that the photon will preferentially scatter 90 degrees to the direction of polarisation. The differential cross-section can be seen in Figure 2.15 and Figure 2.14.

These cross-sections show that as the energy increases the photons are more likely to forward scatter and the angular distribution due to the polarisation becomes more

isotropic. This will have important repercussions on the dimensions of a detector and its ability to detect polarisation.

2.4.3 Pair Production

In this process, a high energy photon is converted into an electron-positron pair. In order to conserve momentum, this must occur in the presence of a third body, usually a nucleus. The minimum energy required for this process is twice the rest mass of an electron, 1.022MeV. In practice, pair production is only important for photons with energy greater than 5MeV, with the remaining energy being split evenly between the particles as kinetic energy. The positron will then annihilate and the electron be absorbed, releasing 1.022MeV as gamma-rays.

If the original photon is linearly polarised then the electron and positron will be produced and travel preferentially in a plane perpendicular to the plane of polarisation (Berlin and Madansky 1950). Detecting polarisation in this manner can be very difficult outside of a controlled laboratory environment, since the electron and positron usually need to be separated using a magnetic field and each particle detected separately, so that the plane they lie in can be found.

2.5 Theory of Compton Polarimeters

As seen previously, the Compton scattering differential cross-section dictates that a photon will scatter preferentially perpendicularly to its polarisation vector. After many photons this will lead to an asymmetry in the number of photons scattered parallel and perpendicular to the electric vector. Using a suitable arrangement of detector elements

this asymmetry can be used to determine the direction and degree of polarisation of the beam.

The simplest way in which to detect polarisation, using Compton scattering, is to use a pixelated detector setup. Small pixels will allow the gamma-rays to Compton scatter in one and be absorbed in another. Due to the speed of gamma-rays both pixels will record an energy deposit at the same time and an analysis of the directions in which these illuminated pixels lie will give the original polarisation of the ray.

To assess the relative effectiveness of any arrangement of detectors, the response of the polarimeter to a 100% polarised beam of photons is calculated. This response is known as the Q polarimetric modulation factor (Q-factor) given by (Suffert et al. 1959)

$$Q = \frac{N_{\perp} - N_{\parallel}}{N_{\perp} + N_{\parallel}} \qquad 2.23$$

where $N_{\perp}$ and $N_{\parallel}$ are the count rates in orthogonal directions in the XY plane. By calculating the cross sections parallel and perpendicular to the polarisation vector this becomes

$$Q = \frac{\sin^2 \theta}{\varepsilon^{-1} + \varepsilon - \sin^2 \theta} \qquad 2.24$$

For increasing photon energy the maximum Q factor is achieved at progressively lower angles due to the probability of photons being forward scattered at higher energies (Figure 2.16). When fully forward or backward scattered the Q factor tends to zero and

therefore the photon can no longer give information about its polarisation through this process. The maximum Q factor also drops as the photon energy increases and above 10MeV tends towards zero.

In practice the peak value of the Q factor will be dependent on the detector used. The physical sizes and passive material as well as the detector thresholds and background will all modify the Q factor from this theoretical maximum.

2.6 Detecting Polarisation in Gamma-Ray Astronomy

With a space based mission, using a rotating detector system that is normally found in a laboratory experiment is not practical. Moving parts are often discouraged by space agencies due to the increased risk of failure. Therefore, the simplest way to build a polarimeter is to use a pixelated array. There have been many different variations in achieving a suitable polarisation sensitive detector. COMPTEL, RHESSI and INTEGRAL are all satellite missions and have met with varying success.

2.6.1 COMPTEL

COMPTEL was launched aboard the Compton Gamma-Ray Observatory in 1991. Designed for imaging, it operated in the 1 – 5MeV energy range and had a 1 steradian field of view. The instrument consisted of two detector layers, where an incoming photon could Compton scatter off the upper low atomic number liquid scintillator and then be detected by the lower sodium iodide detector (Figure 2.17)(Schoenfelder et al. 1993).

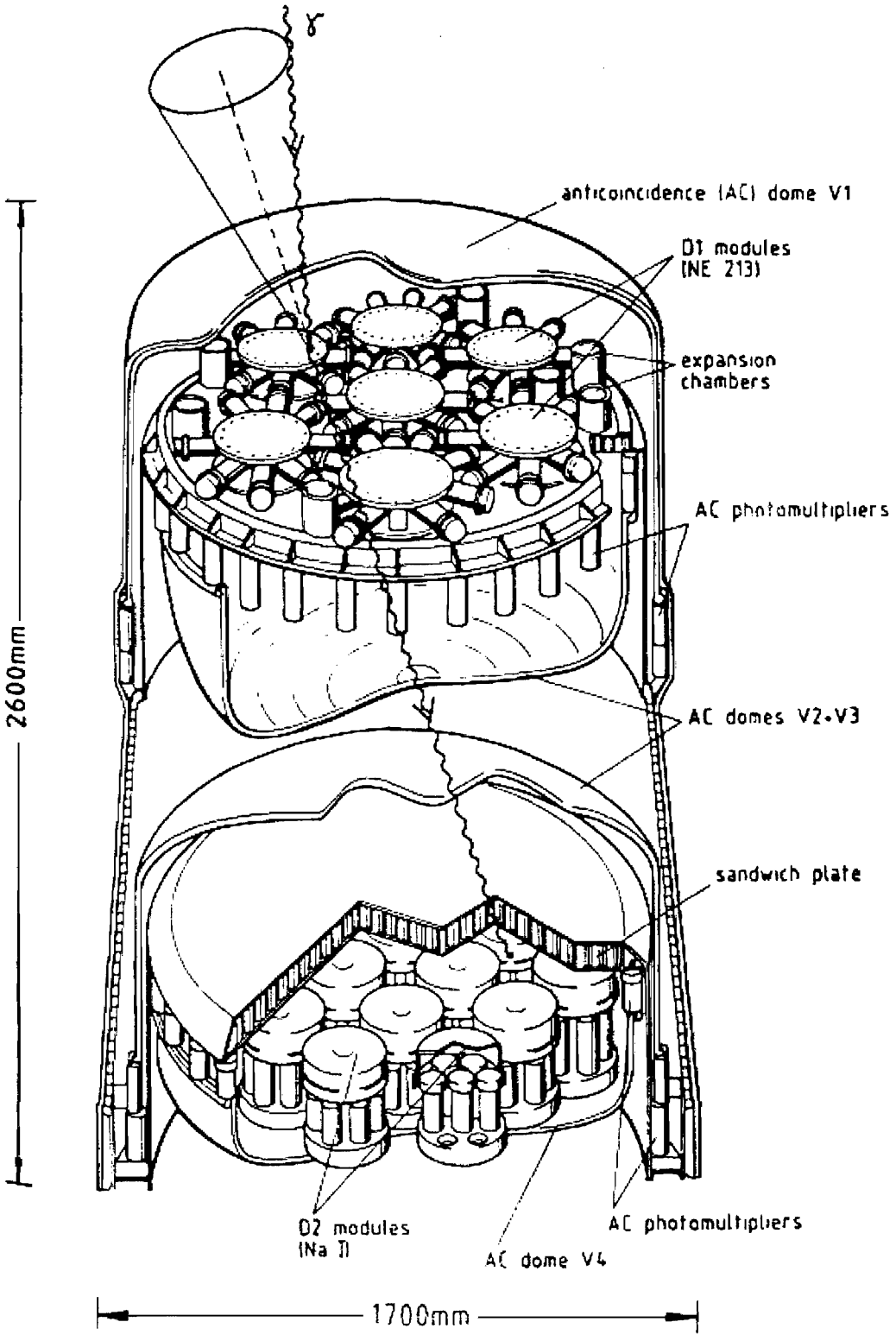

Figure 2.17: The imaging Compton telescope COMPTEL (Schoenfelder et al. 1993).

Despite the large collecting area there is a low probability that a photon will interact as required in both collecting areas, reducing the effective area to ~20cm^2. However, this technique also produces a very low background count rate. The location and energy of the two interactions gives an arc on the sky where the photon may have originated from. Overlaying many of these arcs allows a source to be located and therefore an image can be produced.

Analysis of the azimuthal scattering of these photons can be used to detect polarisation. Unfortunately, the detector was never optimised for polarimetry. The large distance between the two layers resulted in only photons with a small scattering angle being detected. An attempt had been made to detect the polarisation of GRB910503 (Winkler et al. 1992) and GRB940217 (Winkler et al. 1995) using COMPTEL. With the low background both bursts should have produced enough counts to obtain a suitable 3σ polarisation result. However, due to telemetry saturation only a fraction of the counts were recorded and a reliable polarisation result was not obtained (Hills 1997).

2.6.2 RHESSI

The Reuven Ramaty High Energy Solar Spectroscopic Imager (RHESSI) was launched in 1992 as a NASA Small Explorer mission. It is primarily designed to investigate particle acceleration and energy release in solar flares (Lin et al. 2002). The instrument consists of nine imaging rotation modulation collimators, in front of nine cryogenically cooled germanium detectors for spectroscopy (Figure 2.18). This gives the instrument an effective area of up to 200cm^2 and a spatial resolution of ~2.3 arc seconds with a field of view large enough to image the complete sun and corona (>1 degree). The spectrometers spectral resolution is ~1-10keV with an energy range of 3keV to 17MeV. The entire spacecraft is spin-stabilised at ~15rpm.

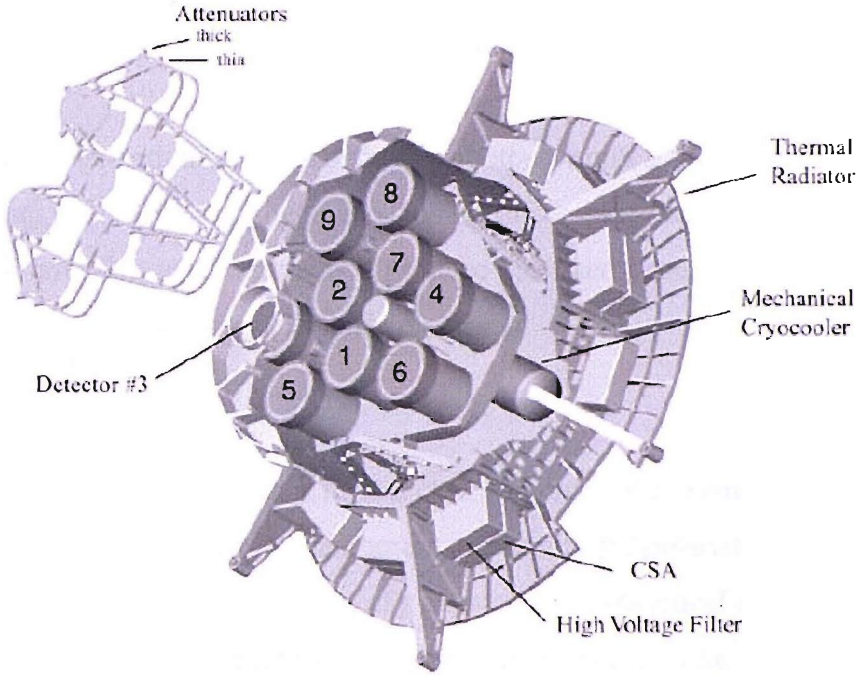

Figure 2.18: A cutaway of the spectrometer on RHESSI, showing the location of the germanium detectors under the imagers. The Stirling-cycle mechanical cooler is below the cold plate holding the detectors. The thermal radiator faces anti-sunward to reject the heat of the cryocooler. The attenuators are automatically moved when the counting rate exceeds thresholds (Lin et al. 2002).

The RHESSI array of germanium detectors are unshielded and open to the whole sky. This means that they regularly record the fluxes from GRBs and in total have seen over 300 bursts. It is possible to use the array of detectors to detect polarisation, by looking at the multiple events produced by photons Compton scattering between detectors (McConnell et al. 2002). However, due to their size and distance apart, careful consideration needs to be made over the number of false multiple events there are. A false multiple is one where the two photons interact at the same time in different detectors which look like a single photon creating multiple deposits. This was demonstrated with the analysis of GRB 021206 (Coburn and Boggs 2003) which reported a high degree of polarisation, but was reanalysed later with different assumptions and produced a much less significant result (Wigger et al. 2004).

2.7 Summary

Studying the polarisation of the gamma-ray photons emitted by an astronomical source can go a long way to helping the understanding of the emission mechanism. Almost all non-nuclear emission mechanisms will produce polarised photons with little or no need for special source geometry or physical conditions.

The polarisation of the flux can lead to a clearer picture of the emission region and the mechanism involved. Within an instrument, the search for polarisation is the search for a small systematic effect within a sea of systematic and statistical effects. If the source is known to emit with synchrotron emission mechanism at radio wavelengths and the gamma-ray emission is seen to be polarised orthogonally to the radio emission, then the gamma-ray emission mechanism is likely to be curvature radiation. Other tracers such as the polarisation percentage dropping as the energy increases can also give information about the emission mechanism, in this case indicating an Inverse Compton scattering process. Although care has to be taken to understand if this is an instrumental effect due to the Q-factor of the detector dropping as the energy increases.

The Compton scattering process is the most important in the 100-1000 keV energy range that most of the work in this thesis uses. Using a pixelated detector geometry gives a relatively simple method for detecting the polarisation of the gamma-ray photon. Due to its simplicity, most missions designed to detect polarisation will use a pixelated detector design. This will also give the detector the ability to image. The limiting factors of gamma-ray polarisation measurements are the angular resolution and sensitivity of the instruments. To date, gamma-ray missions do not have the angular resolution to examine a source in detail and so the origin of the emission region in relation to the astronomical object can be difficult to pinpoint. Since polarisation measurements usually require the full detector plane, the measurement is normally an

averaged measurement over the entire field of view, reducing the detector's sensitivity. This reduction in sensitivity is on top of the sensitivity issues already affecting gamma-ray astronomy, where measurements are usually restricted by the large background noise.

Both COMPTEL and RHESSI have been designed with polarisation in mind. However, only RHESSI was able to produce a polarisation result, which was later shown not to be significant. Using the INTEGRAL satellite will improve the chances of measuring polarisation due to its close packed pixelated detector arrays.

Chapter 3

The INTEGRAL Mission

3.1 Introduction

The INTErnational Gamma Ray Astrophysics Laboratory (INTEGRAL) was launched on 17 October 2002. Selected by the European Space Agency as a medium sized mission for the Horizon 2000 programme, it has produced invaluable results for the field of gamma ray astronomy. The current IBIS/ISGRI survey catalogue (Bird et al. 2006) is the most complete view of the gamma-ray sky to date containing upwards of 400 sources and in doing so has revealed new classes of gamma-ray objects, including the supergiant fast x-ray transients (Sguera et al. 2005; Negueruela et al. 2006) and the highly obscured HMXB (Walter and The Integral Survey Team 2004; Dean et al. 2005; Hill et al. 2005), unseen in previous surveys due to the large absorption ($N_H > 10^{23}$ cm^{-2}).

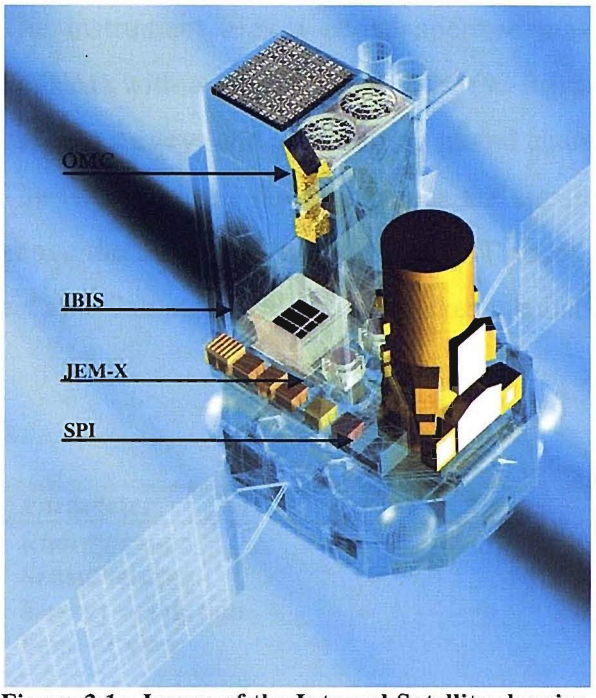

Figure 3.1: Image of the Integral Satellite showing the three main instruments on board: SPI, JEM-X and IBIS (Winkler et al. 2003).

INTEGRAL has been designed for fine spectroscopy ($E/\Delta E$ = 500) and fine imaging (angular resolution =12' FWHM) in the energy range of 15keV to 10MeV combined with X-ray and optical monitoring. To achieve these goals, INTEGRAL consists of four main instruments, the spectrometer – SPI, the imager – IBIS, the x-ray monitor – JEM-X, and the optical monitor - OMC (see Figure 3.1). All the instruments are co-aligned so that data is taken by all instruments in one pointing. The two main instruments, SPI and IBIS are both based on closely packed pixelated detector arrays, making them ideal for Compton gamma-ray polarimetry. In this section the polarimetric characteristics of the two main instruments are examined.

3.2 IBIS

The Imager on Board the INTEGRAL Satellite (IBIS) comprises of two detector planes, the INTEGRAL Soft Gamma-Ray Imager (ISGRI) and the Pixelated Caesium Iodide Telescope (PICsIT). The ISGRI detector plane is a thin pixelated Cadmium Telluride detector array working at 20-100keV (Lebrun et al. 2003b), while the PICsIT detector works between 150keV and 10MeV and is designed for optimal performance at 511keV (Labanti et al. 2003). Both detectors can be used as a Compton telescope, where the double layer discrete element design allows the tracking of gamma-rays in 3D (Ubertini et al. 2003). The complete specification of the IBIS instruments is shown below in Table 3.1.

The instrument uses a coded aperture mask to create fine imaging (12' resolution FWHM) with a large field of view (9° fully coded), making it particularly suitable for galactic surveys and determining global characteristics of the galaxy (Dean et al. 2005). The two pixelated detector planes are situated with the thinner ISGRI detector 10 cm above the thicker high energy PICsIT array. This spacing allows the two detectors to act as a Compton detector and makes it suitable for polarisation.

Table 3.1: Scientific parameters of IBIS (Ubertini et al. 2003).

Parameter	ISGRI	PICsIT
Energy range	15keV – 1MeV	150keV-10MeV
Sensitive area	2600cm^2	2890cm^2
Energy resolution	7% @ 100keV	9% @ 1MeV
Field of view	9°×9° (fully coded) 19°×19° (50% coded)	
Angular resolution (FWHM)	12'	12'
Point source location accuracy (90% error radius)	30" @ 100keV	<5' @ 1MeV
Continuum sensitivity, photons cm^{-2} s^{-1} keV^{-1} (3σ detection, ΔE=E/2, 10^{6}s integration)	3.8×10^{-7} @ 100keV	1-2×10^{-7} @ 1MeV
Line sensitivity, photons cm^{-2} s^{-1} (3σ detection, 10^{6}s integration)	1.3×10^{-5} @ 100keV	4×10^{-5} @ 1MeV
Absolute timing accuracy (3σ)	61μs	0.976 -500ms

3.2.1 ISGRI: The CdTe detector array

ISGRI detector plane contains 16384 (128 × 128) Cadmium Telluride pixels, each read-out by a dedicated electronics channel, creating a total area of 2600cm^2. Each pixel is a 2mm thick CdTe:Cl crystal, 4 × 4mm square (Lebrun et al. 2003b). Pixels are set into a ceramic polycell, 16 pixels square with a gap of 600μm between pixels. 8 polycells are contained within a module in a 32 × 64 pixel layout. 8 modules are used to produce the final detector plane with a gap of 2 pixels between each module. This setup although not ideal for imaging and polarisation studies was necessary from an engineering viewpoint. Each polycell is read-out by 4 Application Specific Integrated Circuits (ASIC) allowing the simultaneous measurement of the height and rise-time of every pulse (Arques et al. 1999). With their small area, the CdTe detectors are ideally suited

to build up a pixelated imager with a good spatial resolution. The small thickness of the pixels restricts their use to the lower energies (50% efficiency at 150keV), but the CdTe can be used at energies as low as 15keV (Lebrun et al. 2003b).

3.2.2 PICsIT: The CsI detector array

PICsIT uses 4096 (64 × 64) scintillator crystals with a photodiode readout to produce an active area of 2890cm^2. With an energy range spanning 150keV to 10MeV the detector plane fulfils the high energy range requirement of the IBIS instrument. Each pixel comprises a 3cm long CsI(Tl) scintillator crystal with an 8.4 × 8.4mm square cross section. The detector plane is separated into 8 modules with the same dimensions as the ISGRI array containing 512 pixels. The modules are 1 PICsIT pixel apart, corresponding to the same separation as that in the ISGRI detector array.

3.2.3 Using IBIS for Polarimetry

IBIS can use two methods for detecting polarisation, the previously mentioned Compton mode and using PICsIT alone. PICsIT benefits from a thick, pixelated detector plane. Incoming polarised photons can multiply scatter and leave energy deposits in multiple pixels. As previously mentioned in section 2.5 the angles of the multiple scatterings are related to the polarisation vector. The multiple scatters can be separated into two types, those that scattered between adjacent pixels and those that scattered to pixels further away. The square pixels in the PICsIT detector create 8 scattering directions between adjacent pixels. This creates a blurring on the scattering angles. All the possible scattering directions do not present the same volume to scatter into, the pixels situated at the corners of the initial pixels will have a lower count rate therefore creating a systematic modulation to the cos 2θ distribution. By increasing the distance between pixels the number of possible angles increases. However, the number

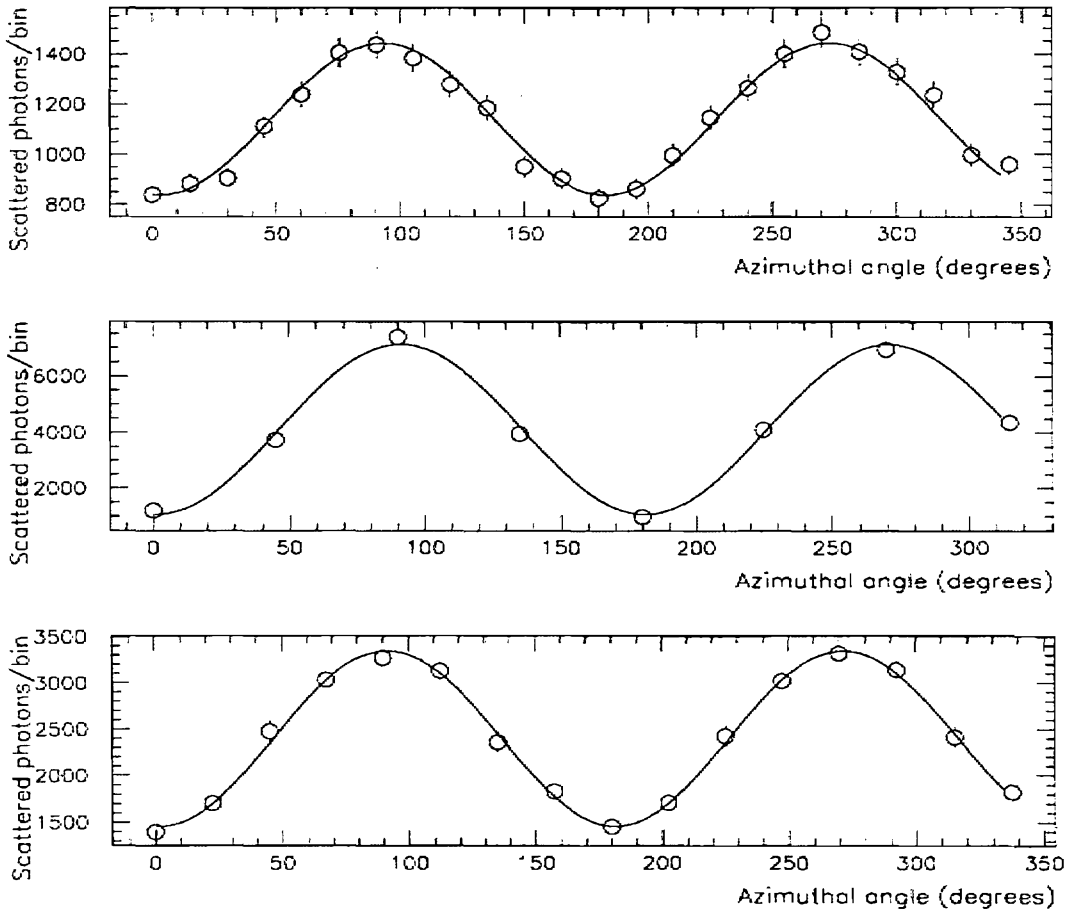

Figure 3.2: The polarimetric distribution of IBIS Compton mode events (top); PICsIT closest pixels (middle) and all PICsIT scatters (bottom), taken from (Lei et al. 1997). Systematic modulations have been removed.

of available counts will drop significantly as the photons are attenuated by the detector plane.

Using the Compton mode there is little restriction on the azimuthal angular resolution due to the pixel sizes as in the previous case. The incoming gamma-ray can scatter from any pixel in the ISGRI detector to any pixel in the PICsIT detector giving a very large number of possible scattering angles. As the distance between the interaction sites is increased, the Q-factor will increase, although the efficiency will decrease. This allows Q_{100} to be optimised for the best signal (Stephen et al. 2001). There are, however, drawbacks to the design of the detector that hinder the polarisation analysis.

The detector planes are both divided up into eight modules with a gap the size of a pixel between them. The complications of the detectors not being a continuous plane and possible edge effects caused by the hopper and veto means that great care needs to be taken in the analysis of polarisation using IBIS (Hills 1997).

Lei et al. 1997 used Monte-Carlo simulation to produce the polarimetric modulations that these methods create for 200-500 keV photons (Figure 3.1). For a flux normal incidence to the detector with the systematic modulations removed, this produces Q-factors of 0.30, 0.22 and 0.39 for the Compton mode and the two PICsIT modes respectively.

Currently PICsIT is not performing as well as expected due to systematic effects, probably caused by the background evaluation, cosmic-ray induced events, and detector non-uniformities. It is likely that this has led to very little work being carried out using IBIS for polarimetry (Segreto et al. 2003).

3.3 SPI

The spectrometer (SPI) is optimised for high-resolution gamma-ray line spectroscopy. It consists of 19 hexagonal germanium (Ge) detectors (Vedrenne et al. 2003), arranged to minimise the volume of the array and the space between each detector. Each detector is individually mounted in an Aluminium capsule (Figure 3.5) and the entire detector plane housed in a Beryllium cold box. A cryostat maintains the detectors at a constant temperature of 85K. The detectors cover the energy range 20keV-8MeV with an energy resolution of 2.5keV at 1.3MeV. Each detector measures 6.9cm in height, with a centre to centre distance of ~6cm between adjacent crystals. A coded mask is situated 1.71m above the detector plane for imaging purposes, giving a 16° fully coded field of view.

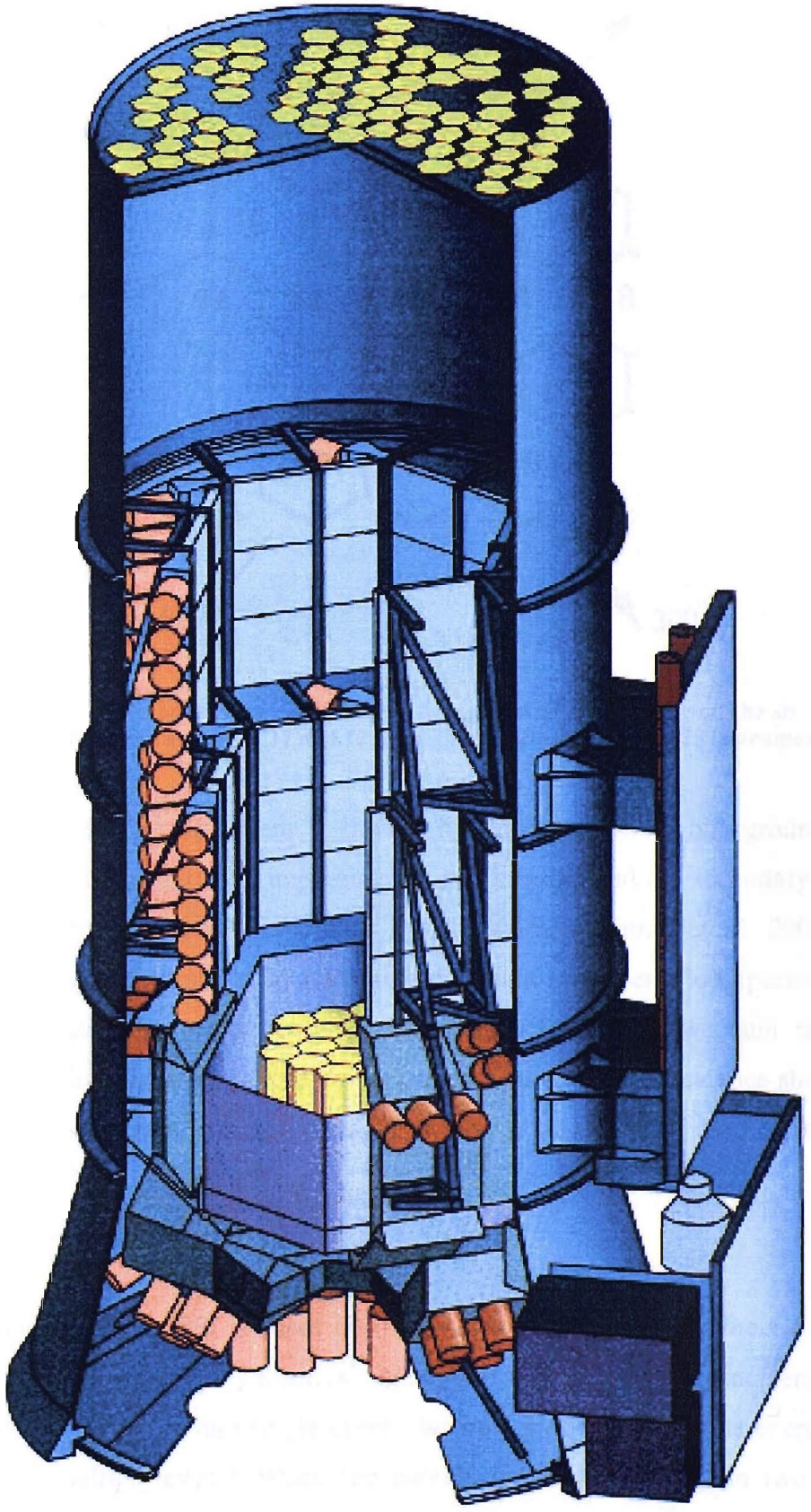

Figure 3.3: Schematic of the spectrometer on INTEGRAL (SPI), taken from ESA website.

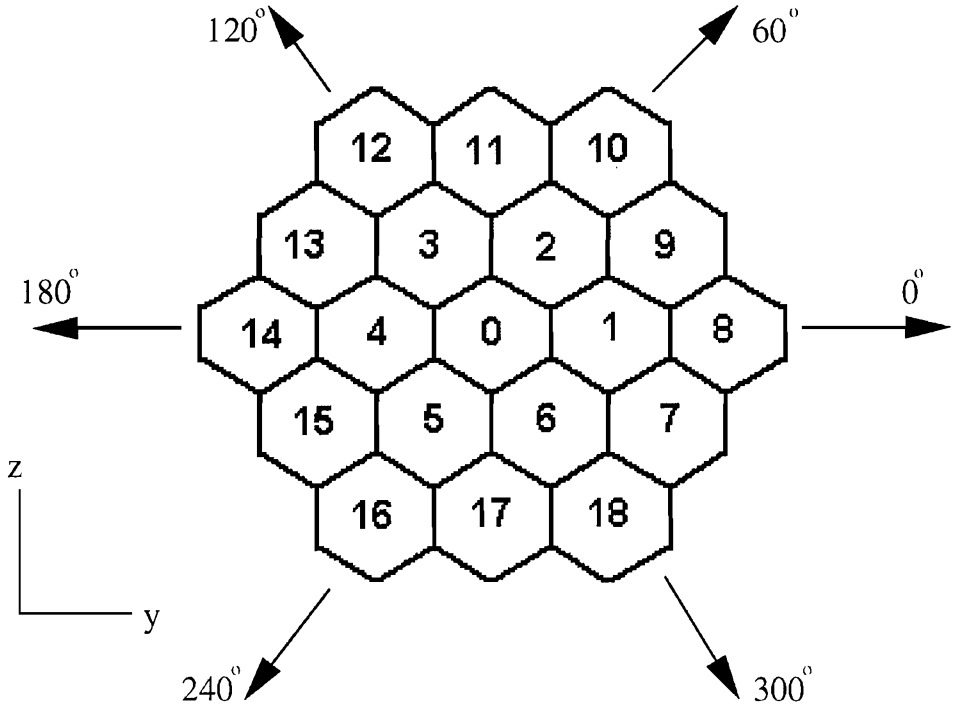

Figure 3.4: The numbering system used for the Germanium SPI detectors and the six directions in the detector plane. Detectors 10, 11 and 12 mark the side closest to the IBIS instrument.

The sensitivity of the instrument is limited by the instrumental background, which consists mainly of cosmic rays impinging on the detectors and the secondary particles created by their interaction (Jean et al. 2003; Weidenspointner et al. 2003). The background can be determined by averaging the count rate over a long period of time during the observation and subtracting this average from the raw count rate. The background is significantly reduced by the presence of an anti-coincidence shield made from BGO crystals surrounding the Ge detectors. A schematic of the SPI instrument can be seen in Figure 3.3.

The operating mode of SPI is based on the detection of events from the Ge detectors which are not accompanied by a corresponding detection in the anti-coincidence shield. The events are separated into single events, where a photon deposits its energy in one detector and multiple events, where the photon deposits its energy in two or more

detectors. All the events are processed by the Digital Front End Electronics (DFEE), which provides event timing and classification.

Detectors 2 and 17 (Figure 3.4) ceased to function on December 6, 2003 and July 17, 2004 respectively. The failure of these detectors has resulted in a decrease of the effective area of the instrument to ~90% of the original area for single events and ~75% for multiple events, due to the much larger drop in possible scattering pairs from 84 to 64. A list of the key performance characteristics of SPI can be seen in Table 3.2.

Table 3.2: SPI instrument characteristics (Vedrenne et al. 2003).

Parameter	SPI
Energy range	20keV-8MeV
Sensitive area	$500cm^2$
Energy resolution	2.5keV @ 1.33MeV
Field of view	16°×16° (fully coded) 35°×35° (zero coded)
Angular resolution (FWHM)	2.5°
Point source location accuracy (90% error radius)	<1.3°
Continuum sensitivity, photons cm^{-2} s^{-1} keV^{-1} (3σ detection, ΔE=E/2, 10^6s integration)	$1\text{-}2\times10^{-7}$ @ 1MeV
Line sensitivity, photons cm^{-2} s^{-1} (3σ detection, 10^6s integration)	5×10^{-6} @ 1MeV
Absolute timing accuracy (3σ)	160μs

3.3.1 Using SPI for Polarimetry

SPI is not optimised to act as a polarimeter, but because of its detector layout, geometry and thick detector plane (Figure 3.5), the modulation from a polarised flux can be measured through multiple scatter events in its detectors. Photons which scatter in the first detector and then scatter or photo absorb in the second and subsequent detectors, within 350ns, are termed multiple events (ME). Since the detectors are hexagonal and closely packed, the cos 2θ distribution does not suffer from the same modulation problems as a square pixel detector array. However, any distribution will be modulated

by the coded mask shadow and the dead pixels. The number of scattering directions is, however, limited to a maximum of 6 if the direction of scatter between the pixels is known. For energies less than 511keV, the photons will predominantly scatter from the detector with the smallest energy deposit to the largest (Lingenfelter and Hua 1991; Kalemci et al. 2004b). There is no positional information available about where in the crystal the energy was deposited, so angles can only be determined by the centre to centre positions of the detectors.

The Q-factor for the modulation in SPI was predicted to be ~0.17 by Lei et al. (1997) with a simulation that contained a very early estimation of the performance of the onboard electronics, but later work by Kalemci et al. (2004) and during the analysis of GRB041219a later in this thesis estimates the Q-factor to be closer to ~0.24. The properties of scattering in SPI will be examined further in the next chapter.

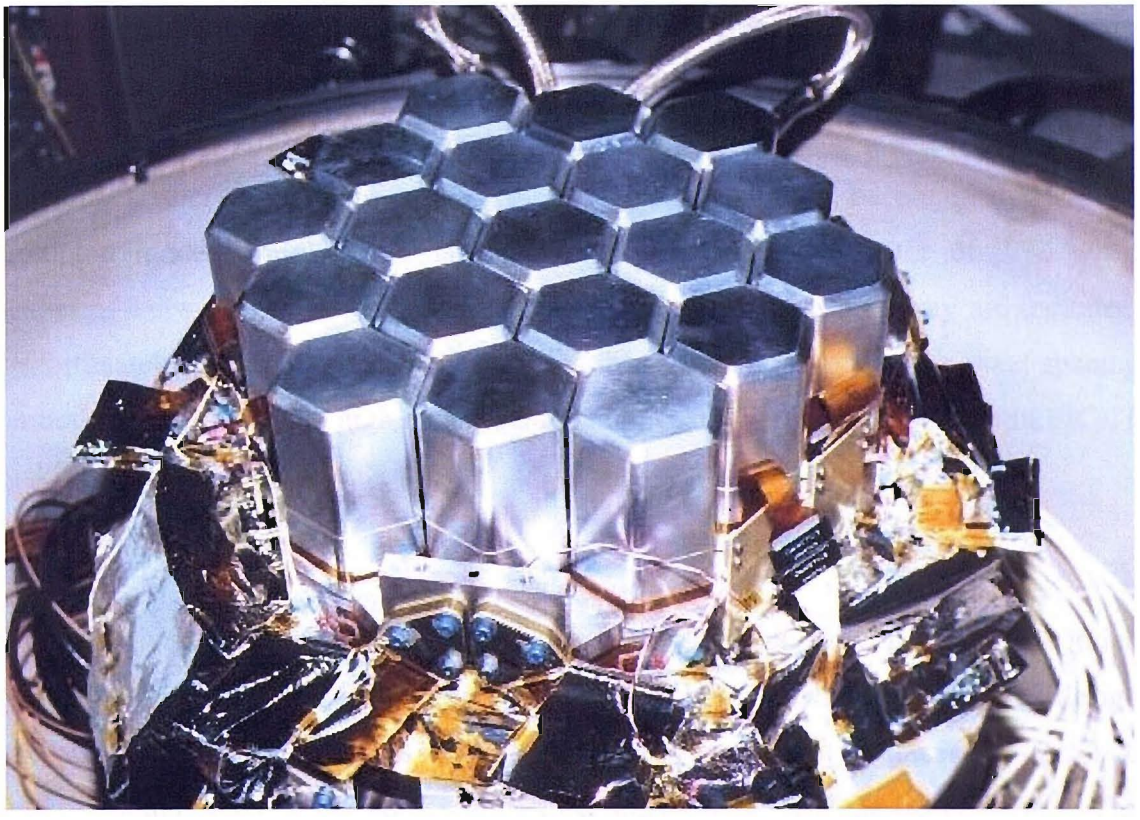

Figure 3.5: The 19 germanium pixels before installation into the spacecraft.

3.4 Summary

The ESA INTEGRAL mission has produced significant advances in the field of gamma-ray astronomy using the great imaging, spectral and timing abilities of the instruments. Although not specifically designed to measure polarisation, both the main instruments are capable of detecting the polarisation of incident gamma-ray fluxes. This ability, until recently unused, could help discriminate between models and offer a unique insight into the geometrical nature of emission zones.

The IBIS instrument provides two methods for detecting polarisation. In the Compton mode photons are scattered between the two detector arrays, ISGRI and PICsIT. The separation between the arrays and the small pixel size produces a very large number of possible scattering directions allowing a much better sampling of the polarisation modulation. The PICsIT layer is capable of polarimetry itself. The pixelated geometry provide a much higher count rate compared to the Compton mode, although the number of possible scatter directions is reduced, especially as photons are unlikely to have scattered further than a few pixels. A Q factor of 0.30 can be obtained from the Compton mode, while PICsIT is capable of producing a Q factor of 0.22 when scattering between the closest pixels and 0.39 when pixels further away are included. Unfortunately, polarimetry with IBIS suffers from non-uniformity in the pixel spacing on both detectors and the high background due to cosmic ray induced events in PICsIT making analysis very difficult.

SPI has a well shielded close packed detector with a uniform layout. The thick germanium pixels produce a large volume to stop photons, while the pixelated design allows multiple interaction sites to be recorded. The instrument produces a Q-factor of 0.24, although only 6 possible scatter directions can define the modulation. The drawbacks to using SPI as a polarimeter mainly involve understanding the effects that

may cause a pseudo-polarisation modulation in the detected count rate. The two dead pixels and the higher background count rate in the pixels closest to the IBIS instrument may produce a phantom polarisation signal. The large field of view of the instrument may also be problematic since any polarisation measurement will be an average over the entire field of view and not just that of the object of interest.

COMPTEL used two detector layers, much like the IBIS Compton mode. However, the distance between the planes was much greater, limiting the photons to those that forward scattered and therefore carry less information about the degree of linear polarisation of the incident photons. The Q factor was hence much smaller than the INTEGRAL instruments at ~0.03 - 0.1 in the 0.7 – 5 MeV energy range.

The RHESSI germanium detectors are very similar to those of SPI and produced a modulation factor of ~0.2. The rotation of the spacecraft helps the polarisation analysis, allowing the removal of systematic effects due to anisotropies in the sampling of the detectors. However, the lack of shielding and the large spacing between the detectors reduces the signal and increases the probability of random coincidence events.

INTEGRAL is currently the best mission for detecting gamma-ray polarisation. Both SPI and IBIS surpass the polarisation abilities of any other mission so far, even though not specifically designed for the task. SPI is the best instrument for attempting to measure polarisation, due to the simpler geometry. Any systematic effects due to dead pixels and non-uniform background will be easily minimised using Mass Modelling and appropriate background subtraction. This ability to detect gamma-ray polarisation will help discriminate between models and offer a unique insight into the geometrical nature of emission zones.

Chapter 4

GEANT 4 Modelling Software

4.1 Introduction

Gamma-ray photons interact with matter through a variety of complex physical mechanisms, which can be readily imitated by other particle processes. For a situation as complicated as a satellite in orbit, these physical mechanisms are too difficult to model in an analytical manner. Even though the processes themselves are very well understood in physics, the number of calculations needed would take a lifetime to complete by hand. The so-called "mass modelling" technique is a truly physics-based approach, which takes the input spectrum of a source or background emission, together with a computer representation of the mechanical structure and chemical composition of the spacecraft, to trace the trajectories and interactions of all incident particles throughout the system. The energy deposits the particles create can then be analysed in the same manner as the real instrument.

In the early days of satellite missions, "mass models" provided a method through which the final payload mass of a mission could be calculated, by combining the mass of the individual components. This was done by constructing a geometrical sequence of simple shapes combined with the material properties that represented each component. The construction of a spacecraft's geometry into a simple list of shapes was then combined with an electron and photon shower code developed for Monte Carlo simulations. The first Monte Carlo technique to study shower propogation was employed by Wilson (1952). Each photons "*fate in passing through a given interval was decided by spinning a wheel of chance*" (Wilson 1952).

With the recent dramatic increase in computer power, it has become feasible to use computer modelling to simulate the passage of radiation through matter. Modern simulations can be incredibly useful in optimising a design, allowing the ability to prototype many different designs quickly and easily. The GEANT 4 toolkit is one of the latest Monte Carlo simulation toolkits available. The subtlety of the physics included increases with every iteration of the software. However, the basic Monte Carlo technique remains, but with the ever increasing capabilities of computers, the intricate tracking of each photon and particle can be maintained to a very detailed level. The toolkit has been designed to contain all aspects of photon, lepton and hadron interactions, together with visualisation and geometry design tools, so all the user has to do is code their desired geometry.

This chapter discusses the GEANT 4 simulation software and modelling used throughout this thesis. The usage and tests of the simulations accuracy are also considered.

4.2 The GEANT 4 Toolkit

Whether the mission is in the design stage, in calibration, in orbit or in post-mission data analysis, a mass model is a vital tool for gamma-ray missions. The basic principle behind a Monte Carlo software toolkit such as GEANT 4 is to simulate a set of individual volumes that, when assembled together, match the technical designs of the instrument. Each volume includes information on the material composition and density. The simulated path of a photon or charged particle is tracked through these volumes and the energy deposits in any "sensitive" volume can be recorded. The paths are simulated for as many photons and charged particles that the instrument experiences in orbit, or at least, enough to minimise the statistical errors. The summation of the individual energy deposits will give the total counts in the detector within the modelled environment. The level of detail available is almost limitless. Every aspect of the events can be recorded but with the obvious trade-off with the size of the end product data file. The usual method is to compile a list of events with as much information on the path and products of that event as is practical.

The first version of GEANT was written in 1974 as a bare framework which initially emphasised the tracking of a few particles through relatively simple detectors. The system has been continually developed over the years up to the current version of GEANT 4 (Agostinelli et al. 2003). GEANT 4's development can be traced back to studies done by CERN and KEK in 1993 (Amako 2000) into constructing a simulation program based on object-orientated technology. A worldwide collaboration grew to develop the software consisting of over 100 scientists and engineers, including the University of Southampton. Since then the technique of Mass Modelling has been employed successfully for the calibration and design of BATSE (Westmore 2002; Shaw et al. 2003; Shaw et al. 2004), INTEGRAL (Ferguson et al. 2003) and Swift (Willis 2002).

This Monte Carlo approach is based on a pure physics and can predict the performance of any gamma-ray instrument. Only two aspects of this process are based on empirical data. The first is the measurement of the radiation environment that the instrument will encounter. The spectrum of the photons or particles measured determines the energy distribution of the input flux. The second aspect of mass modelling that is empirical in nature is the nuclear data such as cross-sections and information on isotope decay. This large amount of information is vital to determining the behaviour of the nuclear interactions and decays. If both these aspects are well defined then the simulation can be relied upon. However, an error in either of these will be replicated in the simulation and possibly magnified.

Only the availability of computing resources limits the complexity of the model that can be created. The more complex the geometry, the greater the number of interactions that must be calculated and the better the statistical accuracy needed in the count rates, the larger the number of photons that need simulating. With a very large detailed detector plane many interactions may need to be recorded increasing the storage requirements needed. Simulating the effect of an on-axis source on a satellite, such as carried out in this thesis, is fairly straight forward. A run of 50 million photons takes ~6hrs with a single modern processor (AMD Opteron 3.6GHz processor) to complete and is equivalent to the count rate ~6hrs of real instrument data. For a simulation of the instrument background, the same 50 million simulated photons is only equivalent to ~1 second of instrument background. One advantage of the photon by photon simulation is that a job may be split into smaller more manageable jobs. If a simulation of 200 million photons is required to observe a statistically significant effect, this may be too much for a single processor to model. The simulation may be split into smaller jobs of say 50 million photons, with each of the smaller jobs given to a different computer to complete. The results of these simulations can be summed together to produce the same results as a single large simulation.

With the large amount of simulations run for this thesis a single processor is not adequate. For example in Chapter 7, 500 pointings are simulated 20 times, each with 50 million photons. This equates to ~60,000 hours (~6.8 years) of CPU time, an impractical amount of time to be spent on a measurement of this scale. Access to the University of Southampton's Iridis2 Beowulf cluster allows this processing to be completed in a much shorter amount of time.

Iridis2 is primarily designed as a batch service for users who need to run either distributed memory parallel jobs, or multiple resource-intensive sequential jobs in order to explore some parameter space. The cluster comprises of:

- Over 1000 processor-cores; consisting of around 600 single-core processors and around 230 dual-core processors.
- Myrinet high-speed interconnect on 64 dual-processor nodes.
- Over 800 GB of memory.
- Over 26 TB of local disk storage.
- ~ 5TB of filestore on RAID5 disk array.

For the simulations of the Crab pulsar required for the polarisation analysis in Chapter 7, this cluster gave the ability to complete 10^{10} photons a day, reducing the total simulation time from 60,000 hours (2500 days) to 1,200 hours (50 days). This still represents a long time, but much more feasible to complete.

The simulations run manager controls the flow of the program and manages the event loop(s) within a run. When G4RunManager is created, the other major manager classes are also created. They are deleted automatically when G4RunManager is deleted. The run manager is also responsible for managing initialization procedures, including

methods in the user initialization classes. Through these the run manager must be given all the information necessary to build and run the simulation, including

- how the detector should be constructed,
- all the particles and all the physics processes to be simulated,
- how the primary particle(s) in an event should be produced and
- any additional requirements of the simulation.

The construction of a detector requires the representation of its geometrical elements, their materials and electronics properties, together with visualization attributes and user defined properties. Defining a simple shape in GEANT 4 requires three C++ objects to be created. First the "solid" object defines the properties of the shape, i.e. a box, $3m^3$. Next the "logical" object defines the interaction properties of the shape, i.e. the material, colour and if it is a "sensitive volume". Finally, the "physical" object describes the position and relation of the object to the rest of the world. Labelling an object as a "sensitive volume" means that if when tracking a photon it interacts within the volume, an event manager will be called. The event manager can be set up to record information about the particle, such as the deposited energy.

The Physics List is very important to the GEANT 4 simulations. In order to examine different processes and deal with the situation of having different theories of how an interaction mechanism works, the toolkit allows a user to specify which physics processes should be used. This has the added effect of allowing the user to strip out unneeded physics to speed up the simulation time. Since the user can define the physics involved, knowledge of the contents of the physics list is important to anyone wishing to recreate the simulation results. For this work the physics list contains all the standard physics processes and can be found in Appendix A. The only alterations that have been made are to *G4LowEnergyPolarizedCompton* as described by Mizuno et al (2005).

The original polarisation algorithm in GEANT 4 did not correctly implement the effect of photons polarisation. If an incident photon is polarised and Compton scatters, this first scatter is modelled correctly. After this scatter the photon is then treated as unpolarised for successive interactions. Thus, the azimuthal distribution of second generation scattered photons predicted by the program will be random and not contribute to the predicted Q factor. This problem was also highlighted and fixed by Hills (1997) in GEANT 3. However, the fix was not propagated into GEANT 4 although is listed for testing and implementation in a future release.

The following is the section of code from *G4LowEnergyPolarizedCompton.cc* where the polarization angle is calculated. Since the angle of cosBeta is randomly distributed, the polarization angle is also randomized.

```
G4double xParallel = normalisation*cosBeta;
G4double yParallel = -(sinSqrTh*cosPhi*sinPhi)*cosBeta/normalisation;
G4double zParallel = -(costheta*sinTheta*cosPhi)*cosBeta/normalisation;
G4double xPerpendicular = 0.;
G4double yPerpendicular = (costheta)*sinBeta/normalisation;
G4double zPerpendicular = -(sinTheta*sinPhi)*sinBeta/normalisation;

G4double xTotal = (xParallel + xPerpendicular);
G4double yTotal = (yParallel + yPerpendicular);
G4double zTotal = (zParallel + zPerpendicular);

gammaPolarization1.setX(xTotal);
gammaPolarization1.setY(yTotal);
gammaPolarization1.setZ(zTotal);
```

The suggested modification is to replace this code with:

```
xTotal = normalisation;
yTotal = -(sinSqrTh*cosPhi*sinPhi)/normalisation;
zTotal = -(costheta*sinTheta*cosPhi)/normalisation;

gammaPolarization1.setX(xTotal);
gammaPolarization1.setY(yTotal);
gammaPolarization1.setZ(zTotal);
```

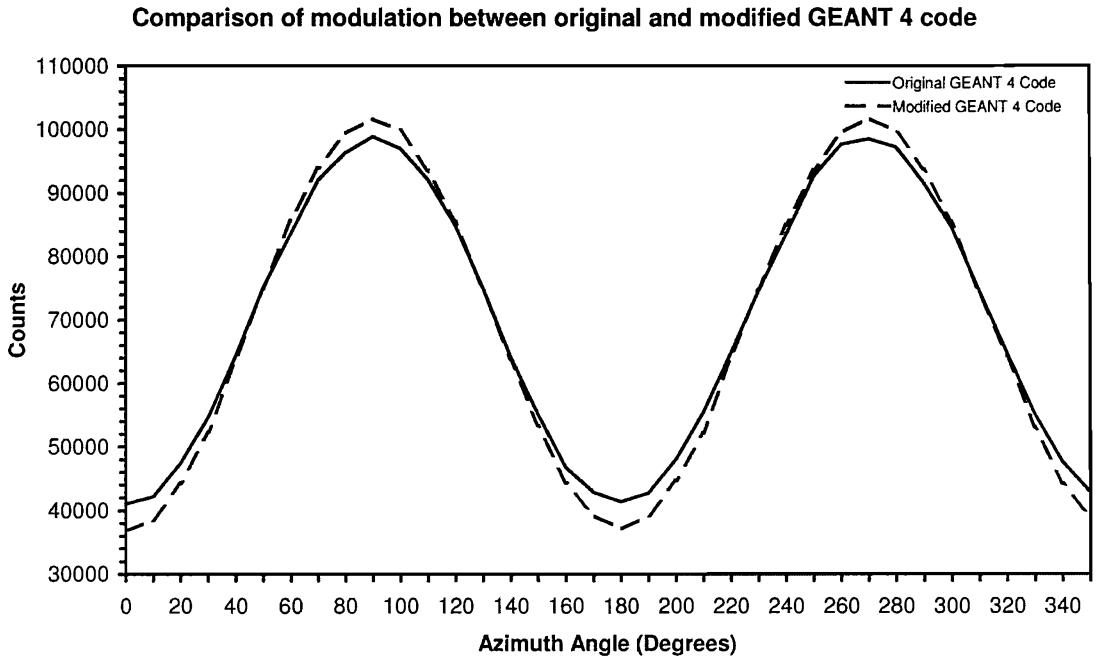

Figure 4.1: Simulated modulation due to Compton scattering in a test geometry. The solid line gives the modulation of the original GEANT 4 Compton scatter code repoducing a Q factor of 40.9% The dashed line gives the modified Compton scatter code modulation with a Q factor of 46.9%.

Testing the modification to the GEANT 4 polarisation code showed that the Q factor of a test geometry increased by 6% from 40.9% for the unmodified code to 46.9% for the modified code (Figure 4.1). This was consistent with the size of the change seen by Mizuno et al (2005). The testing of this modification by Mizuno et al (2005) and Hills (1997) indicate that this modification can be trusted to accurately predict the performance of a polarimeter.

4.3 The INTEGRAL Model

The INTEGRAL Mass Model (TIMM) was started in 1995 and aimed to create a detailed geometrical model of the whole INTEGRAL experiment (Ferguson et al. 2003). INTEGRAL is very complex and due to the penetrative nature of gamma-rays,

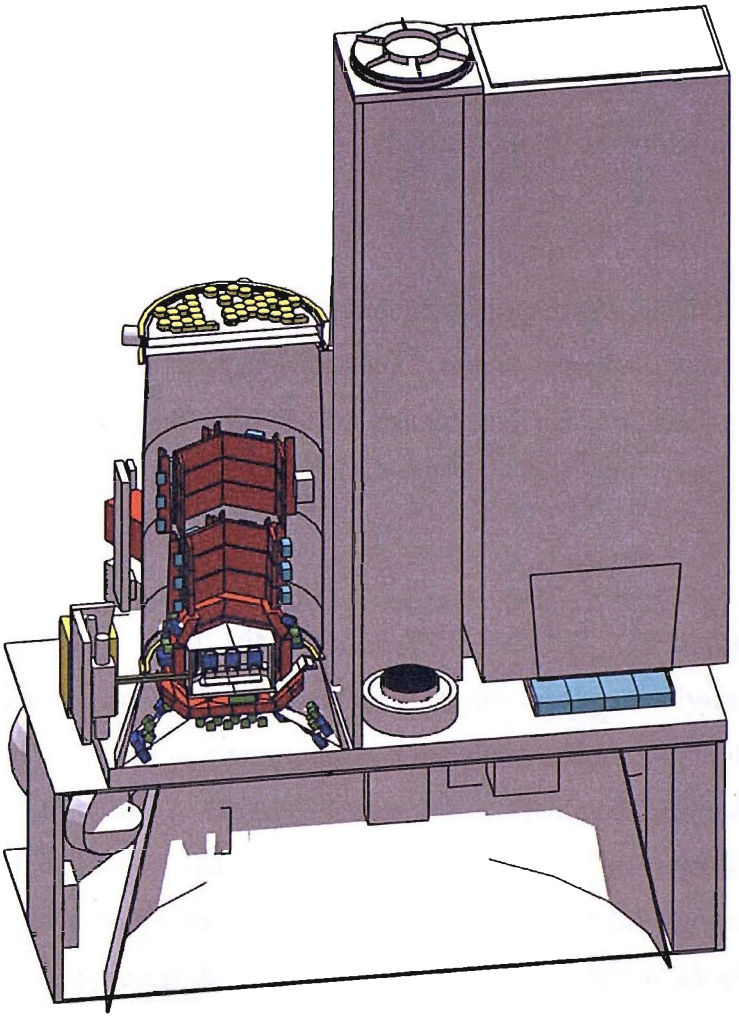

Figure 4.2: The GEANT 4 INTEGRAL Mass Model geometry.

the individual instruments can affect each other's performance. Although the instrument teams are responsible for the design and modelling of their own instruments, experience from past missions proved it was necessary to have an independent system-wide modelling programme to assess or provide support to the following aspects of INTEGRAL:

- Overall background modelling – including the effects of the local environment;
- Instrument design issues including internal event rates and telemetry requirements;
- Possible shadowing of one instrument by another or spacecraft structure;
- Independent assessment of instrument sensitivities;

- Analysis software development;
- Payload Ground Calibration (PLGC) activities;
- Post-launch problem solving and system configuration validation.

The main tasks of TIMM were to build an independent geometrical and chemical model of the entire INTEGRAL payload and spacecraft, and to perform intensive Monte Carlo simulations, thus providing a unified background and performance evaluation of all instruments (Dean et al. 2003).

The original model was coded using the GEANT 3 toolkit. This was a FORTRAN based package that required a lot of external software for data analysis and spacecraft activation calculations. The current model is a recoded version of the GEANT 3 model into the GEANT 4 framework. GEANT 4 uses object orientated C++ and includes extra physics such as polarisation and material activation. In the new model, the SPI and JEM-X detectors have both been fully modelled. However, at the current time the IBIS detector only has an approximate geometry (Figure 4.2). For the work in this thesis this

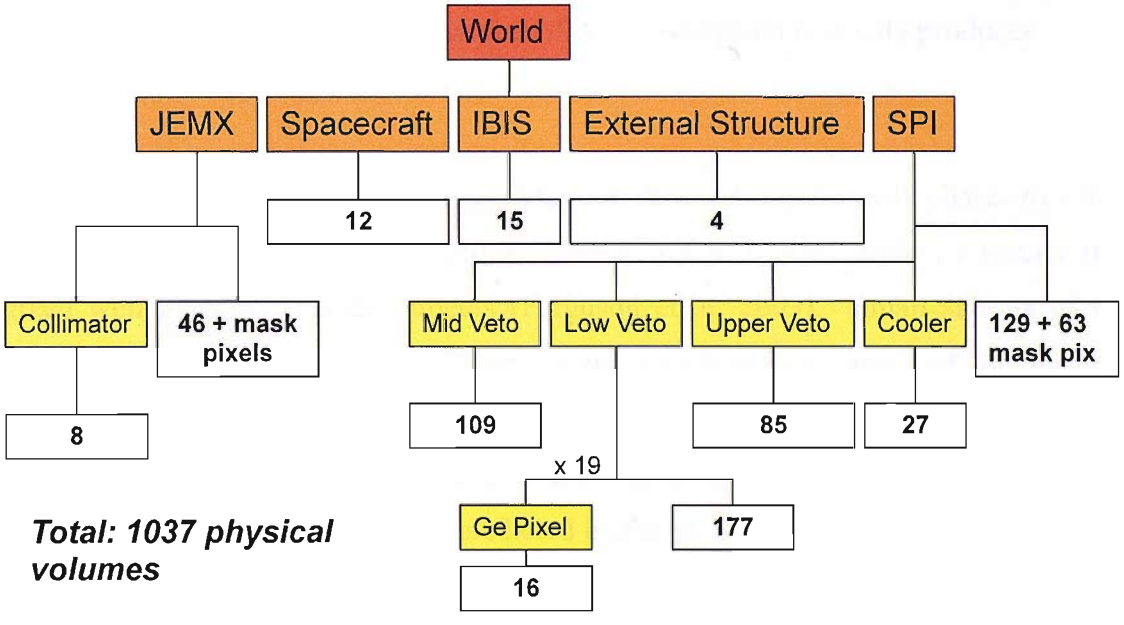

Figure 4.3: Schematic breakdown of the INTEGRAL Mass Model.

does not pose a problem since this work revolves around the SPI instrument. Mass situated away from the SPI instrument will have little or no impact on the results from this instrument. The SPI instrument has been modelled with a high degree of accuracy and comprises the active veto, the Ge detector elements inside a Be housing, and the mask assembly. The detector array consists of 19 hexagonal pixels with a side-length of 3.2 cm and a length of 7 cm, encapsulated in aluminium housing. The array is mounted on a cold plate contained in a cryostat made from Beryllium. The BGO veto shield consists of a massive hexagonal container around the Ge-detector and a collimator extending up towards the mask. The thickness of the BGO crystals is 4.5 cm to 6 cm. The mask assembly consists of 63 hexagonal shaped tungsten elements, 3 cm thick, with a 6 mm plastic scintillator veto underneath. A complete breakdown of the geometry can be seen in Figure 4.3. The GEANT 4 incarnation of the INTEGRAL model was specifically written to assess the line background in the SPI instrument. This meant that there were several areas of particle generation and geometry that had not been coded in the simulation that would become important in simulation the emission from an astronomical object. The exact geometry of the coded mask and the ability to generate photons with a spectrum matching that of a GRB and the Crab required implementing. The simulation output required a large amount of reduction to produce an output that resembles that of the instruments electronics instead of the lists of deposits within sensitive volumes that the GEANT simulation normally produces.

INTEGRAL was the first mission to use mass modelling from the early phases to aid in design, optimisation and background estimation. The model produced results that agreed well with the real instruments (Ferguson et al. 2003). Small subsets of the payload ground calibration (PLGC) runs were modelled, with most of the features present in the real data reproduced by the simulations (Figure 4.4). The biggest difference between the real and simulated data was due to the supplied source positions, while the features observed but not predicted by the simulation were used to update the model.

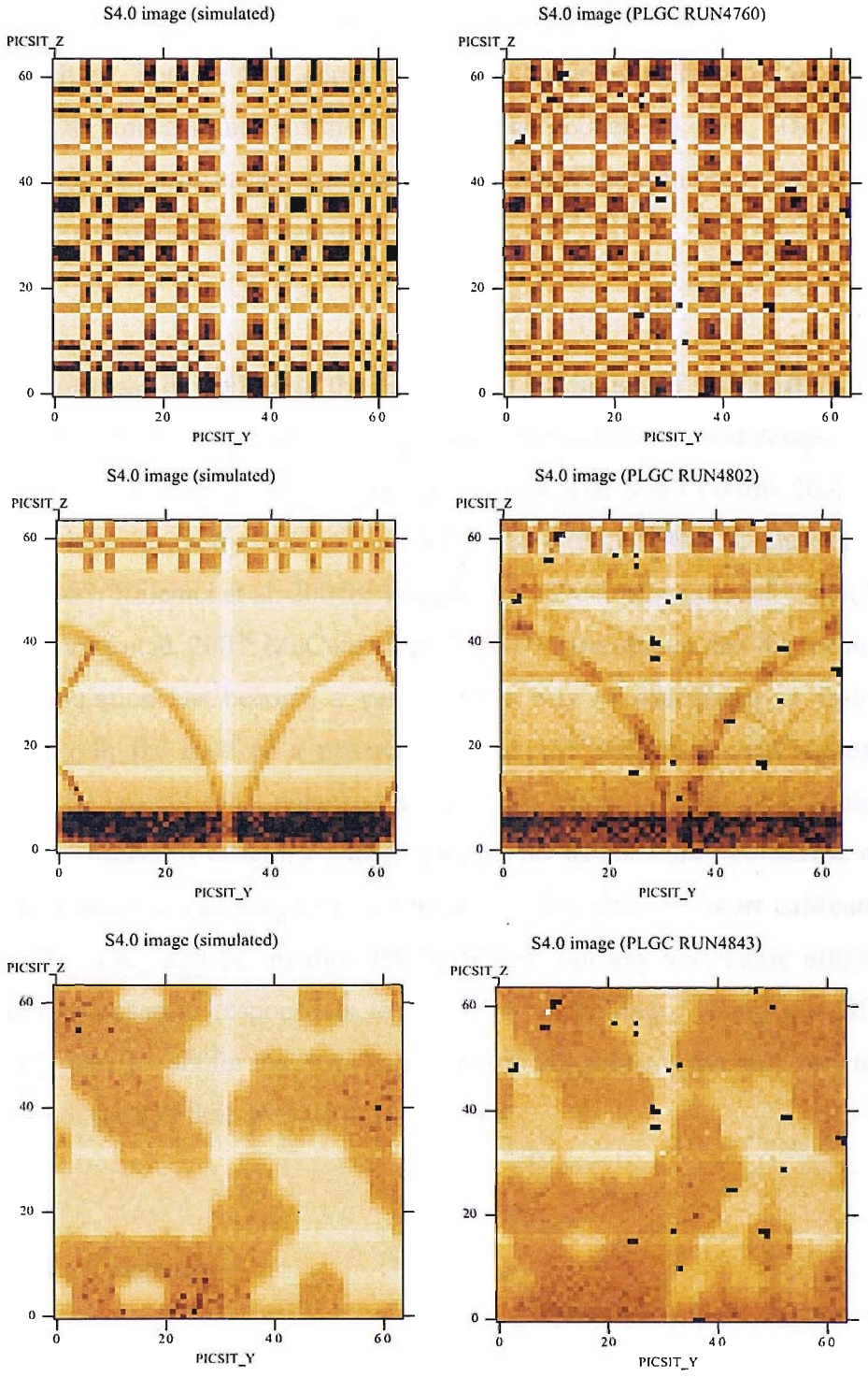

Figure 4.4: Comparison of simulated and real PICsIT shadowgrams produced with TIMM (left) and the payload ground calibration (right) for different source positions. Top: the on axis illumination of the PICsIT detector showing the shadow created by the IBIS mask. Middle: the illumination of PICsIT from the edge of the partially coded field of view, clearly showing the shadow of the JEM-X mask. Bottom: the illumination of PICsIT from an off axis angle where the source shines through the SPI mask onto the detector. The images are slightly offset due to inaccuracy in the supplied source position (Ferguson et al. 2003).

Pre-launch simulations of the in-flight background within the instruments agreed very well in the shape, but the total count rates were lower by a factor of ~2. This was explained by an underestimate of the cosmic ray component in orbit. The model also predicted a non-uniform background in IBIS that may have limited sensitivity if not accounted for appropriately (Ferguson et al. 2003).

The success of mass modelling in the background prediction of INTEGRAL(Ferguson et al. 2003; Jean et al. 2003; Kalemci et al. 2004a), the calibration and design of BATSE (Westmore 2002; Shaw et al. 2003; Shaw et al. 2004) and Swift (Willis 2002), and the successes of the polarimetry code in GEANT 3 and 4 (Hills 1997; Stephen et al. 2001; Dean et al. 2003; Kalemci et al. 2004b; Wigger et al. 2004; Mizuno et al. 2005; Willis et al. 2005; Kalemci et al. 2007; McConnell et al. 2007) have shown that the technology of computer simulation has become a very reliable way of describing an instrument's performance. In the case of a mission such as INTEGRAL it was impossible to calibrate on the ground for a polarised source. Obtaining a source that could evenly illuminate the spacecraft weighing ~4000kg with a polarised beam ~4m across would be nearly impossible and certainly couldn't be achieved within the short calibration time available. The only suitable method for calibrating out any systematic effects in the instruments polarisation response is to use mass modelling. Using the GEANT 4 INTEGRAL mass model for the work carried out in this thesis is the only way to predict the response of the SPI detector to a polarised flux.

4.3.1 Source Positioning

Source positioning is important in the simulations. If the source is not located correctly with respect to the spacecraft, the mask will not create the correct shadow on the detector plane, leading to differences between the modelled events and the real events. This can be seen in the PLGC simulations in Figure 4.4.

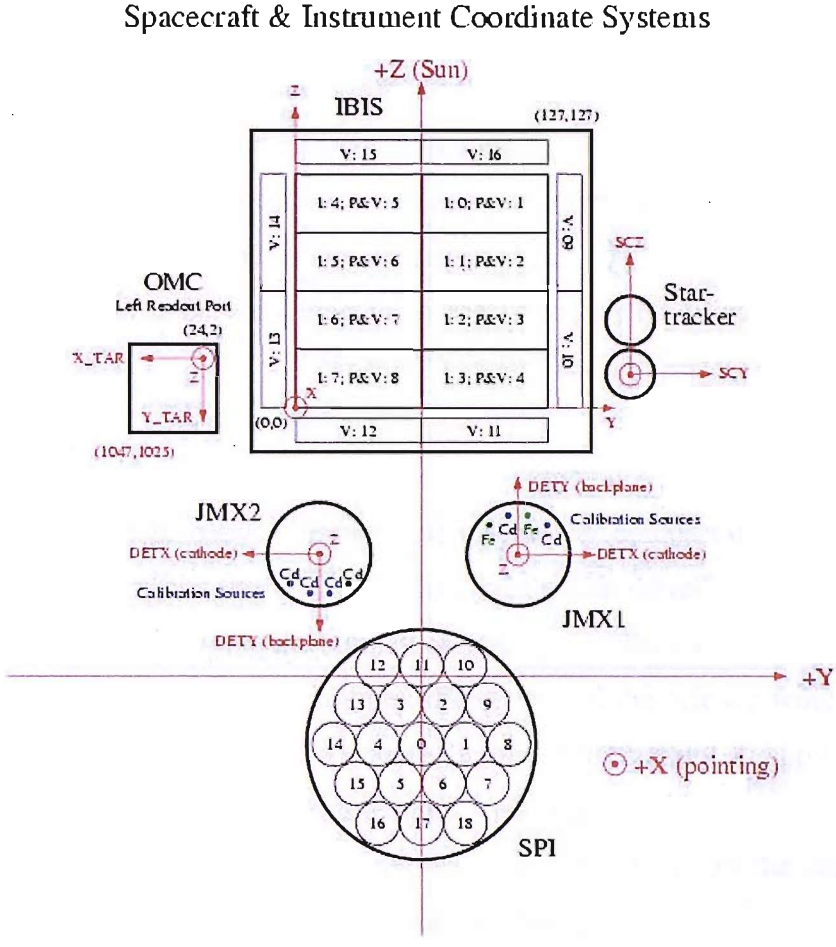

Figure 4.5: Spacecraft & Instrument coordinate systems (Barr and Kuulkers 2003).

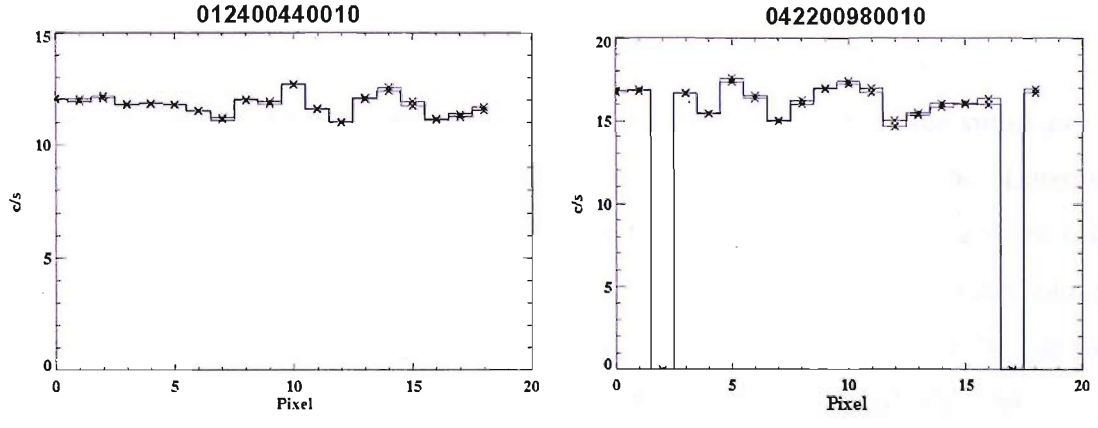

Figure 4.6: Comparison of the real photon count rates for 2 Crab SCWs to the simulated output and background files. SCW 012400440010 produced a best fit of 0.98 while SCW 042200980010 produced a best fit of 1.06.

Each SPI real data file contains the position and roll of the spacecraft during the observation. The RA and DEC measured are the direction that the spacecraft x-axis is aligned to. The roll angle is measured as the angle between the z-axis and the north celestial pole in a clockwise direction, when looking down the x-axis in the +x direction (Figure 4.5). These measurements are all measured in a spherical coordinate system on the sky and so need to be converted in to the Cartesian coordinate system used in GEANT.

Checking the coordinate conversion was carried out by comparing the single events from the Crab observations to the single events of the simulation. Obviously, the real data included background while the simulation does not so the background files used in the Crab analysis are used to make up the difference. All the science windows used in the analysis produced a reduced chi square fit of approximately 1, showing that the simulated Crab data combined with the empty field observations used as background produce a very good description of the real data. Figure 4.6 shows the comparison of the real data to the simulation output for two Crab observations.

4.3.2 Thresholds and Veto

The threshold values for the detectors and veto must also be applied in the simulation to create a more realistic output. Veto thresholds effect the detector dead time. Lowering the veto threshold below ~50keV will result in the veto system triggering more often due to background photons which are unlikely to pass through the veto crystals, causing the detector to be turned off for longer periods. Above ~80keV the main background component is cosmic rays which will pass through the veto easily. If the veto triggers on a cosmic ray the detector will be turned off to avoid recording the background event as a source event. In practice, since the simulation only includes source photons which in most cases are on-axis, and no background photons, the veto makes little difference

to the results (<<1% error), only a very small effect to the count rates in the outer detectors, which is reduced further by the energy range chosen for the analysis. However, they are still included since they will have a larger effect for observations substantially off-axis.

In the real observation data the detector dead time will have a larger effect on the results and this must be taken into account. Any unevenness in the veto effect, due to different thresholds for different veto crystals or higher veto count rate on one side of the instrument, will cause the dead time to be different across the detector plane. This could create an anisotropy in the scattering count rate that may be mistaken for a polarisation signal.

The simulated Ge detector thresholds have been set to 20 keV, the same as those of the SPI instrument at launch. For the Anti-coincidence shield (ACS) things are a little more complicated. The value of each BGO block is different and ranges from ~24 to 170 keV. These values have also changed in flight with no way to verify their values. However, an approximation of 80 keV has been used and verified as acceptable with the instrument working group (Jean 2005). All the thresholds are blurred with a Gaussian probability function to approximate the response of the front-end electronics.

4.4 Using the Simulation to Detect Polarisation

The Klien-Nishina cross-section for a polarised photon describes the probability that a photon will Compton scatter in a specific distribution. On average the photons will scatter orthogonally to the polarisation vector (Lei et al. 1997). However, a single photon may scatter in any direction. The detection of this azimuthal modulation in the real data is the goal when trying to detect polarisation. The analysis in its most basic

form is comparing a simulated detector response to the real detector response. Each observation is modelled 20 times, to show the expected response of the instrument if the source is 100% polarised at an angle of 0 - 180 in 10 degree steps, and once for an unpolarised flux. These simulations produce the counts that the instrument will produce if the source is polarised at each of the angles, not including any background components. It would be possible to model the background as well, however, the simulation time would increase by a factor of ~10. This means the background must be subtracted from the real observation data, either using the observations before and after a transient event like a GRB, or using separate empty field observations for a persistent source such as the CRAB pulsar. With the simulation predicting how the detector responds to each polarisation angle, this data can then be compared to the real data to find the closest match. With the assumption of an accurate model and source position the simulation will be a good match for the real data minus any background.

The SPI observation events are processed using the OSA 5.1 (Diehl et al. 2003) barycentre command and the count rates are dead time corrected. Each multiple event is converted into a scatter direction on the detector plane. The count rates in each direction are converted to a percentage of counts scattered into each direction to allow the comparison with the simulated data without the need to worry about scaling the data by the length of the observation. The unpolarised and polarised simulation data can be combined to produce any percentage polarisation (Π) needed using

$$\boldsymbol{P_{\%}} = \frac{\boldsymbol{\Pi P_{100}}}{\boldsymbol{100}} + \frac{\boldsymbol{(100-\Pi)P_0}}{\boldsymbol{100}} \qquad 4.1$$

where P_{100}, P_0 and $P_{\%}$ are the 100% polarised simulation data, unpolarised simulation data and percentage polarisation data. Since the change due to polarisation angle is a smoothly changing function, it is possible to interpolate between the simulated files, therefore making it possible to produce data sets simulating any polarisation angle and

percentage of polarisation. Each of these data sets can then be fitted to the observation data using a chi squared test to find the best fit.

4.4.1 Obtaining Directional Information

The pixelation of the SPI detector plane allows us only to detect scatters in 6 directions. Unfortunately, there is no positional information on the interaction site from within the pixel, so all interactions must be assumed to be between the centres on the pixels. Detailed modelling of the interactions within a pixel show that it is possible for a photon to scatter at almost 90 degrees to the centre-to-centre direction, although this is unlikely. The distribution of interactions produces a near Gaussian profile with the maximum at the centre direction and with a FWHM of ~25 degrees, consistent with the dimensions of the pixels (Figure 4.7) and showing that most coincident events occur close to the edge of the detector. There is no information on whether a photon scatters from detector A to detector B or detector B to detector A. Although there have been suggestions that this information can be gained from the relative sizes of the energy deposits (Lingenfelter and Hua 1991; Kalemci et al. 2004b), this has been ignored due to adding in a further assumption. This reduces the number of unique possible scatter directions to 3. The count rate in each of the 3 directions is converted into a percentage of the total number of scattered photons. This removes any need for normalisation between the number of counts in the simulation and the real data.

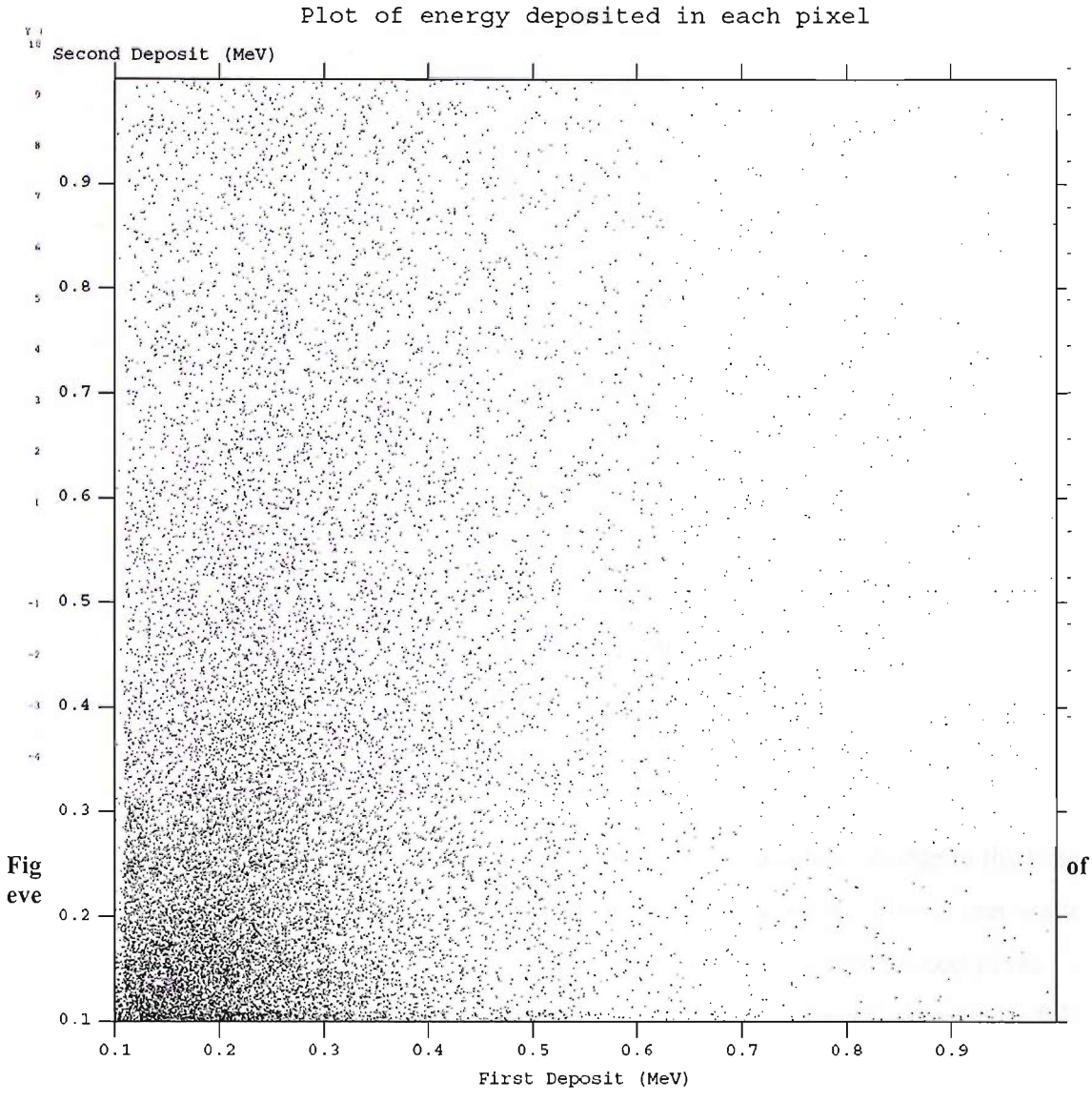

Figure 4.8: Plot of energy deposited in the first and second pixel in multiple events. There is no obvious correlation between whether the first or second pixel has the largest energy deposit.

Kalemci et al (2004b) reported that for energies less that 511 keV, the direction of scatter between two pixels could be deduced from the energy deposits. This argument was based on the work by Lingenfelter and Hua (1991). If a photon of less than 511 keV deposits energy in a pixel through Compton scattering, the deposit is likely to be less than half of the photon energy. If a photon scattered into an adjacent pixel forming a multiple event, the remaining energy will be deposited in the second pixel. This

would mean that the pixel with the smallest energy deposit is the first pixel in the scattering pair. Occasionally there may be a second scatter in the first pixel giving this pixel the largest energy deposit. Using this information it would be possible to split the number of directions in the SPI detector from three to six.

Looking at the scattered energy deposits in the simulated data the effect cannot be seen. This could either be due to the original assumptions of Lingenfelter and Hua (1991), or the implementation of polarised Compton scattering in the GEANT 4 code. Although increasing the number of possible angles from 3 to 6 may be possible, it is probably not advisable. Any improvement that may be gained in fitting over six angles will probably be lost in the uncertainty of the simulation and the reduction of counts in each angle. Using six directions was experimented with for GRB041219a, however, it was dropped from further analysis.

Separating the scatters in to six directions will lead to more information due to the mask covering some pixels. If a pixel is covered by a mask shadow, then a photon can scatter into the pixel, but will not scatter from the covered pixel to the illuminated pixel. In practice most pixels will be partially covered with only a few being fully open or fully closed. This will lead to a small number of scatters in some directions and a larger number in the opposite direction. In order to simulate this scenario the source position must be exact. A small offset in the source position can lead to a large change in the mask shadow. This is likely to cause the poor fitting seen in the analysis of GRB041219a using six directions. Reducing the number of directions to three, removes the effect of the mask and therefore produces a better fit between the simulated and observation data.

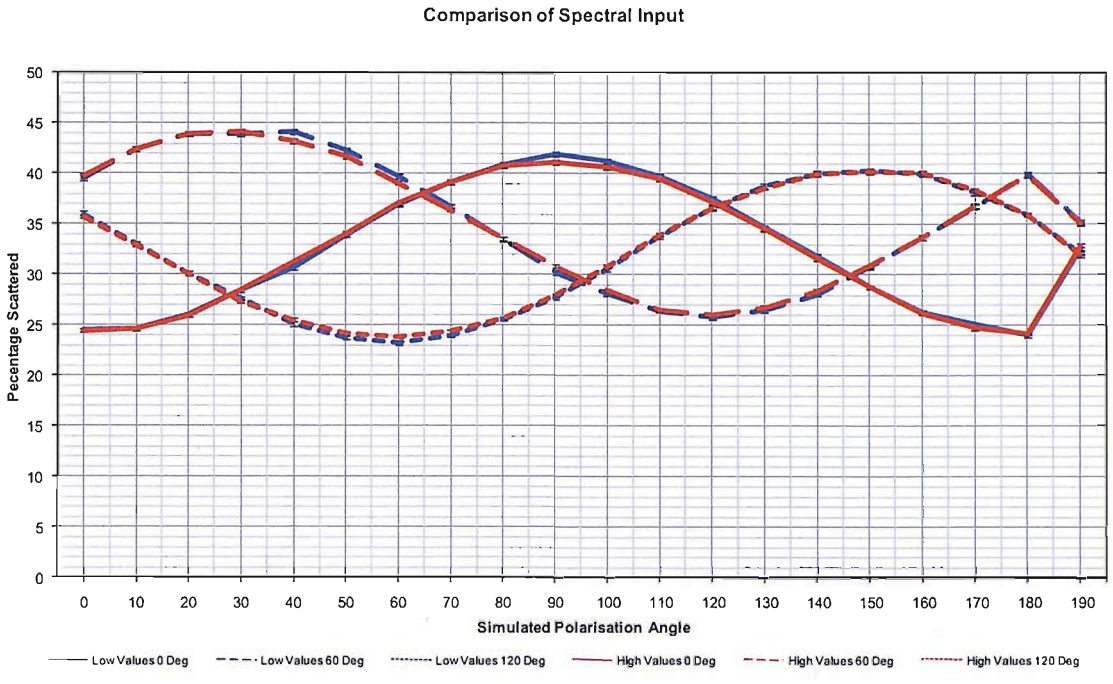

Figure 4.9: Comparison of modulation for upper and lower spectral values of GRB041219a.

4.4.2 Variation in the Source Spectrum

The variation of modulation with the spectrum of the source is an important area for consideration. The reduction of the Q-factor with increasing energy is already known from the theory; how this translates into a system with a real spectrum needs to be examined. This has important implications in the modelling of the incident flux. Any spectrum measured from real observations will include errors. These errors can normally be minimised greatly, but will still be present. Including these errors in the production of the flux in the simulation is not trivial and will greatly increase the processing time of the simulation. Instead, the average spectral parameters are used in the generation of the emission.

The first test is to discover how much the errors will affect the simulation results. Using the Band model spectral parameters of GRB041219a, spectra based on the extreme

errors are simulated and compared. The limits are taken to produce the hardest and softest spectrum. The same number of photons are simulated, so the incident flux is constant between all tests.

Table 4.1: Band model parameters obtained from the errors of the spectral fit for GRB041219a used for spectral test. The parameters α and β are the indices of the spectral slopes before and after the spectral break at the energy E_{break}.

	Soft Limits	Hard Limits
α	-1.40317	-1.32317
β	-1.74	-2.03
E_{break}	525.589	787.889

A comparison of the modulation produced by these two sets of parameters can be seen in Figure 4.9. It is clear in the case of the GRB that the errors in the spectral parameters

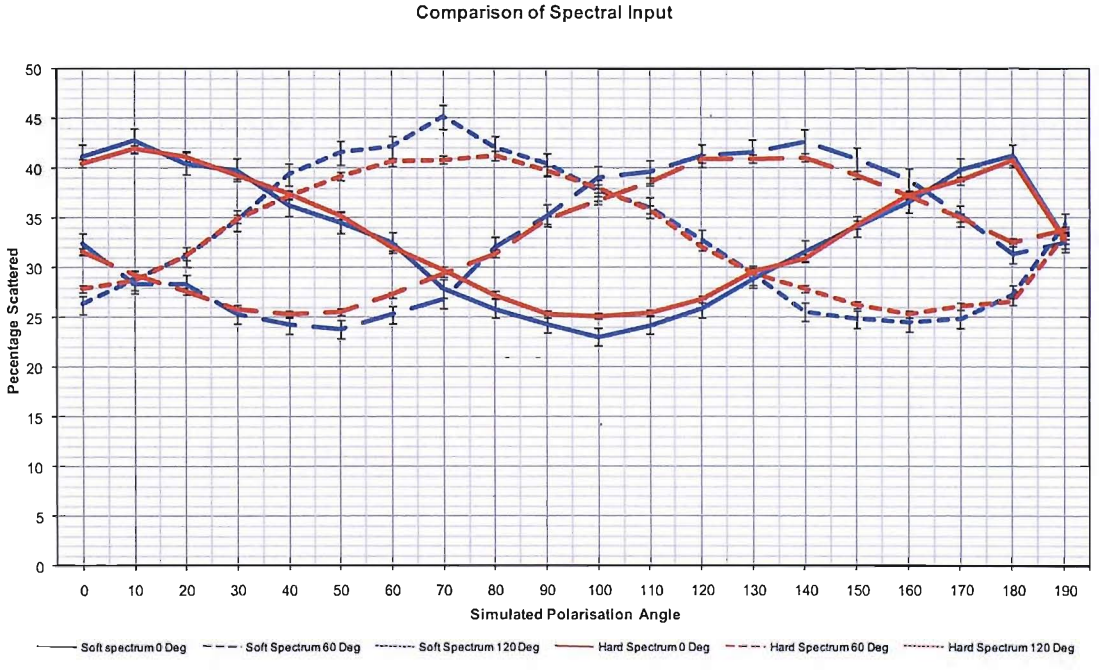

Figure 4.10: Comparison of simulated modulation for a 'hard' input power-law spectrum of α = -1.5 (red) and a 'soft' power-law of α = -3 (blue).

make little difference to the modulation seen in detector count rates, changing the measured Q factor by >2%. This situation considered a small change in the spectral values. Consideration needs to be made as to what a bigger change will make.

In order to test this, a simple power law is used for an on-axis source. A simulation of 50 million photons with a power law slope of -3.0 is compared to a simulation of a much harder spectrum with a slope of -1.5. As can be seen in Figure 4.10, these two significantly different power-laws produce a small difference in the modulation seen in the count rates (<10%). This is small in comparison with the large change in the power-laws. This will only effect the determination of the percentage polarisation. However, a spectrum should always be determined better than the change simulated here.

One noticeable change between the two simulations is the errors derived from the count rates. With the harder spectrum there are many more photons available with energy large enough to create a multiple event. This is reflected in the errors where the hard spectrum has error bars of ~1% while the softer spectrum has errors of ~2.5%, even though both simulations modelled 50 million events. The Q factor for each spectrum has been calculated to be Q = 25.3 ± 1.5 % for the hard spectrum and Q = 33.3 ± 3.0 % for the soft spectrum, showing that the softer spectrum has the larger modulation but also the larger error.

4.4.3 Analysis Energy Ranges

Determining the best energy range for the analysis requires knowledge of the performance of the instrument in several ways. The instrument's sensitivity to polarisation, the background, the source spectrum and the overall efficiency of the detector are all important in calculating the best figure. From the theory of Compton

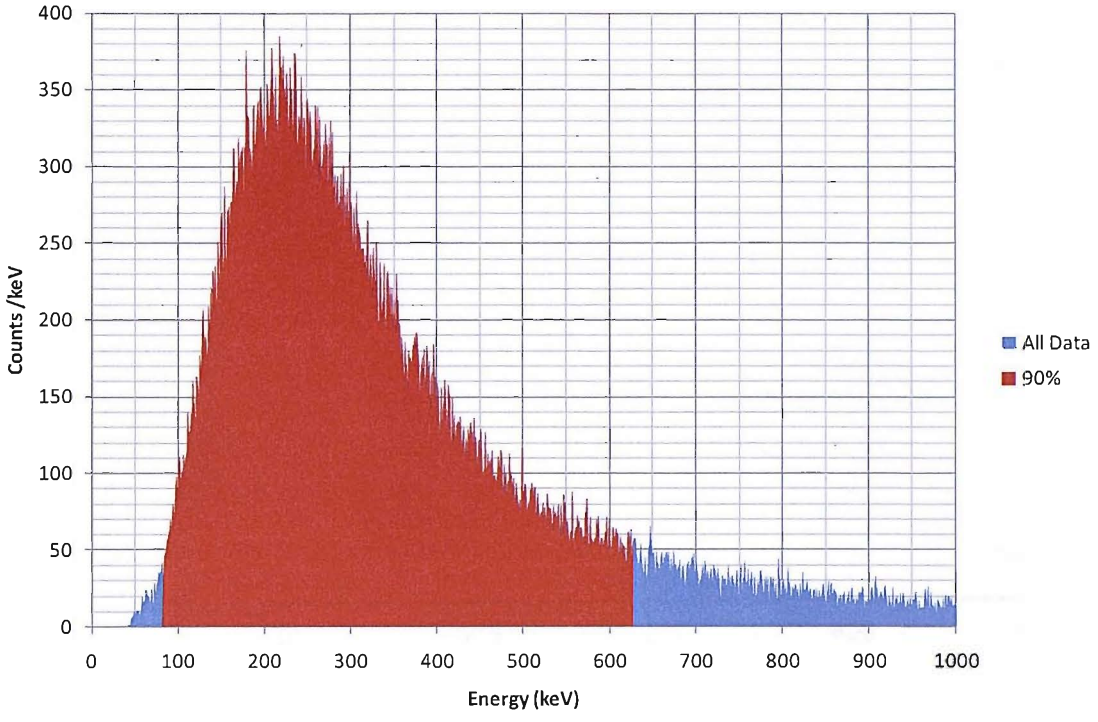

Figure 4.11: Multiple event spectrum for GRB041219a (blue). The distribution is a result of the input spectrum and detector efficiency for multiple events. 90% of the events fall between 85 keV and 630 keV (red). The peak of the counts is ~225 keV.

scattering we would expect the best energy for the analysis to be centred around the rest mass of the electron, where the likelihood of scattering perpendicular to the photons direction is greatest. However, this value will likely come down due to the sensitivity of the instrument.

Plotting the multiple event count rate from the GRB041219a simulations as a function of energy shows that the peak of the sensitivity is ~225 keV (Figure 4.11). Finding the smallest energy range over which 90% of the events occur will give the best signal to noise. This will be weakly dependant on the spectrum of the source and for GRB041219a equates to 85 - 630 keV. This energy range already takes into account the sensitivities of the detector and the production of multiple events, as well as the incoming burst spectrum.

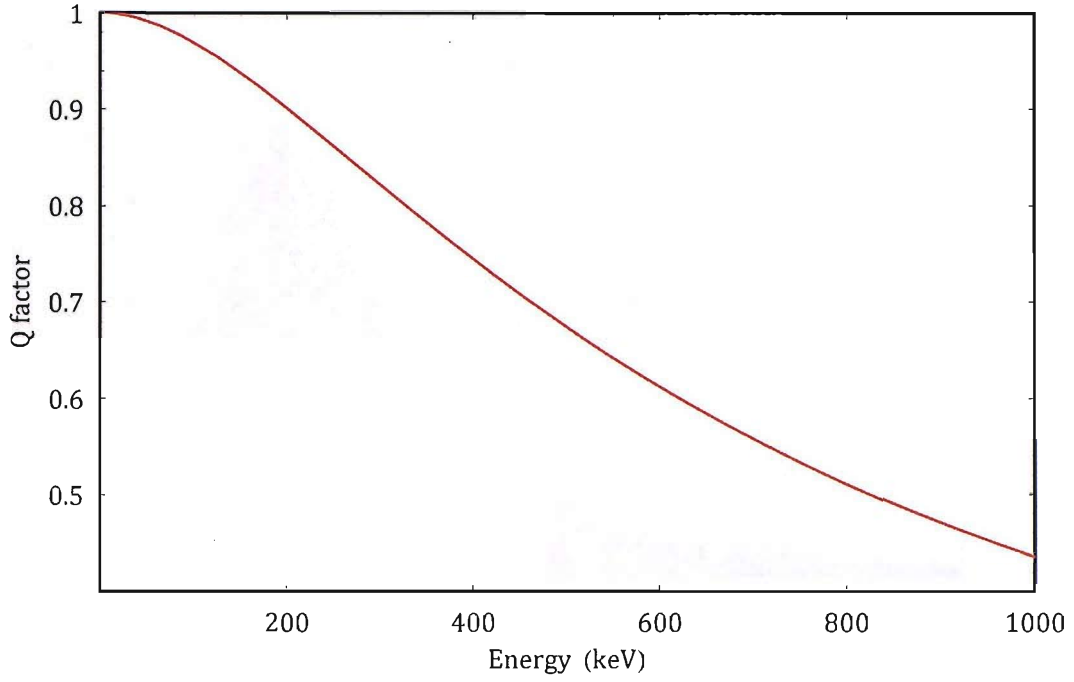

Figure 4.12: Variation of the Q factor representing the modulation due to a polarised flux with energy for a scattering angle of 90°.

By including the Q-factor, we modify the distribution to include the size of the modulation as a function of energy. Ideally a larger modulation is more desirable since the polarisation will be easier to detect. The Q-factor is

$$Q = \frac{N_{\perp} - N_{\parallel}}{N_{\perp} + N_{\parallel}} \tag{4.2}$$

where $N_{\perp}$ and $N_{\parallel}$ are the count rates in orthogonal directions in the XY plane. By replacing the count rates with the cross section for the scattering at 90°, the Q factor becomes

$$Q = \frac{\frac{\left(\frac{1}{x}-x\right)r^2}{2x^2} - \frac{\left(\frac{1}{x}+x\right)r^2}{2x^2}}{\frac{\left(\frac{1}{x}-x\right)r^2}{2x^2} + \frac{\left(\frac{1}{x}+x\right)r^2}{2x^2}} \tag{4.3}$$

with

$$x = 1 + \frac{E}{m_e} \tag{4.4}$$

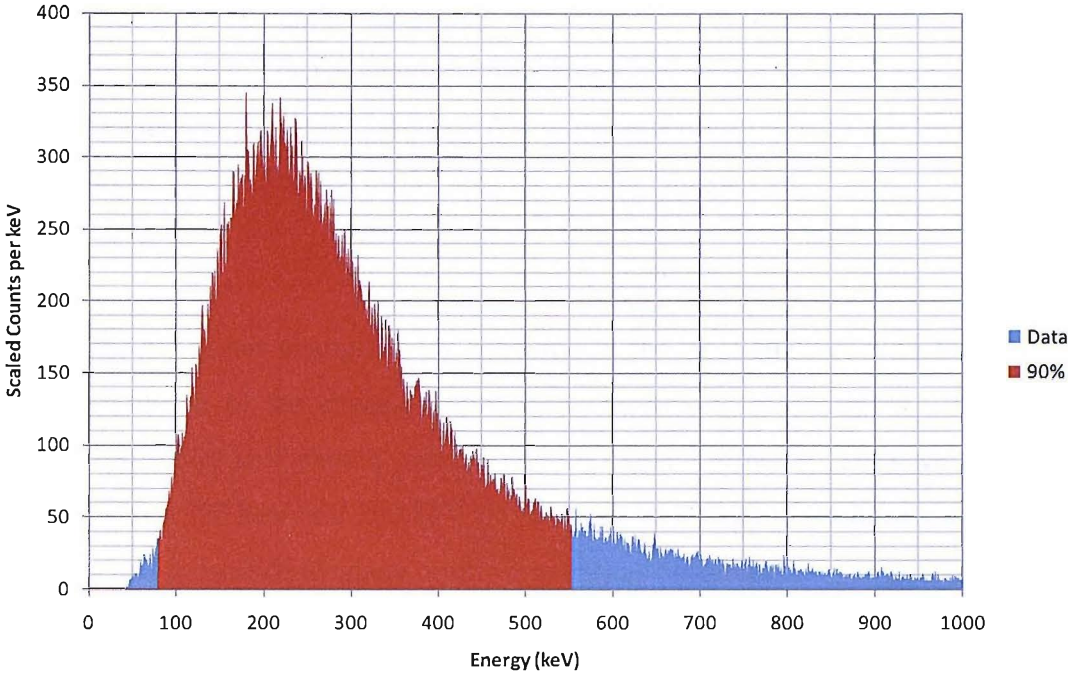

Figure 4.13: Multiple event spectrum folded together with the modulation size (blue). 90% of the counts fall between 81 keV and 554 keV (red).

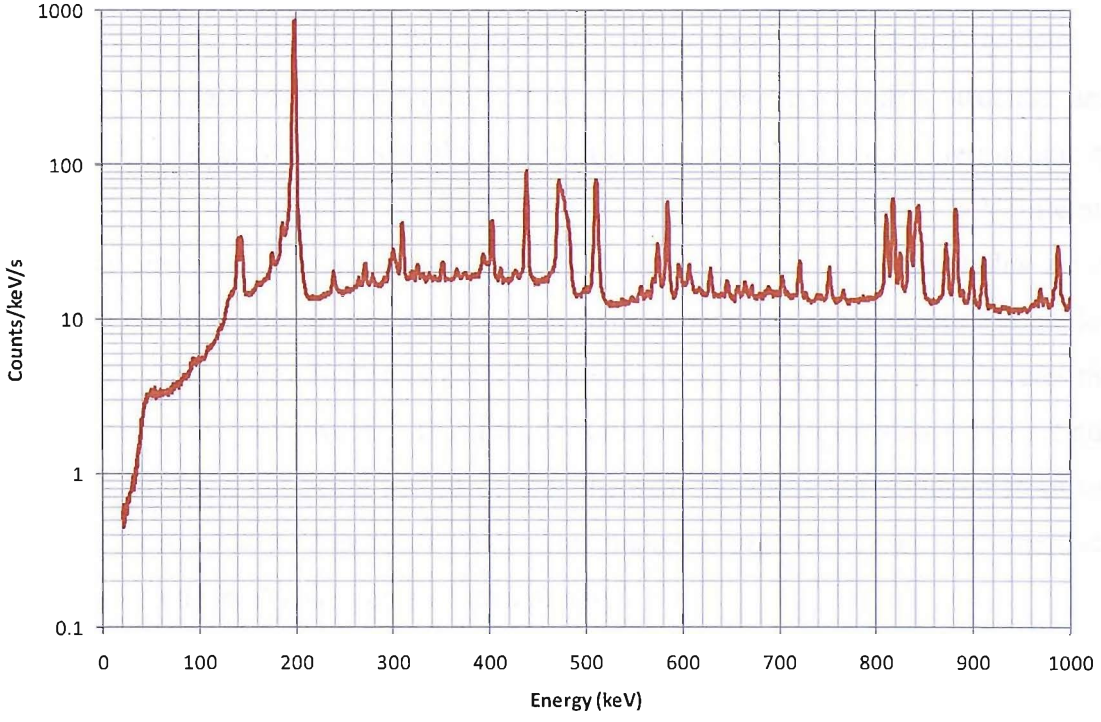

Figure 4.14: SPI multiple event background spectrum.

and where E is the energy of the photon and m_e is the rest mass of the electron. Figure 4.12 shows how the Q factor changes with energy. It clearly shows that a lower energy produces a larger modulation. Adding this to the sensitivity of the detector produces an energy range of 81 - 554 keV for 90% of the data (Figure 4.13).

This energy range has changed very little and in the final analysis with the low count rates optimisation of the energy ranges to a few keV is meaningless. For the final analysis 100 – 500 keV should produce the best signal to noise. However, the energy ranges of 100 - 350 keV and 100 keV - 1 MeV are also used to examine the peak of the efficiency and to include as many multiple events as possible.

The background models for the SPI instrument are very good. The multiple event background has been analysed by the SPI team and shown not to vary much with time (Kalemci et al. 2004a). The multiple event background noise spectrum is reasonably flat (Figure 4.14). However, large spectral lines can be seen caused by the radioactivity induced within the materials in the instrument. These lines are produced by delayed decays due to spallation and neutron activation within the spacecraft's structure and detectors. The biggest and potentially the most damaging line is that of Germanium at 198 keV. This line actually consists of a line at 175 keV and a 23 keV internal conversion electron (Kalemci et al. 2004a). With the SPI detector thresholds set at 20keV the electron will immediately deposit its energy in the pixel, while the photon has enough energy to reach another pixel before its energy it deposited. This creates the large line in the multiple events. This line does not appear in the simulated data set due to delayed emission not being included. For this reason events are excluded from the analysis between 184 keV and 201 keV. This makes a huge difference and improves the fit between the real and simulated data greatly.

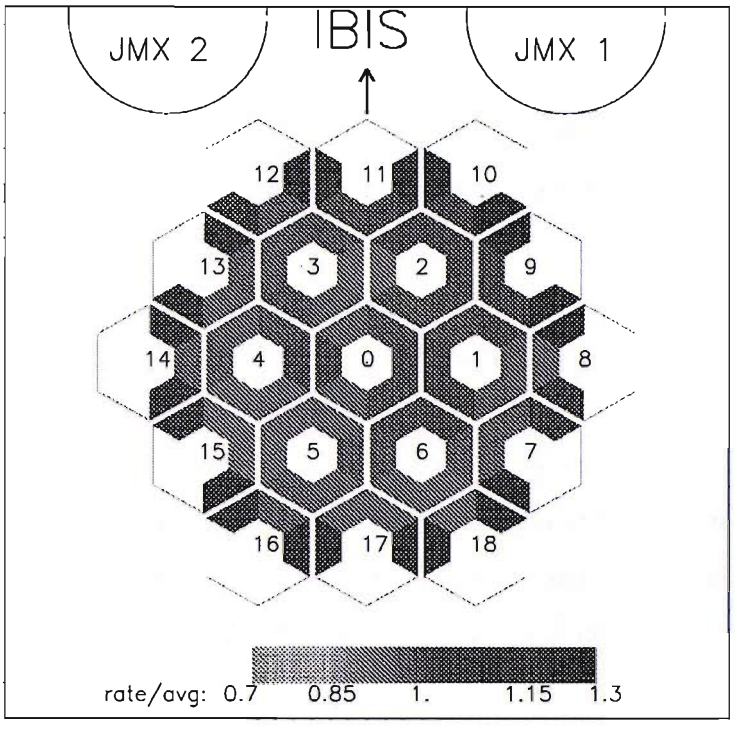

Figure 4.15: The map of multiple event continuum count rates with respect to the average count rate at low energies (E<200 keV). The positions of other detectors on the spacecraft are shown for reference (not to scale) (Kalemci et al. 2004a).

4.4.4 Anisotropies in the Multiple Event Scattering

In order to have any trust in the polarisation results it is important to understand what effects may cause a false polarisation signal. If there are any differences between the numbers of photons scattered into each direction this could be interpreted as a modulation caused by the polarisation of the source. In practice, there are many ways in which a difference in the scattered count rate for each direction may occur. In SPI the background, dead time, mask shadow and dead pixels will all affect the scattered count rate.

The multiple event background count rate in the SPI has been studied by Kalemci et al (2004a). Figure 4.15 shows the continuum distribution of background multiple events. There is clearly an inhomogeneity in the distribution of rates. The outer pairs of

detectors have a higher count rate than that of the inner detector pairs. The detector pairs 8-9, 9-10, 10-11 have significantly higher count rates (~20% higher than average). This region is towards the IBIS and JEM-X1 detectors, which may be responsible for the variations (Jean et al. 2003). As the energy range is increased, the distribution of multiple event scatters across the detector plane becomes more uniform. At energies greater than 800 keV the distribution is very nearly homogeneous with only a slight excess towards JEM-X1. The excess counts in these pixels will increase the number of scattered events counted in the 120° direction in the detector plane (defined in Figure 3.4). This in turn will lead to a polarisation signal orthogonal to the excess count rate. Correctly subtracting the background using empty field observations or the data before and after a transient event will remove this anisotropy effect. However, a weak source may prove difficult to background subtract due to the small number statistics involved.

The dead time of the pixels may also cause an anisotropy in the detector plane. An uneven background triggering the veto will cause differing dead times in each pixel. It may be possible for a large incoming flux (e.g. a GRB) on one side of the instrument to trigger the veto and switch off the detectors on one side of the detector plane. With no dead time correction the count rates in directions relating to the pixels involved will be lower and cause an unwanted anisotropy. Each SPI observation contains the dead time data for each of the pixels which can then be used to remove the effects in the count rates.

The shadow of the mask on the detector plane is an important part when imaging with the SPI instrument. Unfortunately, for polarisation measurements it can produce another unwanted anisotropy in the detected scattering rates. A pixel covered by the mask will have photons scatter into it, but is unlikely to have photons scatter out of it. This problem is minimised when only using three directions on the detector plane, instead of six, as the counts in and out of the pixel in the same direction are summed. The most damaging effect is when the source is off axis, since the mask may severely

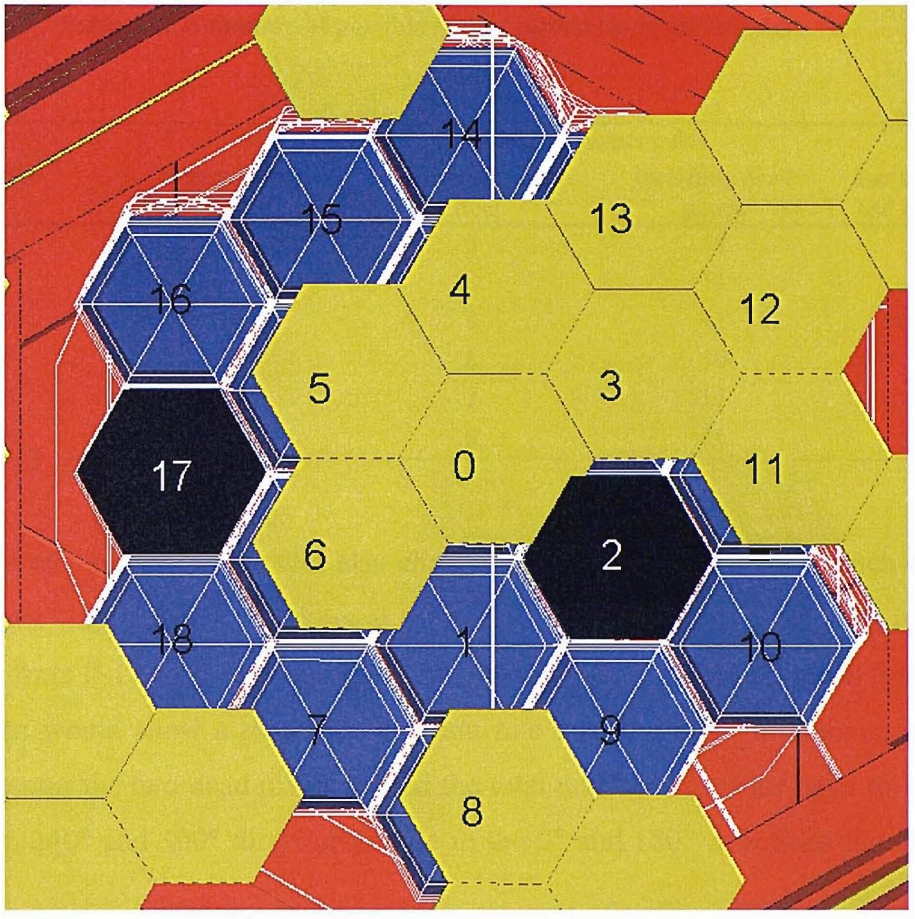

Figure 4.16: Position of the SPI mask with respect to the SPI detector plane at an off axis angle consistent with that of GRB041219a. The black pixels are the two pixels that have failed in SPI.

reduce the possible number of scatters in one direction. Figure 4.16 shows how the mask covers the SPI detector plane for a source position consistent with that of GRB041219a. In this position the number of scatters recorded from 13-14 will be much small than for 14-13. In total there are 14 scatter pairs for each direction on the detector. If the mask is assumed to either cover a pixel completely or completely uncover a pixel in Figure 4.16, then the number of scatters in each direction is much less. The number of scatters in each direction can be seen in Table 4.2.

Table 4.2: Summary of possible scatter directions in the SPI detector.

Direction	Number of scatter pairs			
	Detector only	Including mask effect	Including dead pixels	Including mask and dead pixels
0	14	6	10	3
60	14	8	11	6
120	14	8	11	5
180	14	6	10	3
240	14	5	11	2
300	14	6	11	5

The effect of the dead pixels will also change the number of scatters in each direction. An example can be seen by looking at the possible scatters from pixel 1. It is possible to scatter from 0-1 and 1-8, 6-1 and 1-9, 7-1 but not 1-2. This would mean that the 7-1-2 direction would show a much lower count rate than the other directions. Over the entire detector the two dead pixels reduce the total number of scatter pairs to 11 for the 60°, 120°, 240° and 300° directions while in the 0° and 180° directions the number of

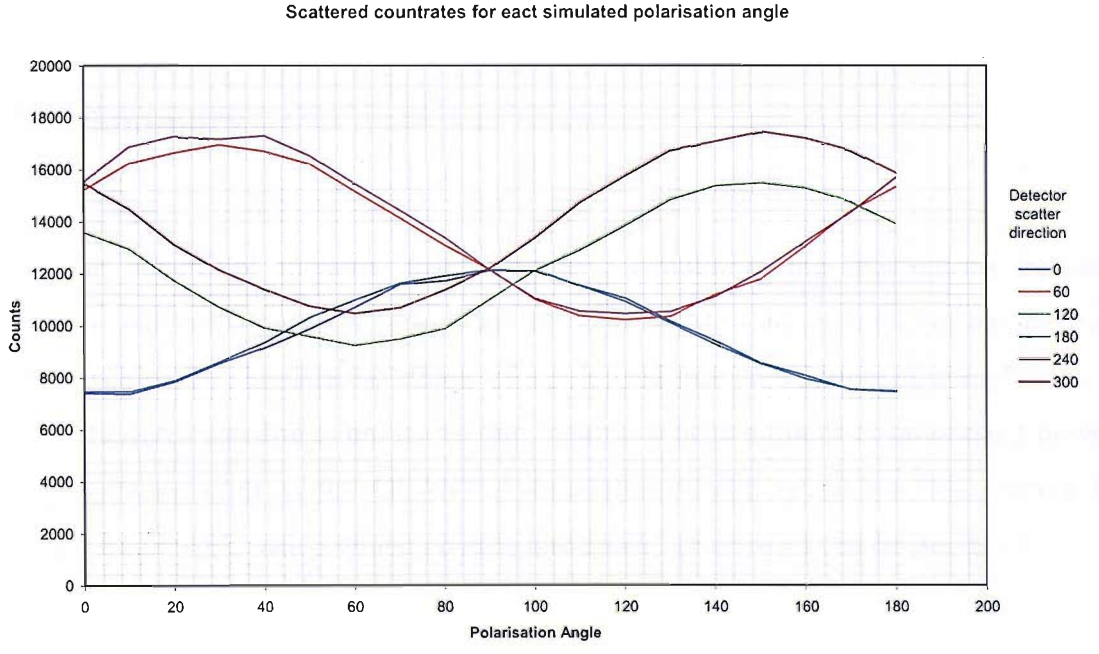

Figure 4.17: Plot of scattered count rate vs. polarisation angle for each direction in the detector. It is clear that some directions will always have a much lower number of counts than other angles regardless of the polarisation.

scatter pairs is only 10. This would lead to a polarisation angle of 0° being found in the analysis of the data if the dead pixels were not taken into account. Including the effects of the mask and pixels will change the number of scatter pairs further still (Table 4.2). Figure 4.17 shows how the numbers of counts in each scatter direction changes with the polarisation of the incoming photons. It is obvious that some directions have more counts than others regardless of the polarisation angle.

Dealing with effects of the mask and dead pixels is the strength of using modelling in the analysis. Attempting to calculate each of these effects on the azimuthal distribution seen in the detector plane due to a polarised flux would be a difficult task with many opportunities for errors. Simulating how the instrument responds to a polarised flux using the accurate modelling described in this chapter, will include the effects of the mask and dead pixels. This allows a straight forward comparison between the model and the observation data to be carried out to find the polarisation of the incident gamma-rays.

4.5 Summary

With the advent of modern, fast computers, simulating the interactions between materials and radiation on a large scale through Monte-Carlo modelling has become more feasible. To simulate the effects of a polarised flux on a system as complicated as the INTEGRAL satellite is not trivial and requires a huge amount of processing power. Using software such as the GEANT 4 simulation toolkit simplifies this process by giving a framework within which physics and model geometries can be designed.

The GEANT 4 INTEGRAL Mass Model has been developed from the original models used for background estimation before the launch of the satellite. Currently the model

only has the SPI instrument completed to a high degree of accuracy. For the background modelling the simulations were originally written for, the mass and composition of the material were important but the fine detail was not required. However, for investigating the effects of a source, the model elements must have the same size and transparency to produce the correct shadowing on the detector plane. For this thesis the detail level of SPI is suitable for the study of sources within the field of view; the model away from this instrument will affect the performance very little when dealing with an on-axis flux. The model still includes over 1000 physical volumes, over 900 of which are within the SPI instrument. Within the simulation event handling follows the same logic as the satellite, including thresholds and energy cuts. The model has been tested to show that the instrument behaves as the real satellite behaves to an incident flux.

When simulating a polarised flux it is clear that the spectral parameters make little difference to the modulation detected when dealing with changes the size of the errors on the measure GRB spectrum. Even dealing with much larger changes of spectrum, such as two power law slopes of -1.5 and -3.0, we find it only makes a slight difference to the modulation observed. In this case the Q factor was seen to change from $Q = 25.3 \pm 1.5$ % to $Q = 33.3 \pm 3.0$ % respectively, showing that as the numbers of high energy photons increase compared to that of the lower energy photons the modulation drops. However, the errors also reduce due to the high probability of a photon producing a multiple event.

The best energy range for carrying out the polarisation analysis has been determined to be 81 – 554 keV. However, due to the low count rates, restricting the energy ranges this precisely is impractical, instead 3 energy ranges have been chosen for the analysis. The energy range of 100 – 500 keV has been chosen since below 500 keV it may be possible to infer a direction of scatter to the photon. 100 – 300 keV will also be tested since it is

centred on the peak of the sensitivity, while 100 – 1000 keV will be tested due to the increased probability of photons repeatedly scattering in the detector.

The search for gamma-ray polarisation is the search for a small systematic modulation in the scattered photon distribution in a sea of systematic effects. Differences in the count rates in each direction on the detector plane can be caused in many ways and not just by the polarisation of the incident flux. Background, dead time, mask shadow and dead pixels will all cause the scattered counts in each direction to be different. The effect of a non-uniform background can be solved with a suitable background subtraction, while the dead time is solved by using the information in the observation data set. The effects due to the mask and dead pixels are accounted for in the modelling. With all these effects accounted for any modulation remaining will be due to the incident polarised flux. Comparing simulations of all angles and percentages of polarisation will result in the measurement of this modulation.

Chapter 5

Theoretical Models of GRBs and GRB Polarisation

5.1 Introduction

Gamma-Ray Bursts (GRB) are brief events that are more luminous than any other source of gamma-rays in the sky, including the Sun. Occurring on time scales from milliseconds to thousands of seconds, two different classes of GRB can be seen: those shorter than 2 seconds and those longer than 2 seconds. There are many possible theories for GRBs. The short bursts are the most difficult to study as a result of their fast nature. It is thought that these are due to coalescing neutron stars (Narayan et al. 1992; Ruffert et al. 1997; Popham et al. 1999), but most of the work on these bursts is theoretical with very little experimental evidence to back up the theories. Evidence from the double pulsar PSR J0737-3039 has shown that these pulsars will slow down and coalesce probably due to radiating energy by gravitational waves (Jenet et al. 2005). The longer bursts are better understood since they allow more time to be located and

give the opportunity to point more instruments in the required direction. A full review can be found in (Zhang and Mészáros 2004). The standard model of long duration GRB's suggests that they are caused by large hyper-novae (Aloy et al. 2000; MacFadyen et al. 2001).

The quick localisation of a GRB is vitally important. The faster the position of a burst can be obtained, the more instruments can be brought to bear on the emission. In general GRB locations are obtained by either the Swift (Gehrels 2004) mission or the third Interplanetary Network (IPN3) collaboration. IPN3 (Hurley and Cline 2004) consists of a group of spacecraft equipped with GRB detectors, including INTEGRAL and RHESSI. By using the timing information recorded by each spacecraft the precise location of the burst can be deduced using triangulation. Swift is a relatively new mission designed specifically for detecting GRBs. With its large field of view (2 steradians) covering 16% of the sky the Burst Alert telescope is able to locate a burst to within 4 arcmin, within seconds of detecting the burst. The satellite is then able to slew 50° in <50s to observe the burst using its X-ray ad UV telescopes and provide a final position to an accuracy of ~0.3 arcsec.

The fast dissemination of information throughout the community is vital. The GRB Coordinate Network (GCN) provides the ability for positions and follow-up measurements obtained by space- and ground-based observations to be distributed, many of which in real time while the burst is still bursting (Barthelmy et al. 2001). With the latest dedicated GRB missions and the fast distribution of results, a huge amount of data is being collected on the burst, allowing the theories to either be confirmed or ruled out. This chapter will describe the current understanding of GRBs and how polarisation can lead to understanding of the emission mechanisms involved.

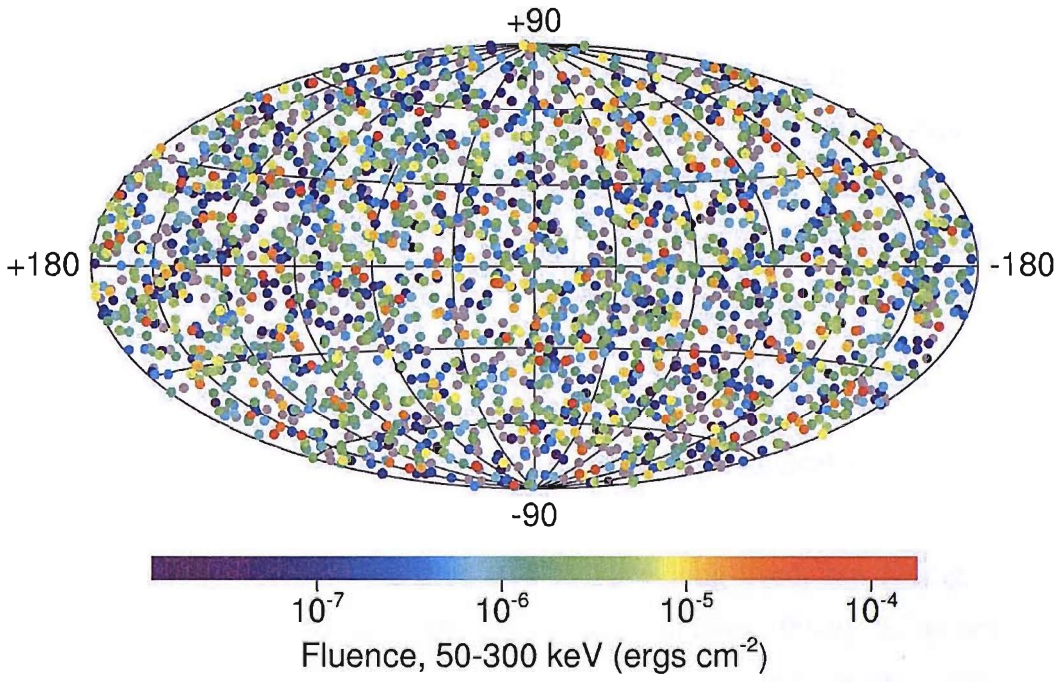

Figure 5.1: The positions of the 2701 GRBs seen by BATSE between 1991 and 2000. CREDIT: The BATSE Team.

5.2 Observations of GRBs

GRBs have been detected by more than 30 spacecraft. BATSE aboard CGRO allowed the accumulation of a large (>2000) and consistent sample of bursts with high spectral and temporal resolution. This greatly contributed to the understanding of GRBs allowing statistical studies of their spectral, temporal and spatial characteristics.

The GRB distributions prior to BATSE suggested an isotropic and homogeneous distribution in space when taking instrument exposure into account. However, a galactic source distribution was favoured due to the energy requirements needed by a burst, and could not be ruled out because of the low number of localised bursts. If located outside our galaxy at high redshift, the energy released would be greater than the energy output of the Sun in 10^{10} years, the approximate age of the universe (Meszaros 2006). Within 5 months of operation, BATSE had localised 132 GRBs

showing an isotropic distribution when allowing for the sky exposure (Meegan et al. 1991). A further study of bursts in 1994 reported the detection of cosmological time dilation by comparing the characteristic timescales of bright and dim GRBs (Norris et al. 1994). After 9 years, BATSE detected 2704 GRBs which continued to show an isotropic distribution (Figure 5.3). This was later confirmed by with the first redshift measurement of a GRB970508 at $z = 0.835$ (Metzger et al. 1997).

With GRBs successfully shown to be situated at cosmological distances they are required to release energy on a scale comparable to supernovae. Based on the supernovae analogy, GRBs were predicted to have long-lived, but fading, emission (Paczynski and Rhoads 1993; Katz 1994; Meszaros and Rees 1997a). Early attempts to find a GRB counterpart focused on two main strategies, searching plate archives for optical transients (Schaefer 1981) and deep imaging observations at X-ray, optical and radio wavelengths (Schaefer 1992) of the GRB location error boxes provided by the IPN (Hurley and Cline 2004). Their lack of success is now attributed to the observations being either too late or lacking the required sensitivity (van Paradijs et al. 2000).

The small error boxes (of order several arc minutes) produced by the BeppoSAX Satellite's Wide Field Cameras (Scarsi 1993) provided a breakthrough in 1997. On February 28 1997, a GRB was detected with the Wide Field Camera (WFC), allowing the rapid derivation of a small error box. Approximately 8 hours later the narrow field instruments aboard the same satellite detected the presence of an unknown soft X-ray point source within the WFC error box. Over the next four days the flux from the afterglow was seen to decrease by a factor of ~20 (Costa et al. 1997). Approximately a week later a decaying 21^{st} magnitude optical counterpart was also discovered (van Paradijs et al. 1997). Later observations established that the GRB had a redshift of 0.695 (Djorgovski et al. 1999), confirming that the host is a distant galaxy.

5.3 Gamma-Ray Properties of GRBs

As mentioned previously GRBs fall in to two categories, short (<2s) and long (>2s). However, within these categories the bursts are very different. Looking at their characteristics has shown that bursts, although being very different, will show similarities.

5.3.1 Temporal Characteristics

The count rate produced by a GRB as a function of time is usually irregular and complex. Approximately 70% of bursts show a multiple peaked time profile. The significant variability on short time scales is often taken as evidence to support a compact origin for these objects on the basis of light travel time and the assumption of isotropic emission. These time profiles can be separated into four distinct categories (Fishman and Meegan 1995):

- Bursts with a single, sharp pulse. These often have very little structure and are usually called FRED (Fast Rise, Exponential Decay) although the fall times may not decay exponentially.
- Bursts with smooth profiles with either single or multiple well-defined pulses, which have similar rise and fall times, but no fine structure.
- Bursts with distinct or separated intervals of emission often with intervals where there is no detectable emission.
- Bursts with uneven or chaotic intervals of emission.

The differences between each type are likely to be caused by different behaviours of the central engine, different emission sites or viewing angles and not different progenitors (Zhang and Mészáros 2004).

The length of a GRB lasts from a few ms up to more than 1000s. Calculating the length of the burst has been standardised by the BATSE team (Fishman et al. 1994). Weak bursts with high background and differing instrument sensitivities can cause different durations to be calculated for a single burst. By using the integrated number of counts a duration can be calculated which is fairly independent of the bursts intensity. The T_{90} time represents the time encompassing 90% of the total flux for a burst, enabling a

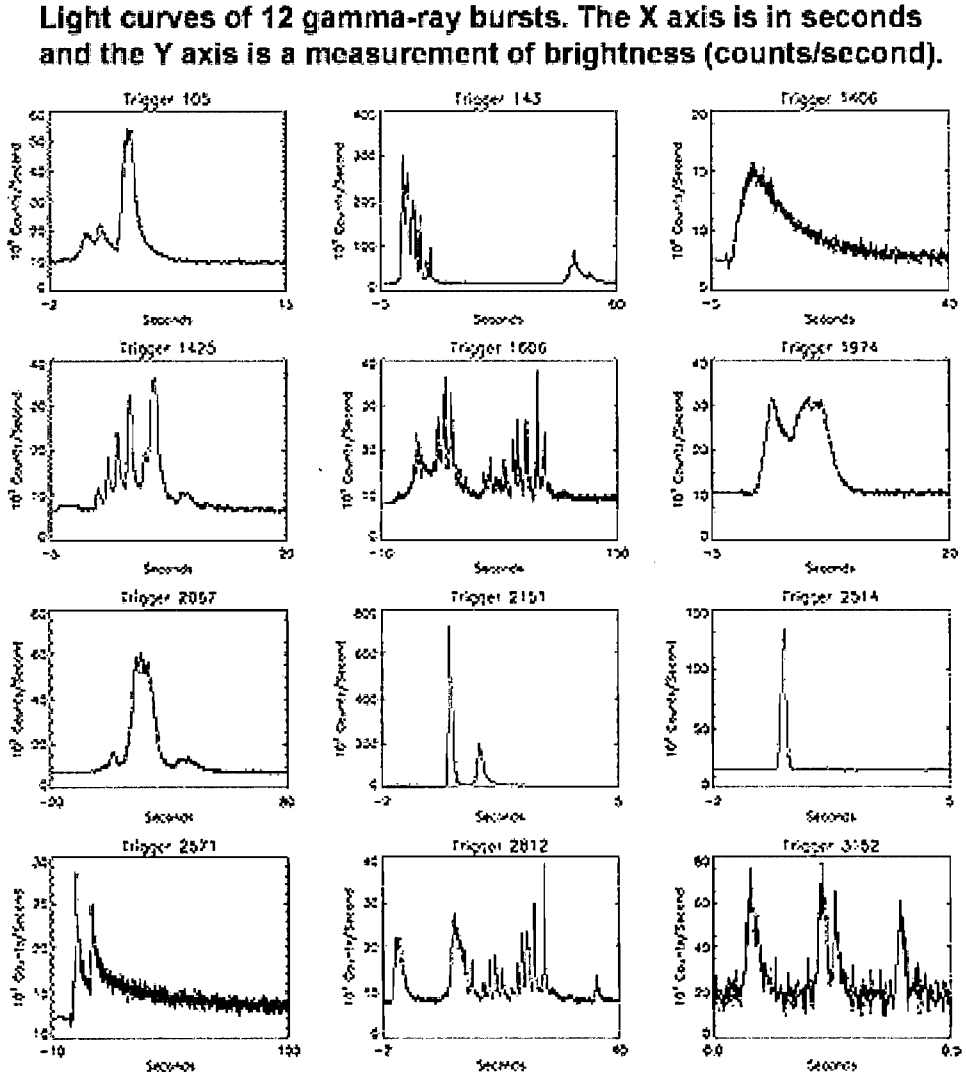

Figure 5.2: The light curves of twelve GRBs observed with BATSE on-board CGRO. Trigger 1425 shows a windup pattern, with the peak of each pulse increasing with time, while the first burst of trigger 143 shows the corresponding wind-down pattern followed by a quiescent period. Trigger 1406 and 2571 both show a FRED profile. CREDIT: J. T. Bonnell (NASA/GSFC)

duration measurement in an unbiased and reproducible way.

On examination of the BATSE T_{90} durations two populations are noticeable. Plotting the log of the T_{90} time highlights this bimodal distribution (Figure 5.3). The 'short' GRBs, with $T_{90} < 2s$, have a significantly higher mean hardness ratio than the second population of 'long' GRBs, with $T_{90} > 2s$, providing further evidence that these are two distinct populations (Dezalay et al. 1992; Kouveliotou et al. 1993; Dezalay et al. 1996).

5.3.2 Spectral Properties

Although GRBs vary widely in length and time profile, their spectra all follow a similar profile. There are two categories of spectral model used for GRBs: those that give meaning and allow for interpretation of the fit (e.g. black-body models) and those that allow characterisation of spectral shapes but have no physical meaning (e.g. power-laws and the Band model (Band et al. 1993)).

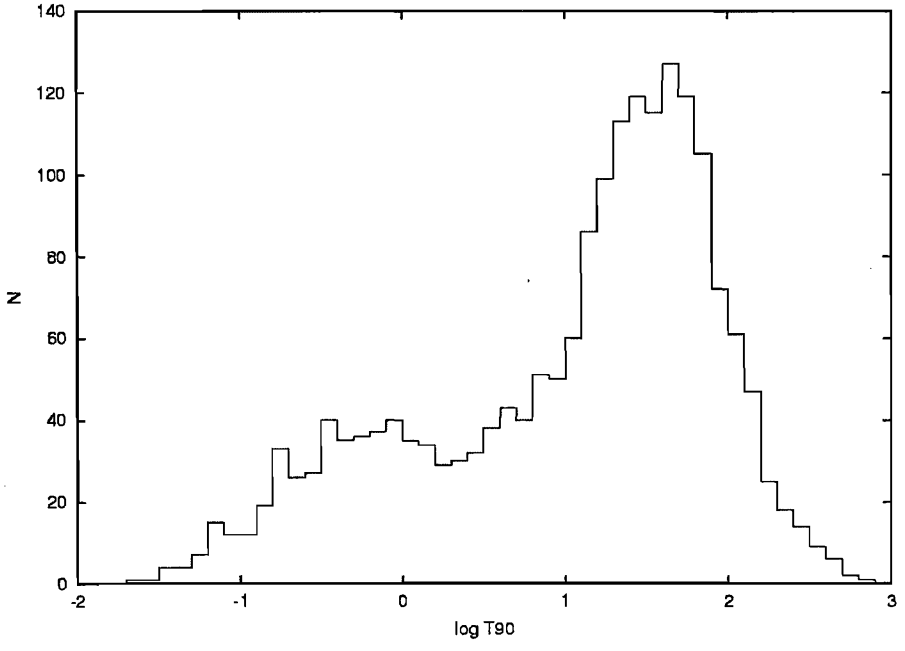

Figure 5.3: The distribution of burst durations for the 2041 BATSE GRBs with duration information. Plotting log T_{90} clearly shows a bimodal distribution (Kouveliotou et al. 1993).

Initially, the KONUS experiment (Mazets et al. 1982) gave the first comprehensive study of GRB spectra (Mazets et al. 1981a; Mazets et al. 1981b). The spectra obtained between 30keV and 2MeV were found to be adequately described by a model describing thermal Bremsstrählung of an optically thin plasma. The gamma-ray spectrometer instrument found that ~60% of GRBs emitted significantly above 1MeV (Matz et al. 1985). This high energy emission is not compatible with the thermal models, and was later confirmed by CGRO.

Since the physical processes that produce a GRB are unknown, the Band model is usually used to describe the GRB spectrum. This model was originally derived from an extensive study of BATSE GRBs (Band et al. 1993). Consisting of a broken power-law, the model is usually described by

$$N(E) = \begin{cases} A\left(\frac{E}{100\ keV}\right)^{\alpha} e^{\left(\frac{E}{E_{break}}\right)} & for\ (\alpha-\beta)E_{break} \geq E \\ A\left(\frac{(\alpha-\beta)E_{break}}{100\ keV}\right)^{\alpha-\beta} e^{(\alpha-\beta)}\left(\frac{E}{100\ keV}\right)^{\beta} & for\ (\alpha-\beta)E_{break} < E \end{cases} \quad 5.1$$

where E_{break} is the energy at which the spectrum turns over; α and β are the slopes below and above the break and A is the amplitude, measured in photons $cm^{-2}\ s^{-1}\ keV^{-1}$.

5.4 Theoretical Models

The origin of a GRB is hidden from direct observation. The complicated temporal behaviour may be due to the inner engine of the burst (Piran 1999). The temporal structure and the large amount of energy released during a burst indicate the formation of a compact object, most likely a black hole.

The favoured model for the progenitor of the 'short' GRBs is the merger of a binary neutron star (Narayan et al. 1992; Katz 1997). These binaries lose energy by gravitational radiation and spiral inwards, eventually coalescing. When a neutron star binary coalesces, the rapidly spinning merged state will be too massive to produce a neutron star, but will have too much angular momentum to immediately form a spinning black hole. The probable outcome, after a few milliseconds is that a black hole will form surrounded by a torus of neutron-density debris (Rees 1999). The dominant energy from a NS-NS event comes after a black hole forms, rather than during the precursor stage. The large amount of energy released may come from the binding energy of the orbiting debris, or the spin energy of the black hole. The energy can be extracted from the torus via thermal neutrinos converting into pairs in low density regions along the rotational axis away from the plane of the torus. To be efficient this process must occur before the neutrinos are consumed by the black hole. However, the conversion process is low if the neutrino production rate is small, suggesting that this mechanism may not be able to produce the energies measured without extreme beaming. It may also be possible for the rotational energy to be extracted from the torus via magnetic fields threading the torus (Paczynski 1991; Narayan et al. 1992; Katz and Piran 1997; Meszaros and Rees 1997b). The rotation of the black hole may also be important in this effect (Blandford and Znajek 1977; Paczynski 1998). The Poynting jets produced are capable of producing much more energy and only modest beaming is needed to produce the gamma-ray energies seen. The neutron annihilation will generally tend to produce short bursts $\leq$ 1s (Katz and Canel 1996; Ruffert et al. 1997), while the jets are likely to produce longer bursts through relativistic shocks in the jet. The strong magnetic fields associated with a Poynting dominated jet will lead to a polarisation signature of up to 60% due to synchrotron emission from electrons travelling along these magnetic fields (Lyutikov et al. 2003).

Long burst models usually centre on the core collapse of a massive star. The core is too massive to form a neutron star, but the star has too much angular momentum to form a black hole directly, often referred to as a hypernova or collapsar (Aloy et al. 2000;

MacFadyen et al. 2001). Again a black hole accreting from a torus is the result of these processes and the formation of a Poynting jet and relativistic shocks are likely to be the source of the emission. The energetics of these models do not differ by more than an order of magnitude and the abundance of these sources is consistent with the rate of GRBs inferred by BATSE of 1000 events per year, requiring 1 event per galaxy per 10^6 years.

At the large redshifts the measured gamma-ray fluencies imply a total energy of $\sim 10^{54}$ergs ($\sim 10^{62}$ keV), if it is emitted isotropically (Kulkarni et al. 1998; Kulkarni et al. 1999). This is $\sim 10^3$ times larger than the total energy of supernovae, which last weeks to months (Meszaros 2006). This large energy requirement can be reduced if it is assumed that the emission is concentrated into a jet rather than isotropically. There is now extensive observational evidence for collimated emission from GRBs, provided by breaks in the optical/IR light curves of their afterglows (Castro-Tirado et al. 1999; Fruchter et al. 1999; Kulkarni et al. 1999).

Observations of a 9th magnitude optical flash by ROTSE (Akerlof et al. 1999) just 15 sec after the gamma-ray burst was detected supports the standard model of GRBs. The discovery of achromatic breaks in the afterglow also matched the theory of jetted emission (Rhoads 1997). The detection of polarisation in the optical afterglow (Covino et al. 1999) gave further support to the jet model.

In a relativistic outflow collimated within a jet solid angle of $\Omega_j < 4\pi$, the observer will be unaware of what is outside the jet if the line of sight angle is within this solid angle and the Lorentz factor $\Gamma \geq \Omega_j^{-1/2}$ so the light-cone is within the jet boundary (Meszaros et al. 1993). As the ejecta decelerates the Lorentz factor will drop and a break is seen in the optical light curve (Rhoads 1997; Rhoads 1999). The jet opening angle θ_j can be calculated from the observed time of the break t_j using

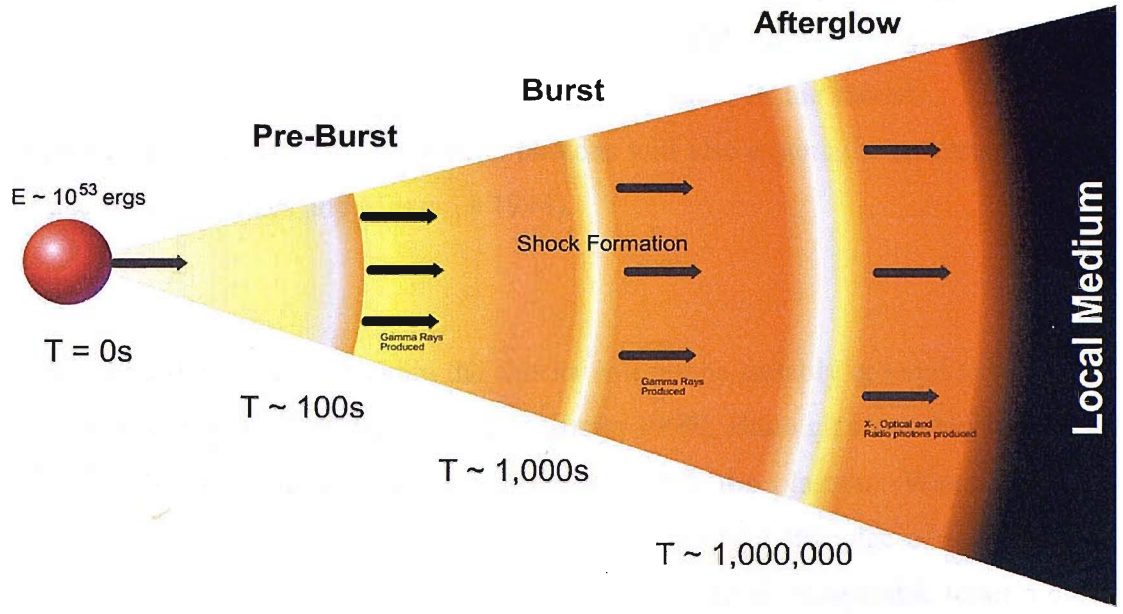

Figure 5.4: Diagram of the relativistic jet in the GRB fireball. As faster material catches up with the slower material shocks may be formed producing gamma-rays.

$$\theta_j \sim 5 \text{ deg } t_j^{\frac{3}{8}} E_i^{-\frac{1}{8}} n_{ex}^{\frac{1}{8}} \left(\frac{\eta_\gamma}{0.2}\right)^{\frac{1}{8}} \left(\frac{[1+z]}{2}\right)^{-\frac{3}{8}} \quad 5.2$$

Where E_i is the isotropic equivalent gamma-ray energy, n_{ex} is the mean density around the burst and η_γ is the radiative efficiency (Frail et al. 2001).

Shocks in the outflow are expected due to velocity variations in the outflow of the jet caused by high magnetic fields around the central engine (Mészáros 2001). These variations cause a multiple bursting effect where slower and fast shocks collide and so explain the structure seen in some bursts. As the escaping matter interacts with the high magnetic fields, it would radiate through synchrotron emission (Figure 5.4)(Meszaros et al. 1994). As explained earlier, the synchrotron emission would be polarised and related to the geometry of the system. Below the energy break the spectrum should be reminiscent of the synchrotron mechanism. This implies a photon index of α between -

3/2 and -2/3. However, the distribution of α seen in GRBs is larger and so attempts have been made to rule out this model on this basis (Celotti and Ghisellini 1999), but the restrictions may simply be due to assumptions made in the model. The inverse Compton scattering of these synchrotron photons will also extend the spectrum into the GeV energy range (Rees and Meszaros 1994).

The magnetic field confined within the shocks will not be suitably ordered to produce a strong polarisation signal (Gruzinov and Waxman 1999), although a suitable field could be dragged out from the centre by being frozen into the plasma. Waxman (2003) suggested that a jet with a small opening angle viewed near the edge of the jet would produce an anisotropy that would lead to a polarisation level comparable to an ordered magnetic field. However, the brightness of GRB021206 (Hurley et al. 2002) at the redshift of $z = 1$ gives a very small opening angle for the jet, making the probability of its alignment unlikely.

A Compton drag model (Lazzati et al. 2004) produces another solution to the prompt emission seen in a GRB. Lazzati et al. (2004) argue that an ionized plasma moving relativistically through a photon field will upscatter photons by a factor $\sim 4\Gamma^2$, where Γ is the electron Lorentz factor. The photons will be beamed into an opening angle of $\sim 1/\Gamma$ at the expense of the kinetic energy of the plasma. The resultant polarisation as a function of observation angle can be seen in Figure 5.5. If a Gaussian jet profile, instead of a uniform profile, is used then the maximum polarisation is fixed between 60% and 80% for all observer angles. However, the probability of observing a large linear polarisation drops rapidly when the jet is larger than $\Gamma\theta j \sim 3$.

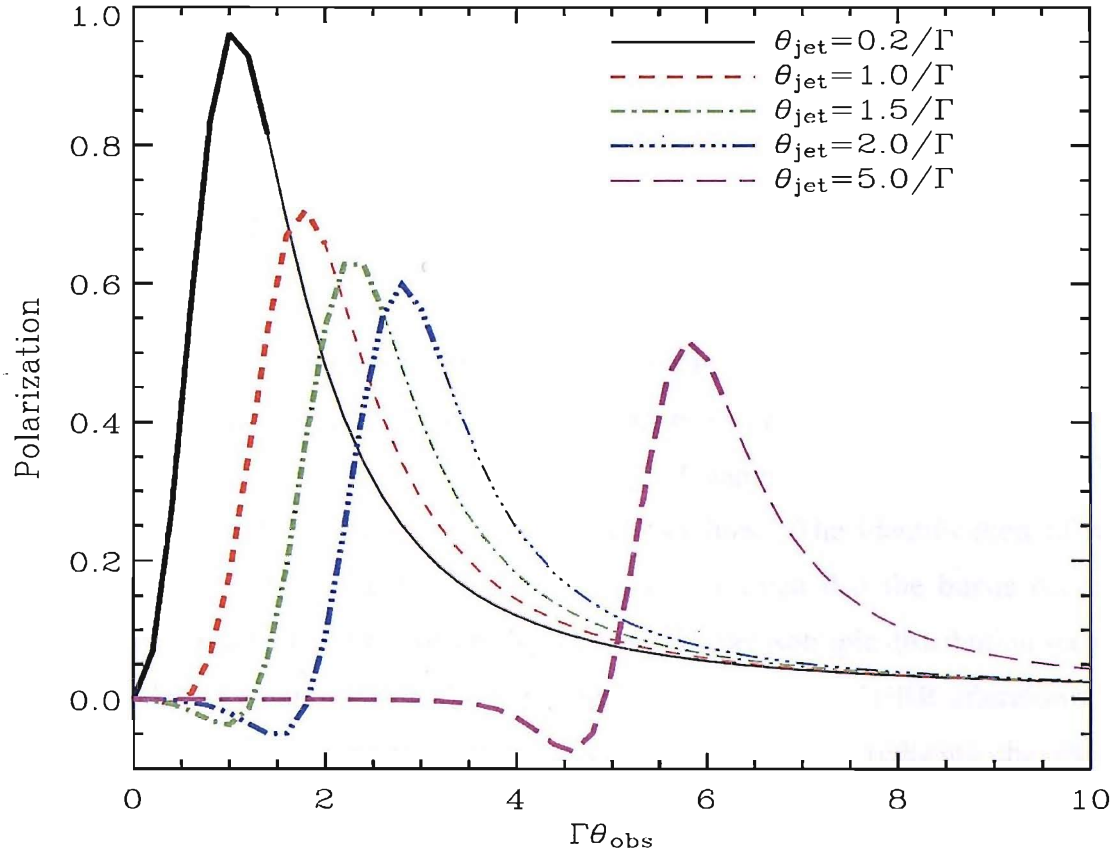

Figure 5.5: Polarisation as a function of observing angle for a uniform jet. Different lines correspond to jets with different opening angles. (Lazzati et al. 2004)

One method through which it is possible to separate these theories is through an accurate detection of the bursts polarisation. If the degree of polarisation, $\Pi \approx 80\%$ then a shock accelerated synchrotron emission or a tuned Compton-drag model (Shaviv and Dar 1995; Lyutikov et al. 2003; Lazzati et al. 2004) may be the case. Between 20% and 60% it is possible that the burst could involve synchrotron emission or be the result of viewing the burst close to the jet (Ghisellini and Lazzati 1999; Granot 2003). For lower degrees of polarisation, the most likely explanations would be a hydro dynamical model or one of the previous models experiencing a depolarisation. The neutrino annihilation is unlikely to create polarised gamma-rays unless their resultant electrons emit via synchrotron emission. However, a measurement of polarisation from a short burst

where this mechanism may be important will be unlikely due small total count rate recorded over the short timescale of the burst.

5.5 Summary

Gamma-ray bursts are the most luminous explosions in the Universe, requiring colossal amounts of energy to produce. Their origin and mechanism have been the focus of much debate and research. The understanding of gamma-ray bursts has advanced considerably since their discovery by the Vela satellites. The identification of host galaxies and the measurements of redshifts have confirmed that the bursts occur at cosmological distances, a result originally predicted by the isotropic distribution seen by BATSE. The observation of breaks in the optical light curves of GRB afterglows has shown that the emission from a GRB is collimated into a jet reducing the energy required to produce such luminous bursts. With the emission being collimated, the true rate of GRBs will be much higher than that seen by the gamma-ray burst monitoring missions.

With all that is currently known about GRBs the origin of bursts still remains a mystery. The favourite models regarding coalescing neutron stars or hypernovae both predict the production of a rapidly rotating black hole. There are many theories of how the gamma-rays are produced and where in the burst they are produced. Measuring the polarisation of the emission may help eliminate models that hint towards a progenitor of the burst. High levels of polarisation require ordered systems and will indicate that magnetic fields are involved. A result with a good statistical significance will help to narrow the range of models and if any change in the polarisation can be observed, such as rotation of the polarisation angle through the burst, this may lead to new explanations or localising the source of the emission further. The measurement of polarisation using RHESSI (Coburn and Boggs 2003) sparked a great deal of interest in the polarisation of

GRBs. Unfortunately, the result was found to be an error and the search of GRB polarisation continues (Chapter 6).

Chapter 6

Detecting GRB Polarisation

6.1 Introduction

Several attempts at measuring the polarisation in GRB flux have been made and met with varying success. A small but significant degree of linear polarisation was discovered in the optical afterglow of GRB990510 (Covino et al. 1999; Wijers et al. 1999). Since then, there have been a number of other detections of polarisation in afterglows (Covino et al. 2004; Gorosabel et al. 2004). The polarisation is observed to be at about the 1-3% level and is reasonably constant (Covino et al. 2003). The polarisation can vary in direction and degree on a time scale of hours if there are deviations from the smooth power law decay (Greiner et al. 2003). For a review of the levels of asymmetry needed to provide a polarisation signal in the prompt and afterglow emission, see Lazzati et al (2006). Unfortunately, there are no polarisation measurements for the bursts studied here at other wavelengths.

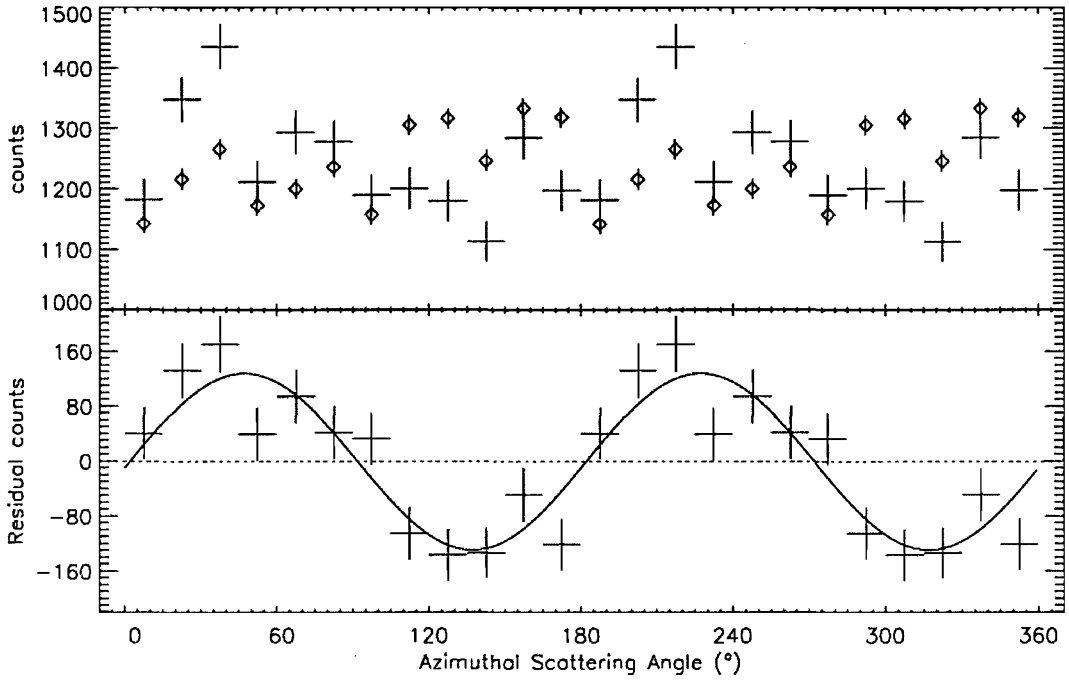

Figure 6.1: The azimuthal scatter distribution for the RHESSI data, corrected for spacecraft rotation. Counts were binned in 15° angular bins between 0°-180°, and plotted here twice for clarity. The top plot shows the raw measured distribution (crosses), as well as the simulated distribution for an unpolarised source (diamonds) as modelled with a Monte Carlo code, given the time-dependant incident flux. The bottom plot shows the RHESSI data with the simulated distribution subtracted. This residual is inconsistent with an unpolarised source (dashed line) at a confidence level > 5.7σ. The solid line is the best-fit modulation curve, corresponding to a linear polarisation of (80 ± 20)% (Coburn and Boggs 2003).

This chapter will look at two important previous attempts at measuring the gamma-ray polarisation in the prompt GRB flux, before describing the process and results of the measurement of polarisation from three bursts, GRB041219a, GRB060901 and GRB061122 using INTEGRAL.

6.1.1 Measurement of GRB021206 with RHESSI

The first measurement of GRB polarisation at gamma-ray energies was made using RHESSI (Coburn and Boggs 2003). As mentioned in a previous chapter, RHESSI has nine large volume germanium detectors that regularly record GRBs. The satellite

rotates with a period of 4s around its optical axis. This has the major advantage of averaging out asymmetries in the detectors and passive material that can lead to a false detection of polarisation.

GRB021206 was found to have a degree of polarisation, $\Pi = 80 \pm 20\%$ by Coburn and Boggs (Coburn and Boggs 2003) using data from the RHESSI experiment. This is extremely high and would be consistent with the maximum polarisation possible of 70% (see Chapter 5). However, any non-uniformity in the magnetic fields or scattering along the line of sight would reduce the maximum polarisation allowed.

The original result was reanalysed (Rutledge and Fox 2004; Wigger et al. 2004) and the polarisation was shown to be $\Pi = 41^{+57}_{-44}\%$. This reanalysis included the random chance that two photons may interact in the detector at the same time and look like a multiple event. With the high flux and the large separation of the detectors the number of accidental coincidences becomes a much larger fraction of the total multiple events than with a smaller, closer packed pixelated array. Wigger et al (2004) also carried out an analysis of GRB030519B using the same techniques and again produced a null result for the detection of polarisation.

6.1.2 Measurement of GRB930131 and GRB960924 with BATSE

A more recent attempt involved analysing the Earth albedo flux seen by BATSE (Willis et al. 2005) for GRB930131 and GRB960924. This investigation used a simulation to see if GRB flux reflecting off the Earth's atmosphere can produce any information regarding the polarisation of the prompt emission. BATSE Albedo Polarimetry Simulation (BAPS) consists of the detailed GEANT 3 BATSE Mass Model (BAMM) (Shaw et al. 2003) and a GEANT 4 model of the Earth's atmosphere (Figure

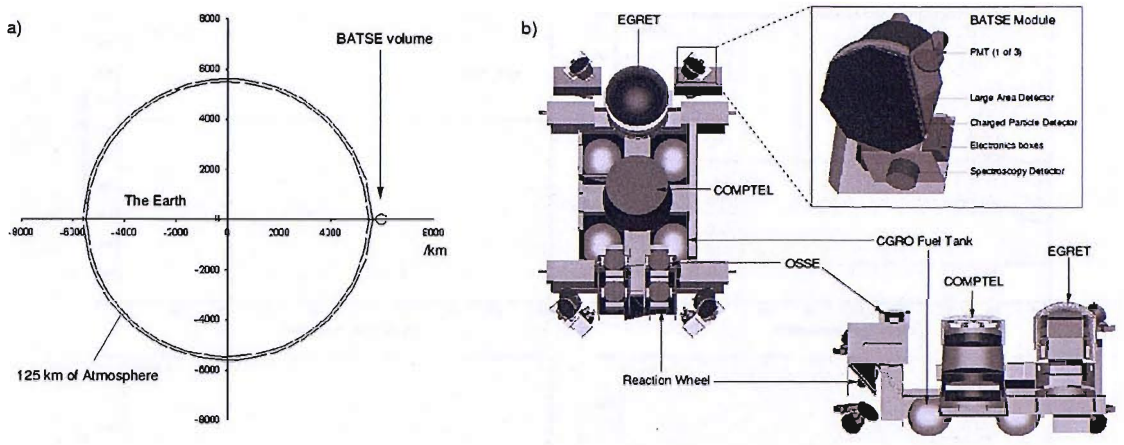

Figure 6.2: a) Schematic showing the relative scale of the Earth, its atmosphere (up to 125 km) and the virtual BATSE volume in the GEANT 4 polarisation sensitive simulation. b) The detailed GEANT 3 model of the CGRO spacecraft including BATSE (Willis et al. 2005).

6.2). A constant density model of the atmosphere is used to reduce the run-time and complexity of the simulation. This approximation is only very slight and produces 99.7% of the results from a more complicated model.

The simulation is done in two parts. The GRB is simulated reflecting off the Earth's atmosphere, for a variety of polarisation angles. This albedo flux will show a diametric excess if the flux is polarised, and be uniform for an unpolarised flux. The simulated scattered flux is then run through BAMM (Shaw et al. 2003), reproducing the count rates BATSE would see in such a case. The resulting simulated count rates are compared to the BATSE data.

The two bursts selected for this study were required to be short, strong, have simple structure and create an angle with Compton Gamma-Ray Observatory and Earth of as close to 180° as possible (i.e. to have BATSE directly between the Earth and the burst). The two most suitable, out of the 30-40 candidate bursts were GRB930131 and GRB960924.

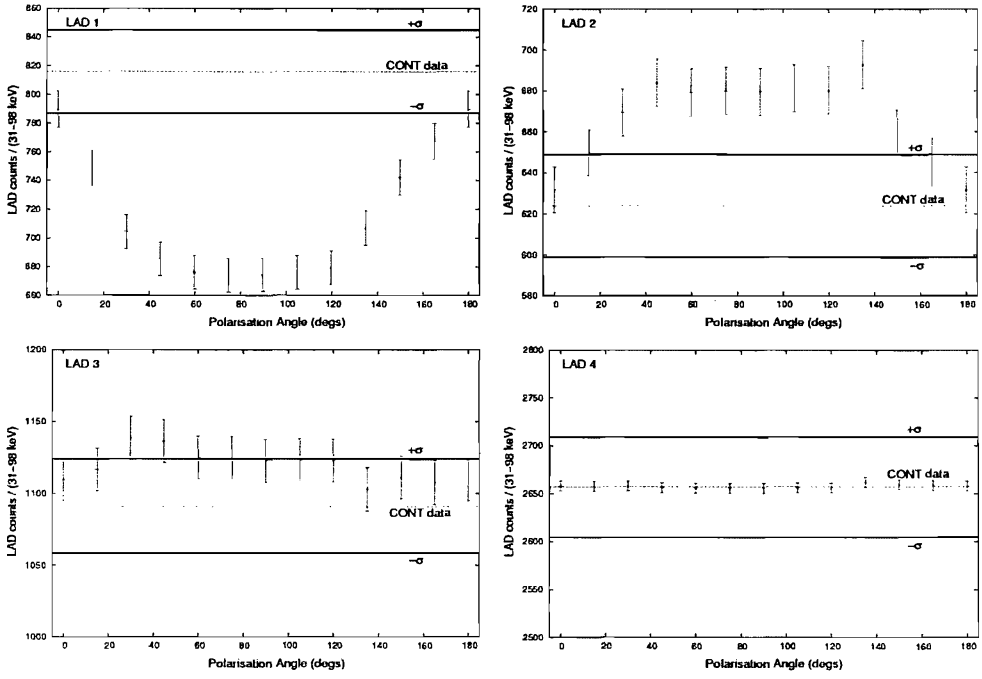

Figure 6.3: For GRB930131 (right) the z-statistic is significant (95%) between 6° and 163°, corresponding to a polarisation >90%.

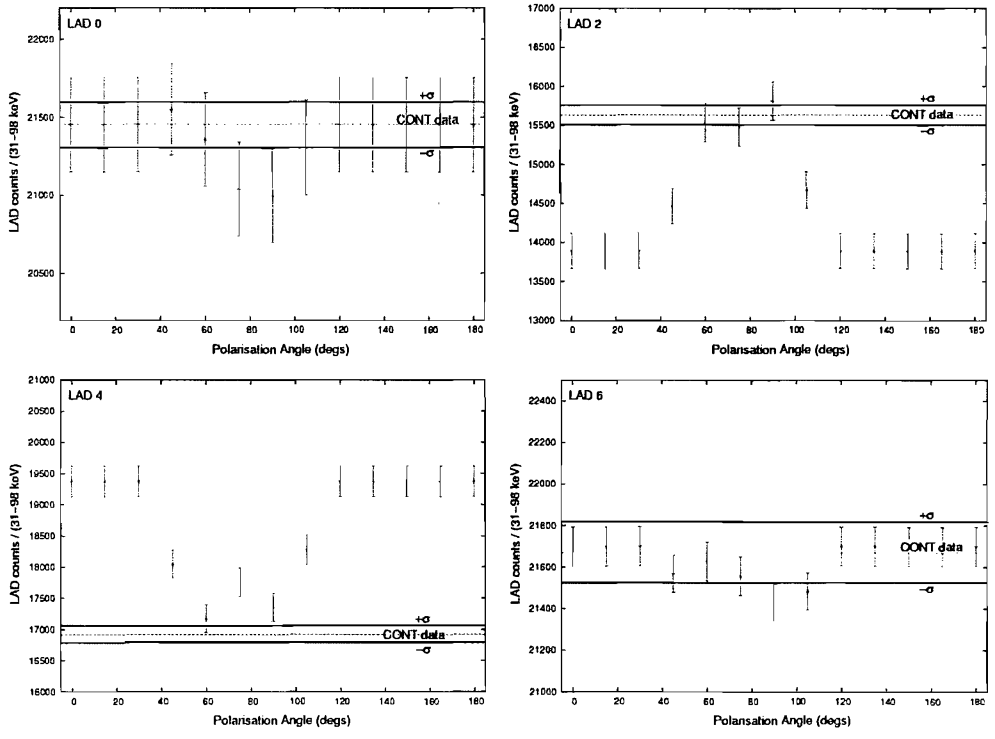

Figure 6.4: For GRB960924 (below left) the z-statistic is significant (95%) between 58° and 64°, corresponding to a polarisation 100%.

The angular distribution of the gamma-ray flux reflected off the Earth's atmosphere was simulated in GEANT 4 for $5x10^7$ incident GRB photons. This pixelated distribution is used as the input for BAMM. The CONT (Fishman et al. 1985) data (dotted line) for each Large Area Detector (LAD) for GRB960924 (Figure 6.3) and GRB930131 (Figure 6.4) are compared to the best fitting polarisation angle from the simulation data using the z-test to include the statistical simulated data errors. For GRB930131 the z-statistic is significant (95%) between 6° and 163°, corresponding to a polarisation >90%. While, for GRB960924 the z-statistic is significant (95%) between 58° and 64°, corresponding to a polarisation 100%.

Due to limitations in GEANT 4 and its capability to fully simulate this situation, including natural anisotropies in the Earth's albedo flux and other possible sources of systematic effects, conservative estimates have been put on the results. The polarisation lower limits are >35% and >50% for each burst respectively. GRB930131 and GRB960924 both show strong evidence of polarisation corresponding to the angles 6-163 and 58-64 degrees respectively. Although this technique is limited in its calculation of the percentage polarisation, a conservative systematics-based estimate puts the degree of polarisation at >35% and >50%, implying that either Inverse Compton or large scale B-field synchrotron emission are responsible for a large proportion of the GRB flux.

6.2 The Detection of Polarisation in GRB041219a

GRB041219a is one of the brightest bursts localised by INTEGRAL. Being a long burst (~200 seconds) with a high flux and relatively close to the optical axis of the spacecraft makes this an ideal candidate for the detection of polarisation. The burst is most likely to be the best long burst that INTEGRAL will record; however, a longer burst with less temporal structure would be more desirable. The structure could imply a

rotating polarisation signal, which would lessen the overall polarisation when looking at the entire burst emission. Due to obvious double burst structure the burst has been divided into the main pulse and second pulse for analysis.

The afterglow of GRB041219a was seen at many wavelengths including, X-ray (Barthelmy et al. 2004; Levine and Remillard 2004), near Infrared (Moon et al. 2004; Barkov and Bisnovatyi-Kogan 2005) and optical (Cenko 2004; Rykoff et al. 2004). Unfortunately, none of the observations include polarisation measurements.

6.2.1 GRB041219a Spectral and Temporal Properties

GRB041219a was detected by IBAS (Mereghetti et al. 1999) at 01:42:18UTC on December 19th 2004 (Gotz et al. 2004) at a location of 00h24m 25.8s, +62°50'05.6", ~3 degrees off the pointing axis of the INTEGRAL telescope. The burst consisted of an initial precursor-type pulse, followed by a quiescent period lasting approximately 200s, before the main emission beginning at ~250s after the trigger. The background subtracted single event light curve summed over all the detectors can be seen in Figure 6.5.

The spectrum of the burst was extracted from the INTEGRAL Offline Scientific Analysis (OSA) software version 5.0 (Diehl et al) and at the time was the brightest burst localised by INTEGRAL with a peak flux of 43 ph cm^{-2} s^{-1} (20keV-8MeV). The spectrum is well fitted by the Band model (Band et al 93), although the parameters of the spectrum evolved during the burst (Figure 6.6). A detailed discussion of the spectral and temporal behaviour is available in McBreen et al (2006). The most intense emission pulse of 66s duration (indicated by the solid lines in Figure 6.5) was selected for the polarisation analysis. The photon indices, α and β, for the emission phase used

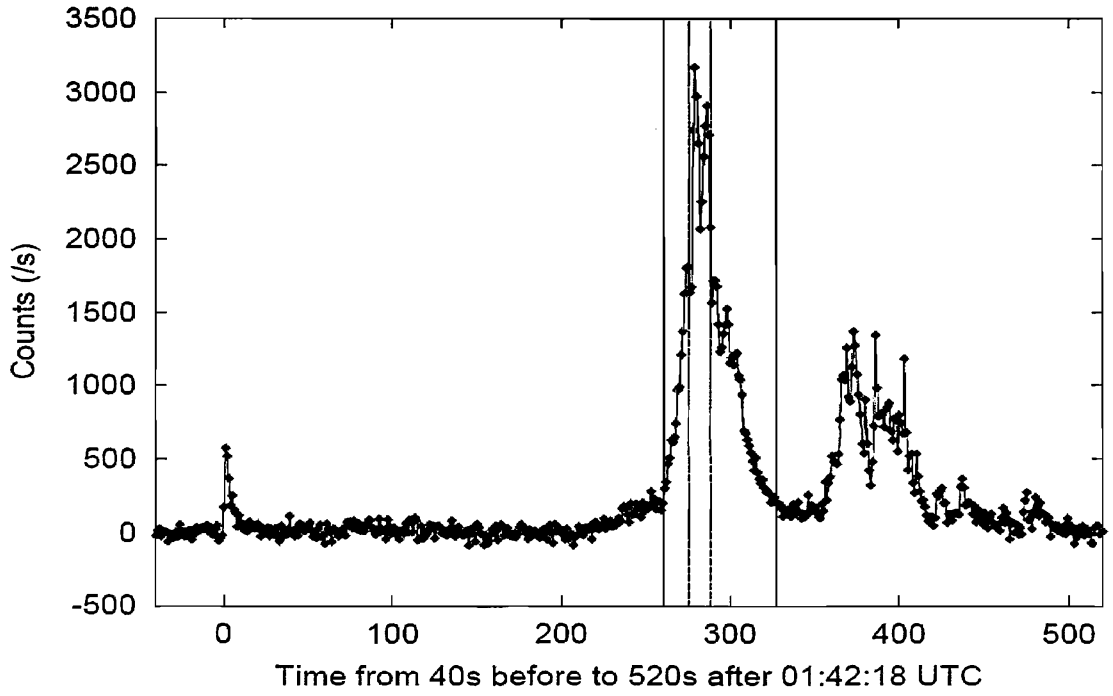

Figure 6.5: Background-subtracted single event light curve of GRB041219a, summed over all SPI detectors in the energy range 20 keV - 8 MeV. The vertical solid lines mark the start and end of the 66 second emission phase (T_0=261s to T_0=327s). The vertical dashed lines mark the start and end of the brightest 12 seconds of the burst (T_0=276s to T_0=288s). T_0 is the IBAS trigger time (01:42:18 UTC).

to calculate the polarisation were $-1.50^{+0.08}_{-0.06}$ and $-1.95^{+0.08}_{-0.21}$ respectively. The break energy E_{break} was 568^{+310}_{-205} keV.

It is interesting to note that the spectrum of GRB041219a was equally well fit by a combination of a black body and power law model (McBreen et al. 2006). Fan et al. (2005) also found that the early optical and infrared emission from GRB041219a can be modelled as a superposition of a reverse and a forward shock component. The ejecta are magnetised to a small extent, which may be due to a magnetic field generation during the internal shock phase. Fan et al. (Fan et al. 2005) predicted that the internal shock emission was very likely to be linearly polarised.

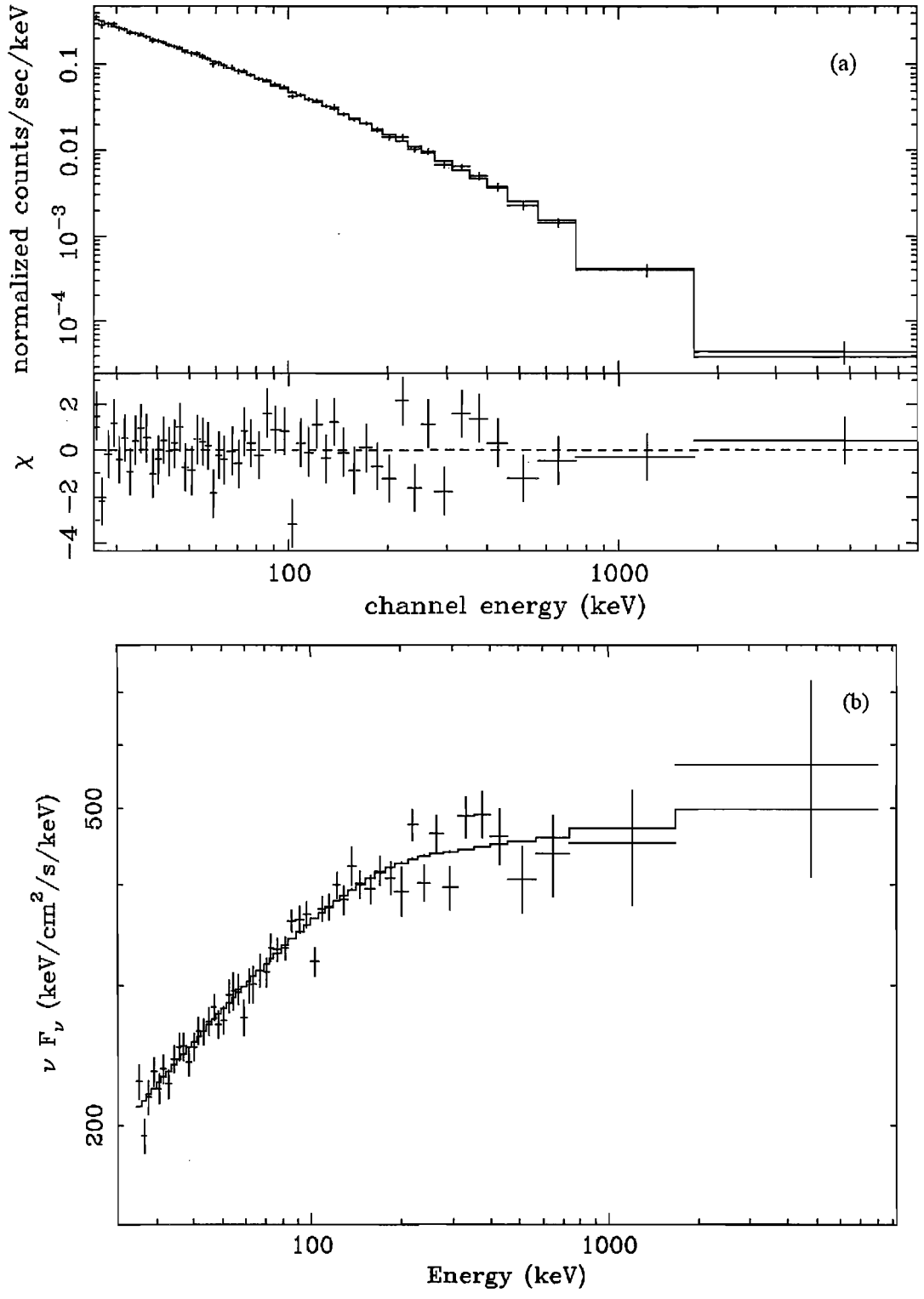

Figure 6.6: The Band model fit to GRB041219a and residuals for the 66s emission phase (top). νF_ν spectrum of GRB041219a (bottom). The Band model parameters are α = -1.50, β = -1.95 and E_0 = 568 keV.

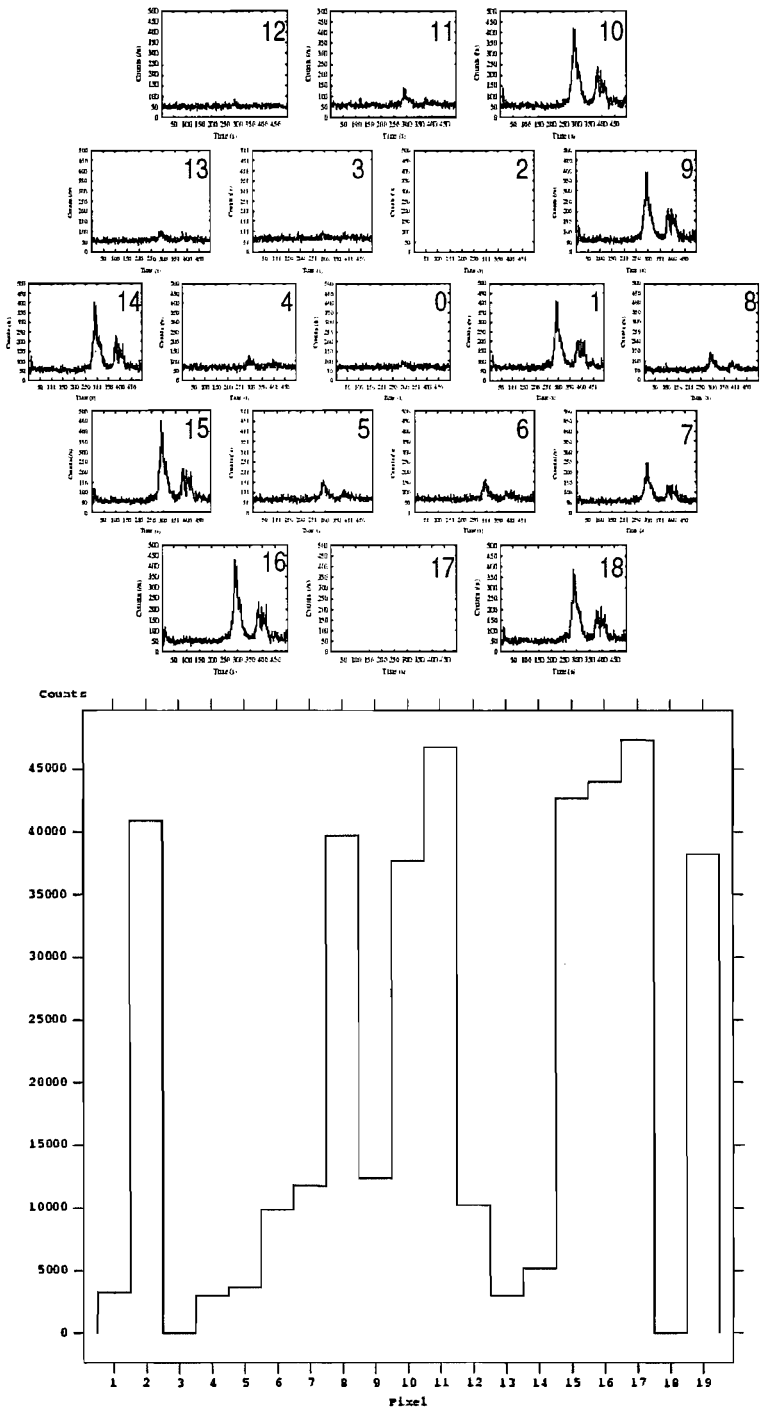

Figure 6.7: The real photon count rates for GRB041219a (top) and the simulated count rates (bottom).

6.2.2 Simulating GRB041219a

The INTEGRAL model, built using the GEANT 4 framework, is used to predict how the instrument's detectors respond to an incident polarised flux. Gamma-ray photons were directed into the model geometry from a plane surface in the direction of the GRB, 3.08° from the INTEGRAL x-axis and 63.95° from the INTEGRAL z-axis, simulating the incoming flux from a source at infinity from the same direction to the spacecraft as the GRB. The photons were fired with a spectrum consistent with the Band model parameters obtained from the burst.

For each simulation run, the polarisation angle of the photons was set between 0° and 180° in 10 degree steps. There was also a run of unpolarised photons. Only the angles between 0° and 180° needed to be simulated due to the 180° symmetry of the polarised scattering distribution. This helped reduce the number of simulations needed. In total 500 million photons were fired for each simulation to ensure that the statistical simulation errors were much less that the statistical errors in the real data.

As mentioned previously in Chapter 4, the simulations produced a list of all the interactions that occurred in the sensitive volumes of the model (Ge detectors and BGO shield). These data were then converted into an event list, for comparison to the real SPI data. Initially the interactions were summed, so that the energy deposits correspond to the total energy deposited for an event in each of the sensitive volumes. These deposits were then filtered according to the energy thresholds of the detectors (~20 keV) and the veto (~80 keV). After subtracting the vetoed events, the event list was separated into single events (where the photon is detected in one pixel) and multiple events (where the photon is detected in multiple pixels). This process produced the final list of events to analyse and compare to the real data. The unpolarised simulation data was combined with the polarised simulation data, allowing the percentage of

polarisation to be changed for each angle. Comparing the SPI real data count rates with the number of counts in each pixel from the simulation shows a very good agreement and indicates that the source is located in the correct position with respect to the telescope (Figure 6.7).

An important consideration in polarisation experiments using coincidence rates is the rate of chance coincidences. In SPI a multiple event is an event where two energy deposits within different pixels occur within the electronics coincidence window of 350 ns (Vedrenne et al. 2003). At the peak of the burst 3000 c/s are received which equates to 157 c/s for each pixel. This will produce an accidental coincidence rate of 8×10^{-3} c/s for all the detector pairs. For this analysis we only consider scatters between adjacent pixels and so the rate of chance coincidences is only 2×10^{-3} c/s, which is negligible for our measurements.

6.2.3 Polarisation Analysis

There is no positional resolution within the SPI detectors and so it is not possible to determine the exact position of the interaction within an individual detector. Centre-to-centre interactions are assumed for multiple events. According to the simulations, this will introduce an uncertainty on each angle of 25 degrees, although interpolation between the angles during the fitting can reduce this greatly. Below 511 keV, the incoming photons predominantly Compton scatter from the detector with the lower energy deposit to the higher one (Kalemci et al. 2004b). Thus 6 directions of scatter can be distinguished. For higher energies, the order of energy deposition does not distinguish between anti-parallel directions and the number of directions is limited to 3. To enable a larger energy range from 100 keV – 1 MeV to be investigated, the analysis was also performed in 3 directions.

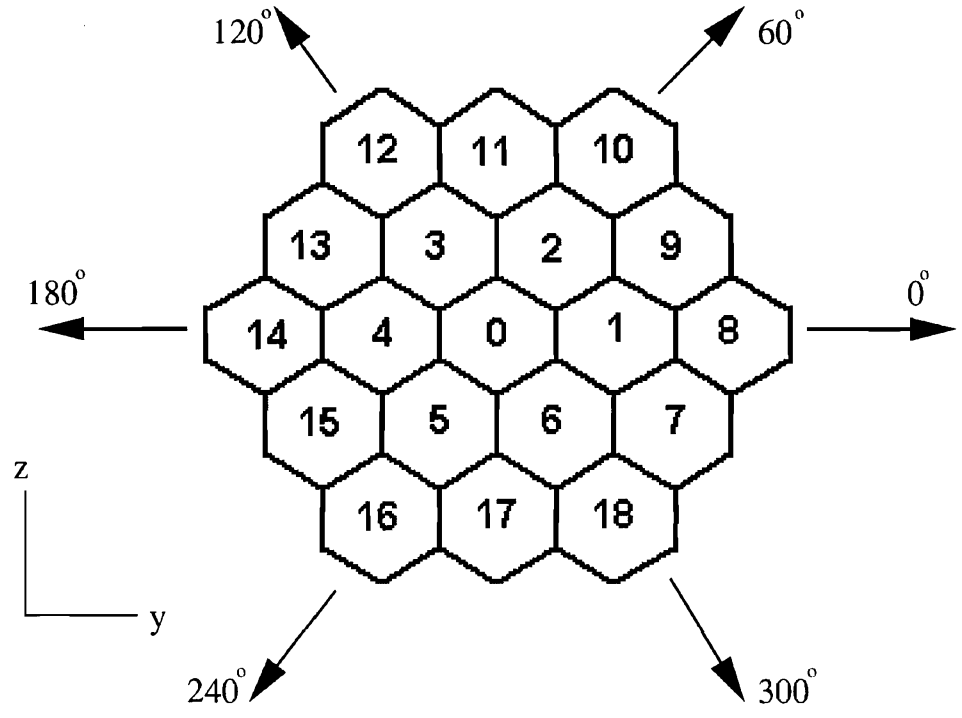

Figure 6.8: The numbering system used for the Germanium SPI detectors and the six directions in the detector plane. Detectors 10, 11 and 12 mark the side closest to the IBIS instrument.

The analysis procedure was carried out, starting with the raw data from SPI, as follows:

- All interactions between detectors (double events) during the defined time intervals were selected.
- Only double events that occurred in adjacent detectors were accepted.
- The list of events was calibrated (using the *spi_gain_corr* tool from OSA 5.0) to convert the original channel number to energy in keV.
- All interactions with less than 30 keV deposited per detector were rejected. Relatively few photons above 100 keV will lose <30 keV in Compton scatter interactions.
- Coincident pairs whose combined energies lie in the analysis energy range were selected. Up to 511 keV, incoming photons predominantly scatter from the

detector with the lower energy deposit to the higher one allowing 6 separate directions to be determined.

- The scatter pairs were divided into 6 different directions (0-300 degrees) and the total number of events in each direction were determined (Figure 6.8).
- Background events (using the same selection process) were selected from intervals in the same science window before the GRB occurred (Table 6.1), since the emission continued up to the end of the science window. The scaled background was then subtracted from the multiple event lists. The set of 19 detectors was also divided into 4 quadrants and the total background was calculated separately for each quadrant to ensure that there were no biases in any specific direction or systematic effects.

The analysis was carried out for 6 directions in the energy ranges 100 – 350 keV and 100 – 500 keV and over two separate time intervals (Figure 6.5) as described above. The analysis was also performed for 3 directions in the 100 – 350 keV, 100 – 500 keV and 100 keV – 1 MeV energy ranges to compare the values obtained from both methods. The simulated and real data sets were scaled by the total number for all directions to ensure that the comparisons between both types of data were valid and anisotropies in the response due to the mask and the two inoperative detectors were taken into account. The counts in each scatter direction were scaled by the total number of counts in all directions, producing a percentage of events scattered in each direction.

Table 6.1: Time intervals used for the background determination in 6 directions.

Observation	Start Time (UTC)	End Time (UTC)
Background 1	01:30:00	01:31:06
Background 2	01:35:00	01:36:06
Background 3	01:36:30	01:37:36
Background 4	01:38:00	01:39:06
Total (sec)		264

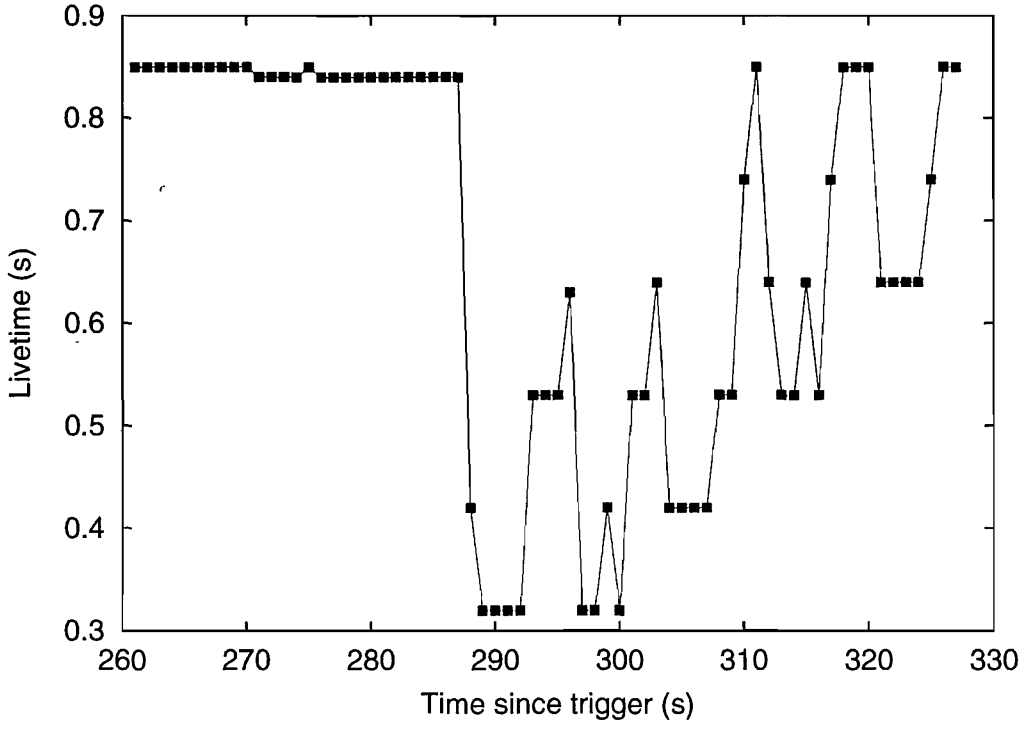

Figure 6.9: The average live time for each SPI detector per second over the most intense phase of emission of the GRB, showing a marked decline ~30 seconds into the pulse.

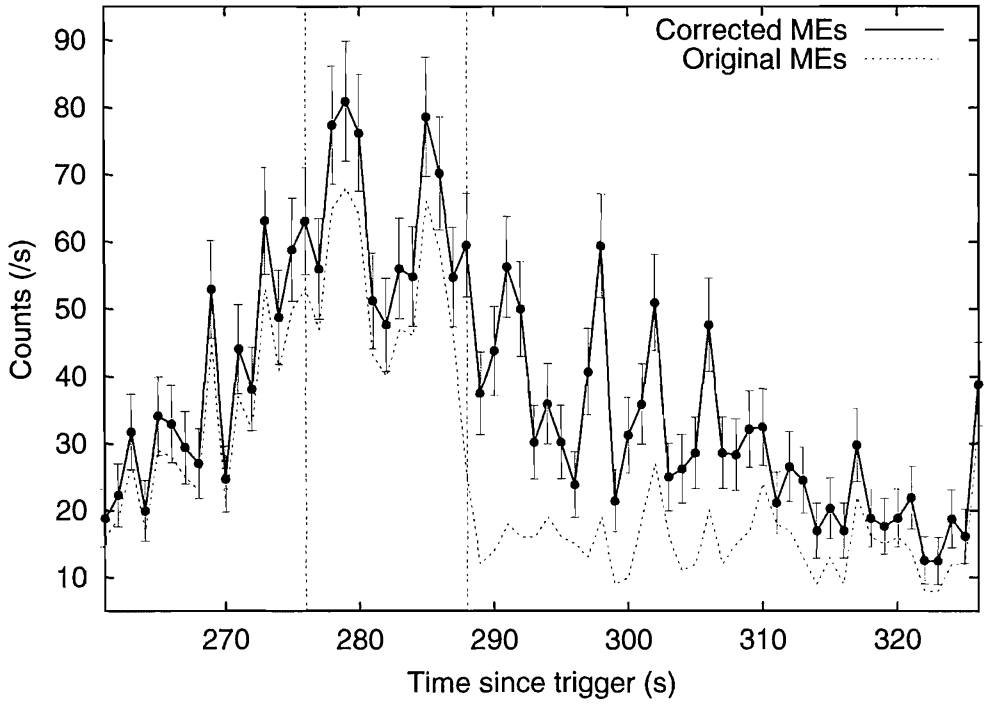

Figure 6.10: The original multiple event light curve (dashed) for all operative detectors for the 66 second interval, and the multiple event light curve (solid line) after the dead time correction was made. The vertical dashed lines indicate the 12 seconds used in the analysis.

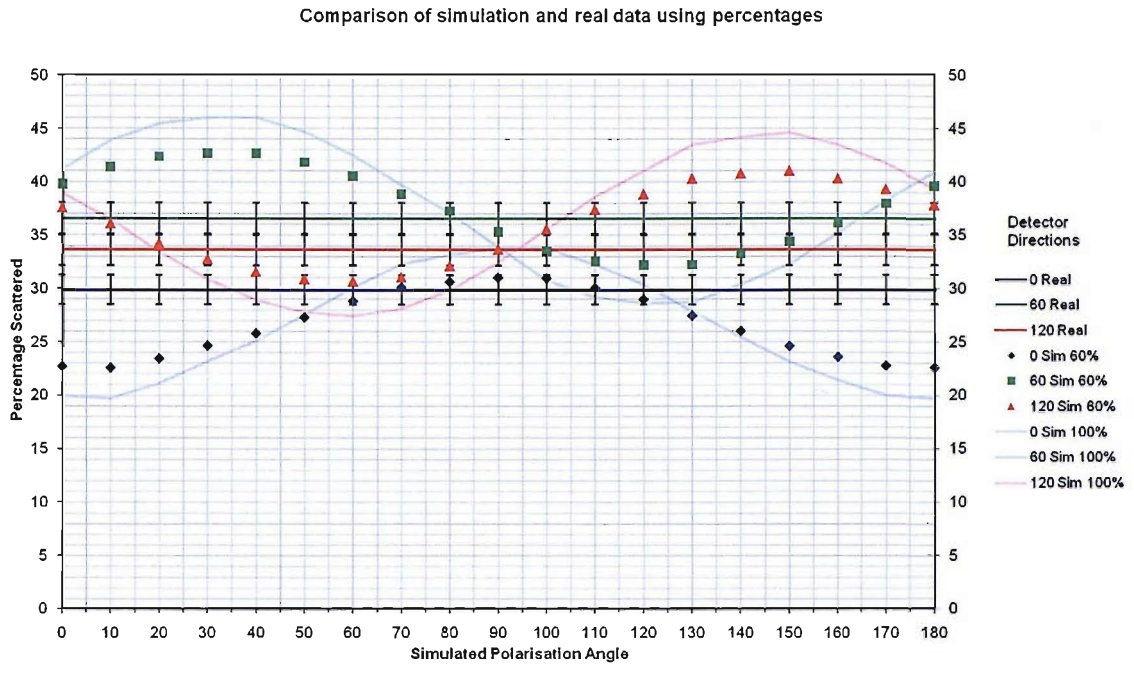

Figure 6.11: Comparison of real data (100-350keV 66 sec interval) and 60% polarised simulated data. The fitting between the two data sets is carried out using the χ^2 statistic and varying the simulated data modulation from 0-100%.

6.2.4 Results

The 100% polarised and 0% polarised data obtained from the Monte-Carlo simulations for each scatter angle were combined to create a partially polarised signal with varying degrees of polarisation. The fitting routine compared the real data with the partially polarised simulated data (Figure 6.11). The percentage polarisation was varied from 0% to 100% in steps of 10% and the angle was varied from 0° to 180° in 10° intervals. The real data were compared with the simulated data and the value of χ^2 calculated for a range of angles and percentages of polarisation. These values were used to generate significance level contour plots, which gave a minimum at the angle and percentage of polarisation that most closely matched the real data.

Each second of data during the 66 seconds was also analysed separately using the standard OSA software. It was observed that approximately 30 seconds into the brightest portion of the burst, the live time per second of each detector dropped dramatically to about half of its original value due to the high data rate and telemetry limitations (Figure 6.9). The result was that almost half of the multiple events during this period were lost, and so it was necessary to reduce the multiple event background to take this loss into account (Figure 6.10). The analysis was carried out for the brightest 12 seconds of the pulse (T_0= 276s to T_0 = 288s) before the event rates were significantly affected by packet loss to check the method and to avail of a higher signal to noise. The two sets of results for the 12 second and the 66 second intervals could then be analysed separately and compared.

The multiple event rates between detectors on opposite sides of the array was examined to determine the random rate between non-adjacent detectors and to investigate if the GRB had sub-microsecond variability (i.e. if events were deposited in a shorter interval than the 350ns coincidence time window). It was observed that even between detectors with high single event count rates (e.g. detectors 10 and 15) in the 66 second interval, the average multiple event rate was approximately 1 count over the 66 second duration. This result agrees with the expected random rate and excludes sub-microsecond variability in GRB041219a.

The event distribution is highly dependent on SPI's geometry (Lei et al. 1997). Since there are inhomogeneities in the detector layout (e.g. inoperative detectors and detectors covered by the coded mask), the Q distribution will also be distorted. This distribution as a function of polarisation angle was simulated and taken into account when estimating an average value of Q. From our simulations, we estimated the average modulation factor Q for 100% polarisation to be 24 ±7%, in agreement with the calculations of Kalemci et al. (2004b).

6.2.4.1 First Burst

The results of the fitting procedures for the main burst are given in Table 6.2, which lists the percentage polarisation and the angle for the 12 second and 66second time intervals in the energy ranges 100-350keV, 100-500keV and 100 keV-1MeV. The errors quoted for the percentage and angle of polarisation are 1σ for 2 parameters of interest.

Figure 6.12 shows the contour plots obtained by comparing the real and simulated data for the six scatter directions in the 12 second interval. Figure 6.13 shows the corresponding contour plots for the three scatter directions in the 12 s and 66 s intervals. The contour plots for the 66 second interval for the six scatter directions are not shown, because the best fit probability indicates that the model was not a good fit to the real data, and a 68% probability contour could not be generated. The contour plots indicate a non-zero value for the level of polarisation in all of the time intervals and energy ranges studied.

Table 6.2: Table of results from χ^2 fitting of real and simulated data. The columns from left to right list the duration of the interval, the polarisation percentage, angle and best-fit probability that the model simulations matched up with the real data, the energy ranges analysed over three directions (columns 6-7) and the energy ranges analysed over six directions (columns 3 and 4). The errors quoted are 1σ for 2 parameters of interest.

	Polarisation	**6 Directions**		**3 Directions**		
		100-350keV	100-500keV	100-350keV	100-500keV	100keV-1MeV
12 second interval	Percentage (%)	98±53	71^{+52}_{-53}	96^{+39}_{-40}	70±37	68±29
	Angle (°)	60^{+16}_{-17}	70^{+22}_{-21}	60^{+12}_{-14}	70^{+15}_{-14}	70^{+14}_{-10}
	Probability (%)	87.2	93.4	99.8	99.5	95.9
66 second interval	Percentage (%)	70±20	52±11	63^{+31}_{-30}	49±24	26±20
	Angle (°)	70^{+9}_{-8}	70±5	71^{+14}_{-11}	70^{+16}_{-11}	70^{+19}_{-27}
	Probability (%)	18.4	36.9	98.0	95.5	97.3

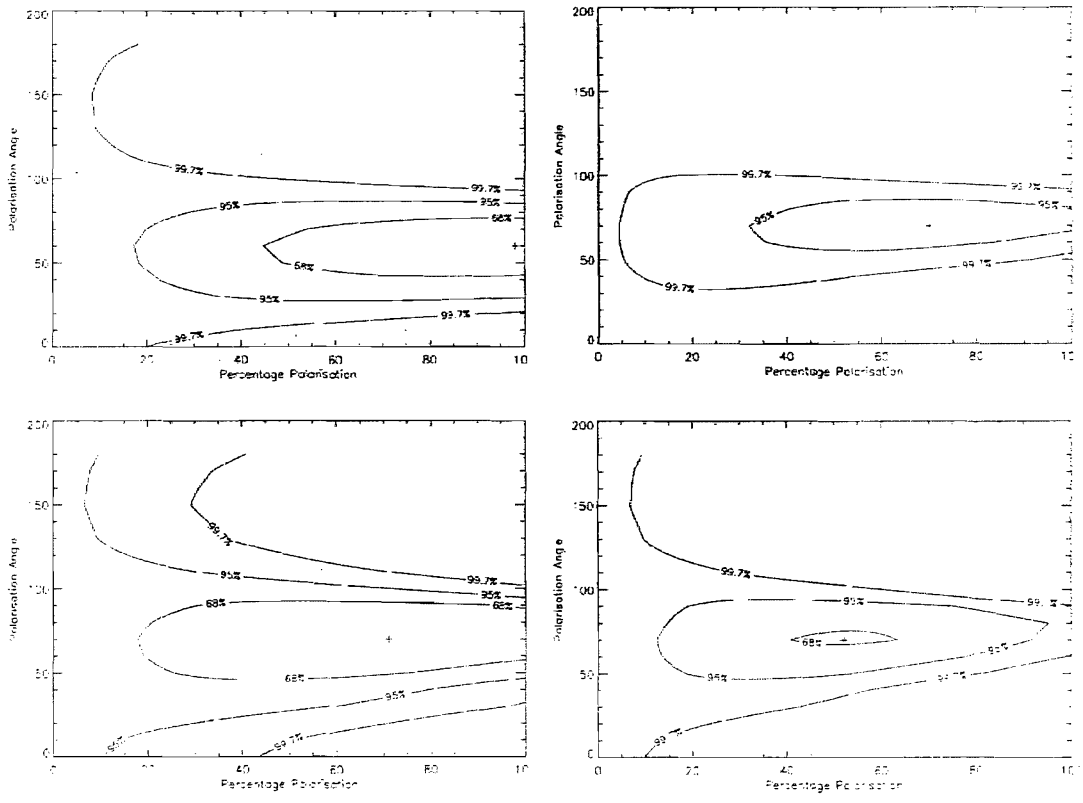

Figure 6.12: Contour plots of the percentage polarisation as a function of the polarisation angle for the six scatter directions (0°, 60°, 120°, 180°, 240° and 300°), showing the 68%, 95% and 99.7% probability contours. The plots for the 12s interval are in the left column and the plots for the 66s interval are on the right. The energy ranges are 100-350keV and 100-500keV for each row respectively.

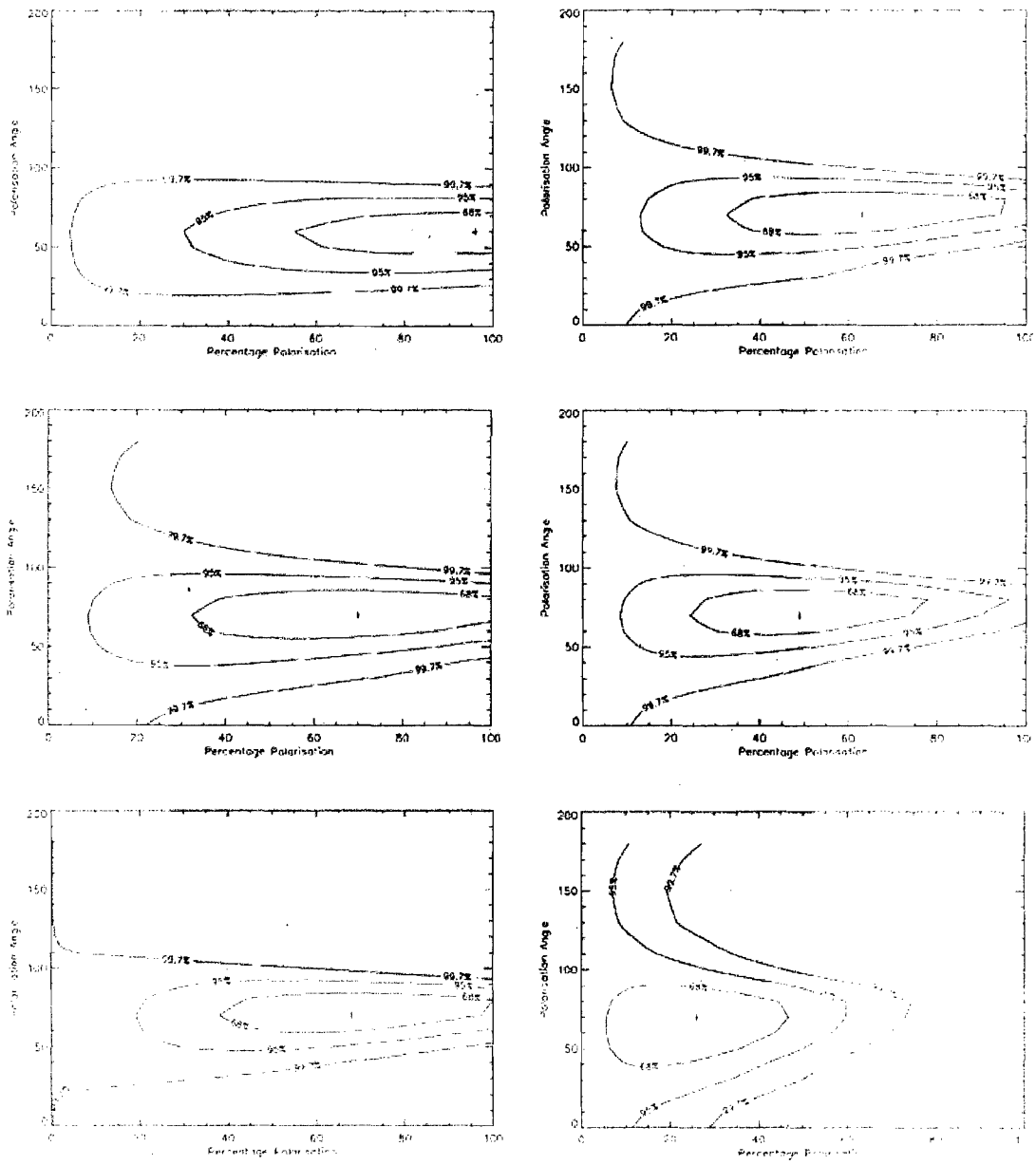

Figure 6.13: Contour plots of the percentage polarisation as a function of the polarisation angle for the three scatter directions (0°, 60° and 120°), showing the 68%, 95% and 99.7% probability contours. The plots for the 12s interval are in the left column and the plots for the 66s interval are on the right. The energy ranges are 100-350keV, 100-500keV and 100keV-1MeV for each row respectively.

Eight of the ten cases listed in Table 6.2 indicate that the percentage of polarisation is greater than 50%. The best fit probability that the simulated values match the real data is greater than 99.8% in the 12 second interval for the three scatter directions in the 100 – 350 keV energy range, corresponding to a percentage polarisation of 96^{+39}_{-40}% at an angle of 60^{+12}_{-14} degrees (Figure 6.13(a)). The best fit probability in the 66 second interval is greater than 98% for the three scatter directions in the same energy range, corresponding to a percentage polarisation of 63^{+31}_{-30}% at an angle of 70^{+14}_{-11} degrees (Figure 6.13(b)). The polarisation angles are consistent in all cases with a value between 60° and 70°.

The errors quoted have been produced from the chi-squared 67% confidence level. In reality the polarisation percentage and polarisation angle are not independent. In the case of the GRBs the assumption of Gaussian statistics holds as there are ~500 counts per scatter direction. The correct probability distribution (Weisskopf et al. 2006) should be used to calculate the confidence levels. If the detected signal is characterized by a mean S and variance σ^2, then the probability of measuring a particular amplitude of modulation a and phase φ is given by

$$P(a,\varphi) = \frac{NS^2 a}{4\pi\sigma^2} \exp\left[-\frac{NS^2}{4\sigma^2}(a^2 + a_0^2 - 2aa_0\cos(\Delta\varphi))\right] \quad 6.1$$

where $\Delta\varphi = \varphi - \varphi_0$ and N is the number of different directions for which measurements were made, in this case 3 or 6.

It follows that the probabilities of measuring a independent of φ and φ independent of a are

$$P(a) = \frac{NS^2 a}{4\pi\sigma^2} \exp\left[-\frac{NS^2}{4\sigma^2}(a^2 + a_0^2)\right] I_0\left(\frac{NS^2 a a_0}{2\sigma^2}\right) \quad 6.2$$

and

$$P(\varphi) = \frac{1}{2\pi}\exp\left[-\frac{NS^2a_0^2}{4\sigma^2}\right] + \left(\frac{N}{2}\right)^{\frac{1}{2}}\frac{a_0 S\cos(\Delta\varphi)}{2\pi\sigma} \times$$
$$\exp\left[-\frac{N^2S^2\sin^2\Delta\varphi}{4\sigma^2}\right]\int_{-\infty}^{\left(\frac{N}{2}\right)^{\frac{1}{2}}\frac{a_0 S\cos(\Delta\varphi)}{\sigma}} \exp\left[-\frac{u^2}{2}\right] du \qquad 6.3$$

Where I_0 is the modified Bessel function of order zero. Both P(a) and P(φ) tend towards normal distributions with $\sigma_a = (2/N)^{0.5}$ and $\sigma_\varphi = \sigma_a/a_0$ when, as in the case for the GRBs, the argument of the Bessel function in Eq 6.2 and the upper limit of the integral in Eq 6.3 become very large. The errors calculated with these equations are shown in Table 6.3.

Table 6.3: Table of results with errors calculated from Weisskopf et al (2006).

	Polarisation	**3 Directions**		
		100-350keV	100-500keV	100keV-1MeV
12 second interval	Percentage (%)	96±21	70±18	68±14
	Angle (°)	60±13	70±15	70±12
66 second interval	Percentage (%)	63±14	49±12	26±10
	Angle (°)	71±13	70±14	70±22

While the errors calculated for the polarisation angle are consistent, the errors for the polarisation percentage are approximately half the size of those calculated in the fitting. The fitting routine selects models that are fitting better than other models. It is likely that this method is not as sensitive to a change in polarisation percentage as the statistics suggest possible. This discrepancy may also be due to the correlation between the parameters.

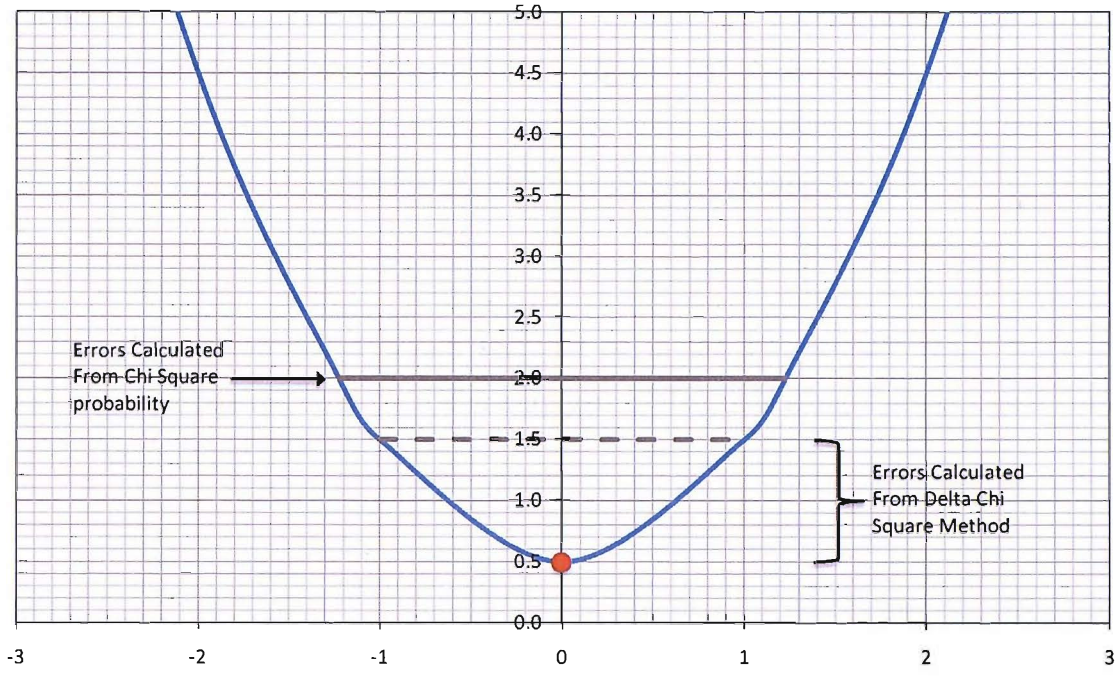

Figure 6.14: If the minimum of the fit is less than 1, then the errors calculated from the $\Delta\chi^2$ will be smaller than those calculated from the 67% percent probability value. In the case of 1 degree of freedom with a minimum $\chi^2 = 0.5$ the errors from $\Delta\chi^2$ will be ±1 while the errors from $\chi^2_{67\%} = 1.22$.

Although using the chi square value for a 67% probability is a legitimate method for calculating errors it has its drawbacks and the more conventional valued used is derived using the delta-chi square (Lampton et al. 1976). The $\Delta\chi^2$ required to produce the 68% contour for 2 parameters is 2.3. This means that the 1 sigma contour should be drawn at the level of $\chi^2_{min}+2.3$. For 2 and 3 sigma $\Delta\chi^2$ is 6.17 and 11.8 respectively. In the case of GRB041219a the best fit χ^2 was less than one, resulting in smaller errors being produced by the $\Delta\chi^2$ method (Figure 6.14).

The differences between the different methods of calculating the errors do not change the conclusions deduced from these results. In order to give a conservative estimate of the errors involved the errors calculated from the 67% probability will be used for the rest of this thesis.

Despite extensive analysis and simulations, we could not exclude a systematic effect that could mimic the weak polarisation signal. In some cases, the percentage polarisation exceeds 100% when the errors are taken into account. This is due to the poor signal to noise of the data and possible systematic instrumental effects.

The best polarisation signal would seem to be in the 100-350keV range since the polarisation percentage drops as the energy gets higher indicating that the signal could be being washed out.

6.2.4.2 Second Burst

The analysis of the second burst in GRB041219a was carried out in the same way as the first burst. The results of which can be seen in Table 6.4. Meaningful analysis of the results is very difficult due to the large errors. These large errors are due to the lack of counts in the background subtracted data. The background data was also analysed and produced a signal at an angle of 90 degrees. This causes a problem when looking at the lower energy results as the results are 90 degrees from the background signal. A signal like this can be produced by the over subtraction of the background creating an inverse of the background modulation in the real data.

Table 6.4: Table of results from χ^2 fitting of real and simulated data for the second burst of GRB041219a. The errors quoted are taken from the 1σ contours.

	Polarisation	**6 Directions**		**3 Directions**		
		100-350keV	100-500keV	100-350keV	100-500keV	100keV-1MeV
GRB041219a Second Peak	Percentage (%)	58±51	50±40	47±50	52±40	97±30
	Angle (°)	180±35	30±25	180±33	30±27	50±10
	Probability (%)	60.16	54.30	99.99	99.92	99.52

6.2.5 Discussion

The results obtained from our simulations and analyses are consistent with linear polarisation at about the 60% level (~2σ) at an angle of ~70°. It is possible that the percentage polarisation varies with energy, angle and time over the duration of the burst. However, the levels of polarisation measured during the brightest 12 seconds of GRB 041219a and the brightest 66 second pulse are consistent at the ~2σ level, indicating that there is no major variation in polarisation during the intense 66 second pulse. It is unlikely that a burst brighter than GRB041219a will be detected by INTEGRAL. A GRB of similar fluence but over a shorter time interval may produce better statistics. Another possibility is a spectrally harder burst, similar to GRB941017 (González et al. 2003), which would produce more multiple events in the MeV energy range and thus create a strong polarisation signature.

Kalemci et al (2007) have independently analysed the SPI data for GRB041219a, with simulations performed using the MGEANT code rather than the GEANT 4 code used here. By fitting the azimuthal scatter angle distribution of the observed data over the 6 directions, the obtained results are consistent with Kalemci et al (2007) in both magnitude and direction, within the limits given by the large error bars. However, the more complete analysis presented here compares the observed data to various combinations of the simulated polarised and unpolarised data (Figure 6.12 and Figure 6.13, Table 6.2). There is a possibility that instrumental systematics may dominate the measured effect.

There are a number of different methods for measuring polarisation using the INTEGRAL instruments. For example, Marcinkowski et al. (2006) described a new method of using the IBIS instrument in Compton mode to detect and analyse an intense burst that was outside the coded and partially coded field of view of IBIS. GRB030406 was detected well through the shield using this method. Since IBIS consists of two layers of detector arrays (Ubertini et al. 2003), Compton scattering can be used to detect the events that interact in one layer and scatter into the second layer. The Compton mode determines the energy deposit and position of the event in each array. Therefore, it may be possible to extend this technique to measure the polarisation fraction of a spectrally hard GRB as well as the spectral and temporal parameters.

The spectra of GRB041219a have been fit well by both the Band model and a combination of a black body plus power law model (McBreen et al. 2006). Recently Ryde (2005) studied the prompt emission from 25 bright GRBs and found that the time resolved spectra could be equally well fit by the black body plus power law model and with the Band model. Rees and Mészáro (2005) suggested that the E_{peak} in the gamma-ray spectrum is due to a Comptonised thermal component from the photosphere. The thermal emission from a laminar jet when viewed head-on would give rise to a thermal spectrum peaking in the X-ray or gamma-ray band. The resulting spectrum would be the superposition of the Comptonised thermal component and the power law from synchrotron emission. Unfortunately, the polarisation measurements of GRB041219a are not sensitive enough to detect the change in polarisation that might result from the combination of the Compton and synchrotron processes.

A significant level of polarisation can be produced in GRBs by either synchrotron emission or by Inverse Compton scattering. The fractional polarisation produced by synchrotron emission in a perfectly aligned magnetic field can be as high as $\Pi = (p + 1)/(p + 7/3)$ where p is the power law index of the electron distribution. Typical values of $p = 2 - 3$ correspond to a polarisation of 70 - 75%. An ordered magnetic field of this

type would not be produced in shocks but could be advected from the central engine (Lyutikov et al. 2003).

Another asymmetry capable of producing polarisation, comparable to an ordered magnetic field, involves a jet with a small opening angle that is viewed slightly off-axis (Waxman 2003). A range of magnetic field configurations have been considered (Ghisellini and Lazzati 1999; Sari 1999; Granot 2003; Nakar et al. 2003; Fan et al. 2005). The intensity distribution and maximum polarisation of the jet are modified if the pitch angle distribution of the electrons is not isotropic, but biased towards the orthogonal direction (Lazzati 2006). The more anisotropic distribution produces larger net polarisation. For broader jets, only a small fraction of random observers would detect a high level of polarisation.

Shaviv & Dar (1995) and Dar & de Rújula (2004) have pointed out that polarisation is a characteristic signature of the Inverse Compton process. This mechanism was also considered in the framework of an ensheathed fireball (Eichler and Levinson 2003). Compton Drag (CD) emission is produced when ionised plasma moves relativistically through a photon field. A fraction of the photons undergo Inverse Compton scattering on relativistic electrons and have their energies increased by $\sim 4\gamma^2$ where γ is the electron Lorentz factor, and under certain circumstances the scattered photons have high polarisation.

Lazzati et al (2004) considered CD from a fireball with an opening angle comparable to the relativistic beaming. The polarisation is lower than that from a point source because the observed radiation comes from different angles. In the fireball model, the fractional polarisation emitted by each element remains the same, but the direction of the polarisation vector of the radiation emitted by different elements within the shell is rotated by different amounts. This can lead to effective depolarisation of the total

emission (Lyutikov et al. 2003), which is not observed in GRB041219a. A lower level of polarisation has recently been predicted for X-ray flashes (Dado et al. 2007).

Lazzati et al (2004) calculated the polarisation as a function of the observer angle for several jet geometries, and showed that a high level of polarisation can be produced if the condition $\Gamma\theta_j \leq 5$ is satisfied, where Γ is the Lorentz factor of the jet and θ_j is the opening angle of the jet. In the case of GRB041219a, it is possible to estimate the values of Γ and θ_j in the following way. GRB041219a is estimated to have a redshift of $z \sim 0.7$ using the Yonetoku relationship (Yonetoku et al. 2004). The fluence from 20keV to 8MeV is $5.7\text{x}10^{-4}$ ergs cm^{-2}, yielding a value of $\sim 10^{54}$ ergs for the total isotropic emission (McBreen et al. 2006). The standard beaming corrected energy for GRBs is $E = 5\text{x}10^{50}$ ergs (Frail et al. 2001). Combining this information with the total isotropic emission yields a value of $\theta_j \sim 2.5°$ (0.044 rad). The Lorentz factor of the fireball can be obtained from the redshift corrected peak energy E_{peak} (E_{peak} = 483keV for GRB041219a) by the relationship

$$E_{peak} \approx 10\Gamma^2 kT \qquad 6.4$$

where $T \sim 10^5$K is the black body spectrum of the photon field (Lazzati et al. 2004). The computed value is $\Gamma \sim 75$, yielding the results:

$$\Gamma\theta_j \sim 3.3 \qquad 6.5$$

The small value of $\Gamma\theta_j$ shows that it is possible to have polarisation of ~60% in GRB 041219a and also produce the lower limit to the values of the polarisation for two BATSE GRBs (Willis et al. 2005) and the value of 41^{+57}_{-44}% obtained by RHESSI for GRB021206 (Wigger et al. 2004).

Synchrotron radiation from an ordered magnetic field advected from the central engine and Compton Drag are both good explanations for a significant level of polarisation. It should be possible to distinguish between the two emission mechanisms. Only a small fraction of GRBs should be highly polarised from Compton Drag because they have narrower jets, whereas the synchrotron radiation from an ordered magnetic field should be a general feature of all GRBs. Another possible distinction between the two processes involves the optical flash because the Compton Drag radiation should be less polarised than synchrotron radiation.

6.3 Analysis of GRB060901 and GRB061122

To date INTEGRAL has observed 46 GRBs. Only a few have been in the field of view of the main instruments and even less have occurred when the instrument has been in a suitable working state (i.e. not in calibration or histogram modes). Aside from GRB041219a only two other bursts seen by INTEGRAL are suitable for an attempt to measure their polarisation, GRB060901 and GRB061122.

6.3.1 Two More On-Axis Bursts

GRB060901 was detected by the INTEGRAL Burst Alert System (IBAS) at 18:44:00 UT on 1 September 2006 at a location of R.A. = 19h 08m 32.82s, Dec = -6° 38' 22.5", at an instrument off-axis angle of 15° (Mereghetti et al. 2006b). GRB060901 was very bright and saturated the ISGRI telemetry (Mereghetti and Gotz 2006a). The KONUS-Wind (Golenetskii et al. 2006) experiment reported a fluence from 20keV to 2MeV of $(1.51^{+0.14}_{-0.19}) \times 10^{-5}$ erg cm^{-2}. The SPI light curve can be seen in Figure 6.15 (top). Only a single optical afterglow measurement was made and included no polarisation data (Wiersema and Thoene 2006).

The second burst, GRB061122 was detected by IBAS at 07:56:45 on 22 November 2006 at a location of R.A. = 20h 15m 20.88s, Dec = +15° 30' 50.8", at an instrument off-axis angle of 7° (Mereghetti et al. 2006a). GRB061122 was also a bright burst with a lower fluence limit of 3×10^{-6} erg cm^{-2} (Mereghetti and Gotz 2006b). The SPI light curve can be seen in Figure 6.15 (bottom). This burst was seen in both the X-ray (Beardmore et al. 2006) and optical (Oates and McBreen 2006), however no polarisation measurements were made.

Table 6.5: Spectral parameters for GRB060901 and GRB061122

GRB	Off-Axis Angle (°)	T_{90} (s)	α	β	Break Energy (keV)
060901	15	12	$-0.61^{+0.71}_{-0.50}$	$-1.95^{+0.23}_{-0.98}$	133^{+285}_{-155}
061122	7	11	$-0.98^{+0.11}_{-0.12}$	$-2.72^{+0.34}_{-0.85}$	166^{+39}_{-28}

Both bursts have been fitted with the Band model which gave the parameters in Table 6.5. The polarisation analysis was carried out in the same way as for GRB041219a. The results of the fitting can be seen in Table 6.6, where the errors quoted are taken from the 1σ contours for the parameters of interest.

Table 6.6: Table of results from χ^2 fitting of real and simulated data for GRB060901 and GRB061122. The errors quoted are taken from the 1σ contours.

	Polarisation	6 Directions		3 Directions		
		100-350keV	100-500keV	100-350keV	100-500keV	100keV-1MeV
GRB060901	Percentage (%)	0	100	100	100	29^{+22}_{-29}
	Angle (°)	0	90	90 ± 18	90	20

	Probability (%)	100	99.7	57.8	0.01	99.99
GRB061122	Percentage (%)	31	32	11^{+48}_{-11}	25^{+45}_{-25}	29^{+25}_{-26}
	Angle (°)	40	90	40	100^{+65}_{-66}	100^{+32}_{-24}
	Probability (%)	26.4	28.0	99.8	99.4	97.3

6.3.2 GRB060901 Results

This burst was a long way off-axis at 14 degrees, but also fell at a roll angle where only 6 pixels were not fully covered by the mask (Figure 6.16). These detectors were also placed at the edge of the detector plane and not evenly distributed leaving little in the way of directional information. The real data and simulations of the instrument have been compared at 100 – 350 keV, 100 – 500 keV and 100 – 1000 keV for both 3 and 6 directions. For the 6 directions all the fits failed to produce any contours, as did the 100 – 500 keV data in 3 directions. In 3 directions the 100 – 350 keV data produced contours showing a polarisation angle of 90 degrees and a percentage of >60% at 1sigma. While the 100 – 1000 keV data showed an angle of 20 degrees with a percentage of <65% at 1 sigma. The background data for the burst was also analysed to see what polarisation this would produce. This data consistently gave a polarisation angle of 10 degrees.

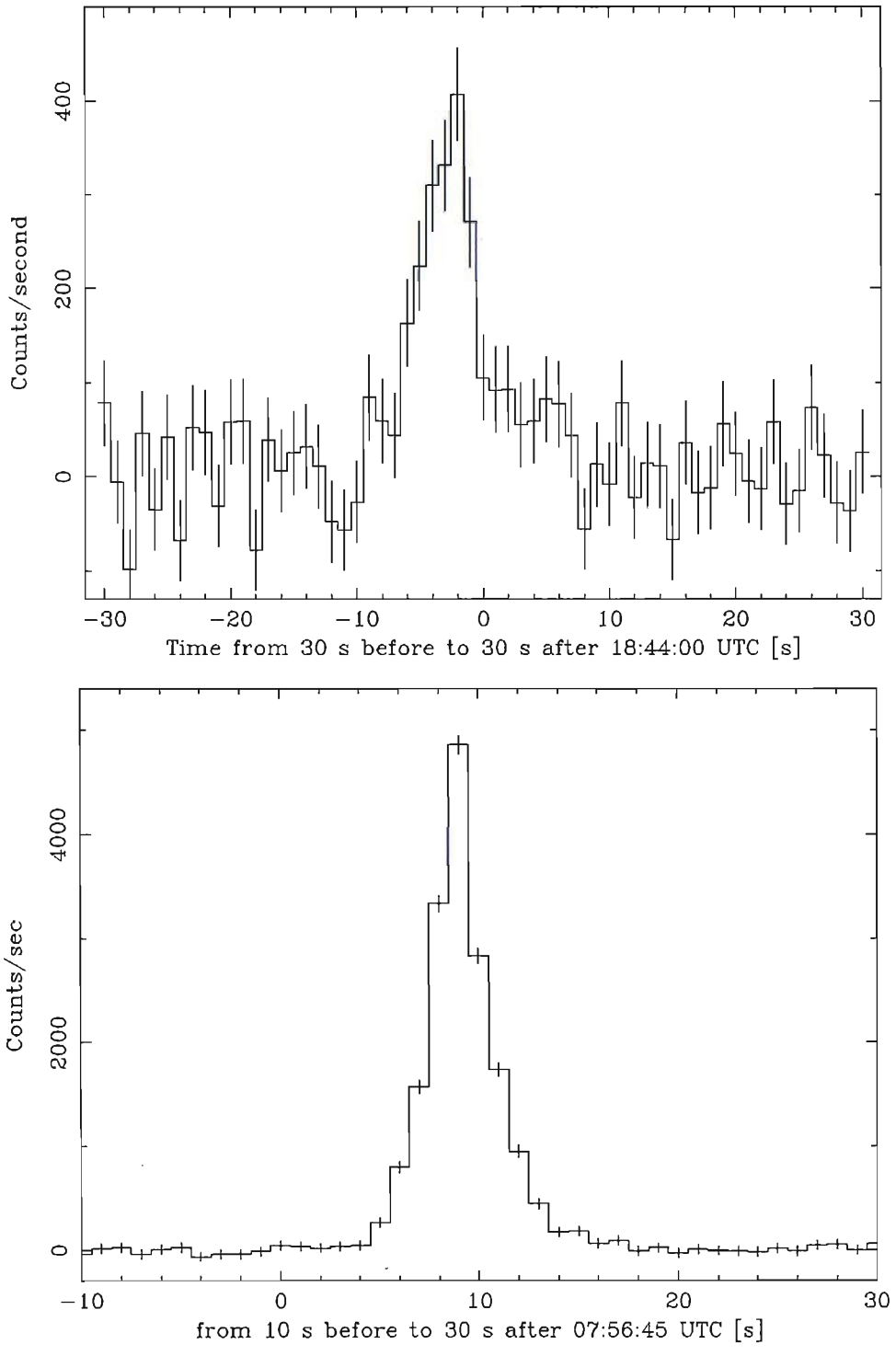

Figure 6.15: The background subtracted SPI light curves for GRB060901 (top) and GRB061122 (bottom).

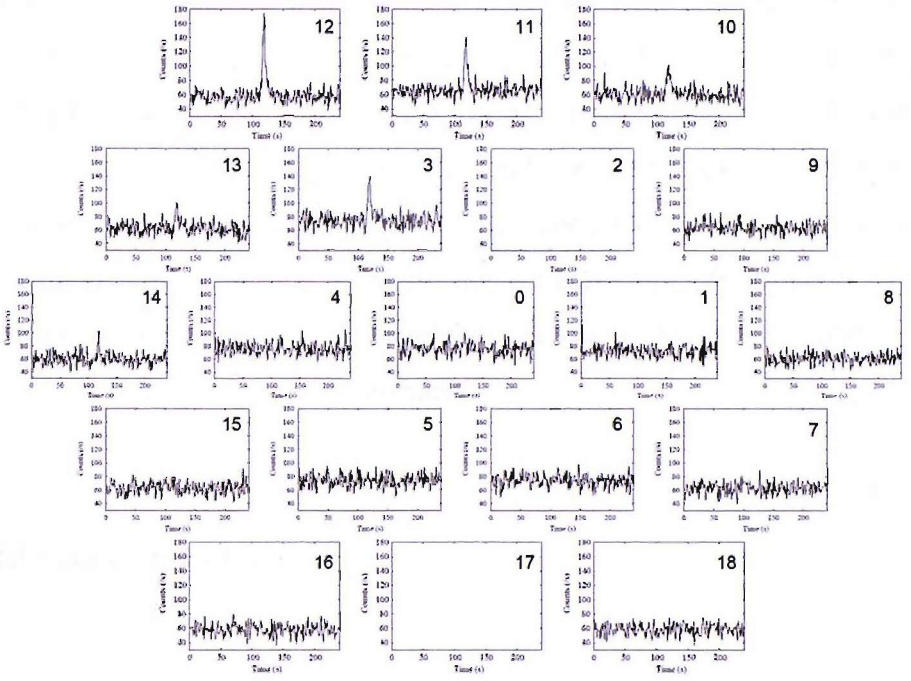

Figure 6.16: The layout of the 19 detectors of SPI with the single event light curves of GRB060901 showing the variation in count rate per detector. The horizontal and vertical axes give the time and count rate in each detector. The detector number is indicated in the corner of each light curve. The detectors with high count rates were not obscured

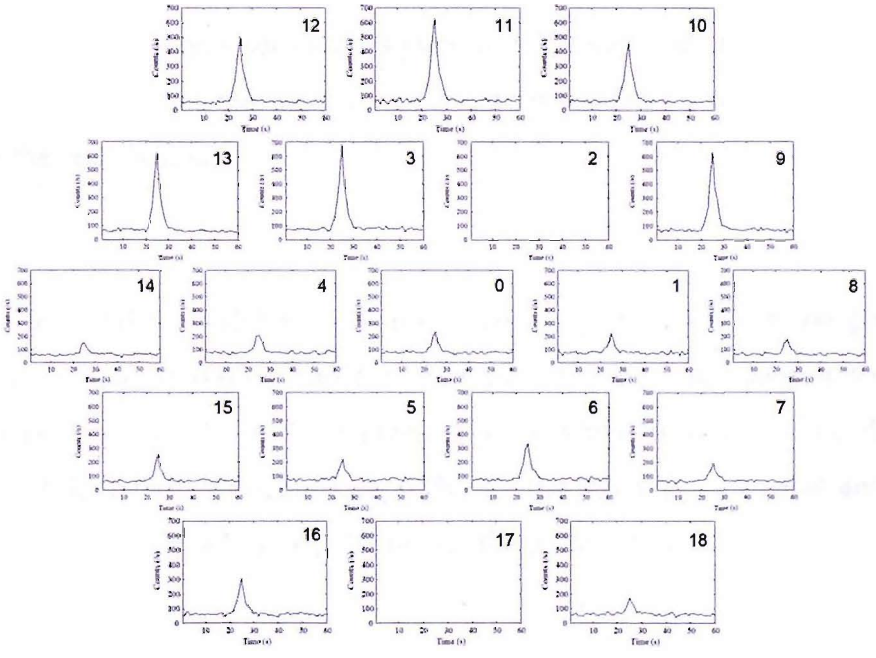

Figure 6.17: The layout of the 19 detectors of SPI with the single event light curves of GRB061122 showing the variation in count rate per detector. The horizontal and vertical axes give the time and count rate in each detector. The detector number is indicated in the corner of each light curve. The detectors with high count rates were not obscured

These results indicate that at 100 – 1000 keV a polarisation signal from the background is being seen due to the polarisation angles being similar. At higher energies the background subtraction becomes problematic. At 100 -350 keV it is possible there is still a contribution from the background. This is because the angle is 90 degrees away from the background angle (within errors). Since this burst is weak and poorly situated on the detector it is possible that there are not enough counts to properly background subtract the data and the data has been slightly over subtracted. This is simply a lack of counts leading to a poor result from this burst.

6.3.3 GRB061122 Results

This burst was 7 degrees off-axis and illuminated the detector plane much better than the previous burst. The same procedure has been followed as before. For this burst the 6 direction and 3 direction analyses both produced agreeing results, however, the 6 direction data produced much lower probabilities of fitting. The 3 direction data gave the results of 40 degrees and <60% at 1 sigma for <350 keV and 100 degrees and <60% for >350 keV. Again, analysis of the background produced a consistent signal of 100 degrees for the polarisation.

The results from GRB061122 show a polarisation signal similar to the polarisation signal of background of 100 degrees for energies >350 keV. At energies <350 keV a different polarisation angle of 40 degrees is seen which is likely to be due to the polarisation of the burst. Unfortunately, <350keV the signal is very weak and not very well bounded. However, a limit can be put on the polarisation of <60% at 1 sigma and <90% at 2 sigma.

6.3.4 Discussion

Both these bursts suffer greatly from a lack of signal. Although both are bright bursts, their durations are short, reducing the number of available counts. With the reduction of polarisation signal seen in GRB041219a as the energy range is increased, it is understandable that with these bursts the chances of obtaining a measurement in the higher energy bands is going to be less.

6.4 Summary

Several attempts at measuring the polarisation in GRB flux have been made and met with varying success. The results obtained from these three bursts have been on the limit of what is possible with the technique used in this thesis. The best results have been obtained from GRB041219a, while the other bursts have suffered from very low count rates. The results obtained are consistent with linear polarisation at about the 60% level (~2σ) at an angle of ~70°. It is possible that there is variation in the polarisation properties over the duration of the burst. However, due to the large errors it is impossible to tell with any statistical significance if this is the case.

Table 6.7: Summary of all gamma-ray GRB polarisation measurements.

Burst	Percentage of polarisation
GRB021206 (Wigger et al. 2004)	41^{+57}_{-44}%
GRB930131 (Willis et al. 2005)	>35%
GRB960924 (Willis et al. 2005)	>50%
GRB041219a (Kalemci et al. 2007)	98±33%
GRB041219a	63^{+31}_{-30}%
GRB060901	Null
GRB061122	<60%

Table 6.7 gives a summary of all the gamma-ray polarisation measurements for GRBs. All the measurements indicate a high level of polarisation of around 50%-60%. A polarisation percentage this high indicates that the source of the emission must be well ordered, probably with strong magnetic fields. All the measurements calculated in this thesis show a drop off of signal as the energy range gets larger. This could be an indication of an Inverse Compton scattering process being involved, such as that suggested by Shaviv & Dar (1995) and Dar & de Rújula (2004). However, this is more likely to be due to the number of multiple events dropping off rapidly with higher energies. It is still too early in the measurement of gamma-ray burst polarisation to be able to remove models from consideration, although the high levels of polarisation measured would rule out a hydrodynamic model.

GRB041219a is likely to be the best burst for polarisation analysis that will be seen by INTEGRAL. It was very long and bright producing a large number of events in the SPI detectors. The further bursts analysed highlight how difficult it is to get the perfect burst. GRB060901 and GRB061122 were both very bright bursts, however, the combination of their large off axis angle and short T_{90} time means that they simply did not produce enough events in the detector to analyse. The ideal burst would have to be brighter and longer than GRB041219a in order to produce better results than those presented here. Unfortunately, GRBs occurring within the field of view of SPI are a rare and random occurrence, so it is unknown if this result will be able to be improved with this instrument. At this stage a persistent source becomes more attractive since more data can be obtained and stacked to obtain more counts, even though the source is much fainter than a GRB.

Chapter 7

The Theory and Detection of Polarised Emission from the Crab Pulsar

7.1 Introduction

A natural follow on to the GRB polarisation measurements with SPI is to use the same technique to look at other sources of gamma-rays. The obvious candidate is the Crab pulsar since it is the brightest source and there is already a vast amount of archive observations. There has also been a great deal of polarisation measurements made at other wavelengths, giving a good set of results to make comparisons with.

The Crab nebula is the remnant of a supernova explosion, first recorded by Chinese astronomers in 1054 (T'o-t'o 1313-1355). The nebula was discovered in the 18th century and has provided a source of fascination to astrophysicists ever since. The spin down energy loss of the 33ms pulsar visible near the centre of this object is known to power

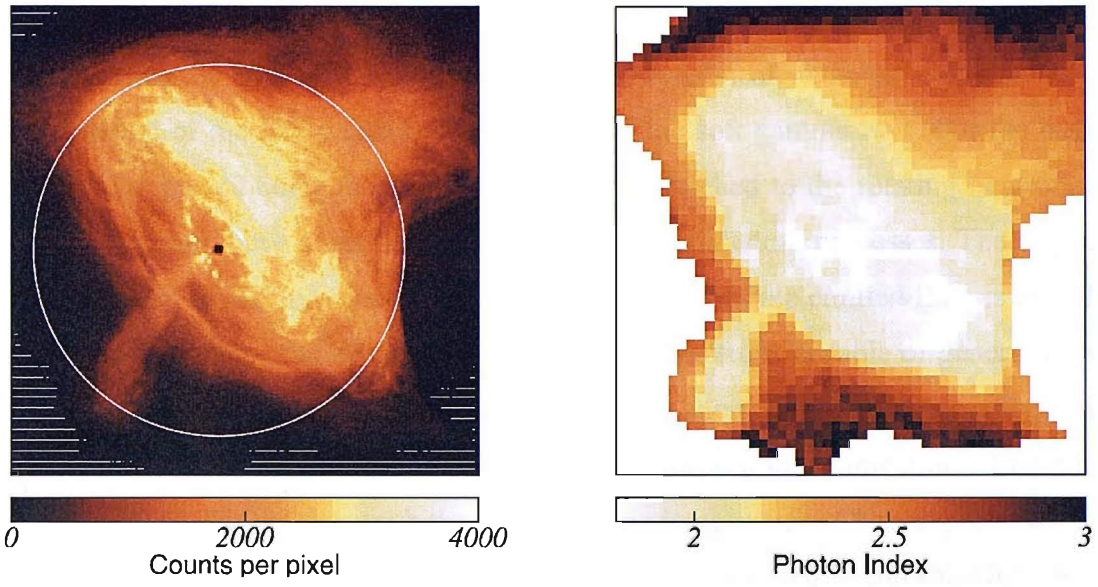

Figure 7.1: The Chandra ACIS-S image of the Crab Nebula (left). The "hole" at the pulsar position is caused by severe event pileup, while the circle centred on the pulsar shows the structure extends to ~50" radius. From this a map of the photon index can be produced (right) (Mori et al. 2004).

the system that emits non-thermal radiation over all wavelengths from radio to the highest detectable gamma-rays. Recent high resolution Chandra X-ray images (Weisskopf et al. 2000; Willingale et al. 2001; Hester et al. 2002) have revealed a large amount of structure to the high energy emission, including a jet, aligned with the pulsar spin axis, an equatorial torus and wisps moving outwards from an inner ring at ~0.5c. The X-ray spectrum varies throughout the torus and jet structure (Mori et al. 2004) which measures ~50" across (Figure 7.1). Current gamma-ray instrumentation does not have the angular resolution to identify the site of the high energy emission.

The origin of the high energy emission of rotation-powered pulsars and their associated PWN is an unresolved problem. The observed pulsating radiation constitutes only a small fraction of the pulsar's spin-down energy losses. A large fraction of the energy is carried off in the form of a magnetised relativistic pulsar wind, and in a number of cases, including the Crab, a highly collimated jet, thought to be aligned with the spin axis of the pulsar, is also seen (Hester et al. 1995; Gotthelf and Wang 2000; Weisskopf et al. 2000; Gaensler et al. 2001; Helfand et al. 2001; Pavlov et al. 2001; Gaensler et al.

2002; Hester et al. 2002; Helfand et al. 2003; Pavlov et al. 2003; Roberts et al. 2003). The presence of the torii, jet structures and dynamical features complicates the identification of the likely site(s) of the origin of the soft gamma-rays. For the case of the Crab the pulsed component is unambiguously attached to the rotating neutron star, although we only have scant ideas as to the detailed radiation processes. The origin of the non-pulsed emission, which constitutes the majority of the emitted flux, is even less clear. However, since the lifetimes of the energetic electrons capable of generating soft gamma-rays through the synchrotron process is very short, they will necessarily radiate close to their acceleration zone and hence identify the source of injection. Comparing the INTEGRAL/ISGRI data with the spectroscopic images from Chandra, together with the implications of the INTEGRAL/SPI polarisation measurement, can shed light on the location of the origin of the INTEGRAL gamma-ray fluxes.

7.2 Polarisation at Other Wavelengths

7.2.1 Radio

Measurements of polarisation at radio wavelengths of the Crab emission have been carried out since the 1950s (Brown et al. 1955). However, it was not until much later that phase resolved polarisation measurements were made (Manchester 1971; Manchester et al. 1972). At this time the only three components of the pulsar's profile known were: a steep-spectrum precursor, which was approximately 100% polarised, the main pulse and secondary pulse, which were 15% and 25% polarised respectively.

The best radio polarisation measurement to date was made by Moffett and Hankins (1999). Their measurements made between 1.4 and 8.4 GHz with the Very Large Array (VLA) radio telescope showed a large sweeping change in the polarisation (Figure 7.2). The polarisation percentage also varies between 20% and 80%.

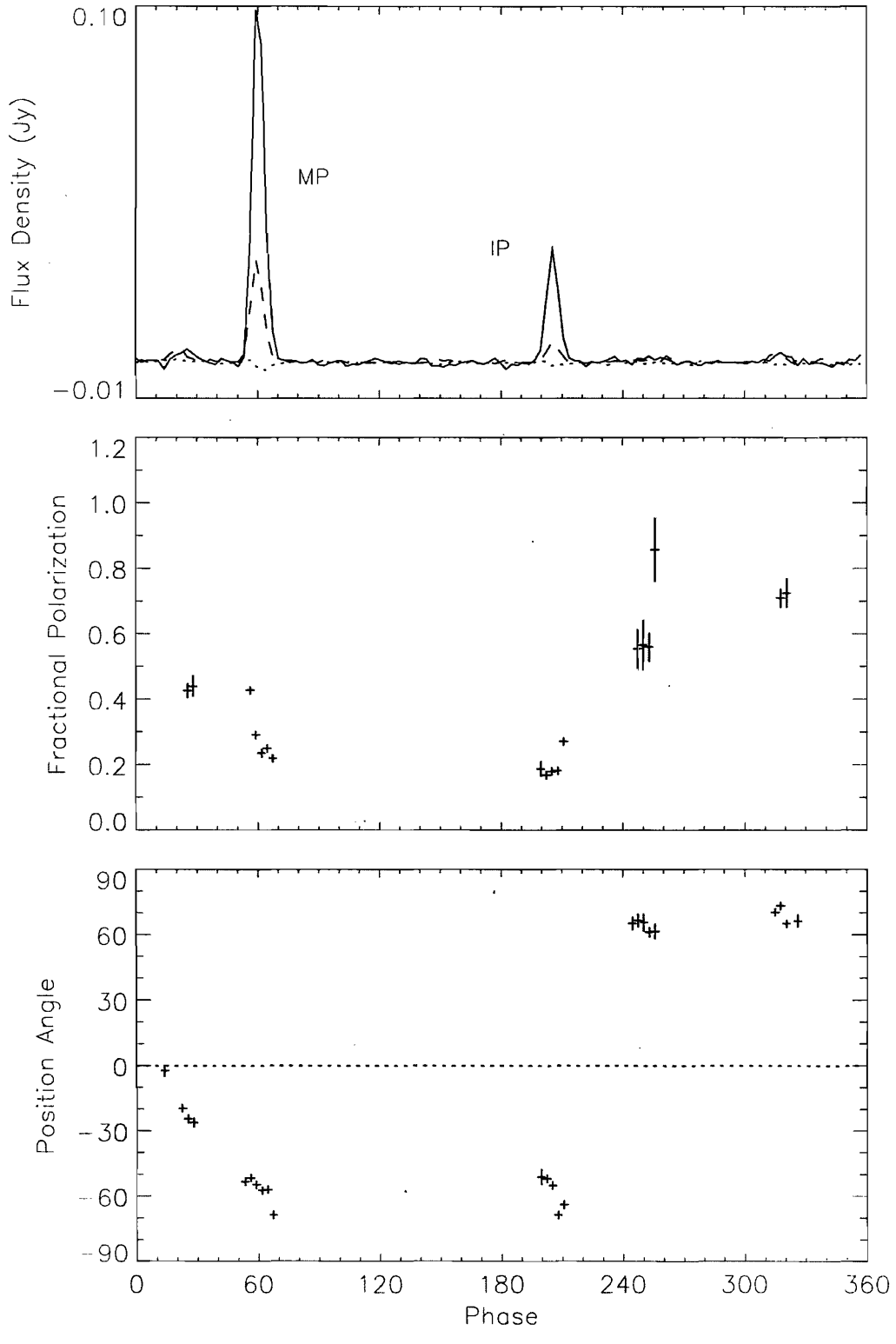

Figure 7.2: Plots of pulse profile, fractional polarisation and linear polarisation angle of the Crab pulsar emission at 1.4 GHz (Moffett and Hankins 1999). Where MP is the main pulse and IP is the interpulse.

The evidence for a slow 'S' shaped rotation of the polarisation angle is strong in the radio (Figure 7.2). If the gamma-ray polarisation behaves in a similar manner then phase resolved measurements may be easier, as a faster changing angle may be washed out if the phase binning is too coarse. However, there are large gaps in the phase resolved data in the radio which may be hiding structure reminiscent of the polarisation found in other bands.

7.2.2 Optical

The characteristics of the polarisation have been measured in the greatest detail at optical wavelengths. The polarisation of the optical emission was discovered by Wampler et al (1969), and subsequently investigated by Lynds et al (1969), Smith et al (1978; 1988) and Jones et al (1981). Early observations assumed that the pulsar's emission was negligible between the pulses allowing this part of the cycle to be used to establish the background polarisation. However Peterson et al and Jones et al (1981) showed that emission persisted though the pulsar's cycle, and were able to measure the polarisation by subtracting the background taken from a 2 arcsec annulus centred on the pulsar.

The latest optical results have been performed using OPTIMA (Optical Pulsar TIMing Analyser) (Kanbach et al. 2003; Kanbach et al. 2005; Slowikowska et al. 2007), however, measurements have also been made in the ultra-violet (Graham-Smith et al. 1996) and using the Hubble Space Telescope (Dolan et al. 1996).

OPTIMA uses a rotating Polaroid filter, with images taken every 2° at a wavelength range of 450-750 nm (Kanbach et al. 2003). The phase resolved results from the instrument used in combination with the Nordic Optical Telescope can be seen in Figure

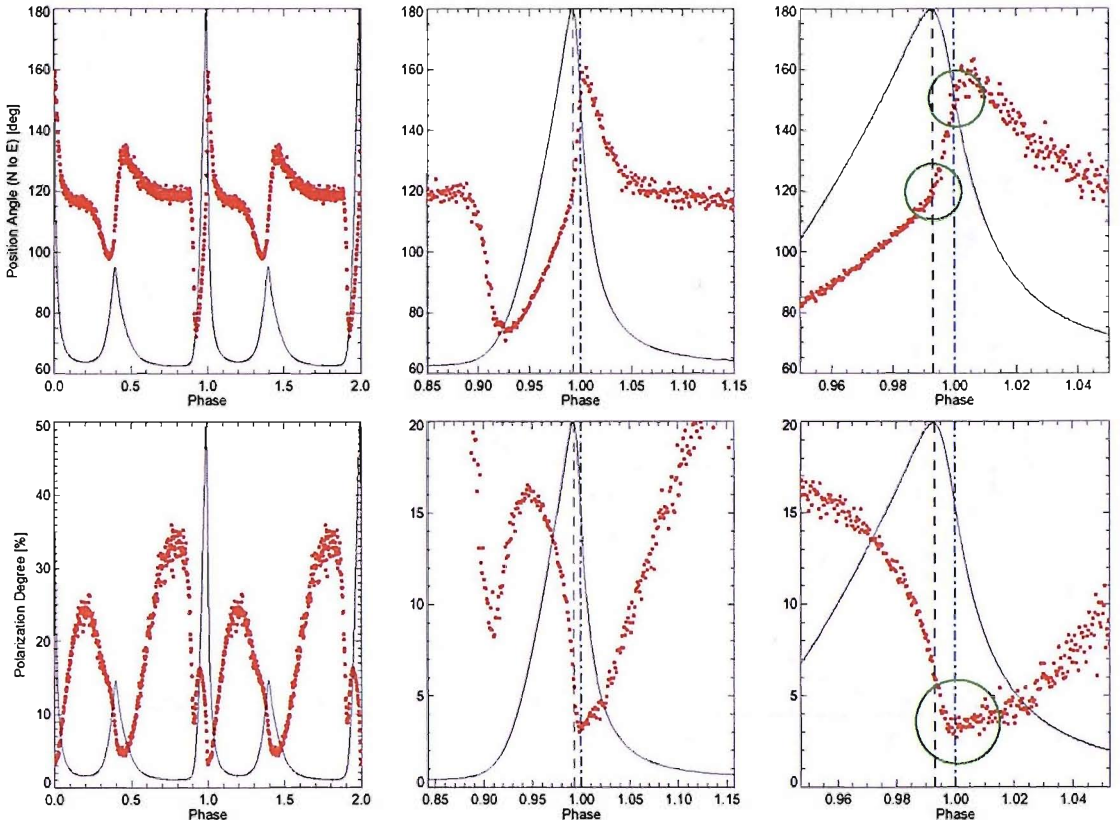

Figure 7.3: Optical polarisation characteristics of Crab pulsar. The polarisation angle (top row) and polarisation percentage (bottom row) are shown against the phase of the pulses. For clarity the Crab pulse profile is over plotted (black line). It can be seen that the polarisation changes rapidly across the Main pulse (middle and right columns). The black dashed line indicates the optical maximum phase, while the blue dashed line indicates the peak radio phase. A DC component of phase range 0.78-0.84 has been removed with the polarisation angle of 118.9° and a percentage polarisation of 33% (Slowikowska et al. 2007).

7.3 (Slowikowska et al. 2007). The optical polarisation is seen to change rapidly as the pulsar rotates. In a previous paper Kanbach et al (2005) subtracted a DC component polarisation signal of the off pulse (123° and 33%, 0.72-0.82 phase) from the polarisation of the pulsed emission (Figure 7.4). Removing a DC component in this way would only be valid if the off pulse emission was assumed to be a different emission mechanism than that of the pulsed emission. The DC component removed by Kanbach et al (2005) is aligned very close to the pulsar's spin axis and since the polarisation measurement was made of a region ~2" across, the emission region is much smaller than the torus and jet structure seen in Figure 7.1.

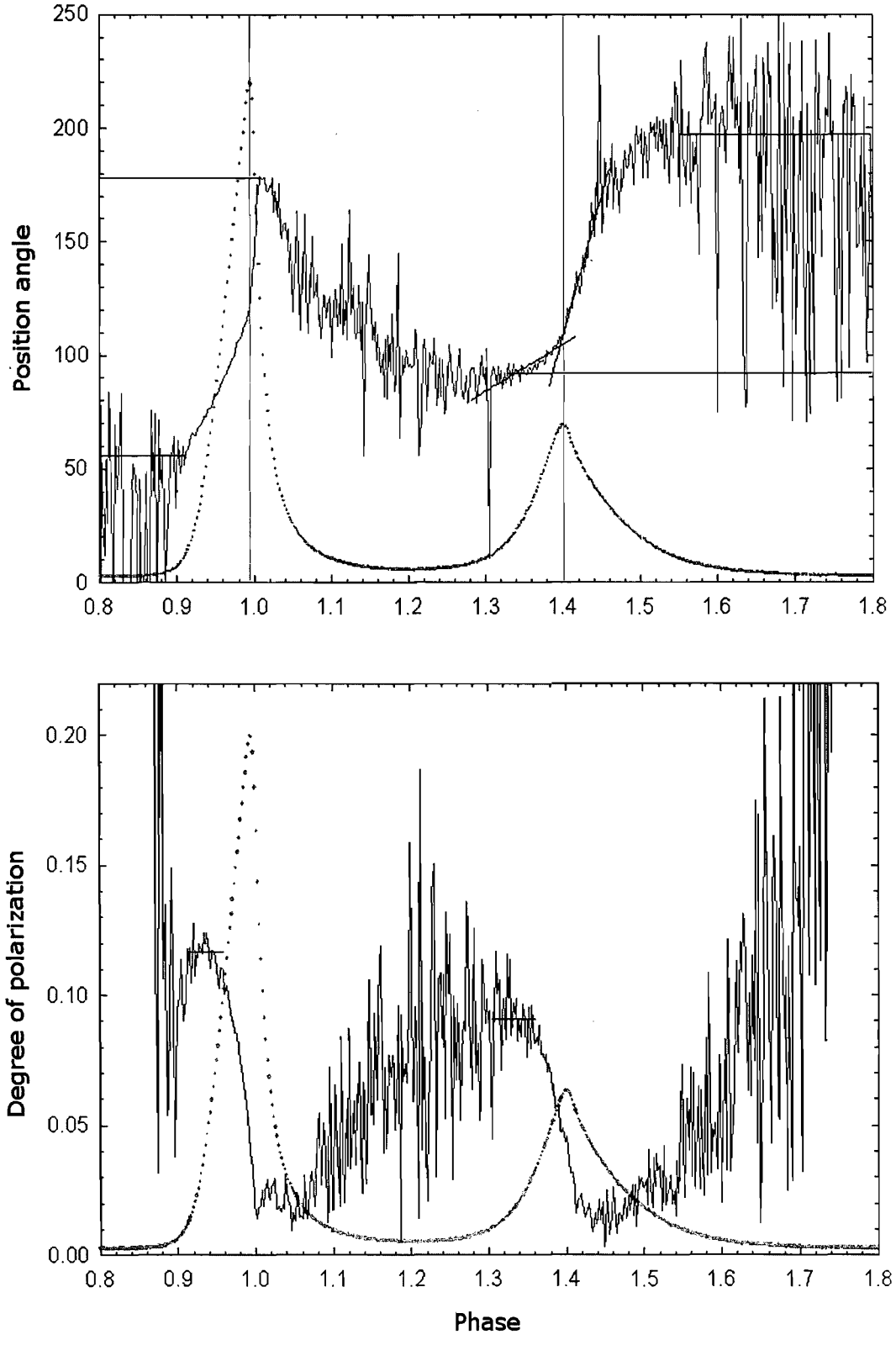

Figure 7.4: Polarisation characteristics of the 'pulsed component' of the Crab pulsar after the subtraction of DC component. The Crab light curve is over plotted for clarity (Kanbach et al. 2005).

The results of Slowikowska et al (2007) clearly show how the polarisation percentage drops to a minimum during the pulses as the polarisation angle rapidly changes. The rotation of the polarisation angle appears related to the profile of the main peak. At the beginning of the pulse the polarisation rapidly rotates to ~75° from the off pulse value of ~120°, and rotates smoothly through the pulse until the peak where the rotation increases until the angle reaches a maximum of ~160°, whereupon the polarisation returns to the DC value. The polarisation percentage does not reach its minimum precisely on the peak of the optical emission but on the peak of the radio emission. The quality of the optical polarisation results is excellent and has led to improvements in the various models of the Crab emission.

7.2.3 X-Ray

The measurement of polarisation at x-ray energies has not been extensively studied. The first evidence for linear polarisation from the Crab was obtained with a rocket experiment in 1971 (Novick et al. 1972). The result of ~156° and ~15% was later confirmed using the OSO8 satellite (Weisskopf et al. 1976; Silver et al. 1978; Weisskopf et al. 1978). Silver et al (1978) presented evidence that the polarisation rotated through the pulse, similar to the optical polarisation; however, the results had a low statistical significance. Weisskopf et al (1978) removed the pulsed component and produced a result from the off pulse phase of 156.4° ± 1.4° and 19.5% ± 2.8% at 2.6 keV from a region of 3° centred on the pulsar.

No further attempts at measuring the x-ray polarisation of the Crab pulsar have been published, although attempts were made to study the polarisation from other x-ray luminous sources. More results should become available with a successful launch of the Micro Pattern Gas Detector on the Xeus satellite (Bellazzini et al. 2006).

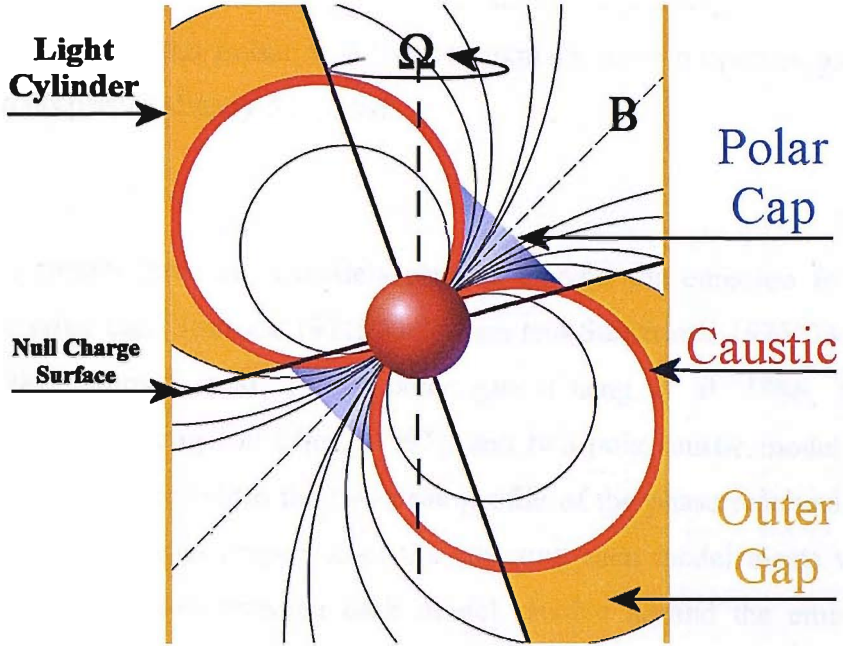

Figure 7.5: Schematic of a pulsar's dipole magnetic field showing the regions the three main pulsar models produce emission from. The Caustic model emits from the last field line to close with the light cylinder ($R_c = c\Omega^{-1}$), while the Outer Gap model emits from a region beyond the last closed field line and bounded by the light cylinder and the null charge surface. The Polar Cap model emits from a region several stellar radii from the surface around the magnetic pole.

7.3 Theories of the Polarised Emission

Being the brightest and youngest gamma-ray emitting pulsar, there is a wealth of observational results to explain when producing theories of the Crab pulsar's emission mechanisms. The Crab exhibits a spectrum consistent with non-thermal emission from radio to gamma-ray wavelengths, with photons emitted at energies, E, proportional to a power-law of the form $E^{-\alpha}$, where α is the photon index. At optical wavelengths, $\alpha \sim 0$, while as the energies increase to X-rays the power-law becomes steeper with $\alpha \sim 0.5$, finally reaching $\alpha \sim 2$ at gamma-ray energies. The pulsating signal is the most challenging property for a model to explain. A phase resolved analysis of the Crab pulsar shows a double peaked emission within a single period. The maximum of each peak stays at approximately the same phase at all energies (Kuiper et al. 2001), however, the relative sizes of the two peaks change with energy. At lower energies the first peak is much larger, as the energy increases the second peak increases while the first shrinks, until the second peak dominates at soft gamma-ray energies. As the

energy climbs above 10 MeV the first peak dominates again (Figure 7.6). Any theory of emission for the Crab pulsar will have to explain these properties as well as the polarisation properties already discussed.

There are currently three main models used to explain the emission from the Crab pulsar. The polar cap (Sturrock 1971; Ruderman and Sutherland 1975; Daugherty and Harding 1982; Sturner et al. 1995), outer gap (Cheng et al. 1986; Romani and Yadigaroglu 1995; Zhang and Cheng 1997), and two pole caustic models (Dyks and Rudak 2003) can all reproduce the two peak profile of the phase resolved light curve. When recreating the other properties of the emission each model meets with varying success. The differences between each model revolve around the emission region within the pulsars magnetosphere (Figure 7.5).

For the polar cap model, the characteristic double-peak light curve forms when the line of sight crosses the polar cap beam where the highest energy emission occurs through curvature radiation. The first pulse is produced as the leading edge of the beam passes the line of sight, followed by a bridge emission due to the inner parts of the beam. When the line of sight exits the beam the trailing peak forms. This model relies on the angle between magnetic axis and the spin axis being of a comparable size to the polar cap region (Daugherty and Harding 1996). Measurements of the observer angle (the angle between the ΩB plane and the line of sight of the observer) for the Crab have produced values of ~60° (Hester et al. 1995) requiring a very large polar cap region to produce the detected light curve. This does not rule out the model, but does make it difficult to explain. The polarisation properties from the polar cap model does not match the optical results, however, the swing in polarisation angle do resemble the polarisation seen at radio wavelengths (Figure 7.7).

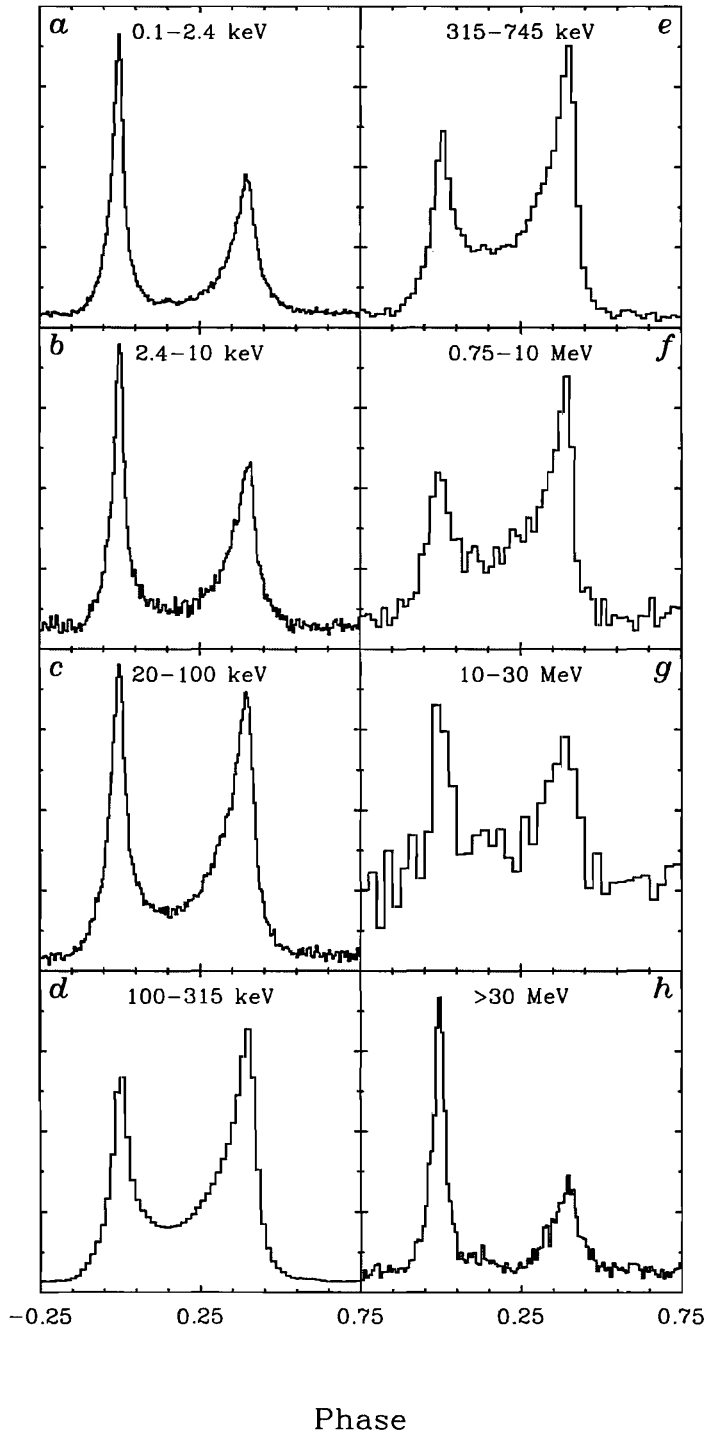

Figure 7.6: High energy pulse profiles of the Crab from 0.1 keV to 10 GeV showing the morphology change for the profiles as a function of energy (Kuiper et al. 2001).

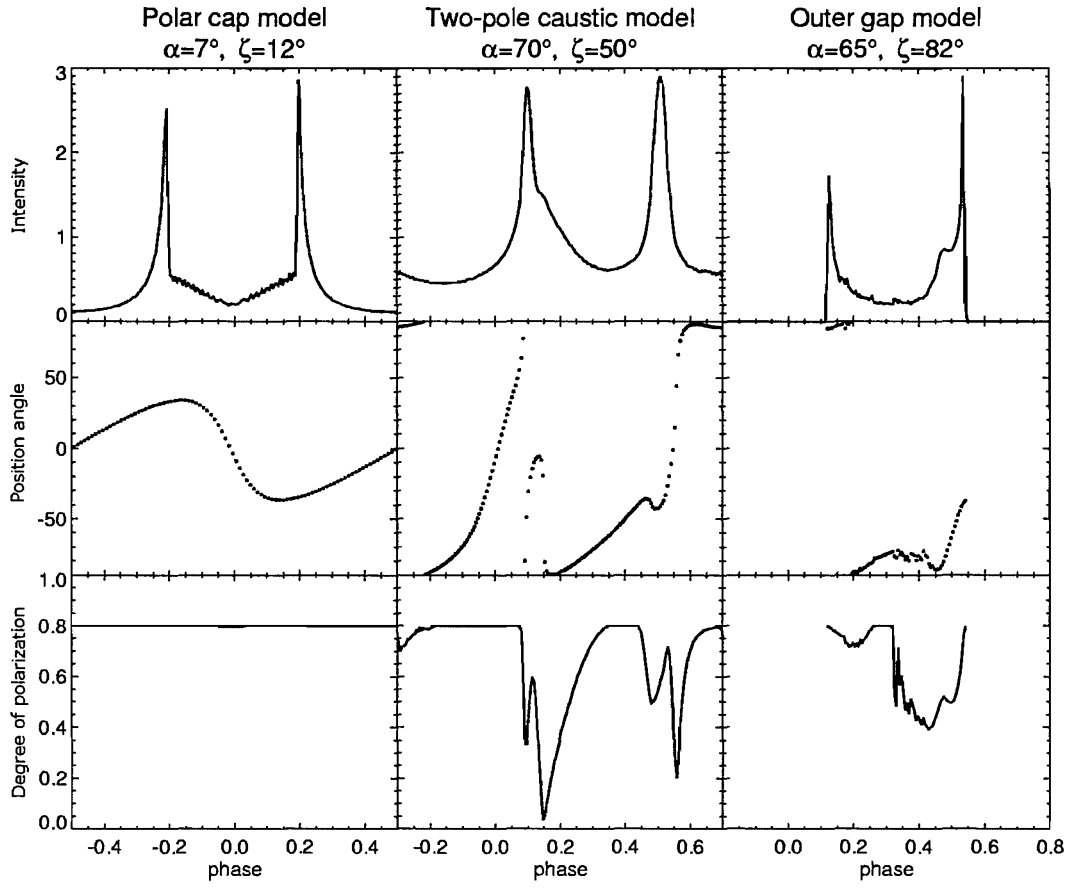

Figure 7.7: The optical light curve, polarisation angle and polarisation percentage for the polar cap, two pole caustic and outer gap models (Kanbach et al. 2005).

The two pole caustic model postulates that the emission comes from the last closed field lines of the pulsar's dipole field. This emission region stretches from pole to pole along the field lines extending out the light cylinder (Dyks and Rudak 2003). Special relativity effects such as the aberration of photon emission direction and time of flight delays, cause the photons emitted at different altitudes within some regions of the magnetosphere to pile up at the same phase and produce a pulse (Romani and Yadigaroglu 1995). Unlike the other models, each peak is identified with a different magnetic pole. However, this causes a problem with single peaked profiles and light curves where the two peaks are close together (Dyks and Rudak 2003). The model was very successful at simulating the emission from the Vela pulsar light curve measured by

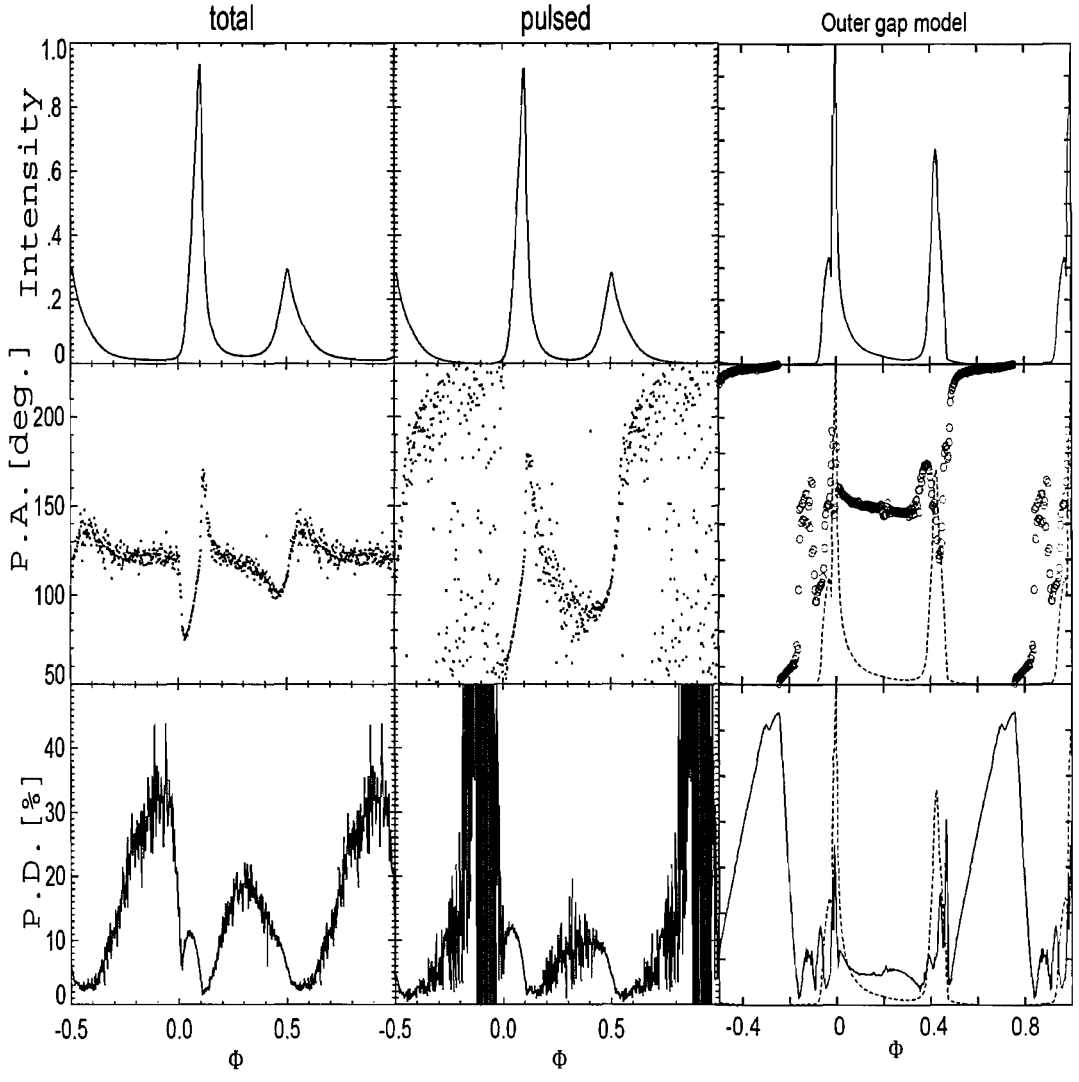

Figure 7.8: Total optical polarisation of the Crab pulsar (left), polarisation characteristics after the subtraction of the DC level (middle), and the predicted polarisation at 1eV (Takata et al. 2007).

EGRET (Kanbach 1999) and produced the closest match to the optical light curve of the Crab (Kanbach et al. 2005) until the modified outer gap model of Takata et al (2007).

The outer gap model concerns an emission region between the null surface (where the charge density is zero) out to the light cylinder. The gamma-rays are produced within this region by curvature radiation from electrons travelling along the field lines. This model prefers a larger angle between the rotation and magnetic axis unlike the polar cap

model, but cannot account for the off pulse emission. Chen et al (1996) considered synchrotron emission, instead of curvature radiation in the model, however, they could not reproduce the wings on the two peaks. Including emission from inside the null surface, Takata et al (2007) produced results consistent with the optical results after the subtraction of the DC component (Figure 7.8). By extending the emission region beyond the null charge surface the outer gap model becomes closer to the two pole caustic model and therefore has the strengths of both models.

Table 7.1: Comparison of Crab emission models.

	Polar Cap	Two-Pole Caustic	Slot Gap	Outer gap models		
				Basic	Chen et al (1996)	Takata et al (2007)
Caustic origin of peak	✗	✓	✓	✓	✓	✓
Each peak associated with a different magnetic pole	✗	✓	✗	✗	✗	✗
Photon emitted along the entire length of magnetic field lines	✓	✓	✗	✗	✗	✗
Match optical polarisation	✗	Close	✗	Approximate match to angle but not percentage	Close match to angle but not percentage	✓
Match radio polarisation	Close	✗	✗	✗	✗	✗
Separate DC component needed	✗	Needed to match optical polarisation but not light curve	✓	✓	✓	✓
Explains wings on pulses	✓	✓	✓	✗	Main pulse only	Main pulse only

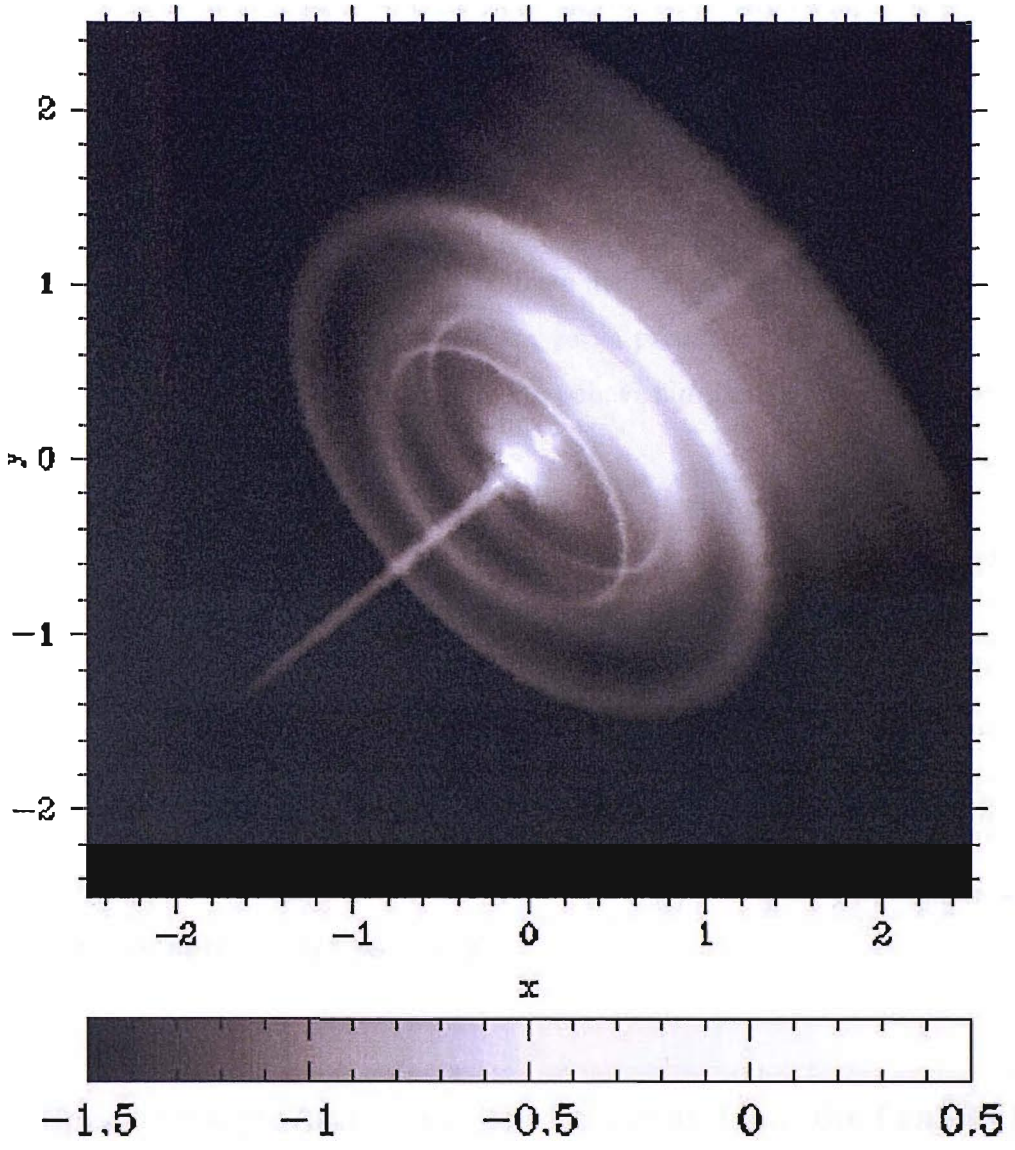

Figure 7.9: Simulated X-ray image of synchrotron emission. The brightness distribution is shown in the logarithmic scale (Komissarov and Lyubarsky 2004).

Looking at the properties of each model it is clear that the two-pole caustic and modified caustic models fit the optical data better. However, the polar cap model fits with the radio polarisation better than the other models. In order for many of the models to match the optical data better a DC component needs to be included. This component needs to be a continuous emission, showing none of the variability of the pulsed component.

Magnetohydrodynamical simulations carried out by Komissarov et al (2004) and Del Zanna et al (2006) have shown that the jet and torus structures seen in high resolution images of the Crab using CHANDRA (Mori et al. 2004), are probably due to synchrotron emission. There is a clear jet structure aligned with the spin axis of the pulsar (Figure 7.9) which could lead to a polarisation signature aligned with the jet in gamma-rays if there is substantial emission from the jet. In the simulations of the X-ray synchrotron emission, the polarisation of the jet is predicted to lie along the jet (Del Zanna et al. 2006) and it should be expected to behave similarly at higher energies.

Most models have not considered what would happen at MeV gamma-ray energies. Takata et al (2007) show very little change in their model predictions up to 10 keV. The percentage polarisation does increase slightly. This could be due to the life times of the higher energy electrons being shorter, resulting in a smaller emission region. Due to the low spatial resolution of gamma-ray imaging, determining this emission site visually is currently impossible. A measurement of the off pulse polarisation and pulsed polarisation may help locate the emission region by using information known about the geometry from other wavelengths.

7.4 Spectroscopic Analysis of the Emission from the Crab Pulsar

The INTEGRAL-IBIS image of the Crab derived from the third IBIS-ISGRI catalogue (Bird et al. 2007) shows a 4530σ point source, which is consistent with the location of the pulsar, within the 12' accuracy of the instrumental point spread function. The soft gamma-ray emission is well described by a power law spectrum of index $\Gamma = 2.23 \pm 0.02$ (Massaro et al. 2006) and an associated 20-100 keV flux of 1.15 10^{-8} erg cm^{-2} s^{-1}, which corresponds to a source luminosity of 5.23 10^{36} erg s^{-1} for a source distance of 2 kpc, equivalent to ~1% of the pulsar's spin down luminosity. Spectral analyses of the spatial structure of the Crab nebula in the X-ray band has been reported (Willingale et

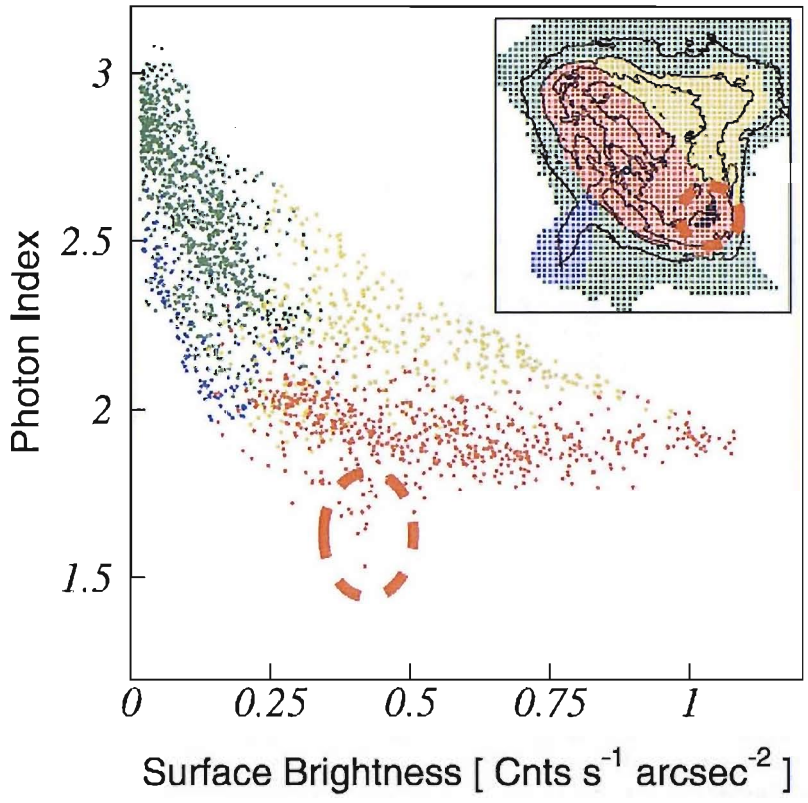

Figure 7.10: Plot of photon index against surface brightness. The data points of the torus, the jet, the umbrella-shaped northwest region, and faint peripheral region are colour-coded as red, blue, yellow, and green respectively (Mori et al. 2004).

al. 2001; Mori et al. 2004; Kirsch et al. 2006; Seward et al. 2006) in the literature. Generally the spatial variation of the X-ray spectrum over the entire region of the Crab shows a gradual spectral softening from the inner pulsar region to the outer nebula, with a variation in photon index, Γ, from ~1.9 to ~3.0. Four key zones have been identified (Mori et al. 2004) (Figure 7.10): the jet and an umbrella-shaped northwest region each with Γ ~2.2, the torus with $\Gamma \leq 2.0$, and the fainter peripheral region with $\Gamma \geq 2.5$. The similarity of the spectrum of the jet core and the torus suggests that the spectra of the electrons injected from the pulsar are similar in these two different directions. The spectral index of the soft gamma-ray flux as measured by INTEGRAL-IBIS provides an excellent match to that observed in X-rays from the central zone, including the jet, possible counter jet and torus, thus indicating that the majority of the soft gamma-rays are derived directly from the jet or possibly the torus structure.

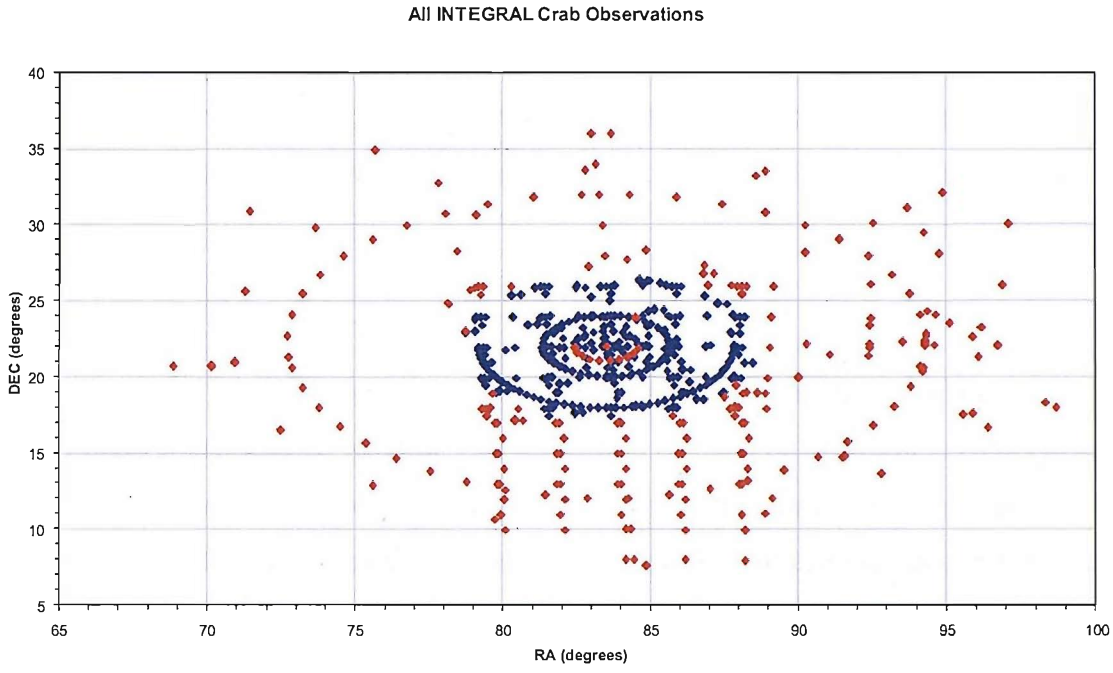

Figure 7.11: Plot of all observations surrounding the Crab position of 83.77 degrees RA and 21.96 degrees DEC. The observations used are shown in Blue, while the observations that were not simulated due to time constraints and due to occurring in the bad time interval list are shown in red.

7.5 Polarisation Analysis of the Emission from the Crab Pulsar

In a single SPI observation of the Crab pulsar, the flux received is barely enough to produce an image or a spectrum of the source. This means that for a more complicated analysis such as trying to detect polarisation, many observations need to be summed together. Unfortunately, over many observations the instrument changes greatly as the off axis angle changes, pixels break and thresholds and other parameters are varied. The modelled data is fit to the real detected data contemporaneously on science window by science window and a pseudo detector by pseudo detector basis. A pseudo detector is defined as a unique pair of adjacent pixels, resulting in a total of 42 pseudo detectors for the entire 19 detector complement. In the phase of operation with 2 non-operational pixels, the number of live pseudo-pixels is reduced to 32. The recorded data from the Crab can be modelled as

$$F_{is} = S \times C_{is}(\%, \Pi) + B_s \times B_i$$

where S is the Crab strength; C = count distribution from the crab simulation model, B_i is the average background spatial distribution and B_s is the background variation in time.

The Crab model $C_{is}(\%,\Pi)$ describes the number of counts from the simulation in each pseudo pixel *i*, per science window *s* as a function of Crab polarisation percentage and angle Π. These values are then weighted by the source strength S which is a function of the phase angle, the measured Crab spectrum, the livetime of each science window and the simulation timescale.

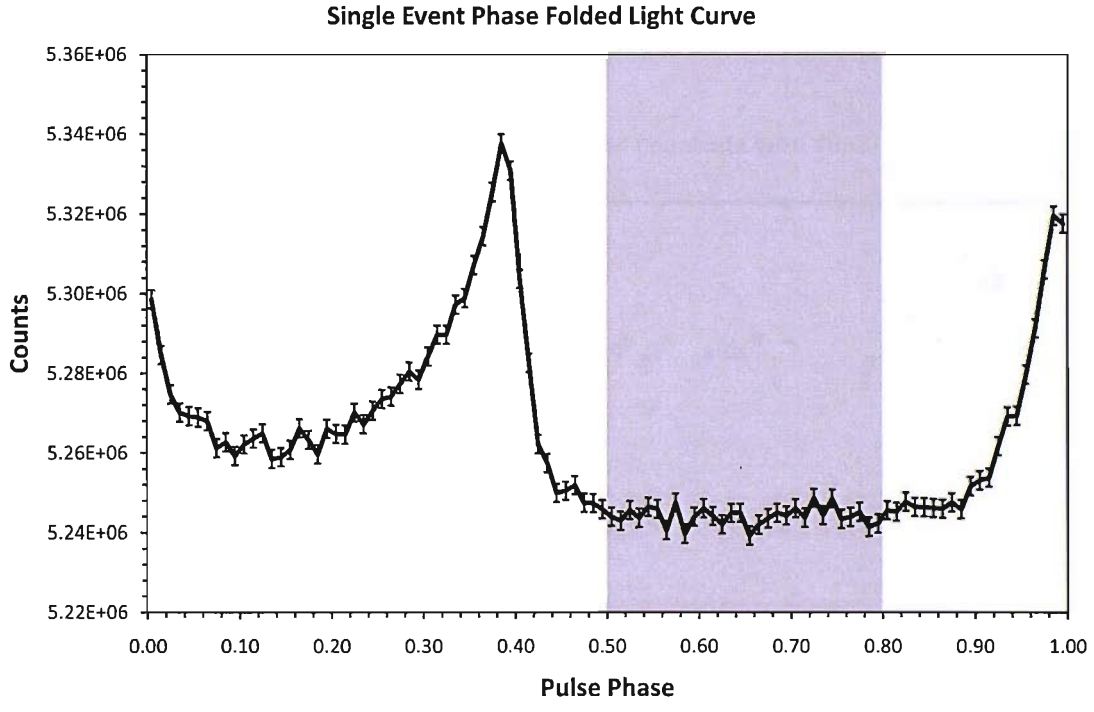

Figure 7.12: Phase-folding the light curve on the period of the pulsar PSR J0534+2200 enables the rejection of events from pulsar and the selection of non-pulsed emission from the nebula. The gamma-ray events used for the polarisation analysis for the off pulse were selected from within the phase interval 0.5 – 0.8 of the pulsar period and with energies between 100keV and 1 MeV. The 40% polarisation measured was derived from events in this interval. Phase-resolved polarimetry over this interval showed that the polarisation was constant within the errors of uncertainty, indicating that contamination from the pulsar was negligible.

The science window list is then filtered using the ISDC bad time interval list to ensure that no data is used that has been tagged with an error code. Each SCW is processed using the OSA5.1 tools (Diehl et al. 2003) to correct the energies and barycentre the timing information. The Crab ephemerides supplied by Jodrell Bank (Hobbs et al. 2003) are used to tag each photon with the phase in the crab pulse profile that the photon was emitted from. Phase folding the data on the pulse period of the Crab (~33ms) allows the evolution of the polarisation through the pulses to be studied (Figure 7.12).

The background consists of two terms $-B_i$ describing the spatial variation which is constant in time (Kalemci et al. 2004a) and B_s which changes the overall background countrate over the lifetime of the mission (see Figure 7.13).

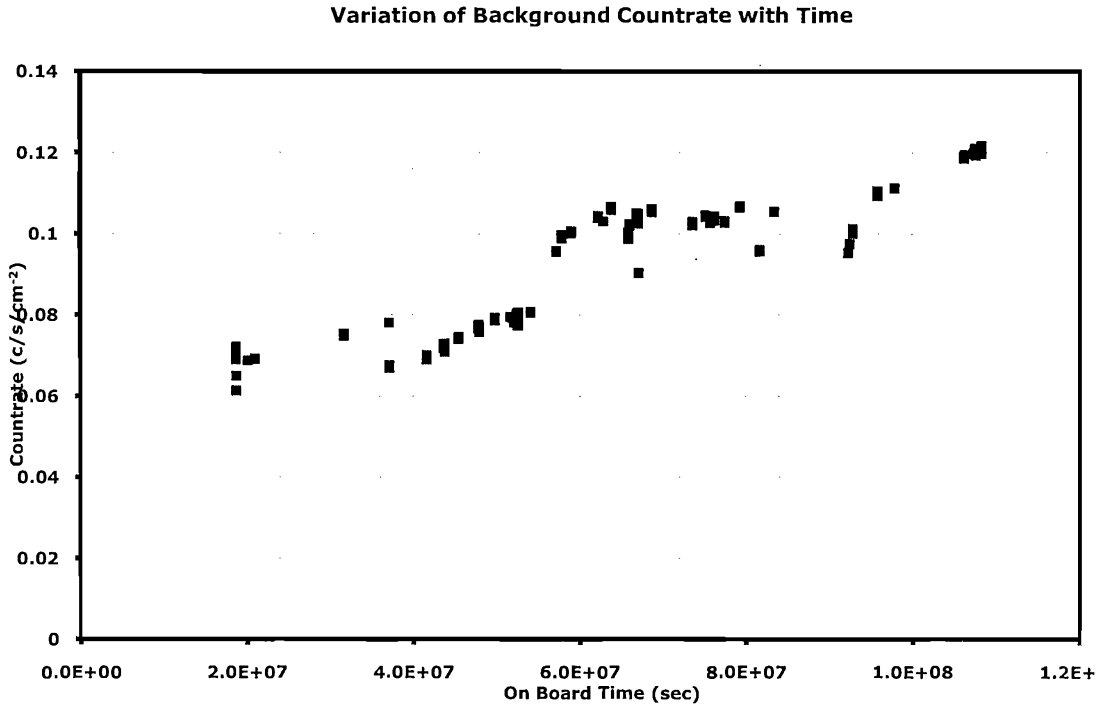

Figure 7.13: The variation in total background counting rate per science window over the duration of the mission. Variations are mainly due to the radiation environment (solar flares, etc.)

7.6 Detailed Description

7.6.1 SPI Background

The multiple event background count rate in the SPI has been studied by Kalemci et al (2004a). While there is a spatial non-uniformity across the detection plane, with the outer pairs of detectors having a higher background count rate than that of the inner detector pairs, this non-uniformity is constant in time. As the mass model is calibrated to the real instrument, this non-uniformity is automatically included in the simulation data and hence any effect on the polarisation analysis is removed on a statistical basis.

The multiple event background noise spectrum is reasonably flat (Figure 7.14). However, intense spectral lines can be seen which are created by the radioactivity induced within the materials in the instrument. These lines are produced by delayed

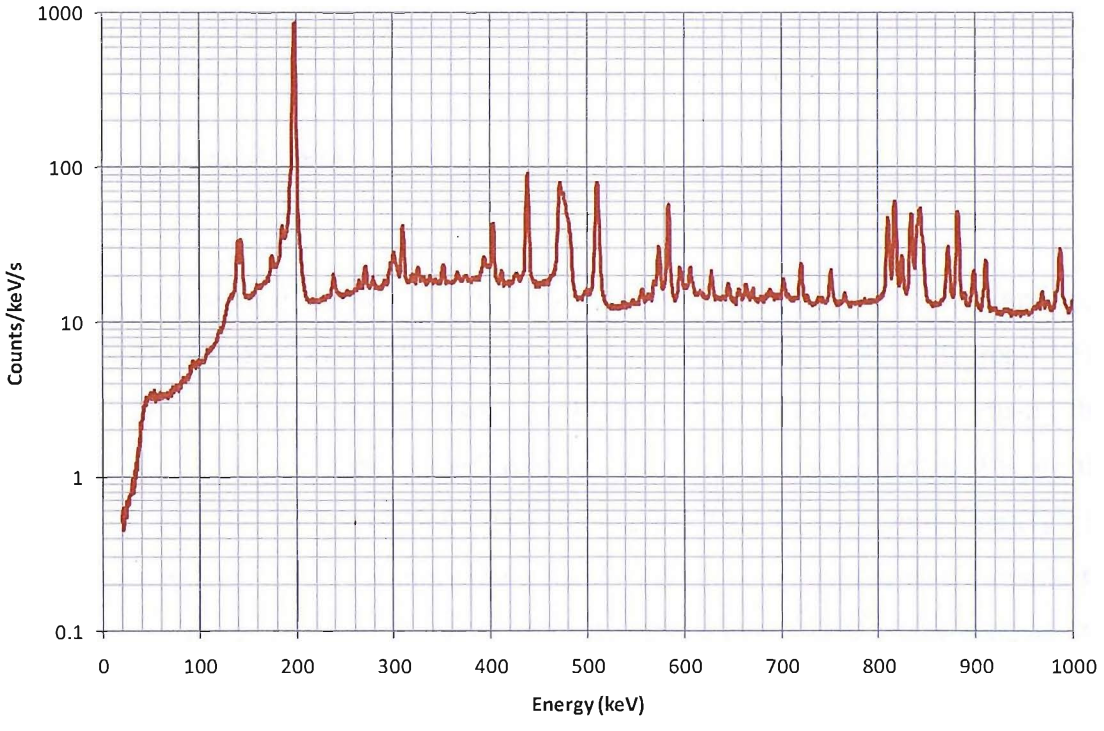

Figure 7.14: SPI multiple event background spectrum

decays due to spallation and neutron activation within the spacecraft's structure and detectors. The biggest and potentially the most damaging line is that of the ^{81}Ge and ^{76}Ge complex at around 198 keV. For this reason events are excluded from the analysis between 184 keV and 201 keV. This makes a significant difference and improves the fit between the real and simulated data.

Background events for this analysis are taken from INTEGRAL observations where no IBIS catalogue sources are present in the extended field of view (FWZR), resulting in a set of 413 science windows. Nineteen of these science windows were further rejected due to clear anomalies in the recorded data, giving 394 science windows and a total observation time of 0.92 Ms. From this data the B_i values are constructed as a 42-element vector containing the fractional countrate for each psuedo pixel averaged over the entire set of science windows. As the total background is increasing over the mission lifetime, we also include a background scaling factor B_s which is calculated at the time of fitting in order to conserve the total number of counts detected (see section 7.6.4).

7.6.2 Observational Data

For this analysis we use science windows ranging from revolution 43 to 422, and with the Crab in the field of view from on-axis to an off-axis angle of 10 degrees. The science window list is then filtered using the ISDC bad time interval list to ensure that no data is used that has been tagged with an error code, and a further 1% of the observations are rejected for obvious data anomalies. This leaves approximately 600 SPI science windows (SCW) comprising around ~1.5Ms of on-source data suitable for polarisation analysis. The total number of Crab events in the data set is around 10^7. Approximately 10% of these events are double and therefore suitable for the polarisation analysis, while the total number (Crab + Background) of double events is

1.75×10^7. The SPI observation events are processed using the OSA 5.1 (Diehl et al. 2003) barycentre command and the count rates are dead time corrected.

7.6.3 Simulated Data

For each individual pointing, photons taken from the same spectrum as that of the Crab were fired into the modelled geometry from the direction of the source. The emission region in the simulation was 140x140 cm centred on the SPI detector and large enough to completely illuminate the instrument and surrounding spacecraft. Although this area of emission is inefficient for the detection of photons as many will scatter in the surrounding spacecraft and not interact within the detector volume, it does ensure that scattered events from the instrument's structure and the precise shadowing of the coded aperture mask on the detector plane are included in the detected events. Nineteen sets of 50 million test photons were processed for each of the ~600 pointings: 18 were polarized beams for each 10° azimuthal step between 0° and 170°; and one of an unpolarized flux. Only the polarisation angles between 0° and 170° need be modelled due to the 180° symmetry of the Compton scattering process. Of the incident photons ~700,000 produce single events in the detector, while ~70,000 multiple events are seen. This is consistent with the ratios seen in the real data. These simulations produce the counts that the instrument will produce if the source is polarized at each of the angles not including any background components. With the simulation predicting how the detector responds to each polarisation angle this data can then be compared to the real data to find the closest match. The unpolarized and polarized simulation data can be combined to produce any percentage polarisation (Π) needed using

$$P_{\%} = \frac{\Pi P_{100}}{100} + \frac{(100 - \Pi) P_0}{100}$$

where P_{100}, P_0 and $P_{\%}$ are the 100% polarized simulation data, unpolarized simulation data and percentage polarisation data. Since the change due to polarisation angle is a

smoothly changing function it is possible to interpolate between the simulated files, therefore making it possible to produce data sets simulating any polarisation angle and percentage of polarisation.

7.6.4 Fitting the two data sets

The comparison between the measured data and the simulated observations was carried out using the following procedure:

- The entire measured data set is read into memory
- Looping over the entire range of 180 degrees and 100% polarisation percentage, the number of counts expected from the Crab in each of the 42 pseudo-pixels is calculated by scaling the simulated counts for observation livetime.
- The number of counts in the science window is compared with the total simulated counts and the difference is attributed to background.
- Background counts are added to the simulated counts according to the spatial countrate distribution calculated in 4.1.1
- The chi-square statistic formed by comparing the observational data and this data set is calculated resulting is a 180 x 101 matrix of chi-square values, corresponding to the 180 degrees range in polarisation angle and the 0-100% polarisation modulation.
- The minimum chi-square is used as the indicator of the best-fit.

7.7 Results

Using traditional propagation of errors, it is possible to calculate the theoretical statistical error on both the measurement of the polarisation angle and the percentage

modulation. Inevitably, due to the complexity of the instrument and the relatively low signal to noise ratio, many non-statistical perturbations will affect the analysis procedure. While the majority of these are compensated for by the simulation technique, some will remain and reduce the quality of the measurement.

From a statistical point of view the instrument is very sensitive to polarisation in a strong source such as the Crab. We can, for instance, calculate the minimum detectable polarisation at the 99% confidence level using the formula (Weisskopf et al. 2006):

$$MDP_{99} = \frac{4.29}{QR_S}\left[\frac{R_S + R_B}{T}\right]^{1/2}$$

where Q is the degree of modulation expected for a 100% polarized beam in the absence of background as defined in section 3.1; R_S and R_B are the source and background countrates respectively and T is the observation time. In our case we should be able to detect polarisation of the order of 0.03% which is clearly totally unrealistic and therefore a reasonable estimate of the dominant non-statistical errors is required.

7.7.1 The polarization angle

Due to the undoubted presence of residual systematics, we attempt to obtain a more accurate measurement, and at the same time provide an estimate of the errors by subdividing the data into many smaller subsets. It may be expected that there will be several residual systematic errors each contributing and varying independently. We have therefore adopted an approach which may separate out those which are changing in time, from those which depend on other parameters more constant throughout the mission. The former should be susceptible to estimation by means of subdividing the data into a series of subsets which still retain sufficient data quality to yield a meaningful result. We were able to select 5 groups of observational data and we

performed the chi-squared fitting procedure independently on each subset. The results are show in table 1 below.

	Angle (°)	**Modulation (%)**
Set 1	124	39
Set 2	104	35
Set 3	112	83
Set 4	126	100
Set 5	154	71
Average	124	65

Table 7.2: The polarisation angle and fraction as a function of 5 sequential time bins.

The spread of the data can be used to provide some indication of the errors, in that for 5 numbers drawn from a normal distribution, the average spread is equivalent to 2.1 times the standard deviation. Each of these values can then be associated with an error equivalent to the spread divided by 2.1 while the average value will have an associated error which is smaller by a factor of $\sqrt{5}$. Applying this technique we arrive at the following estimate for the best fit solution for the polarisation angle of $124° \pm 11°$. For the case of the modulation percentage, the situation is not so simple. As can be seen from the table, the fractional modulation is always higher as the strength of the signal decreases (i.e. including shorter data segments). The reason for this is that the modulation fraction depends on the spread of the detected source count rates. As the noise to signal ratio increases, the effect on the count rates is to increase the spread, thereby resulting in a higher apparent depth of modulation.

For those effects which are more constant in time, we must find another parameter which can be used to split the data longitudinally in time. To achieve this we have selected phase as the fixed parameter. We can also use this to investigate any systematic variation with phase. The data were first divided into 5 phase bins, covering the off-

pulse period and the chi-square fitting procedure was rerun. The results are shown in table 2

Phase	Angle (°)	Modulation (%)
0.4-0.5	134	100
0.5-0.6	98	53
0.6-0.7	126	26
0.7-0.8	124	44
0.8-0.9	124	30
Average	122	51

Table 7.3: The polarisation angle and fraction as a function of 5 sequential phase bins.

In an analogous way to the elapsed time evaluation above, the best fit polarisation angle becomes 122±7°. A weighted mean of these two methods leads to a final evaluation of the polarisation angle of 123±11°.

It is interesting to note the difference in the estimated error on the polarisation angle from these two methods. Assuming that there is no intrinsic change of polarisation angle with phase then the relatively smaller error calculated here indicates that the major contributions to the residual systematics vary in time.

7.7.2 The modulation fraction

As has been noted in the previous section, while the average polarisation angle is highly consistent however the data is subdivided, the percentage modulation is more susceptible to this data selection, and one measurement must have a large associated error. In order to obtain a best estimate of both the absolute value and the associated

error on the modulation, we subdivided the entire phase range into smaller phase bins and then calculated the mean and error for the modulation in each selection. The result is shown in Figure 7.15. Whilst there is some evidence for a larger value at the smallest bin size, we take as the best estimate the weighted mean of all measurements with an error equal to the weighted standard deviation, giving 46±10%.

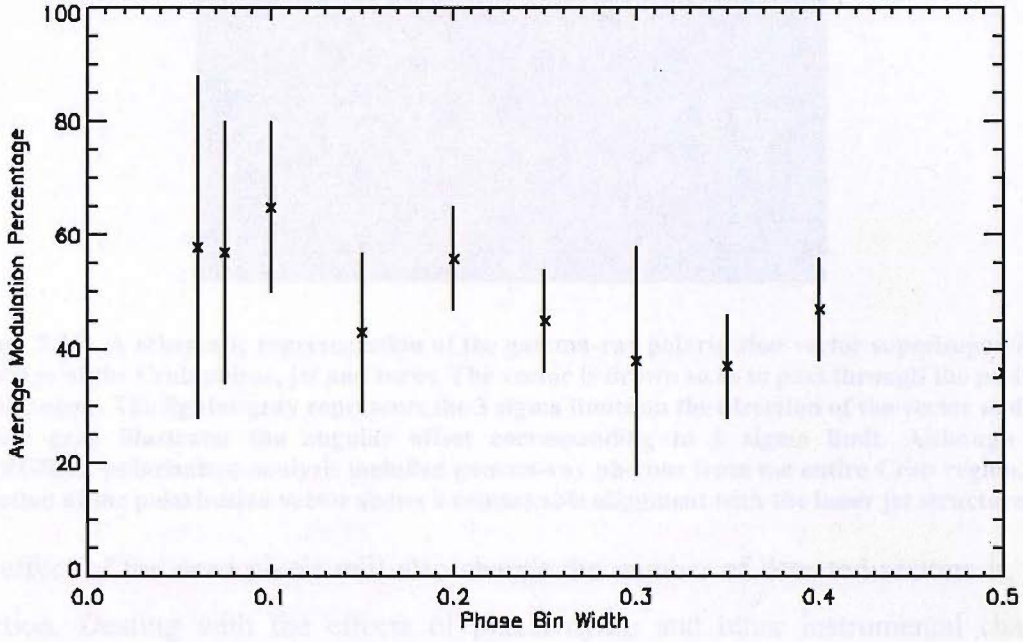

Figure 7.15: The average modulation percentage as a function of phase bin width

7.7.3 Other possible systematics and their suppression

An important consideration in polarisation experiments using coincidence rates is the rate of chance coincidences. In SPI a multiple event is an event where two energy deposits within different pixels occur within the electronics coincidence window of 350 ns (Vedrenne et al. 2003). For the Crab observations the total source count rate, including single events, is around 6 c/s for each pixel. This will produce a random coincidence rate of less than 3×10^{-5} c/s for each detector pair which is negligible for our measurements.

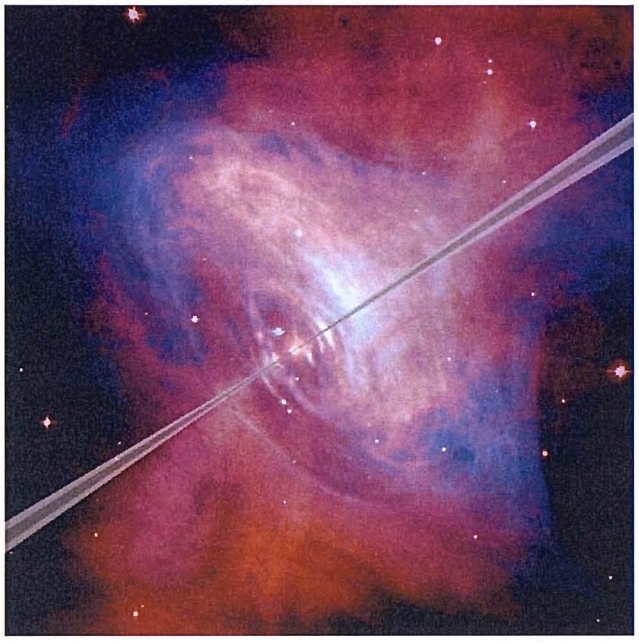

Figure 7.16: A schematic representation of the gamma-ray polarisation vector superimposed on an image of the Crab pulsar, jet and torus. The vector is drawn so as to pass through the position of the pulsar. The lighter gray represents the 3 sigma limits on the direction of the vector and the darker gray illustrates the angular offset corresponding to 1 sigma limit. Although the INTEGRAL polarisation analysis included gamma-ray photons from the entire Crab region, the direction of the polarisation vector shows a remarkable alignment with the inner jet structure.

The effect of the dead pixels will also change the number of detected scatters in each direction. Dealing with the effects of pixels dying and other instrumental changes demonstrates the strength of using modelling in the analysis as attempting to calculate or calibrate for these would be an unrealistic task with many opportunities for error.

In order to test for the occurrence of any residual systematic polarisation signal in the analysis a randomisation test has been performed. This analysis was designed to reveal any end to end instrumental or software systematics that could masquerade as a polarized beam. For this test we took all the scattered events in the data set and randomly assigned a new SPI detection element as the site of the second interaction. The subsequent analysis of the data set was carried out in exactly the same way as for the unadulterated data set. We found no evidence of significant polarization at a probability of greater than 99.99%

The orientation of the electric vector, and associated 1σ and 3σ errors, is overlaid on a Chandra image in Figure 7.16. A major advantage of the mass model simulation technique is that the process automatically removes a great many of the systematic errors. The errors in the simulation are related to the quality of the modelling and may be estimated from a comparison of the simulated results and the real data. The overall systematic error is estimated to be small and amounts to no more than a few degrees rotational error on the measured angle attributed to the polarization angle.

The 46% linear polarization in the gamma-ray domain as measured by SPI is high. The spectra of the unpulsed gamma-ray fluxes are well represented by a power law of index $\Gamma \sim 2.2$, and if the gamma-ray photons are created through the synchrotron process, the parent electrons will have a power law distribution of index $p = 2\Gamma - 1 \sim 3.4$. For such a power law distribution of electrons the maximum degree of linear polarization that is possible is defined by the expression (Lei et al. 1997):

$$\Pi = \frac{p+1}{p+\frac{7}{3}} \qquad 7.1$$

For the Crab this becomes $\Pi \sim 77\%$.

Clearly any inhomogeneities in the structure of the magnetic field will result in the degree of linear polarisation being reduced. The 40% linear polarisation measured by SPI thus implies a very high degree of uniformity in the magnetic field configuration associated with the unpulsed gamma-ray emission from the Crab, and immediately eliminates emission from the rather tangled magnetic field associated with the plerion. A measurement with SPI integrates the emission from the entire production zone and so would produce a result of the average polarisation over the entire field of view. Likewise an origin from the torus may also be discounted.

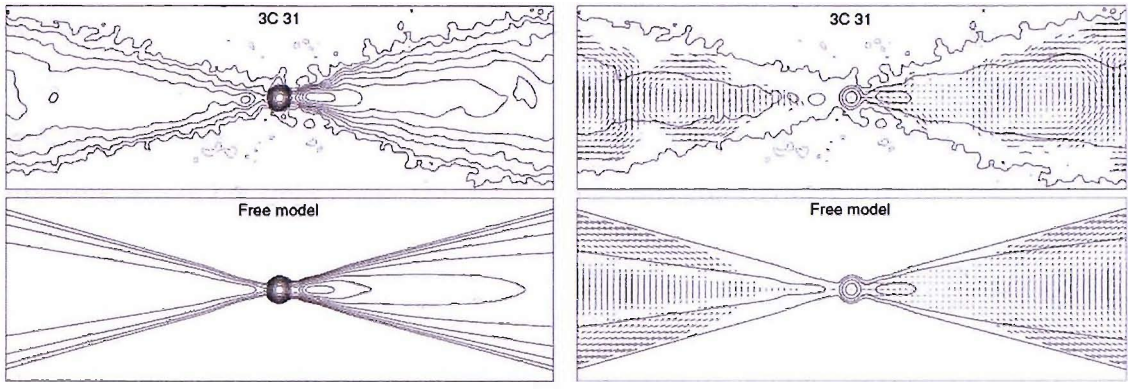

Figure 7.17: Contours of total intensity and magnetic-field vectors at a resolution of 0.75 arcsec. The plots cover 27 arcsec on either side of the nucleus. The left-hand panels show the total intensity contours at levels of -1, 1, 2, 4, 8, 16, 32 × 20 μJy beam^{-1} area. The right-hand panels show the vectors whose magnitude and directions are proportional to the magnetic-field (Laing and Bridle 2002).

The direction of the electric vector associated with the polarised gamma-rays shows a remarkable alignment with the Crab jet and strongly indicates that this feature is the site of the gamma-ray production. The alignment of the polarisation vector to the rotational axis of the pulsar implies an emission sight close to the pulsar. This is supported by the similarity between the optical and gamma-ray polarisation vectors, which suggests the polarised emission originates in the same location. The alignment of the polarisation vector along the jet axis implies an orthogonal magnetic field configuration if the synchrotron process operates. Analysis of radio and optical polarisation studies of jets in radio galaxies (Laing and Bridle 2002; Perlman et al. 2006) indicate that the apparent magnetic field vector is parallel to the jet axis for the inner reaches of the jet, becoming perpendicular to the jet axis closer to the termination point (Figure 7.17). Taking the value for the magnetic field within the Crab jet close to the termination point derived from Chandra observations (Seward et al. 2006) to be 9.1×10^{-4} G, the synchrotron process would require electrons with energies ~ 2×10^{14} eV to create the polarised gamma-ray photons at 400 keV and ~ 5×10^{13} eV for the 25 keV X-rays detected by Weisskopf et al (1978).

The Chandra image of the Crab indicates that the jet is curved so that under these conditions energetic electrons streaming along the jet could radiate by curvature

radiation, for which the electric vector is parallel to the jet, as observed by INTEGRAL. In the relativistic limit the equations relating to curvature radiation can be generated by replacing the gyration radius associated with the synchrotron process with the radius of curvature, R_c, of the field lines. This leads to an emission frequency of

$$\nu_c = \frac{3c}{4\pi R_c}\gamma^3 \qquad 7.2$$

where γ is the Lorentz factor of the radiating electrons.

Taking an estimate of the radius of curvature associated with the Crab jet to be $R_c \sim 2.5\ 10^{18}$ cm, in order to generate the few hundred keV photons detected by INTEGRAL-SPI, we require electrons with energies of typically 10^{15} eV for the production of polarised gamma-rays by this mechanism, which is entirely plausible in the context of the Crab pulsar.

The soft gamma-ray spectral and polarimetric emission characteristics are consistent with the production of these energetic photons within the jet structure observed close to the Crab pulsar. Approximately 1.5% of the pulsar's spin down power is converted into soft gamma-ray photons in the 20 to 100 keV energy range. The unpulsed gamma-ray emission from the Crab is persistent and extremely stable, implying a steady injection of energetic electrons into pulsar induced jets. This scenario is very different to the erratic emission observed from the accretion-powered jets associated with microquasars and extragalactic systems.

7.7.4 Pulsed Emission

The pulsed emission analysis is obviously very important to understanding how the pulsar works. With the optical results subtraction of the DC component produced

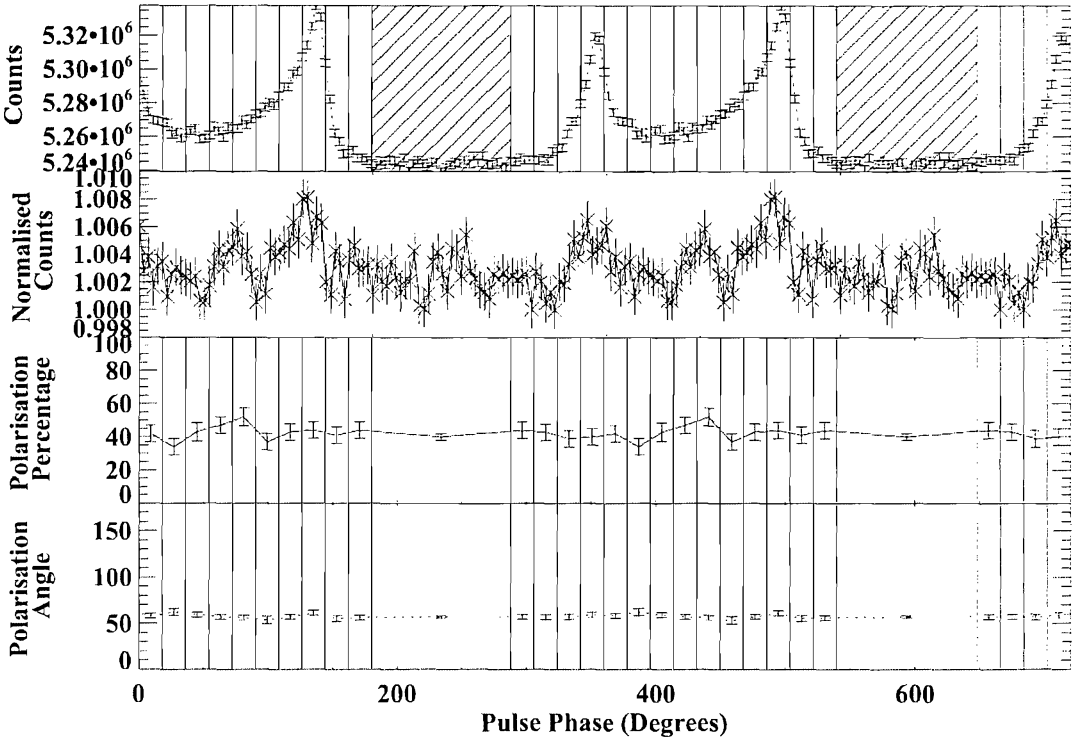

Figure 7.18: Gamma-ray polarisation results from the pulsed phase of the Crab light curve without the off-pulse subtracted. The single event light curve, multiple event light curve, polarisation percentage and polarisation angle are shown as a function of pulse phase. 1.6 ms binning is used through the pulse.

polarisation profiles very similar to the outer gap and two-pole caustic models. It is likely that this approach will be needed in the gamma-ray regime as well. The off-pulse emission has already been shown to have a constant polarisation profile. If we assume that this off-pulse component is from a separate source of gamma-rays then we can subtract it from the rest of the phase folded light curve. After subtraction, only 4.65% of the single deposit events remain, which causes a problem for the polarisation analysis.

Analysis of the pulsed section of the light curve shows very little variation of the polarisation (Figure 7.18). Since only a small percentage of the events are contained within the pulse itself, this is understandable as the signal will be swamped by any DC component.

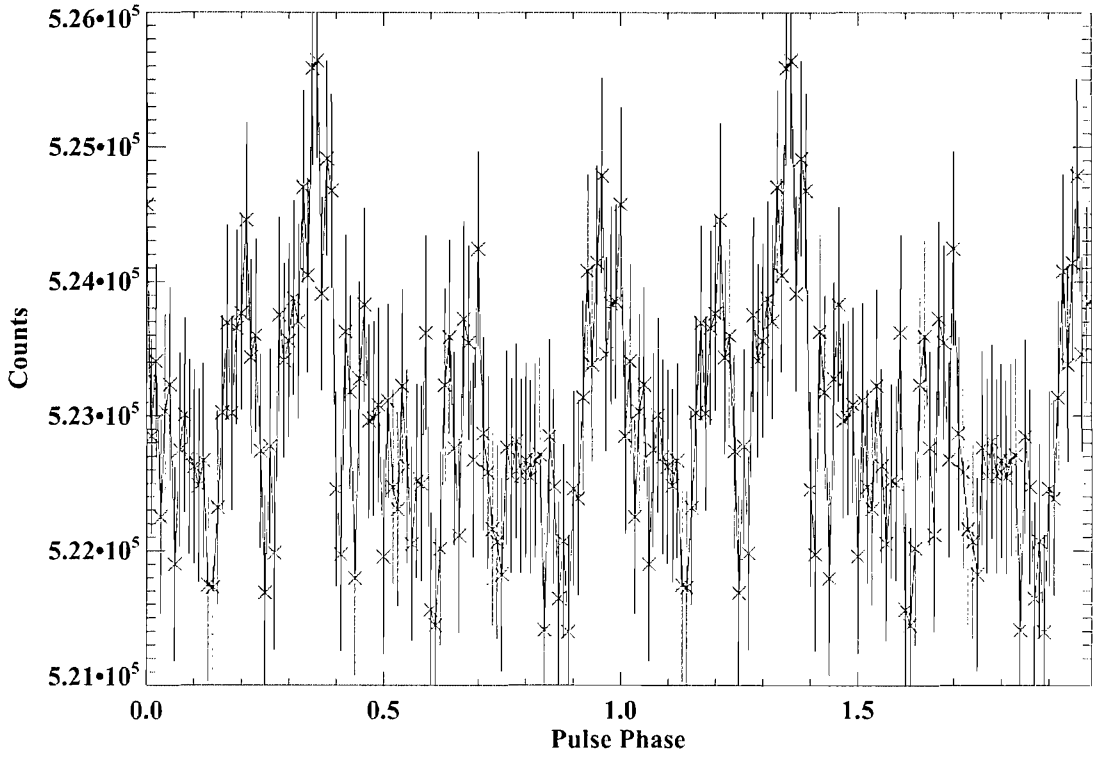

Figure 7.19: Multiple event phase folded light curve of 500 SCWs of Crab pulsar observations. The two peak profile is very difficult to see.

With the Crab data recorded by SPI, approximately 10% of the total events are double events suitable for the polarisation analysis. This means that within a given data set, after subtraction of the DC component, only ~0.4% of the counts are used in the analysis. During the analysis the events are separated into three directions of scatter, reducing the number of events and therefore increasing the relative size of the statistical errors. The phase folded total multiple event light curve for the 500 simulated SCWs can be seen in Figure 7.19. The pulse profile is only just visible and after the separation into three directions it becomes almost impossible to subtract the off-pulse data. In order to improve this situation more data is needed. There are a total of 1080 SCWs available of Crab observations including data out to ~15° off-axis. However, as the off-axis angle increases the anisotropies in the detector illumination will begin to become more problematic. Each SCW also requires ~160 hours of computer processing time to

simulate and even using the University of Southampton's Beowulf Cluster, the extra 580 SCWs will take ~6 months to process.

7.8 Summary

Polarisation measurements of unpulsed emission have been taken from approximately the same phase interval that have been reported from the Crab in both X-ray (Weisskopf et al. 1978) and optical (Kanbach et al. 2005) wavelengths. In the former, linear polarization at 2.6 keV and 5.2 keV was found at a level of 19.2% and 19.5% respectively, with corresponding angles of 156°.4 and 152°.6 degrees, while in the latter case, the polarisation found was 33% with an angle of around 123 degrees, in close agreement with our values. The optical results come from an area of several arcseconds around the pulsar, but the X-ray measurements integrate over a 3° (FWHM) field of view containing the Crab. Since it is known that X-rays are emitted from many of the morphological features associated with the Crab plerion, we might expect to find a lower degree of linear polarization in this case. While the optical polarisation angle is well aligned with that of the gamma-ray, the X-ray vector is rotated further, thus implying that there is no continuous rotation with photon energy.

Due to the pulsed emission accounting for only a small fraction of the total Crab emission, it has proved impossible with the current data set to obtain meaningful polarisation results from the on pulse sections of the phase folded Crab light curve. Without subtracting a DC component, any variation is swamped by the signal relating to the off pulse, while, attempting to subtract the DC component suffers from the small number statistics, meaning much more data is needed.

In conclusion, it has been shown that the ability to measure gamma-ray polarisation provides a powerful diagnostic tool for deepening our understanding of complex astronomical objects. The findings have clear implications on many aspects of high energy accelerators, such as, for example, the production of the VHE emission observed by ground based Cerenkov detectors. These TeV-emitting sources are associated with young energetic, soft gamma-ray emitting pulsars. If it is assumed that the VHE photons are produced by Inverse Compton scattering of high energy electrons from the pulsar on the cosmic microwave background and local starlight, there is a need for a constant supply of these electrons to be channelled from the pulsar to the extended site of the VHE emission. These results demonstrate that a substantial fraction of the unpulsed gamma-ray emission from the Crab, known to be persistent and extremely stable, is consistent with a jet origin, thereby providing the steady injection of energetic electrons into the local interstellar medium required to power the TeV emission.

Chapter 8

Designing a Next Generation Polarimeter for a Laue Lens Mission

8.1 Introduction

In the analysis of GRB polarisation in Chapter 6, it is clear that a major obstacle to these measurements is the sensitivity of the detectors used. In all but the brightest bursts and persistent gamma-ray sources there will not be enough photons for a precise measurement of the gamma-ray polarisation. To increase the sensitivity of a gamma-ray astronomical telescope, the area over which photons are collected must be increased. In traditional gamma-ray detectors the collecting area relates to the dimensions of the detector. These detectors normally use coded masks (which halves the flux detected) or the kinematics of Compton scattering to gain directional information from the incoming gamma-rays. This means that a large collecting area requires a large detector which therefore increases the background count rate. In 'conventional' optics dealing with lower energy electromagnetic radiation, the focusing of photons using lenses or mirrors

onto a smaller area is straight forward and has been known about for centuries. At gamma-ray energies the photons are highly penetrating and will pass through a standard glass lens or interact in the material forming a mirror without affecting the trajectory of the gamma-ray. X-rays are also very penetrating and so are difficult to focus using a lens. However, it is possible to use grazing incidence optics to focus X-ray photons, the technique employed in the mirrors used by XMM (Peacock et al. 1990). A similar technique to grazing incident optics can be used for gamma-rays. Instead of the photons reflecting off the surface of a metal, the photons can be scattered by a small angle by Bragg-diffraction from crystal planes to form a Laue Lens. In a Laue Lens Mission the telescope effective area and the detector volume are decoupled by using a gamma-ray lens to focus the incoming photons onto the detector plane (Halloin et al. 2004; von Ballmoos et al. 2004).

The Bragg-diffraction that derives from the periodic atomic structure inside a crystal can be used to modify the path of the gamma-rays by ~1 degree. This diffraction can be used to create a diffraction lens by orientating a large number of crystals so that the photons are deflected to a common focal point (Lund 1992; Smither et al. 1995; Halloin et al. 2004; von Ballmoos et al. 2004). However, the angle at which the gamma-rays deflect is a function of their energy (Figure 8.1). This is analogous to the chromatic aberrations seen at optical wavelengths, where the focus of a lens is energy dependant. Therefore, the more accurately the energy can be ascertained the better the imaging quality.

The goal of making a detector that can reconstruct the original photon energy as precisely as possible and for the majority (~100%) of the incident photons is the main driver behind this research. In the gamma-ray spectral range of interest (10 keV to 2 MeV) a major loss of energy, stopping the full energy of a photon being detected, is due to the Compton scattered products that back scatter out from the surface of the detector. In traditional detectors these losses produce the Compton continuum in the spectra that

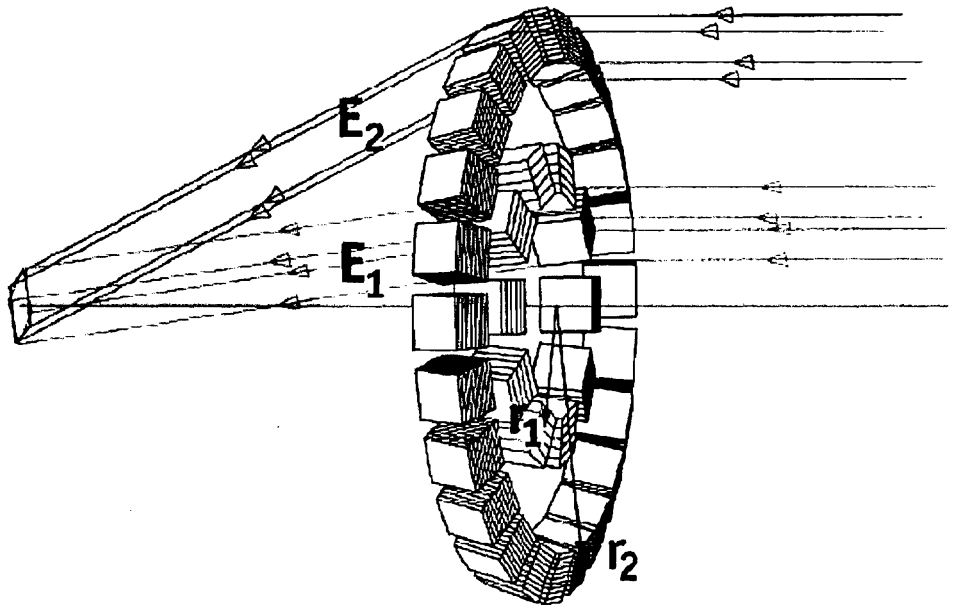

Figure 8.1: The basic design of a Laue Lens. Photons E_1 have a higher energy than E_2 and therefore a smaller angle of deflection (von Ballmoos et al. 2004).

these detectors always produce. The ability to capture these products will remove this continuum and increase the counts at the photopeak energy and at the same time reduce unwanted background noise and hence imaging artefacts.

In order to be able to collect all the scattered products, there needs to be a detecting mass in all the directions in which the scattering photons may travel. This is obviously impractical since these detectors would block the incoming photons from reaching the main detector. The aim is to create a box analogous to a traditional Black Body cavity where radiation can enter but not escape (however this is not entirely possible) while maintaining a useful aperture. An approximation to this setup can be made by creating a cavity in the detector so that all but the angles at which the radiation enters are covered by a detection element.

The work in this chapter describes the initial design and modelling of a focal plane instrument for GRI – The Gamma-Ray Imager, a mission proposed by the GRI Consortium for ESAs Cosmic Vision plan. Section 8.3, covers the design of this detector in more detail and the simulations involved. Section 8.4 will cover the results obtained from the simulations and the optimisations that can improve the performance of the detector. In section 8.5, the final proposed instrument design will be discussed. To start, section 8.2 will cover the Laue Lens to understand the requirements the detector must fulfil.

8.2 Laue Lens Missions

Laue Lens missions increase the sensitivity by decoupling the collecting area and size of the detector, allowing an increase in the signal without a significant increase in the background noise. By using a lens to focus the gamma-rays onto a detector the collecting area becomes a function of the lens properties and no longer relies on the size of the detector. Traditionally the lensing of gamma-rays was thought to be virtually impossible. Recently, the Laue Lens design has made great advances in the field of gamma-ray astronomy possible (Frontera and Pareschi 1995; von Ballmoos et al. 2004). The idea revolves around exploiting Bragg diffraction of gamma-rays from the periodic planes in a crystal. It has long been known that the planes in a crystal can be used to diffract gamma-rays (Lund 1992; Smither et al. 1995; Halloin et al. 2004; von Ballmoos et al. 2004). Normally, in crystallography, the crystals are rotated and the change in the deflection of the gamma-rays is measured and used to calculate the spacing of the crystal planes. Equation 9.1 describes the variation of angle with plane spacing in a perfect crystal and is called the Bragg-relation.

$$2d\,sin\theta_b = n\lambda \qquad 8.1$$

where d is the crystal plane spacing, θ_B the angle of the photon to the crystal planes, n the reflection order, and λ the wavelength of the gamma-ray (von Ballmoos et al. 2004). These crystals can be arranged in a circle in such a way that the gamma-rays are all deflected to a common focus (Figure 8.1). A range of energies can be focused by creating rings with different orientations of crystals. A lens of this type should achieve 1000 cm^2 collection area between 200 and 1000 keV and have more than 200 cm^2 all the way up to >2 MeV.

In order to recreate the images from the lens, the exact energy needs to be known. The energy dependence of the diffraction will cause the focus to be different for different energies. If the incoming photon's energy has not been correctly measured this will result in artefacts in images.

8.3 Detector Design

As previously discussed, an effective Laue Lens system requires a position sensitive detector for imaging, with excellent (~100%) photopeak efficiency and the best possible energy resolution. A material such as germanium has a good energy resolution of a few percent, so the biggest area to improve is the photopeak efficiency of the detector. The best way in which to do this is to capture and measure the energy of all the Compton scatter products produced as the incoming gamma-rays scatter inside the detector. There are two main directions in which the Compton scatter products leave the detector and therefore create a loss of energy in the recorded energy of the photon. The first is the rear of the detector, where at high energies the photon preferentially scatters forward through the detector. This can simply be solved by increasing the thickness of the detector to produce a detector plane analogous to a Compton cube detector (Lebrun et al. 2003a). However, increasing the detector's thickness, increases the detector's mass at the cost of increased background. The second area in which energy is lost is in the

direction of the incoming photons, where at lower energies the photons tend to backscatter back out of the detector plane.

Collecting all the events that backscatter out of the detector is much more difficult to achieve. Any mass placed in the direction of the incoming photons to capture the backscattered products will also attenuate the incoming photons. However, not all of the backscattered photons go straight back along their original path. Most will leave the surface at an angle and so can be collected by walls placed around the edge (Figure 8.2). Using computer modelling we can simulate this design, optimize the setup and see how effectively the design performs.

With the advent of modern fast computing clusters, designing and optimizing new detector systems has become a much easier task. A simulated detector geometry can be built inside the computer and tested against the various radiation it will have to deal with. This allows the detector to be optimized without the need to produce many prototype detectors. For these simulations the GEANT 4 toolkit was used (Agostinelli

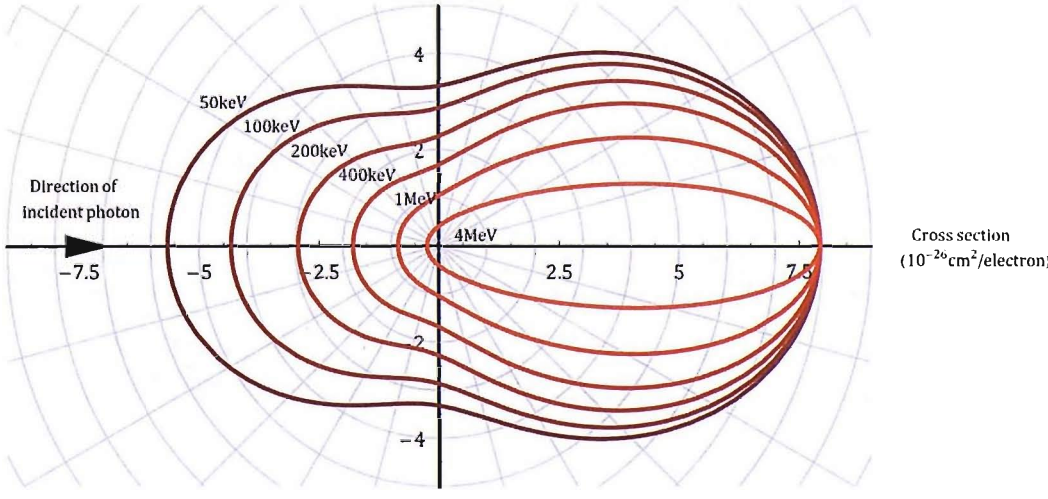

Figure 8.2: Probability of the direction of scatter from a Compton event at the origin according to the Klien-Nishina function (Davisson and Evans 1952).

et al. 2003). The GEANT 4 toolkit contains all the physics to allow the tracking of photons and particles through a modelled geometry.

A schematic of the initial geometry coded in GEANT 4 can be seen in Figure 8.3. It consists of a germanium pixelated detector plane (10cm across, 4mm pixels) and segmented germanium walls. Segmenting the germanium in the walls creates smaller crystals which aid the charge transportation and improve the energy resolution of the germanium. Using 1cm germanium crystals will also have the effect of giving position sensitivity on the walls which can help with polarisation measurements. The dimensions of the detector plane and walls were all coded allowing them to be varied and the effect of the variations examined. In addition a 5cm BGO anti-coincidence shield was added to assist in the vetoing of background events from the signal and to reduce the numbers of non-photopeak events caused when a photon escapes the germanium system. To ensure that the detector performs over the required energy range the geometry was tested for energies of 10, 20, 40, 100, 200, 511, 1000 and 2000keV. The values over which the dimensions of the detector were varied can be seen in Table 8.1.

Table 8.1: Value ranges used to test detector geometry.

	Value Range /cm	Value Step /cm
Detector Thickness (a)	1.0 – 10.0	1
Wall Thickness (b)	1.0 – 5.0	1
Wall Depth (c)	0.0 – 40.0	5

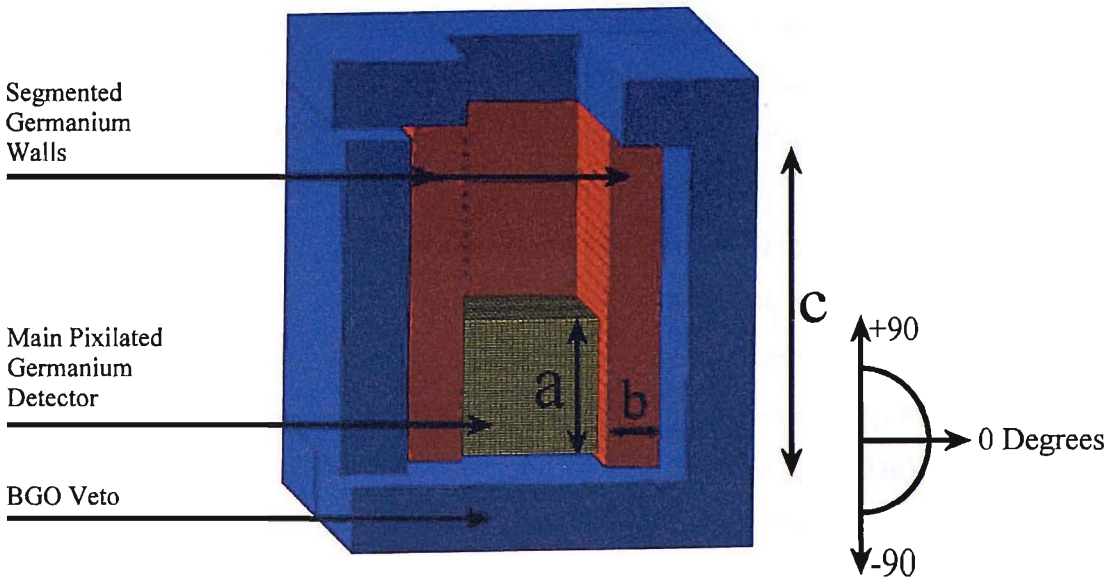

Figure 8.3: Labelled visualisation of the detector geometry used in the GEANT 4 simulation. Phi is the angle relating to the forward and backward scattering of a photon. Phi of +90 indicates that the photon has scattered through the front of the detector.

8.4 Detector Results

The detector dimensions were varied over the ranges mentioned in section 8.3 to optimize the design and to ascertain the performance of the detector. While a dimension is being varied the rest of the dimensions are held constant. The results are based on 10^6 photons fired at each step to ensure the result is a good statistical representation. The BGO veto threshold is set to 80 keV, the value used for the SPI veto.

8.4.1 Variation of Detector Thickness

The detector thickness has been varied between 1.0cm and 10.0cm in 1.0cm steps, the results of which can be seen in Figure 8.4. In this simulation, the model included walls 40cm high and 5cm thick. The thicker the detector plane the better its performance in stopping more high-energy photons. The heavy black line shows the performance of a 10cm Compton cube detector with no walls around it. Already it can be seen that the Compton cube is only as efficient as a 4cm detector plane with walls. At lower energies, the detector thickness makes less of an impact than at the higher energies, due to low energy photons being stopped within the first few centimetres of the detector plane. Since the detector would need to deal with energies of ~1MeV, the thicker the detector is, the better. As mentioned previously, at these higher energies the photons will preferentially forward scatter and penetrate deeper into the detector. Although at this stage the background component is not included and so optimisation between the detector thickness and background count rate may result in reducing the detector thickness slightly.

8.4.2 Variation of Wall Thickness

The results from varying the wall thickness can be seen in Figure 8.5. As the wall thickness increases, it is clear that at the high end of the energy range the performance improves. As the thickness increases this increase in performance gets smaller with each increment. After 4cm the improvement becomes less, and increasing the thickness any further will increase the weight greatly without having a significant impact on the performance.

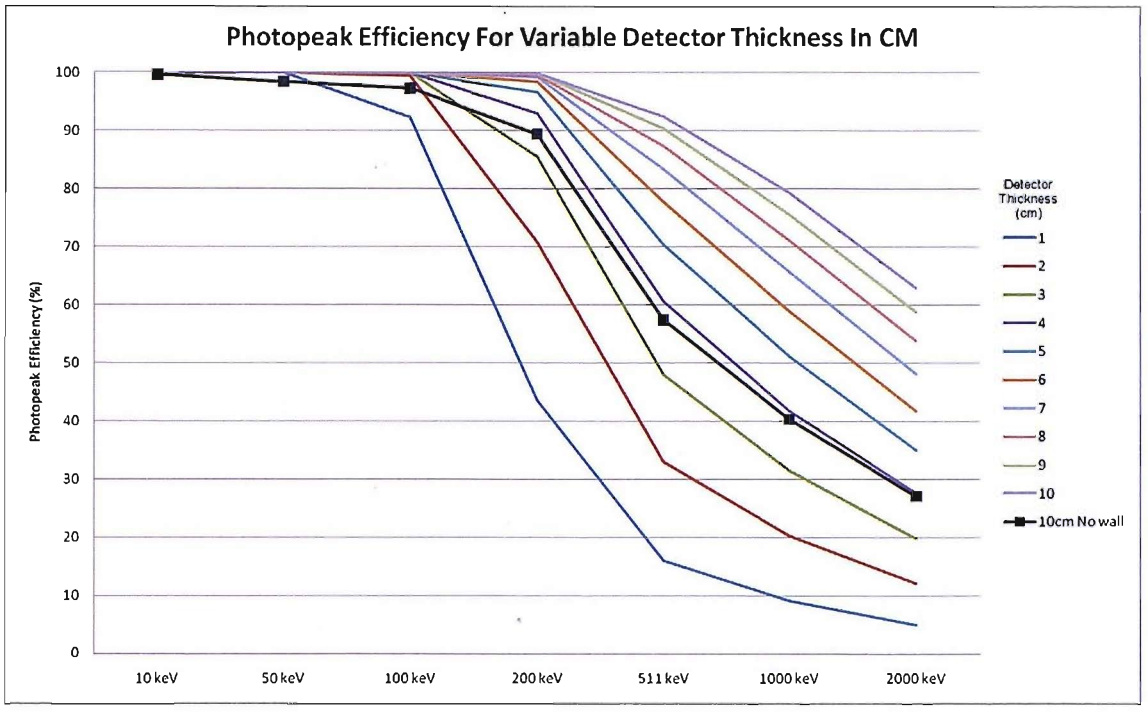

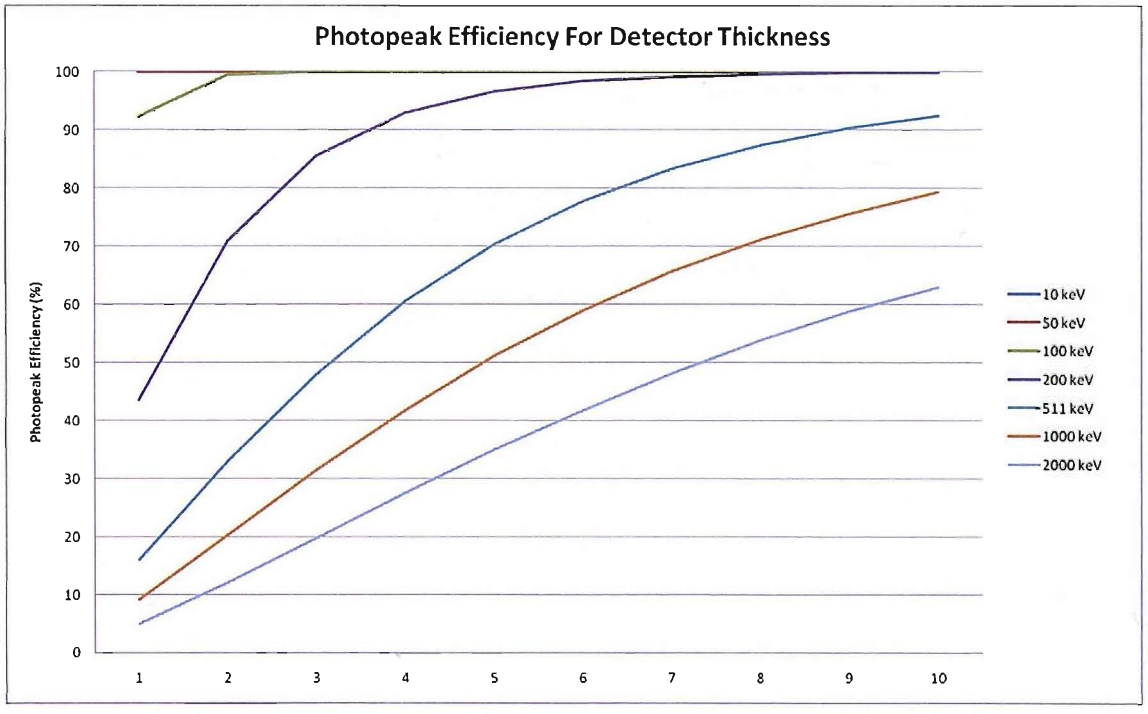

Figure 8.4: Effect of detector thickness on the photopeak efficiency. The wall height has been fixed at 40cm and a thickness of 5cm.

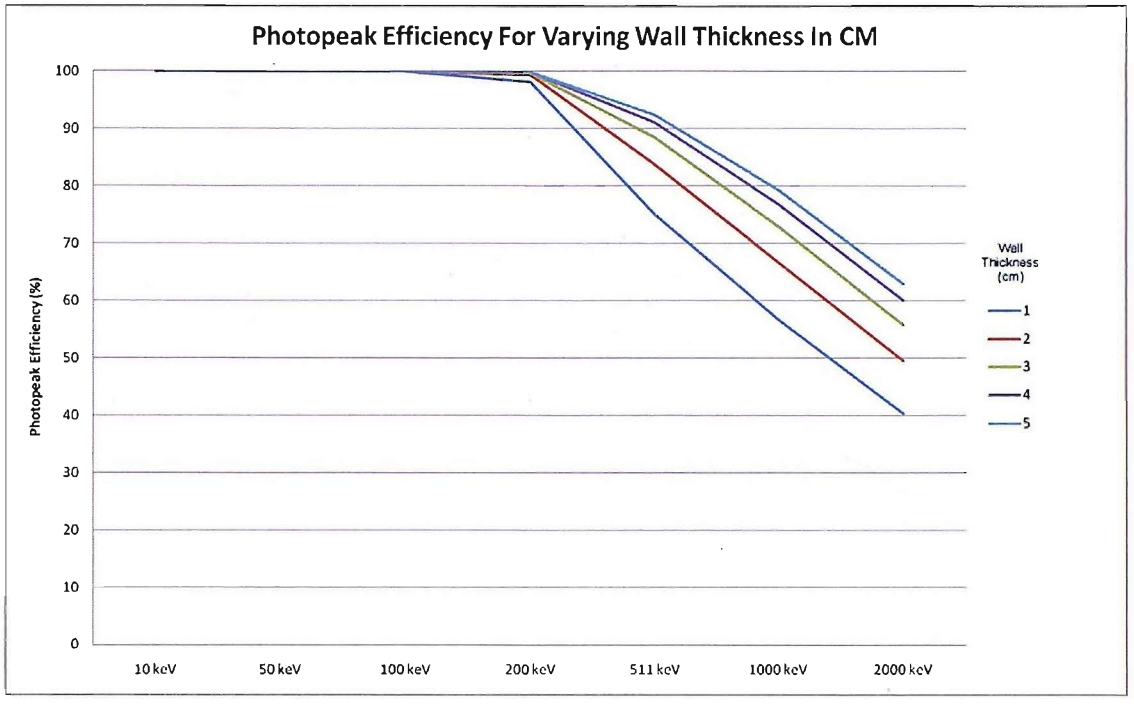

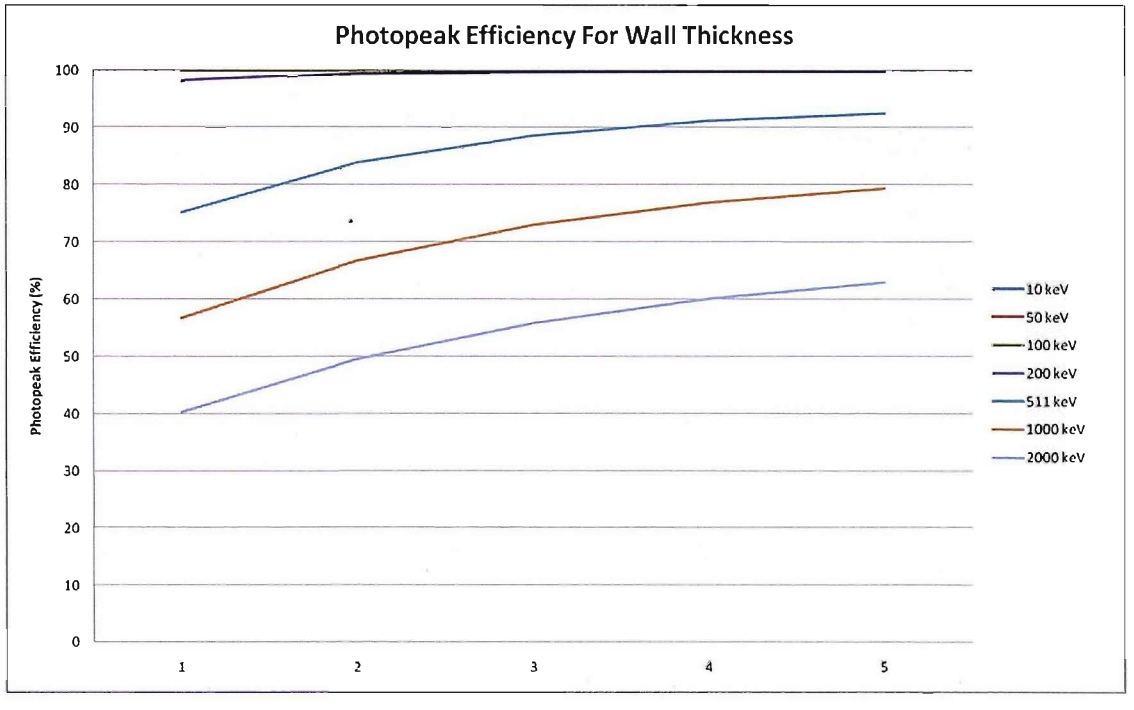

Figure 8.5: Effect of varying wall thickness on the photopeak efficiency. The detector thickness has been fixed at 10cm and the wall height has been fixed at 40cm.

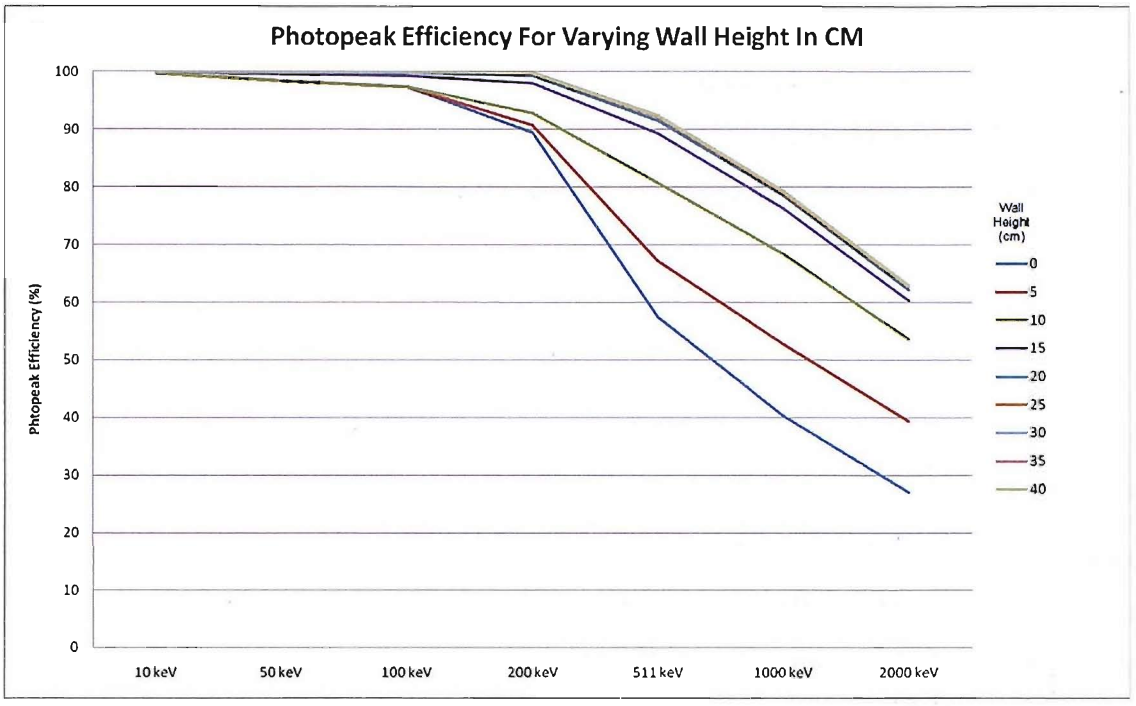

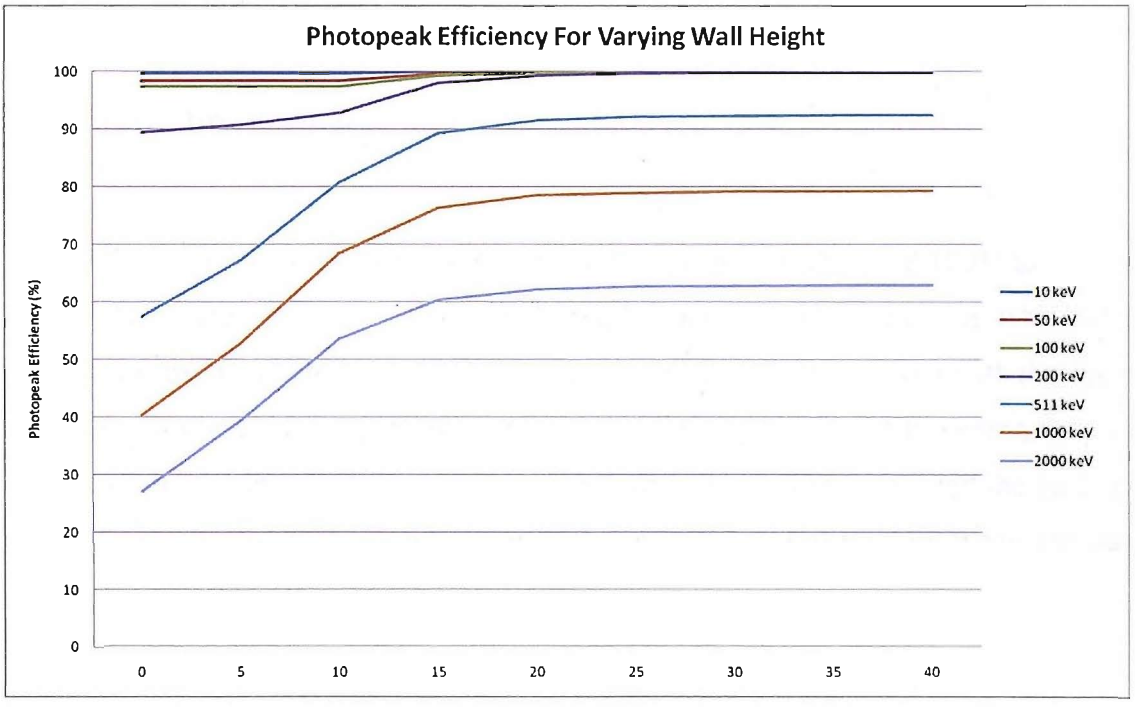

Figure 8.6: Effect of varying the wall height on the photopeak efficiency of the detector. The detector thickness and wall thickness have been fixed at 10cm and 5 cm respectively.

Greater performance for the weight can be gained by varying the thickness up the height of the wall. By taking into account the line of sight of the photon trajectories from the main detector to the top of the walls, the walls can be made thinner at the top and thicker at the base. This would use the same mass of germanium more efficiently and therefore improve performance.

8.4.3 Variation of Wall Height

Varying the wall height has the greatest effect on the efficiency of the detector (Figure 8.6). However, this effect reduces very quickly as the wall height increases. After 15cm there is little effect on the photopeak efficiency when increasing the height of the walls. This is probably due to the geometry of the system and the solid angle effect of the photons scattering off from the surface.

8.4.4 Event Distribution

Figure 8.7 shows where incident 511keV photons that are not absorbed 100% inside the detector leave the detector. As the wall height increases, the area over which this effects the escaping photons can clearly be seen. It is also clear that even with the 10cm thick detector plane a large percentage of the escaping photons are still passing through the base of the detector ($\varphi < 0°$). However, including the BGO veto around the detector can not only remove background events, but can also be used to veto events passing through the detector, cleaning the signal further.

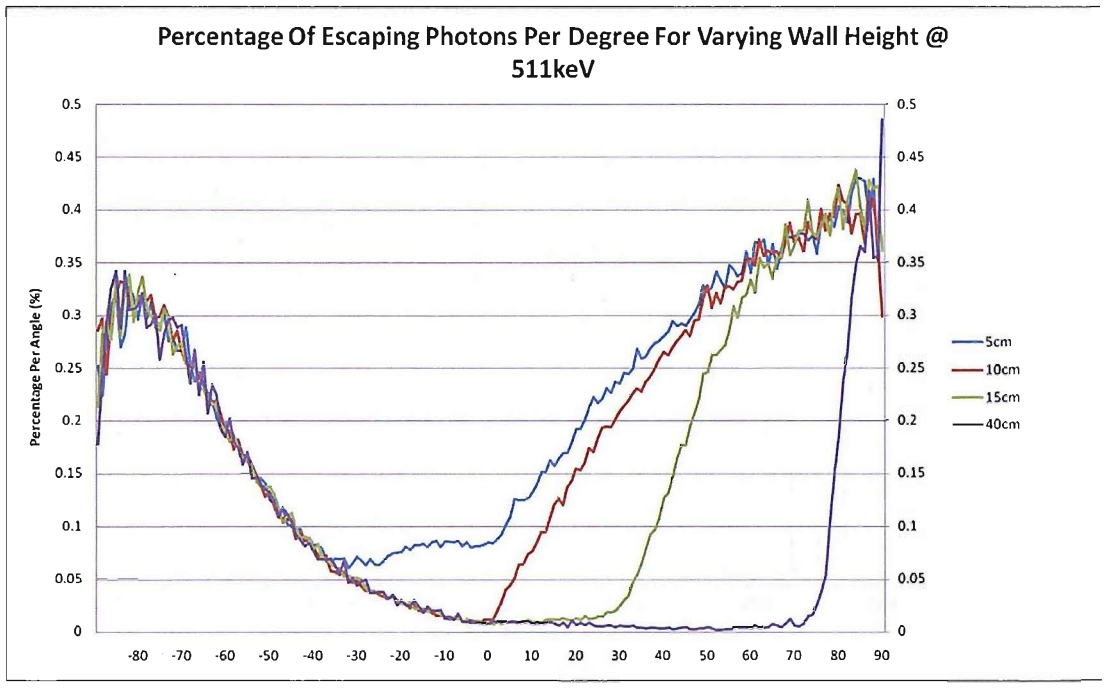

Figure 8.7: Percentage of photons not being detected as photopeak events and where they leave the detector. Positive Phi angle corresponds to Laue lens direction.

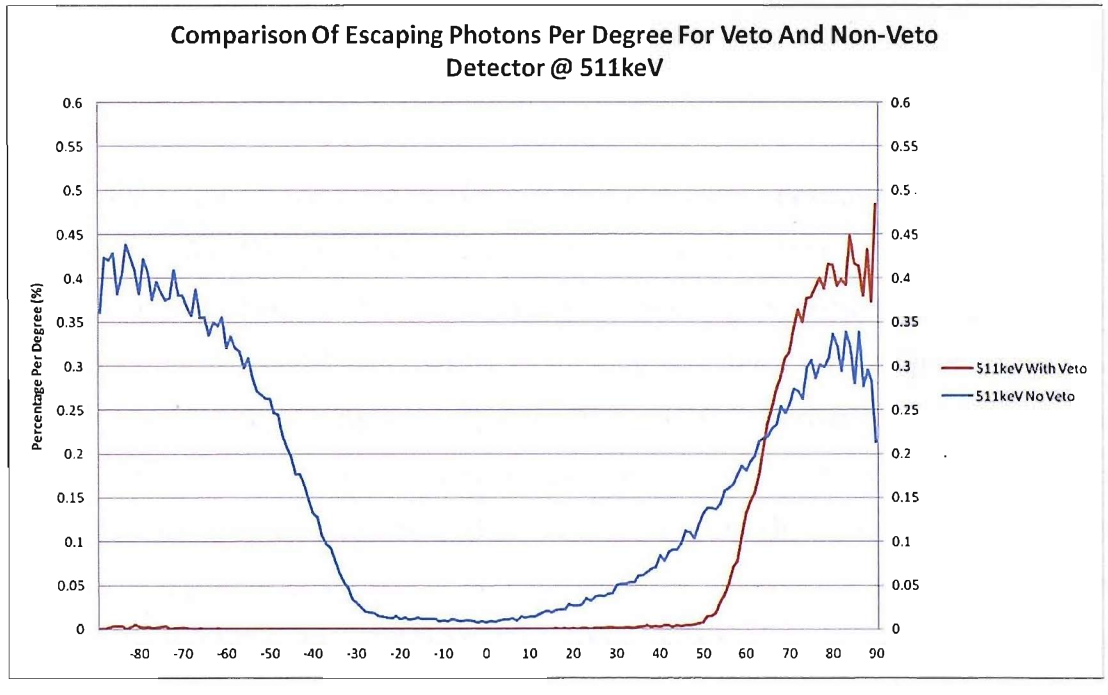

Figure 8.8: Effect at 511keV of adding a BGO veto to the detector design.

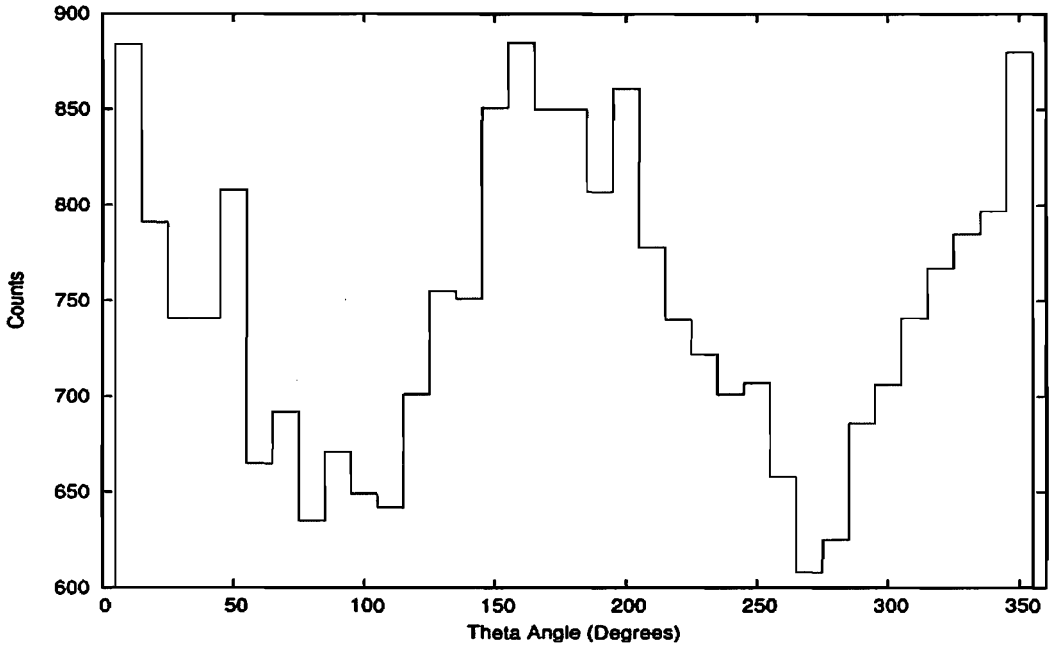

Figure 8.9: Profile of count rate around the wall for a 511keV polarised flux for a 1cm segmented wall.

8.4.5 Polarisation

An interesting property of the Laue Lens is that it does not destroy the polarisation of the incoming flux (Frontera and Pareschi 1995). It is therefore a major benefit if the detector is able to detect the polarisation of the incoming gamma-rays. The polarisation of a gamma-ray is usually detected by examining how the rays Compton scatter. A gamma-ray will preferentially scatter perpendicular to its polarisation vector (Lei et al. 1997). Looking at the azimuthal scatter of the gamma-rays is particularly easy with this detector design. The count rates in the walls will clearly show the polarisation since there will be a greater count rate at 90 degrees to the polarisation angle. This can be seen in Figure 8.9, where a 511keV flux 100% polarised at 90° was fired into the detector.

8.4.6 Background

For the sensitivity of a telescope employing a cavity germanium detector to be evaluated, the background must be investigated. Due to the Laue Lens system's need for a long focal length (~150m), most designs are planned to orbit the L2 Lagrange point in the Earth - Sun system. This would mean that any background would be mainly due to Cosmic diffuse gamma-ray emission or Galactic cosmic rays. Both were assumed to be isotropic sources around the detector. The spectra for the Cosmic diffuse emission and the cosmic rays, taken from Gehrels (1992) and Webber and Lezniak (1974) respectively, were used as the input for the GEANT 4 simulation to estimate the background count rate in the detector. A standard 2GeV cut-off for the Cosmic ray protons was implemented to account for the mission being in interplanetary space. Table 8.2 shows the predicted sensitivity of the detector at 511keV and at 1MeV. While the Compton cube is an order of magnitude better than the Spectrometer onboard INTEGRAL (SPI) (Roques et al. 2003) at 511keV, the cavity detector is a further order of magnitude better than the Compton cube detector (Weidenspointner et al. 2005).

The background rejection is efficient in this design, since a photon from the lens has to interact in the base of the detector, all events that do not can automatically be rejected. When combined with a standard anti coincidence shield a background count rate of 0.29 cts cm^{-2} s^{-1} remained between 10keV and 2MeV. This count rate gives rise to the line sensitivities at a statistical significance of 3σ shown in Table 8.2, assuming a 10^6s observation time and the energy resolution of germanium of 2keV.

Table 8.2: Predicted line sensitivity of detector, including a comparison with a standard Compton cube detector and SPI the spectrometer onboard INTEGRAL(all 3σ, 106 seconds).

Energy [keV]	Photopeak Efficiency [%]	Cavity Detector Line Sensitivity [10^{-6} ph/cm^2/s]	Compton Cube Line Sensitivity [10^{-6} ph/cm^2/s]	SPI Line Sensitivity [10^{-6} ph/cm^2/s]
511	92.4636	0.046	~1.5	28
1000	79.2595	0.054	~1.5	5.1

8.5 GRI – The Gamma-Ray Imager Proposal

In July 2007, the GRI Consortium, an international collaboration consisting of 40 institutions of which the University of Southampton is a member, presented the European Space Agency with a proposal for a mission based around the concept of a Laue Lens to form part of the Agencies Cosmic Vision plan (Knödlseder and The GRI Consortium 2007). The mission has been designed to explore the gamma-ray universe with unprecedented sensitivity and angular resolution. The final proposed design is very different to the preliminary concept designed in the production of this thesis; however, aspects of the concept can be seen in the final design.

The proposed instrument consists of 4 stacked CZT (Cadmium Zinc Telluride) layers, surrounded by CZT side walls. The 5mm thick top layer optimised for photoelectric

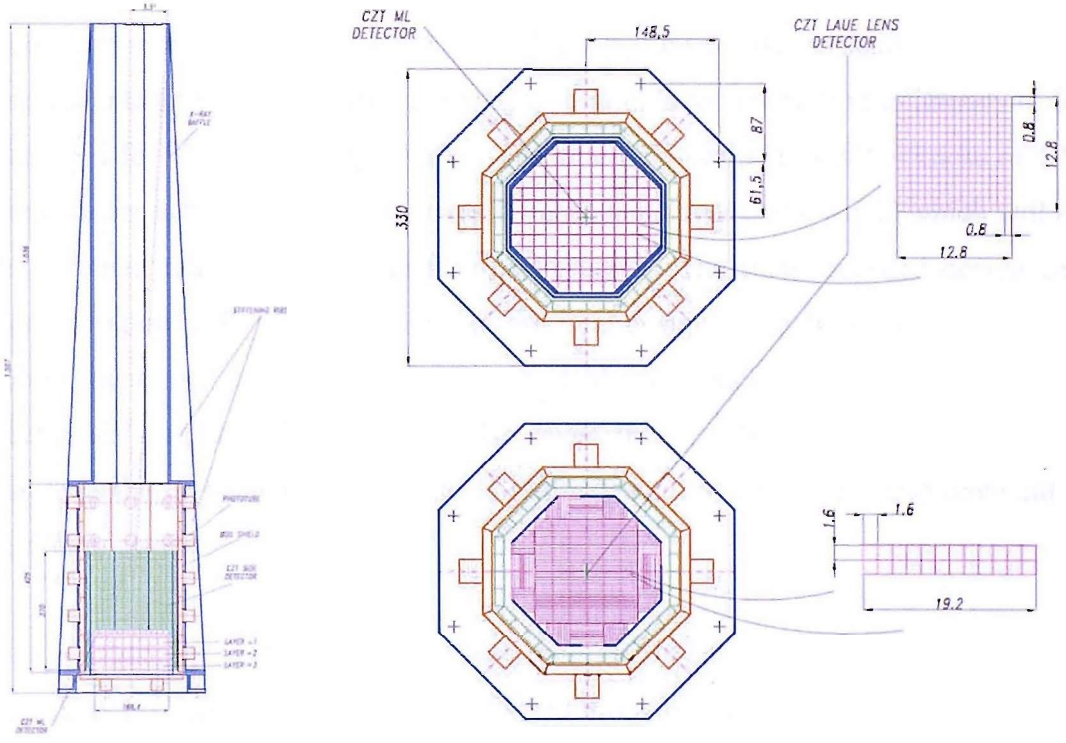

Figure 8.10: Schematic representation of the proposed detector payload (Knödlseder and The GRI Consortium 2007).

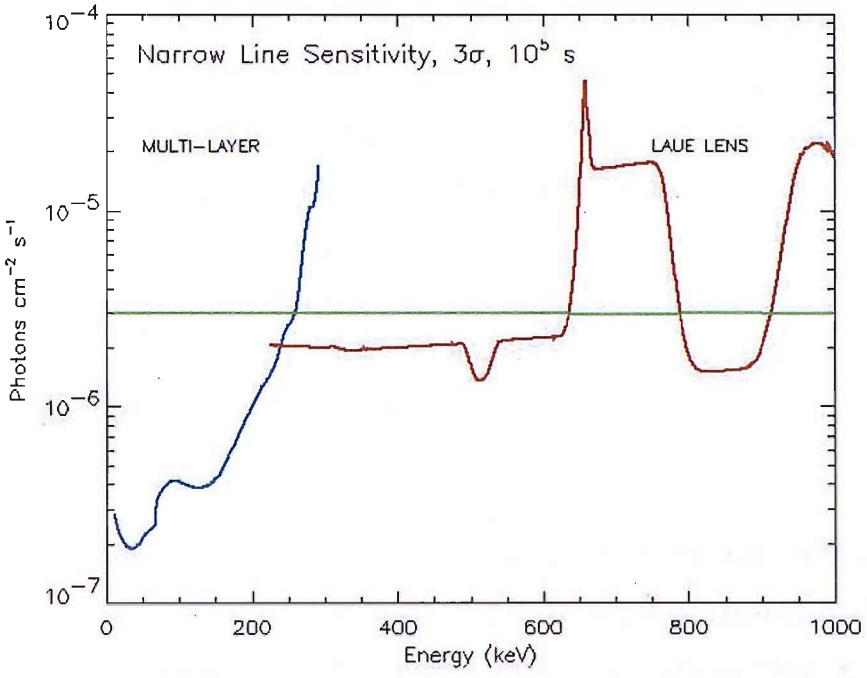

Figure 8.11: Narrow line sensitivity as a function of energy for an observing time of 100ks (Knödlseder and The GRI Consortium 2007).

absorption in the 10-250 keV band, while the lower layers use vertically placed crystals. These create a thickness of 20mm per layer to grant a total detection efficiency of better than 75% for photons below 1 MeV. The side CZT walls have a thickness of 10mm. The detector is then surrounded by a BGO anti-coincidence veto shield which will allow and efficient reduction of the diffuse background. The final proposed design can be seen in Figure 8.10. The sensitivity of the final design is much lower that the concept design mentioned before, due to the more realistic modelling including structure and electronics' response (Figure 8.11). However, this sensitivity is only a factor of ~10 less than the original design and so is still expected to be a great improvement over current missions.

The final instrument may be very different from the proposed design. Much more research will be performed on optimising the design. Currently the detector material is not set and instead of using CZT operating at room temperature CdTe (Cadmium

Telluride) crystals could be used for improved spectroscopic performance. Another option would be cooled high-purity Ge (Germanium) which would provide improved spectral resolution and better background rejection and potentially increase the scientific performance. Ge would require active cooling and detector annealing cycles that would increase the complexity of the mission.

8.6 Summary

Using a GEANT Monte Carlo simulation we have calculated the performance of a new detector configuration, specifically tailored to suit the needs of prospective Laue Lens missions. By capturing the Compton scattered products of the incoming gamma-rays a very high photopeak efficiency is achieved. A high photopeak efficiency and low background count rate for the detector with the collecting area of a Laue Lens prove to be a very powerful combination for high sensitivity observations in gamma-ray astronomy. The initial optimisation of the detector can be seen in Table 8.3. There are still areas in which the design can be improved, including optimising the thickness of the germanium walls to account for the path of the scattered photons. This will make more efficient use of the detector material and improve the performance for the mass available.

Table 8.3: Initial optimisation of detector dimensions in this thesis compared to the final design dimensions of GRI.

Parameter	Initial Optimisation (cm)	Final GRI Optimisation (cm)
Detector thickness	10	6.5
Wall thickness	4	1
Wall height	15	27

After being fully optimised in the realistic context of the GRI mission (Knödlseder and The GRI Consortium 2007) the detector dimensions have changed slightly (Table 8.3). The GRI detector plan was slightly broader in the final design. This affected the optimum wall height, requiring it to be increased. After a full background analysis, the thickness of the detector and the walls was reduced creating a smaller volume for background photons to interact in. The pixelated base in the design is ideally suited to exploit the limited imaging capabilities of the Laue Lens design, while pixelating the walls as well will make the design a very powerful polarimeter.

With the small field of view of GRI, the number of GRBs occurring within the observed region will be low. The likelihood of GRI obtaining a polarisation measurement of a GRB will be very small. However, the observation's persistent sources will be able to provide excellent polarisation measurements due to GRI's excellent collecting area.

Chapter 9

Conclusions

Astronomical gamma-rays allow the observation of the most energetic processes in the universe. These non-thermal processes through a range of interaction mechanisms often dominated by the local magnetic field configuration are usually driven by electrons and other elementary particles interacting with magnetic fields producing high energy photons. This will create an ordered structure in the emission region. Over the emission region, the polarisation of a gamma-ray produced by a single electron will be reduced when averaged over the differences in orientation of many electrons. However, the short lifetimes of the electrons will reduce the size of the emission region, in turn, reducing the area over which the alignment of a magnetic field needs to be maintained. Hence the emission measures the geometrical field configuration close to the site of acceleration. Therefore, a measurement of the gamma-ray polarisation will give a very good indicator of the presence and geometry of magnetic fields.

The most practical way of detecting the polarisation of gamma-rays is to analyse the azimuthal distribution of Compton scattered gamma-rays. The SPI detector onboard the INTEGRAL satellite provides an excellent instrument to measure polarisation, even though it had not been designed for this purpose. Using a highly detailed GEANT 4 Monte-Carlo Mass-Model to simulate the detector's response to an incident polarised flux, measurements have been attempted for three gamma-ray bursts and the Crab pulsar, each with varying success.

GRBs provide a good starting point for polarisation measurements. A burst gives a high number of counts in a short period of time. This results in a very clean data set where the instrument and background environment change very little throughout the length of the observation. The best results have been obtained from GRB041219a, while the analysis of GRB060901 and GRB061122 suffered from very low count rates. The results obtained for GRB041219a are consistent with linear polarisation at about the 60% level ($\sim 2\sigma$) at an angle of $\sim 70°$. It is possible that there is variation in the polarisation properties over the duration of the burst. However, due to the statistical quality of the data it is impossible to tell if this is the case.

The measurements made to date of GRB polarisation from Willis et al (Willis et al. 2005) and in this thesis, indicate a high level of polarisation of around 50%-60%. A polarisation percentage this high indicates that the source of the emission must be well ordered, probably with strong magnetic fields. All the measurements calculated in this thesis show a drop off of signal as the photon energies increase. This could be an indication of an Inverse Compton scattering process being involved, such as that suggested by Shaviv & Dar (1995) and Dar & de Rújula (2004). However, this could also be due to the poor statistical quality of the measurement at higher energies. We are still in the preliminary stages in the measurement of gamma-ray burst polarisation and it is not possible to differentiate between model theories, although the high levels of polarisation measured would rule out a hydrodynamic origin for GRB emission.

For a better measurement of the polarisation of a GRB flux, a brighter burst is needed. Unfortunately, GRB041219a is likely to be the best burst for polarisation analysis that will be seen by INTEGRAL. It was very long and bright producing a large number of events in the SPI detectors. The subsequent bursts analysed highlight how difficult it is to obtain sufficient data. GRB060901 and GRB061122 were both very bright bursts, however, the combination of their large off axis angle, short T_{90} time and the saturation of the telemetry means that they simply did not produce enough events in the detector to analyse. The ideal burst would have to be brighter and longer than GRB041219a in order to produce better results than those presented here. Unfortunately, GRBs observed within the field of view of SPI are a rare and random occurrence, so it is unknown if this result will be able to be improved within the lifetime of this instrument. A more sensitive, dedicated polarimeter may be required to fully determine the polarimetric properties of GRB emission.

A persistent source such as the Crab is more complex to analyse, with multiple observations needed to gain a sufficient number of counts to detect polarisation. This creates many problems with the instrument attitude and other parameters changing throughout the data set. The advantage of the Crab is that there is a vast amount of data available and more data can be collected if a significant result is not initially obtained. The pulse profile of the Crab emission shows a double peaked structure with an off-pulse section for which the emitted flux remains constant. Polarisation measurements of the unpulsed emission that have been taken from approximately the same phase interval (0.5-0.8) have been reported from the Crab in both X-ray (Weisskopf et al. 1978) and optical (Kanbach et al. 2005) wavelengths. A polarisation angle of 123° ± 1.5° at a percentage of 40% ± 3% has been measured in the gamma-ray energy range of 100 keV to 1 MeV. At X-ray energies, linear polarisation at 2.6 keV and 5.2 keV was found at a level of 19.2% and 19.5% respectively with corresponding angles of 156°.4 and 152°.6 degrees, while in the optical energy range the polarisation found was 33% with an angle of around 123 degrees, in close agreement with our values.

Due to the pulsed emission accounting for only a small fraction (~5%) of the total Crab emission, it has proven more difficult with the current data set to obtain meaningful polarisation results from the on-pulse sections of the phase folded Crab light curve. Without subtracting a DC component, any variation is swamped by the signal relating to the off-pulse, while attempting to subtract the DC component suffers from the small number statistics meaning much more data is needed. The production of simulated data to use in the pulsed analysis will take longer than the time available

A number of further investigations into the gamma-ray polarisation characteristics are possible. Further work needs to be carried out on the Crab pulsar. The polarisation of the off-pulse emission is very useful and has given an insight into the origin of the Crab gamma-ray emission that must originate close to the pulsar, possibly at the source of the jet structure. The analysis of the pulsed emission will improve the understanding of the magnetic field environment and processes involved in the pulses, allowing the selection of either the polar cap, the two pole caustic or the outer gap models as the best description for the pulsed emission.

The gamma-ray emission from Cygnus X-1 may also be polarised. A bright X-ray source, Cygnus X-1 has been the target of a significant number of observations in the INTEGRAL archive. The system is a High Mass X-ray Binary containing a black hole accreting from a supergiant star. This accretion will form a disk of matter around the black hole. Viironen & Poutanen (2004) have predicted polarised emission from a Comptonised hot disk, and therefore would make this an ideal candidate for future attempts at polarisation measurements.

As more data is collected by INTEGRAL it may become possible to attempt polarisation measurements of more sources in the INTEGRAL catalogue. Unfortunately, the large simulation time needed for each attempt means this will be a

very slow process and the technology of gamma-ray polarimeters may become sufficiently advanced to make such an analysis redundant. A future mission such as GRI will undoubtedly be much more suited for polarisation measurements of faint sources. GRI would be unlikely to make a GRB polarisation measurement due to its small field of view and the inability to predict where a GRB may occur. A detector capable of very sensitive polarisation measurements with a large field of view will be required to study the polarisation properties of a GRB in finer detail.

The field of gamma-ray polarimetry is still in its infancy, but is growing all the time. The future contains many exciting prospects with polarisation results holding the key to understanding the precise origin of the gamma-ray emission.

Appendix A

GEANT 4 Physics List

The complete physics list used in all simulations contained within this thesis.

```
#include "PIMPPhysicsList.hh"

#include "G4ParticleDefinition.hh"
#include "G4ParticleWithCuts.hh"
#include "G4ProcessManager.hh"
#include "G4ProcessVector.hh"
#include "G4ParticleTypes.hh"
#include "G4ParticleTable.hh"
#include "G4Material.hh"
#include "G4ios.hh"
#include "G4ShortLivedConstructor.hh"
#include "G4IonConstructor.hh"
extern G4String SpectralType ;
PIMPPhysicsList::PIMPPhysicsList(): G4VUserPhysicsList()
{
 currentDefaultCut = defaultCutValue = 0.05*mm;
 cutForGamma     = defaultCutValue;
 cutForElectron  = defaultCutValue;
 cutForProton    = defaultCutValue;

 SetVerboseLevel(0);
}
```

```
PIMPPhysicsList::~PIMPPhysicsList()
{}

void PIMPPhysicsList::ConstructParticle()
{
 ConstructBosons();
 ConstructLeptons();
 ConstructMesons();
 ConstructBaryons();
 ConstructAllShortLiveds();
 ConstructAllIons();
}

void PIMPPhysicsList::ConstructBosons()
{
 // pseudo-particles
 G4Geantino::GeantinoDefinition();
 G4ChargedGeantino::ChargedGeantinoDefinition();

 // gamma
 G4Gamma::GammaDefinition();

 // optical photon
 G4OpticalPhoton::OpticalPhotonDefinition();
}

void PIMPPhysicsList::ConstructLeptons()
{
 G4Electron::ElectronDefinition();
 G4Positron::PositronDefinition();
 G4MuonPlus::MuonPlusDefinition();
 G4MuonMinus::MuonMinusDefinition();

 G4NeutrinoE::NeutrinoEDefinition();
 G4AntiNeutrinoE::AntiNeutrinoEDefinition();
 G4NeutrinoMu::NeutrinoMuDefinition();
 G4AntiNeutrinoMu::AntiNeutrinoMuDefinition();
}

void PIMPPhysicsList::ConstructMesons()
{
 G4PionPlus::PionPlusDefinition();
 G4PionMinus::PionMinusDefinition();
 G4PionZero::PionZeroDefinition();
 G4Eta::EtaDefinition();
 G4EtaPrime::EtaPrimeDefinition();
 G4KaonPlus::KaonPlusDefinition();
 G4KaonMinus::KaonMinusDefinition();
 G4KaonZero::KaonZeroDefinition();
 G4AntiKaonZero::AntiKaonZeroDefinition();
 G4KaonZeroLong::KaonZeroLongDefinition();
 G4KaonZeroShort::KaonZeroShortDefinition();
}
```

```
void PIMPPhysicsList::ConstructBaryons()
{
 G4Proton::ProtonDefinition();
 G4AntiProton::AntiProtonDefinition();
 G4Neutron::NeutronDefinition();
 G4AntiNeutron::AntiNeutronDefinition();
}

void PIMPPhysicsList::ConstructProcess()
{
 G4cout << "Contruct Processes for *" << PrimaryParticleType << "*" <<G4endl ;
 AddTransportation();
 ConstructEM();
}

#include "G4ComptonScattering.hh"
#include "G4GammaConversion.hh"
#include "G4PhotoElectricEffect.hh"
#include "G4PolarizedComptonScattering.hh"
#include "G4LowEnergyPolarizedCompton.hh"
#include "G4MultipleScattering.hh"
#include "G4eIonisation.hh"
#include "G4eBremsstrahlung.hh"
#include "G4eplusAnnihilation.hh"
#include "G4MuIonisation.hh"
#include "G4MuBremsstrahlung.hh"
#include "G4MuPairProduction.hh"
#include "G4hIonisation.hh"
#include "G4LowEnergyIonisation.hh"
#include "G4hLowEnergyIonisation.hh"
#include "G4LowEnergyBremsstrahlung.hh"
#include "G4LowEnergyPhotoElectric.hh"
#include "G4LowEnergyCompton.hh"
#include "G4LowEnergyRayleigh.hh"

void PIMPPhysicsList::ConstructEM()
{
 theParticleIterator->reset();
 while( (*theParticleIterator)() ){
   G4ParticleDefinition* particle = theParticleIterator->value();
   G4ProcessManager* pmanager = particle->GetProcessManager();
   G4String particleName = particle->GetParticleName();

   if (particleName == "gamma") {
     pmanager->AddDiscreteProcess(new G4LowEnergyPolarizedCompton());
     pmanager->AddDiscreteProcess(new G4GammaConversion());
     pmanager->AddDiscreteProcess(new G4LowEnergyPhotoElectric());
     pmanager->AddDiscreteProcess(new G4LowEnergyRayleigh());

   } else if (particleName == "e-") {
     //electron
     pmanager->AddProcess(new G4MultipleScattering(),-1, 1,1);

     // for fluorescence
     pmanager->AddProcess(new G4LowEnergyIonisation(), -1,  2, 2);
```

```
    pmanager->AddProcess(new G4LowEnergyBremsstrahlung(), -1, -1, 3);

   } else if (particleName == "e+") {
    //positron
    pmanager->AddProcess(new G4MultipleScattering(),-1, 1,1);
    pmanager->AddProcess(new G4eIonisation(),      -1, 2,2);
    pmanager->AddProcess(new G4eBremsstrahlung(),  -1,-1,3);
    pmanager->AddProcess(new G4eplusAnnihilation(), 0,-1,4);

   } else if( particleName == "mu+" ||
         particleName == "mu-"    ) {
    //muon
    pmanager->AddProcess(new G4MultipleScattering(),-1, 1,1);
    pmanager->AddProcess(new G4MuIonisation(),     -1, 2,2);
    pmanager->AddProcess(new G4MuBremsstrahlung(), -1,-1,3);
    pmanager->AddProcess(new G4MuPairProduction(), -1,-1,4);

   } else if ((!particle->IsShortLived()) &&
              (particle->GetPDGCharge() != 0.0) &&
              (particle->GetParticleName() != "chargedgeantino")) {
    //all others charged particles except geantino
    pmanager->AddProcess(new G4MultipleScattering(),-1,1,1);
    pmanager->AddProcess(new G4hIonisation(),      -1,2,2);
   }
  }
}

#include "G4Decay.hh"
#include "G4RadioactiveDecay.hh"
#include "G4IonTable.hh"
#include "G4Ions.hh"

void PIMPPhysicsList::ConstructGeneral()
{
 G4cout << "Adding DECAY" << G4endl ;
 // Add Decay Process
 G4Decay* theDecayProcess = new G4Decay();
 theParticleIterator->reset();
 while( (*theParticleIterator)() ){

  G4ParticleDefinition* particle = theParticleIterator->value();
  G4ProcessManager* pmanager = particle->GetProcessManager();
  if (theDecayProcess->IsApplicable(*particle)) {
   pmanager ->AddProcess(theDecayProcess);
   // set ordering for PostStepDoIt and AtRestDoIt
   pmanager ->SetProcessOrdering(theDecayProcess, idxPostStep);
   pmanager ->SetProcessOrdering(theDecayProcess, idxAtRest);
  }
 }
 // Declare radioactive decay to the GenericIon in the IonTable.
 const G4IonTable *theIonTable =
  G4ParticleTable::GetParticleTable()->GetIonTable();
 G4RadioactiveDecay *theRadioactiveDecay = new G4RadioactiveDecay();

 for (G4int i=0; i<theIonTable->Entries(); i++)
```

```
    {
     G4String particleName = theIonTable->GetParticle(i)->GetParticleName();
     G4String particleType = theIonTable->GetParticle(i)->GetParticleType();

     G4cout << "Ion Table Entry: " << particleName << " Type: " << particleType << G4endl ;
     if (particleName == "GenericIon")
          {
           G4ProcessManager* pmanager =
            theIonTable->GetParticle(i)->GetProcessManager();
           // pmanager->SetVerboseLevel(VerboseLevel);
           pmanager ->AddProcess(theRadioactiveDecay);
           pmanager ->SetProcessOrdering(theRadioactiveDecay, idxPostStep);
           pmanager ->SetProcessOrdering(theRadioactiveDecay, idxAtRest);
          }
    }
}

void PIMPPhysicsList::SetCuts()
{
 // reactualise cutValues
 if (currentDefaultCut != defaultCutValue)
    {
     if(cutForGamma    == currentDefaultCut) cutForGamma    = defaultCutValue;
     if(cutForElectron == currentDefaultCut) cutForElectron = defaultCutValue;
     if(cutForProton   == currentDefaultCut) cutForProton   = defaultCutValue;
     currentDefaultCut = defaultCutValue;
    }

 if (verboseLevel >0){
   G4cout << "PIMPPhysicsList::SetCuts:";
   G4cout << "CutLength : " << G4BestUnit(defaultCutValue,"Length") << G4endl;
 }

 // set cut values for gamma at first and for e- second and next for e+,
 // because some processes for e+/e- need cut values for gamma
 SetCutValue(cutForGamma, "gamma");
 SetCutValue(cutForElectron, "e-");
 SetCutValue(cutForElectron, "e+");

 // set cut values for proton and anti_proton before all other hadrons
 // because some processes for hadrons need cut values for proton/anti_proton
 SetCutValue(cutForProton, "proton");
 SetCutValue(cutForProton, "anti_proton");

 SetCutValueForOthers(defaultCutValue);

 if (verboseLevel>0) DumpCutValuesTable();
}

// Hadron Processes

#include "G4HadronElasticProcess.hh"
#include "G4PionPlusInelasticProcess.hh"
#include "G4PionMinusInelasticProcess.hh"
#include "G4KaonPlusInelasticProcess.hh"
```

```
#include "G4KaonZeroSInelasticProcess.hh"
#include "G4KaonZeroLInelasticProcess.hh"
#include "G4KaonMinusInelasticProcess.hh"
#include "G4ProtonInelasticProcess.hh"
#include "G4AntiProtonInelasticProcess.hh"
#include "G4NeutronInelasticProcess.hh"
#include "G4AntiNeutronInelasticProcess.hh"
#include "G4LambdaInelasticProcess.hh"
#include "G4AntiLambdaInelasticProcess.hh"
#include "G4SigmaPlusInelasticProcess.hh"
#include "G4SigmaMinusInelasticProcess.hh"
#include "G4AntiSigmaPlusInelasticProcess.hh"
#include "G4AntiSigmaMinusInelasticProcess.hh"
#include "G4XiZeroInelasticProcess.hh"
#include "G4XiMinusInelasticProcess.hh"
#include "G4AntiXiZeroInelasticProcess.hh"
#include "G4AntiXiMinusInelasticProcess.hh"
#include "G4DeuteronInelasticProcess.hh"
#include "G4TritonInelasticProcess.hh"
#include "G4AlphaInelasticProcess.hh"
#include "G4OmegaMinusInelasticProcess.hh"
#include "G4AntiOmegaMinusInelasticProcess.hh"

// Low-energy Models < 20 GeV

#include "G4LElastic.hh"
#include "G4LEPionPlusInelastic.hh"
#include "G4LEPionMinusInelastic.hh"
#include "G4LEKaonPlusInelastic.hh"
#include "G4LEKaonZeroSInelastic.hh"
#include "G4LEKaonZeroLInelastic.hh"
#include "G4LEKaonMinusInelastic.hh"
#include "G4LEProtonInelastic.hh"
#include "G4LEAntiProtonInelastic.hh"
#include "G4LENeutronInelastic.hh"
#include "G4LEAntiNeutronInelastic.hh"
#include "G4LELambdaInelastic.hh"
#include "G4LEAntiLambdaInelastic.hh"
#include "G4LESigmaPlusInelastic.hh"
#include "G4LESigmaMinusInelastic.hh"
#include "G4LEAntiSigmaPlusInelastic.hh"
#include "G4LEAntiSigmaMinusInelastic.hh"
#include "G4LEXiZeroInelastic.hh"
#include "G4LEXiMinusInelastic.hh"
#include "G4LEAntiXiZeroInelastic.hh"
#include "G4LEAntiXiMinusInelastic.hh"
#include "G4LEDeuteronInelastic.hh"
#include "G4LETritonInelastic.hh"
#include "G4LEAlphaInelastic.hh"
#include "G4LEOmegaMinusInelastic.hh"
#include "G4LEAntiOmegaMinusInelastic.hh"

// High-energy Models > 20 GeV
#include "G4HEPionPlusInelastic.hh"
#include "G4HEPionMinusInelastic.hh"
```

```
#include "G4HEKaonPlusInelastic.hh"
#include "G4HEKaonZeroInelastic.hh"
#include "G4HEKaonZeroInelastic.hh"
#include "G4HEKaonMinusInelastic.hh"
#include "G4HEProtonInelastic.hh"
#include "G4HEAntiProtonInelastic.hh"
#include "G4HENeutronInelastic.hh"
#include "G4HEAntiNeutronInelastic.hh"
#include "G4HELambdaInelastic.hh"
#include "G4HEAntiLambdaInelastic.hh"
#include "G4HESigmaPlusInelastic.hh"
#include "G4HESigmaMinusInelastic.hh"
#include "G4HEAntiSigmaPlusInelastic.hh"
#include "G4HEAntiSigmaMinusInelastic.hh"
#include "G4HEXiZeroInelastic.hh"
#include "G4HEXiMinusInelastic.hh"
#include "G4HEAntiXiZeroInelastic.hh"
#include "G4HEAntiXiMinusInelastic.hh"
#include "G4HEOmegaMinusInelastic.hh"
#include "G4HEAntiOmegaMinusInelastic.hh"

// High precsion > 20 GeV
#include "G4NeutronHPElastic.hh"
#include "G4NeutronHPElasticData.hh"
#include "G4NeutronHPCapture.hh"
#include "G4NeutronHPCaptureData.hh"
#include "G4NeutronHPInelastic.hh"
#include "G4NeutronHPInelasticData.hh"
#include "G4LCapture.hh"

// Capture
#include "G4LFission.hh"
#include "G4HadronCaptureProcess.hh"

// Stopping processes

#ifdef TRIUMF_STOP_PIMINUS
#include "G4PionMinusAbsorptionAtRest.hh"
#else
#include "G4PiMinusAbsorptionAtRest.hh"
#endif
#ifdef TRIUMF_STOP_KMINUS
#include "G4KaonMinusAbsorption.hh"
#else
#include "G4KaonMinusAbsorptionAtRest.hh"
#endif

void PIMPPhysicsList::ConstructHad()
{
  G4cout << "Hadronic Processes" << G4endl ;
  G4HadronElasticProcess* theElasticProcess =
    new G4HadronElasticProcess;
  G4LElastic* theElasticModel = new G4LElastic;
  theElasticProcess->RegisterMe(theElasticModel);
  theParticleIterator->reset();
```

```
 while ((*theParticleIterator)()) {
  G4ParticleDefinition* particle = theParticleIterator->value();
  G4ProcessManager* pmanager = particle->GetProcessManager();
  G4String particleName = particle->GetParticleName();
  G4cout << particleName << G4endl ;

  if (particleName == "pi+") {
   pmanager->AddDiscreteProcess(theElasticProcess);
   G4PionPlusInelasticProcess* theInelasticProcess =
        new G4PionPlusInelasticProcess("inelastic");
   G4LEPionPlusInelastic* theLEInelasticModel =
        new G4LEPionPlusInelastic;
   theInelasticProcess->RegisterMe(theLEInelasticModel);
   G4HEPionPlusInelastic* theHEInelasticModel =
        new G4HEPionPlusInelastic;
   theInelasticProcess->RegisterMe(theHEInelasticModel);
   pmanager->AddDiscreteProcess(theInelasticProcess);
  }
  else if (particleName == "pi-") {
   pmanager->AddDiscreteProcess(theElasticProcess);
   G4PionMinusInelasticProcess* theInelasticProcess =
        new G4PionMinusInelasticProcess("inelastic");
   G4LEPionMinusInelastic* theLEInelasticModel =
        new G4LEPionMinusInelastic;
   theInelasticProcess->RegisterMe(theLEInelasticModel);
   G4HEPionMinusInelastic* theHEInelasticModel =
        new G4HEPionMinusInelastic;
   theInelasticProcess->RegisterMe(theHEInelasticModel);
   pmanager->AddDiscreteProcess(theInelasticProcess);
#ifdef TRIUMF_STOP_PIMINUS
   pmanager->AddRestProcess(new G4PionMinusAbsorptionAtRest, ordDefault);
#else
   G4String prcNam;
   pmanager->AddRestProcess(
                              new G4PiMinusAbsorptionAtRest(
                                                          prcNam="PiMinusAbsorptionAtRest"),
ordDefault);
#endif
  }
  else if (particleName == "kaon+") {
   pmanager->AddDiscreteProcess(theElasticProcess);
   G4KaonPlusInelasticProcess* theInelasticProcess =
        new G4KaonPlusInelasticProcess("inelastic");
   G4LEKaonPlusInelastic* theLEInelasticModel =
        new G4LEKaonPlusInelastic;
   theInelasticProcess->RegisterMe(theLEInelasticModel);
   G4HEKaonPlusInelastic* theHEInelasticModel =
        new G4HEKaonPlusInelastic;
   theInelasticProcess->RegisterMe(theHEInelasticModel);
   pmanager->AddDiscreteProcess(theInelasticProcess);
  }
  else if (particleName == "kaon0S") {
   pmanager->AddDiscreteProcess(theElasticProcess);
   G4KaonZeroSInelasticProcess* theInelasticProcess =
        new G4KaonZeroSInelasticProcess("inelastic");
```

```
    G4LEKaonZeroSInelastic* theLEInelasticModel =
          new G4LEKaonZeroSInelastic;
    theInelasticProcess->RegisterMe(theLEInelasticModel);
    G4HEKaonZeroInelastic* theHEInelasticModel =
          new G4HEKaonZeroInelastic;
    theInelasticProcess->RegisterMe(theHEInelasticModel);
    pmanager->AddDiscreteProcess(theInelasticProcess);
   }
   else if (particleName == "kaon0L") {
    pmanager->AddDiscreteProcess(theElasticProcess);
    G4KaonZeroLInelasticProcess* theInelasticProcess =
          new G4KaonZeroLInelasticProcess("inelastic");
    G4LEKaonZeroLInelastic* theLEInelasticModel =
          new G4LEKaonZeroLInelastic;
    theInelasticProcess->RegisterMe(theLEInelasticModel);
    G4HEKaonZeroInelastic* theHEInelasticModel =
          new G4HEKaonZeroInelastic;
    theInelasticProcess->RegisterMe(theHEInelasticModel);
    pmanager->AddDiscreteProcess(theInelasticProcess);
   }
   else if (particleName == "kaon-") {
    pmanager->AddDiscreteProcess(theElasticProcess);
    G4KaonMinusInelasticProcess* theInelasticProcess =
          new G4KaonMinusInelasticProcess("inelastic");
    G4LEKaonMinusInelastic* theLEInelasticModel =
          new G4LEKaonMinusInelastic;
    theInelasticProcess->RegisterMe(theLEInelasticModel);
    G4HEKaonMinusInelastic* theHEInelasticModel =
          new G4HEKaonMinusInelastic;
    theInelasticProcess->RegisterMe(theHEInelasticModel);
    pmanager->AddDiscreteProcess(theInelasticProcess);
#ifdef TRIUMF_STOP_KMINUS
    pmanager->AddRestProcess(new G4KaonMinusAbsorption, ordDefault);
#else
    pmanager->AddRestProcess(new G4KaonMinusAbsorptionAtRest, ordDefault);
#endif
   }
   else if (particleName == "proton") {
    pmanager->AddDiscreteProcess(theElasticProcess);
    G4ProtonInelasticProcess* theInelasticProcess =
          new G4ProtonInelasticProcess("inelastic");
    G4LEProtonInelastic* theLEInelasticModel = new G4LEProtonInelastic;
    theInelasticProcess->RegisterMe(theLEInelasticModel);
    G4HEProtonInelastic* theHEInelasticModel = new G4HEProtonInelastic;
    theInelasticProcess->RegisterMe(theHEInelasticModel);
    pmanager->AddDiscreteProcess(theInelasticProcess);
    pmanager->AddProcess(new G4hLowEnergyIonisation,-1,2,2);

    /*
          G4MultipleScattering theProtonMult;
          pmanager->AddProcess(&theProtonMult);
          pmanager->SetProcessOrdering(&theProtonMult, idxAlongStep, 1);
          pmanager->SetProcessOrdering(&theProtonMult, idxPostStep, 1);
    */
   }
```

```
else if (particleName == "anti_proton") {
  pmanager->AddDiscreteProcess(theElasticProcess);
  G4AntiProtonInelasticProcess* theInelasticProcess =
        new G4AntiProtonInelasticProcess("inelastic");
  G4LEAntiProtonInelastic* theLEInelasticModel =
        new G4LEAntiProtonInelastic;
  theInelasticProcess->RegisterMe(theLEInelasticModel);
  G4HEAntiProtonInelastic* theHEInelasticModel =
        new G4HEAntiProtonInelastic;
  theInelasticProcess->RegisterMe(theHEInelasticModel);
  pmanager->AddDiscreteProcess(theInelasticProcess);
}
else if (particleName == "neutron") {

  G4cout << "Neutron Physics.." ;
  G4cout << "Inelastic.. " ;
  G4NeutronInelasticProcess* theInelasticProcess =
        new G4NeutronInelasticProcess("inelastic");
  G4LENeutronInelastic* theLEInelasticModel =
        new G4LENeutronInelastic;
  theLEInelasticModel->SetMinEnergy(19*MeV);
  theInelasticProcess->RegisterMe(theLEInelasticModel);

  G4NeutronHPInelastic * theLENeutronInelasticModel =
        new G4NeutronHPInelastic;
  theInelasticProcess->RegisterMe(theLENeutronInelasticModel);
  G4NeutronHPInelasticData * theNeutronData1 =
        new G4NeutronHPInelasticData;
  theInelasticProcess->AddDataSet(theNeutronData1);
  // pmanager->AddDiscreteProcess(theInelasticProcess);

  // #include "G4HENeutronInelastic.hh"

  G4HENeutronInelastic * theHENeutronInelasticModel =
        new G4HENeutronInelastic ;
  theInelasticProcess->RegisterMe(theHENeutronInelasticModel);
  theHENeutronInelasticModel->SetMinEnergy(20*GeV);
  pmanager->AddDiscreteProcess(theInelasticProcess);

  G4cout << "Elastic.. " ;
  G4HadronElasticProcess* theNeutronElasticProcess =
        new G4HadronElasticProcess;
  G4LElastic* theNeutronElasticModel = new G4LElastic;
  G4NeutronHPElastic * theElasticNeutron = new G4NeutronHPElastic;
  theNeutronElasticProcess->RegisterMe(theNeutronElasticModel);
  theNeutronElasticModel->SetMinEnergy(19*MeV);
  theNeutronElasticProcess->RegisterMe(theElasticNeutron);
  G4NeutronHPElasticData* theNeutronData = new G4NeutronHPElasticData;
  theNeutronElasticProcess->AddDataSet(theNeutronData);
  pmanager->AddDiscreteProcess(theNeutronElasticProcess);

  G4cout << "Capture and Fission. " << G4endl ;
  // Capture
  G4HadronCaptureProcess* theNeutronCapture = new G4HadronCaptureProcess;
  G4LCapture* theNeutronCaptureModel = new G4LCapture;
```

```
  theNeutronCaptureModel->SetMinEnergy(19*MeV);
  theNeutronCapture->RegisterMe(theNeutronCaptureModel);

  G4NeutronHPCapture * theLENeutronCaptureModel = new G4NeutronHPCapture;
  theNeutronCapture->RegisterMe(theLENeutronCaptureModel);
  G4NeutronHPCaptureData * theNeutronData3 = new G4NeutronHPCaptureData;
  theNeutronCapture->AddDataSet(theNeutronData3);
  pmanager->AddDiscreteProcess(theNeutronCapture);

  // Fission
  G4LFission* theNeutronFissionModel = new G4LFission ;
  G4HadronFissionProcess* theNeutronFission = new G4HadronFissionProcess;
  theNeutronFission->RegisterMe(theNeutronFissionModel);
  pmanager->AddDiscreteProcess(theNeutronFission);

 }
 else if (particleName == "anti_neutron") {
  pmanager->AddDiscreteProcess(theElasticProcess);
  G4AntiNeutronInelasticProcess* theInelasticProcess =
        new G4AntiNeutronInelasticProcess("inelastic");
  G4LEAntiNeutronInelastic* theLEInelasticModel =
        new G4LEAntiNeutronInelastic;
  theInelasticProcess->RegisterMe(theLEInelasticModel);
  G4HEAntiNeutronInelastic* theHEInelasticModel =
        new G4HEAntiNeutronInelastic;
  theInelasticProcess->RegisterMe(theHEInelasticModel);
  pmanager->AddDiscreteProcess(theInelasticProcess);
 }
 else if (particleName == "lambda") {
  pmanager->AddDiscreteProcess(theElasticProcess);
  G4LambdaInelasticProcess* theInelasticProcess =
        new G4LambdaInelasticProcess("inelastic");
  G4LELambdaInelastic* theLEInelasticModel = new G4LELambdaInelastic;
  theInelasticProcess->RegisterMe(theLEInelasticModel);
  G4HELambdaInelastic* theHEInelasticModel = new G4HELambdaInelastic;
  theInelasticProcess->RegisterMe(theHEInelasticModel);
  pmanager->AddDiscreteProcess(theInelasticProcess);
 }
 else if (particleName == "anti_lambda") {
  pmanager->AddDiscreteProcess(theElasticProcess);
  G4AntiLambdaInelasticProcess* theInelasticProcess =
        new G4AntiLambdaInelasticProcess("inelastic");
  G4LEAntiLambdaInelastic* theLEInelasticModel =
        new G4LEAntiLambdaInelastic;
  theInelasticProcess->RegisterMe(theLEInelasticModel);
  G4HEAntiLambdaInelastic* theHEInelasticModel =
        new G4HEAntiLambdaInelastic;
  theInelasticProcess->RegisterMe(theHEInelasticModel);
  pmanager->AddDiscreteProcess(theInelasticProcess);
 }
 else if (particleName == "sigma+") {
  pmanager->AddDiscreteProcess(theElasticProcess);
  G4SigmaPlusInelasticProcess* theInelasticProcess =
        new G4SigmaPlusInelasticProcess("inelastic");
  G4LESigmaPlusInelastic* theLEInelasticModel =
```

```
        new G4LESigmaPlusInelastic;
  theInelasticProcess->RegisterMe(theLEInelasticModel);
  G4HESigmaPlusInelastic* theHEInelasticModel =
        new G4HESigmaPlusInelastic;
  theInelasticProcess->RegisterMe(theHEInelasticModel);
  pmanager->AddDiscreteProcess(theInelasticProcess);
 }
 else if (particleName == "sigma-") {
  pmanager->AddDiscreteProcess(theElasticProcess);
  G4SigmaMinusInelasticProcess* theInelasticProcess =
        new G4SigmaMinusInelasticProcess("inelastic");
  G4LESigmaMinusInelastic* theLEInelasticModel =
        new G4LESigmaMinusInelastic;
  theInelasticProcess->RegisterMe(theLEInelasticModel);
  G4HESigmaMinusInelastic* theHEInelasticModel =
        new G4HESigmaMinusInelastic;
  theInelasticProcess->RegisterMe(theHEInelasticModel);
  pmanager->AddDiscreteProcess(theInelasticProcess);
 }
 else if (particleName == "anti_sigma+") {
  pmanager->AddDiscreteProcess(theElasticProcess);
  G4AntiSigmaPlusInelasticProcess* theInelasticProcess =
        new G4AntiSigmaPlusInelasticProcess("inelastic");
  G4LEAntiSigmaPlusInelastic* theLEInelasticModel =
        new G4LEAntiSigmaPlusInelastic;
  theInelasticProcess->RegisterMe(theLEInelasticModel);
  G4HEAntiSigmaPlusInelastic* theHEInelasticModel =
        new G4HEAntiSigmaPlusInelastic;
  theInelasticProcess->RegisterMe(theHEInelasticModel);
  pmanager->AddDiscreteProcess(theInelasticProcess);
 }
 else if (particleName == "anti_sigma-") {
  pmanager->AddDiscreteProcess(theElasticProcess);
  G4AntiSigmaMinusInelasticProcess* theInelasticProcess =
        new G4AntiSigmaMinusInelasticProcess("inelastic");
  G4LEAntiSigmaMinusInelastic* theLEInelasticModel =
        new G4LEAntiSigmaMinusInelastic;
  theInelasticProcess->RegisterMe(theLEInelasticModel);
  G4HEAntiSigmaMinusInelastic* theHEInelasticModel =
        new G4HEAntiSigmaMinusInelastic;
  theInelasticProcess->RegisterMe(theHEInelasticModel);
  pmanager->AddDiscreteProcess(theInelasticProcess);
 }
 else if (particleName == "xi0") {
  pmanager->AddDiscreteProcess(theElasticProcess);
  G4XiZeroInelasticProcess* theInelasticProcess =
        new G4XiZeroInelasticProcess("inelastic");
  G4LEXiZeroInelastic* theLEInelasticModel =
        new G4LEXiZeroInelastic;
  theInelasticProcess->RegisterMe(theLEInelasticModel);
  G4HEXiZeroInelastic* theHEInelasticModel =
        new G4HEXiZeroInelastic;
  theInelasticProcess->RegisterMe(theHEInelasticModel);
  pmanager->AddDiscreteProcess(theInelasticProcess);
 }
```

```
else if (particleName == "xi-") {
  pmanager->AddDiscreteProcess(theElasticProcess);
  G4XiMinusInelasticProcess* theInelasticProcess =
        new G4XiMinusInelasticProcess("inelastic");
  G4LEXiMinusInelastic* theLEInelasticModel =
        new G4LEXiMinusInelastic;
  theInelasticProcess->RegisterMe(theLEInelasticModel);
  G4HEXiMinusInelastic* theHEInelasticModel =
        new G4HEXiMinusInelastic;
  theInelasticProcess->RegisterMe(theHEInelasticModel);
  pmanager->AddDiscreteProcess(theInelasticProcess);
}
else if (particleName == "anti_xi0") {
  pmanager->AddDiscreteProcess(theElasticProcess);
  G4AntiXiZeroInelasticProcess* theInelasticProcess =
        new G4AntiXiZeroInelasticProcess("inelastic");
  G4LEAntiXiZeroInelastic* theLEInelasticModel =
        new G4LEAntiXiZeroInelastic;
  theInelasticProcess->RegisterMe(theLEInelasticModel);
  G4HEAntiXiZeroInelastic* theHEInelasticModel =
        new G4HEAntiXiZeroInelastic;
  theInelasticProcess->RegisterMe(theHEInelasticModel);
  pmanager->AddDiscreteProcess(theInelasticProcess);
}
else if (particleName == "anti_xi-") {
  pmanager->AddDiscreteProcess(theElasticProcess);
  G4AntiXiMinusInelasticProcess* theInelasticProcess =
        new G4AntiXiMinusInelasticProcess("inelastic");
  G4LEAntiXiMinusInelastic* theLEInelasticModel =
        new G4LEAntiXiMinusInelastic;
  theInelasticProcess->RegisterMe(theLEInelasticModel);
  G4HEAntiXiMinusInelastic* theHEInelasticModel =
        new G4HEAntiXiMinusInelastic;
  theInelasticProcess->RegisterMe(theHEInelasticModel);
  pmanager->AddDiscreteProcess(theInelasticProcess);
}
else if (particleName == "deuteron") {
  pmanager->AddDiscreteProcess(theElasticProcess);
  G4DeuteronInelasticProcess* theInelasticProcess =
        new G4DeuteronInelasticProcess("inelastic");
  G4LEDeuteronInelastic* theLEInelasticModel =
        new G4LEDeuteronInelastic;
  theInelasticProcess->RegisterMe(theLEInelasticModel);
  pmanager->AddDiscreteProcess(theInelasticProcess);
}
else if (particleName == "triton") {
  pmanager->AddDiscreteProcess(theElasticProcess);
  G4TritonInelasticProcess* theInelasticProcess =
        new G4TritonInelasticProcess("inelastic");
  G4LETritonInelastic* theLEInelasticModel =
        new G4LETritonInelastic;
  theInelasticProcess->RegisterMe(theLEInelasticModel);
  pmanager->AddDiscreteProcess(theInelasticProcess);
}
else if (particleName == "alpha") {
```

```
    pmanager->AddDiscreteProcess(theElasticProcess);
    G4AlphaInelasticProcess* theInelasticProcess =
          new G4AlphaInelasticProcess("inelastic");
    G4LEAlphaInelastic* theLEInelasticModel =
          new G4LEAlphaInelastic;
    theInelasticProcess->RegisterMe(theLEInelasticModel);
    pmanager->AddDiscreteProcess(theInelasticProcess);
   }
   else if (particleName == "omega-") {
    pmanager->AddDiscreteProcess(theElasticProcess);
    G4OmegaMinusInelasticProcess* theInelasticProcess =
          new G4OmegaMinusInelasticProcess("inelastic");
    G4LEOmegaMinusInelastic* theLEInelasticModel =
          new G4LEOmegaMinusInelastic;
    theInelasticProcess->RegisterMe(theLEInelasticModel);
    G4HEOmegaMinusInelastic* theHEInelasticModel =
          new G4HEOmegaMinusInelastic;
    theInelasticProcess->RegisterMe(theHEInelasticModel);
    pmanager->AddDiscreteProcess(theInelasticProcess);
   }
   else if (particleName == "anti_omega-") {
    pmanager->AddDiscreteProcess(theElasticProcess);
    G4AntiOmegaMinusInelasticProcess* theInelasticProcess =
          new G4AntiOmegaMinusInelasticProcess("inelastic");
    G4LEAntiOmegaMinusInelastic* theLEInelasticModel =
          new G4LEAntiOmegaMinusInelastic;
    theInelasticProcess->RegisterMe(theLEInelasticModel);
    G4HEAntiOmegaMinusInelastic* theHEInelasticModel =
          new G4HEAntiOmegaMinusInelastic;
    theInelasticProcess->RegisterMe(theHEInelasticModel);
    pmanager->AddDiscreteProcess(theInelasticProcess);
   }
  }
}

void    PIMPPhysicsList::SetCutForGamma(G4double cut)
{
 ResetCuts();
 cutForGamma = cut;
}

void    PIMPPhysicsList::SetCutForElectron(G4double cut)
{
 ResetCuts();
 cutForElectron = cut;
}

void    PIMPPhysicsList::SetCutForProton(G4double cut)
{
 ResetCuts();
 cutForProton = cut;
}

G4double  PIMPPhysicsList::GetCutForGamma() const
{
```

```
 return cutForGamma;
}

G4double  PIMPPhysicsList::GetCutForElectron() const
{
 return cutForElectron;
}

G4double  PIMPPhysicsList::GetCutForProton() const
{
 return cutForProton;
}

void PIMPPhysicsList::ConstructAllShortLiveds()
{
 G4ShortLivedConstructor pConstructor;
 pConstructor.ConstructParticle();
}

void PIMPPhysicsList::ConstructAllIons()
{
 G4IonConstructor pConstructor;
 pConstructor.ConstructParticle();
}
```

Appendix B

Crab Observation SCW List

SCW	RA (Degrees)	DEC (Degrees)	GTI (Seconds)	ROLL (Degrees)	Off-axis Distance (Degrees)
036500810010	83.77054167	21.95883333	556	-88.18929009	0
036500790010	83.77045833	21.95852778	2939	-88.19316383	0.000317
036500790020	83.77045833	21.95852778	2843	-88.19316383	0.000317
036500790030	83.77045833	21.95852778	2405	-88.19316383	0.000317
030000160010	83.48995833	22.06263889	1751	92.26215774	0.29917
042201010010	83.488375	22.06794444	2757	92.2281075	0.302528
042201010020	83.488375	22.06794444	2745	92.2281075	0.302528
042201010030	83.488375	22.06794444	2300	92.2281075	0.302528
042200280010	83.48833333	22.06808333	1349	92.27278054	0.302617
042200900010	83.48804167	22.06761111	2764	92.24884047	0.302719
042200900020	83.48804167	22.06761111	2749	92.24884047	0.302719
042200900030	83.48804167	22.06761111	2300	92.24884047	0.302719
042200520010	83.48820833	22.06808333	1352	92.2712241	0.302734
010200360010	83.49325	21.94763889	624	-86.75281732	0.277518
042201120010	83.48770833	22.06833333	2756	92.19971596	0.30329
042201120020	83.48770833	22.06833333	2741	92.19971596	0.30329
042201120030	83.48770833	22.06833333	8208	92.19971596	0.30329
042201120040	83.48770833	22.06833333	1424	92.19971596	0.30329
030000300010	83.487	22.06866667	315	92.2474874	0.304071
010300010010	83.49395833	21.94419444	649	-86.73963824	0.27697
036500780010	83.79045833	22.05188889	619	-88.15830661	0.095163
030000290010	83.48595833	22.08413889	663	92.2502457	0.310949

SCW	RA (Degrees)	DEC (Degrees)	GTI (Seconds)	ROLL (Degrees)	Off-axis Distance (Degrees)
030000430010	83.52945833	22.15675	304	92.25261669	0.311917
030000340010	83.48070833	22.12455556	306	92.2623526	0.333867
030000370010	83.44441667	21.98155556	301	92.23793184	0.326916
030000360010	83.43895833	22.03655556	304	92.25550005	0.34057
030000350010	83.43133333	22.09161111	324	92.27390276	0.364269
030000440010	83.47466667	22.1795	303	92.27756605	0.369101
030000480010	83.390125	22.00352778	370	92.26164238	0.383033
030000450010	83.42525	22.14666667	304	92.28913521	0.393075
030000470010	83.383375	22.05863889	303	92.27993242	0.399824
030000460010	83.377875	22.11447222	303	92.2979587	0.422387
023900010010	83.49458333	22.26277778	577	-87.70458183	0.41053
042200800010	83.98175	21.86625	1831	92.01304431	0.230609
042200790010	83.54645833	21.57097222	1811	92.09816109	0.447939
042200750010	83.924125	22.36261111	1818	92.17248601	0.432
004400890010	83.65895833	21.51516667	5015	93.18093484	0.457483
023900100010	84.20595833	22.01925	1997	-88.04548988	0.439588
042200760010	83.42945833	22.56530556	1810	92.41981983	0.695806
042200780010	83.05429167	21.77227778	1807	92.34305973	0.740147
023900040010	83.45695833	22.66038889	2000	-87.6253835	0.76845
042200770010	82.99308333	22.26908333	1816	92.50728214	0.837076
023900080010	83.516375	21.32775	2000	-87.91123433	0.680343
023900110010	84.17970833	22.68563889	1999	-87.91733458	0.834065
023900060010	82.76858333	21.96469444	1998	-87.49917385	1.001975
023900090010	84.23104167	21.35313889	1996	-88.17397415	0.760872
042201090010	84.20766667	21.325	1750	91.7194083	0.76995
042201100010	84.42016667	21.56711111	1756	91.70581876	0.75859
042201080010	83.92495833	21.15458333	1758	91.77901053	0.81894
042201110010	84.54275	21.85805556	1758	91.73755743	0.778757
042201070010	83.60116667	21.07458333	1758	91.87766997	0.900325
042200910010	84.562	22.16766667	1766	91.8559725	0.818546
042200920010	84.47641667	22.47030556	1763	91.96833938	0.871701
042200930010	84.293875	22.73430556	1766	92.11030245	0.93554
042201060010	83.26675	21.08986111	1756	92.00933004	1.004449
042200940010	84.03195833	22.93238889	1764	92.26579259	1.008042
017000400010	83.729	23.03480556	1975	92.49193621	1.076774
004500300010	83.89408333	21.02038889	2190	93.19853115	0.946541
042200950010	83.71445833	23.04502778	1767	92.42326728	1.087641
042201050010	82.95304167	21.20172222	1751	92.15957273	1.114237
004400640010	82.555125	22.01869444	2192	93.41789353	1.21689
042200960010	83.37529167	23.06213889	1761	92.56406523	1.171967
004400630010	84.7125	22.03230556	3020	92.65307183	0.944819
023900050010	82.7365	22.63047222	1996	-87.35024635	1.233021
023900070010	82.80166667	21.29894444	2000	-87.64910459	1.172251
042201040010	82.69054167	21.39733333	1755	92.31906433	1.217244
042200970010	83.04633333	22.98047222	1760	92.67079939	1.252287
042200980010	82.76241667	22.80941667	1761	92.73390679	1.319018
042201030010	82.50508333	21.65883333	1759	92.47125406	1.300533

SCW	RA (Degrees)	DEC (Degrees)	GTI (Seconds)	ROLL (Degrees)	Off-axis Distance (Degrees)
042200990010	82.550625	22.56511111	1761	92.7431319	1.362266
042201020010	82.41566667	21.95977778	1751	92.59858667	1.354875
017000390010	84.85708333	22.07880556	1978	92.22547009	1.093145
042201000010	82.43129167	22.27266667	1763	92.69999158	1.37553
023900250010	84.92454167	22.04169444	2000	-88.33991163	1.156971
023900130010	83.42745833	23.3255	2002	-87.50094625	1.409072
023900210010	83.54533333	20.66175	2001	-88.07934124	1.316489
023900120010	84.153375	23.35130556	2001	-87.78789776	1.44414
023900260010	84.90170833	22.70730556	1996	-88.21571743	1.356373
023900240010	84.946375	21.37619444	2000	-88.46335258	1.31227
023900220010	84.257	20.68761111	1997	-88.33188463	1.36112
004400940010	83.65925	23.51544444	2035	92.47875596	1.560585
023900140010	82.702375	23.29591667	1997	-87.21392231	1.711365
023900170010	82.05108333	21.933	2002	-87.25192113	1.719652
023900200010	82.83291667	20.63333333	2001	-87.82660624	1.623604
023900180010	82.08675	21.26736111	1997	-87.41372656	1.820244
023900160010	82.01420833	22.59841667	2000	-87.09021942	1.869164
042200870010	81.90845833	21.93688889	2204	88.17492974	1.862213
042200890010	81.90833333	21.93694444	714	92.87629733	1.862337
042200880010	81.90816667	21.93688889	411	97.56915524	1.862504
023900270010	84.879375	23.37388889	1998	-88.09068417	1.797747
024200110010	85.48395833	21.90769444	3828	-88.78047725	1.71418
023900230010	84.96879167	20.70888889	1999	-88.5844898	1.731521
042200660010	84.345875	20.23544444	1350	91.46753549	1.816887
042200670010	84.609875	20.36361111	1358	91.40611005	1.802558
042200650010	84.06545833	20.14319444	1352	91.54312085	1.839435
042200680010	84.85366667	20.5245	1352	91.35984098	1.797351
030000150010	83.99383333	20.11911111	1721	91.56053387	1.853223
042200640010	83.77391667	20.08691667	1356	91.63230095	1.87192
042200690010	85.07075	20.71608333	2771	91.32727958	1.798602
042200630010	83.47733333	20.06969444	1354	91.73132806	1.911758
042200700010	85.25833333	20.93383333	1351	91.31346149	1.806696
042200710010	85.41229167	21.17333333	1347	91.3126014	1.819987
017000820010	83.77929167	20.04566667	1764	92.8749569	1.913187
042200620010	83.18175	20.08938889	1350	91.842208	1.959974
042200720010	85.52870833	21.42991667	1354	91.32838143	1.836002
010200160010	83.484125	23.99430556	2200	-87.99244653	2.055525
023900790010	83.39995833	23.99177778	1796	-87.34852782	2.066445
042200130010	83.98729167	20.051	1731	91.7120106	1.920106
042200730010	85.606125	21.69972222	1354	91.36498472	1.853781
036501000010	81.68525	21.56611111	1799	-87.46139719	2.12195
004300650010	83.63304167	24.01444444	2191	92.29314513	2.060205
004400330010	83.63295833	24.0145	2194	92.27065517	2.060266
004400090010	83.633	20.01433333	2194	93.80101722	1.949358
004300410010	83.632875	20.01427778	2190	93.95119363	1.949423
004400190010	83.63304167	24.01472222	2190	92.26974819	2.060482
004300510010	83.63325	24.01475	2193	92.29265231	2.060496

SCW	RA (Degrees)	DEC (Degrees)	GTI (Seconds)	ROLL (Degrees)	Off-axis Distance (Degrees)
004400430010	83.63283333	20.01413889	2196	93.80249697	1.949564
004300750010	83.63270833	20.01413889	2195	93.86321087	1.949573
004300250010	83.51316667	24.0115	2187	93.18107794	2.068739
004300290010	83.74916667	20.01719444	2192	93.09201777	1.941757
004300110010	83.51354167	24.01158333	2193	93.1804806	2.068775
004300080010	83.749125	20.01713889	2192	93.09281119	1.941813
004300150010	83.74925	20.01713889	2193	93.0927093	1.941811
004300220010	83.74925	20.01713889	2188	93.0928972	1.941811
004300320010	83.51333333	24.01161111	2191	93.18025347	2.068829
004300180010	83.51341667	24.01163889	2191	93.18266727	2.068846
036500940010	83.27858333	23.98586111	1780	-86.97054439	2.085873
042200190010	85.5885	22.44919444	1759	91.67739781	1.88293
042200610010	82.89020833	20.14794444	1353	91.96084495	2.013531
042200740010	85.64304167	21.97680556	1357	91.41582457	1.872586
017000860010	81.62295833	22.01772222	1766	93.41028175	2.148391
010200220010	85.64425	21.97930556	2201	-87.47792686	1.87382
017000950010	81.62066667	22.0135	1776	93.40957504	2.15057
023900850010	85.645625	22.05608333	1752	-88.64042131	1.877604
042200350010	84.78675	23.66891667	1363	92.15724276	1.989237
042200360010	84.53079167	23.82169444	1359	92.29805474	2.012022
023900830010	83.57158333	19.99619444	1869	-88.31077297	1.972698
023900840010	83.57158333	19.99619444	788	-88.31077297	1.972698
042200290010	85.63970833	22.24352778	1360	91.49029404	1.890723
042200340010	85.0165	23.48641667	1360	92.01951167	1.971274
042200370010	84.25325	23.93841667	1359	92.44255408	2.037586
042200330010	85.21558333	23.27475	1360	91.88894082	1.954426
042200300010	85.59391667	22.51938889	1357	91.56872261	1.907595
042200320010	85.38045833	23.03997222	1364	91.77029291	1.939251
042200310010	85.50658333	22.78608333	1362	91.66284195	1.923066
030000210010	85.59570833	22.53011111	1772	91.56462208	1.912483
036500960010	84.2665	20.08652778	1741	-89.1010203	1.93688
042200380010	83.961	24.01888889	1355	92.58535907	2.068841
010200260010	83.48933333	19.98816667	2199	-85.50282148	1.990629
042200150010	82.9735	23.93588889	1779	93.08289509	2.131672
017000800010	83.783	24.04377778	1778	92.3356704	2.084982
042200600010	82.61095833	20.24394444	1354	92.08858451	2.070139
042200390010	83.65920833	24.06052778	1357	92.72189461	2.104641
042200400010	83.35304167	24.06325	1356	92.85130285	2.145431
023900190010	82.12229167	20.60255556	1998	-87.57486305	2.13453
046800040010	84.48245833	23.90372222	2209	-88.11243302	2.071091
023900150010	81.97770833	23.26455556	1999	-86.92810015	2.217918
042200590010	82.3475	20.37572222	1354	92.22207656	2.128682
042200410010	83.04991667	24.02586111	1354	92.9690739	2.189042
042200830010	81.97266667	20.73827778	2302	92.84895162	2.173042
030000170010	82.97320833	24.01011111	1796	93.0026341	2.200791
004300160010	81.840125	20.91147222	2193	93.79209377	2.196241
004300090010	81.83995833	20.91152778	2197	93.7919558	2.196361

SCW	RA (Degrees)	DEC (Degrees)	GTI (Seconds)	ROLL (Degrees)	Off-axis Distance (Degrees)
004300300010	81.83995833	20.91152778	2193	93.7920965	2.196361
004300230010	81.83991667	20.9115	2197	93.79164335	2.196411
042200840010	81.842875	23.13558333	663	92.8974418	2.25846
046800030010	84.487375	23.95225	574	-88.14789926	2.118386
004300130010	85.45370833	23.09761111	2192	92.43540504	2.032207
004300270010	85.45370833	23.09766667	2192	92.43589779	2.032238
004300060010	85.45370833	23.09777778	2189	92.43556879	2.0323
004300200010	85.45375	23.09777778	2189	92.43620712	2.032335
004300280010	85.545	21.09952778	2163	92.43252686	1.971575
004300140010	85.54504167	21.09952778	2163	92.43262118	1.971613
004300070010	85.54491667	21.09919444	2158	92.43335289	1.971645
004300210010	85.54508333	21.09925	2159	92.43434943	1.971771
042200580010	82.10658333	20.53955556	1350	92.35654193	2.187031
042200420010	82.75554167	23.94972222	1354	93.0719306	2.234695
004500310010	81.75175	21.00977778	2191	93.93374905	2.230746
004300310010	81.696	22.90719444	2163	93.87425434	2.281033
004300100010	81.69595833	22.90711111	2158	93.87533248	2.281036
004300170010	81.69595833	22.90711111	2162	93.8737904	2.281036
004300240010	81.69591667	22.90711111	2159	93.8746058	2.281074
004400390010	85.790125	22.00061111	2189	92.27308319	2.020015
004400130010	85.790125	21.99983333	2194	92.27361529	2.019999
004300450010	85.79029167	21.99980556	2192	92.36376454	2.020166
004300710010	85.79033333	22.00063889	2193	92.35394048	2.020224
004400370010	81.47595833	22.00038889	2194	93.808137	2.29496
004400150010	81.47583333	22.00005556	2195	93.80870608	2.295079
004300470010	81.47575	22.00005556	2194	93.89019848	2.295162
004300690010	81.47566667	22.00030556	2192	93.88079637	2.29525
042200430010	82.476625	23.83747222	1354	93.15913521	2.281119
042200570010	81.891125	20.73163889	1351	92.49271327	2.244596
042200440010	82.21770833	23.68933333	1356	93.22490819	2.325064
042200560010	81.70591667	20.95152778	1352	92.62661071	2.297246
042200450010	81.98483333	23.50902778	1355	93.27158996	2.364711
004400880010	85.80883333	21.50116667	2194	92.43258914	2.089041
042200550010	81.55416667	21.19197222	1356	92.7562981	2.345292
004400570010	82.58383333	20.0185	2195	94.08676747	2.27446
042200460010	81.78179167	23.302	1351	93.29275803	2.399838
004400580010	84.71266667	20.03244444	2196	93.40040661	2.144429
042200540010	81.440125	21.45005556	1352	92.87742458	2.385309
030000110010	81.39729167	21.58469444	1795	92.92697676	2.40256
042200470010	81.6135	23.07061111	1359	93.29539095	2.426701
004400670010	82.52620833	24.01419444	2153	92.76673409	2.402681
042200530010	81.365375	21.72080556	1355	92.9872564	2.416916
004400680010	84.71275	24.03269444	2193	91.9020446	2.277862
042200090010	81.39725	21.51083333	1777	93.04394917	2.415205
042200480010	81.481875	22.818	1358	93.27562274	2.444619
036500900010	85.88579167	22.47463889	1788	-88.6917486	2.177232
042200510010	81.33191667	21.99761111	1354	93.08635235	2.438933

SCW	RA (Degrees)	DEC (Degrees)	GTI (Seconds)	ROLL (Degrees)	Off-axis Distance (Degrees)
010200200010	81.33058333	21.97547222	2155	-86.00511202	2.440015
023900810010	81.33308333	21.89936111	1799	-87.02447233	2.438184
017000760010	85.93658333	22.02030556	2613	91.83040384	2.166914
042200490010	81.39033333	22.55225	1355	93.23058146	2.453066
042200500010	81.33925	22.27713889	1352	93.16793506	2.452039
004500290010	86.036375	21.00972222	2196	92.46820838	2.456586
004400930010	81.47820833	23.50136111	731	93.32041359	2.763003
035200310010	84.92095833	24.33419444	3573	-88.84642744	2.63928
035200170010	84.92091667	24.33422222	3573	-88.84649378	2.639287
035200240010	84.92108333	24.33419444	3521	-88.84800131	2.639334
035200100010	84.921	24.33427778	3573	-88.83802757	2.639373
035200520010	84.92245833	24.33422222	3567	-88.7645144	2.639959
035200450010	84.92229167	24.33433333	3549	-88.78037545	2.639986
035200380010	84.92225	24.33438889	3572	-88.7899826	2.640018
035200590010	84.92225	24.33438889	5094	-88.74449423	2.640018
004400950010	85.840125	23.501	1905	91.63928081	2.580979
036500990010	82.19558333	19.62144444	1800	-88.59601567	2.818489
042200180010	85.107375	24.39736111	1740	92.30244428	2.780925
017000850010	81.650875	20.01783333	1762	93.59833279	2.874103
017000940010	81.64683333	20.01294444	1772	93.59742451	2.880386
023900860010	85.58629167	24.05861111	1799	-88.23395024	2.775971
030000220010	86.06925	20.57944444	1744	90.93547875	2.680816
010200150010	85.67354167	23.98219444	2195	-88.83687023	2.777661
010200250010	85.61858333	19.97747222	2144	-86.12845417	2.709437
042200200010	86.06095833	20.50008333	1716	91.08397175	2.715504
017000870010	81.5915	24.02358333	1796	93.21977279	3.001902
017000960010	81.59129167	24.02358333	1798	93.21997507	3.002053
030000200010	85.10608333	24.47855556	1737	92.22897983	2.851784
036501010010	81.159125	23.50802778	1796	-86.28282694	3.036363
030000120010	81.92316667	19.64777778	1797	92.15198626	2.958677
004400420010	85.76104167	20.00086111	2194	93.12920408	2.792086
004300740010	85.761375	20.00055556	2196	93.19152749	2.792538
004300400010	81.504875	20.00058333	2196	94.62598422	2.99466
004400080010	81.50470833	20.00055556	2192	94.4841709	2.994804
004300420010	85.7615	20.00027778	2193	93.28370034	2.792822
004400100010	85.761625	20.00033333	2196	93.12833237	2.792872
004300760010	81.50458333	20.00038889	2192	94.54055837	2.995008
004400440010	81.504625	20.00022222	2190	94.48369604	2.995085
004300500010	81.444875	23.99758333	2154	93.15118032	3.09277
004400180010	81.44420833	23.99708333	2157	93.13350843	3.092942
004400200010	85.82220833	24.00013889	2189	91.41118641	2.894178
004300640010	85.82216667	24.00030556	2191	91.43562448	2.894266
004400320010	85.822125	24.00036111	2194	91.4104848	2.894275
004300520010	85.82241667	24.00005556	2193	91.4364431	2.894267
004400340010	81.44358333	24.00022222	2195	93.13180678	3.095481
004300660010	81.443375	24.00027778	2191	93.15278451	3.095674
042200100010	81.92170833	19.5735	1774	92.30508329	3.017946

SCW	RA (Degrees)	DEC (Degrees)	GTI (Seconds)	ROLL (Degrees)	Off-axis Distance (Degrees)
036500910010	85.41891667	24.42830556	1752	-87.7000562	2.96908
004500250010	83.89429167	19.02086111	2192	93.84725676	2.940577
004500560010	83.997375	19.02366667	2192	93.73901689	2.943919
017000410010	83.62654167	25.03183333	1968	92.22002114	3.076372
017000750010	85.90508333	20.01325	1790	92.19464088	2.888176
023900820010	81.44804167	19.90313889	1799	-87.58961261	3.101594
010200170010	81.29504167	23.97827778	2199	-87.14407937	3.194723
010200270010	81.36129167	19.97283333	2197	-84.8678171	3.122288
023900800010	81.215125	23.89536111	1795	-86.45676035	3.20629
017000770010	85.971	24.01938889	1796	91.46144647	3.014615
036500890010	86.34575	20.51763889	1752	-89.64824135	2.951057
042200080010	80.85495833	23.44511111	1736	93.81802998	3.27256
030000100010	80.854375	23.52622222	1755	93.74164853	3.3107
004400650010	80.39845833	21.97586111	2193	94.19909168	3.372126
004400620010	86.87008333	22.01836111	2195	91.87995036	3.100113
004400830010	81.5375	19.50144444	1250	94.52924347	3.320427
004400850010	85.78104167	19.50133333	1338	93.20355097	3.175125
035200400010	82.985375	25.28736111	3572	-87.94292949	3.419881
035200470010	82.985375	25.28736111	3571	-87.92592645	3.419881
035200540010	82.98520833	25.28736111	3572	-87.90503669	3.419919
035200050010	82.98479167	25.28816667	3567	-87.9875435	3.420799
035200190010	82.98470833	25.28825	3572	-87.99465477	3.420899
035200330010	82.98470833	25.28830556	3572	-87.98193742	3.420953
035200260010	82.98475	25.28836111	3568	-87.99150006	3.420997
035200120010	82.98458333	25.28836111	3573	-87.99455651	3.421036
017000380010	87.013	22.14325	3534	91.40995913	3.247699
017000380020	87.013	22.14325	3485	91.40995913	3.247699
017000380030	87.013	22.14325	2918	91.40995913	3.247699
004500570010	81.88195833	19.01433333	2192	94.39154571	3.498118
004500040010	83.659125	25.51494444	2186	91.81021292	3.557856
004500240010	81.77879167	19.01019444	2197	94.49588523	3.558306
004200150020	86.32220833	19.72375	2773	93.50312225	3.392138
042200850010	80.07870833	21.84163889	2359	93.55414616	3.693693
004400560010	80.45833333	19.97111111	2145	94.77936145	3.86287
004400590010	86.84095833	20.01872222	2192	92.71725697	3.632009
004500260010	86.009625	19.00969444	2195	93.2035942	3.702825
004400660010	80.33620833	23.97094444	2149	93.63884508	3.980356
004400690010	86.90245833	24.01861111	2193	91.03550018	3.748545
004500550010	86.11295833	19.01455556	2196	93.09133216	3.762404
030000140010	84.477375	18.17977778	1799	90.89963645	3.84459
017000830010	83.77758333	18.04661111	1752	93.14570812	3.912229
010200110010	83.481625	25.99761111	2201	-89.24401421	4.049099
023900880010	83.309375	25.98827778	1800	-86.84579732	4.055749
023900510010	84.66566667	18.15233333	2000	-89.0155499	3.910331
042200120010	84.47379167	18.10508333	1780	91.08194705	3.917391
023900500010	84.94579167	18.23705556	2107	-89.08587584	3.902927
004300800010	83.633125	18.01466667	1457	94.64348817	3.94656

SCW	RA (Degrees)	DEC (Degrees)	GTI (Seconds)	ROLL (Degrees)	Off-axis Distance (Degrees)
004300360010	83.63291667	18.01466667	2762	94.79361888	3.946567
004400480010	83.63304167	18.01463889	2194	94.55959941	3.94659
004400040010	83.63275	18.01458333	2197	94.56048102	3.946656
004400240010	83.632875	26.01441667	2189	91.49737442	4.057919
004300560010	83.63270833	26.01441667	2192	91.46820886	4.057925
004300600010	83.63283333	26.01452778	2192	91.46810721	4.058032
004400280010	83.63308333	26.01461111	2193	91.49731446	4.058106
023900520010	84.38220833	18.085	2001	-88.94279651	3.921826
023900490010	85.21741667	18.34027778	2001	-89.15019183	3.8971
023900530010	84.09258333	18.03688889	1996	-88.86332587	3.935144
023900480010	85.48233333	18.4615	2000	-89.21088714	3.893786
036500930010	82.76754167	25.93055556	1800	-85.85336801	4.096411
023900540010	83.80175	18.00661111	1998	-88.78079232	3.952345
023900470010	85.737875	18.59855556	1998	-89.26523035	3.893824
023900960010	83.65429167	17.99838889	2579	-88.8007032	3.96215
023900460010	85.98404167	18.75269444	1996	-89.31763221	3.896012
023900550010	83.50945833	17.99563889	2001	-88.69320194	3.971785
017000790010	83.783625	26.03491667	1799	92.06179303	4.076104
023900450010	86.21791667	18.92191667	2001	-89.3629644	3.900321
010200310010	83.492	17.98575	3779	-84.2730324	3.982835
023900560010	83.216125	18.00419444	1994	-88.6022439	3.993313
036500970010	84.74195833	18.13430556	1761	-90.10982522	3.945968
023900440010	86.43991667	19.10591667	2000	-89.40323509	3.907006
042200160010	82.44520833	25.87863889	1719	93.82426785	4.137799
023900570010	82.92491667	18.03125	1996	-88.50474644	4.017585
023900430010	86.648125	19.30369444	1998	-89.4402735	3.915386
023900580010	82.63591667	18.07680556	1998	-88.40528628	4.044442
023900420010	86.84233333	19.51375	1996	-89.47132013	3.92611
023900590010	82.35025	18.14169444	2001	-88.30119827	4.07281
023900410010	87.020125	19.73813889	2000	-89.49564481	3.935896
023900400010	87.1825	19.97130556	2000	-89.51518198	3.948636
023900600010	82.07004167	18.22347222	2000	-88.19413074	4.10422
030000180010	82.44529167	25.94430556	1751	93.77673548	4.200033
023900390010	87.32670833	20.21505556	1998	-89.52792167	3.960692
004500050010	81.44316667	25.50105556	2193	92.74596264	4.238397
004400520010	84.715625	18.03947222	378	94.14360198	4.031696
004400530010	84.715625	18.03947222	3081	94.14360198	4.031696
023900380010	87.45329167	20.46797222	1996	-89.53563328	3.973074
023900610010	81.79683333	18.32430556	3196	-88.08325144	4.135857
004400540010	82.60916667	18.01897222	2195	94.74306251	4.107468
023900370010	87.56120833	20.72841667	2000	-89.53681983	3.985358
036501050010	79.60554167	21.06938889	1715	-86.90870666	4.258913
023900360010	87.64916667	20.99538889	2000	-89.52939189	3.996493
023900620010	81.53083333	18.44291667	1995	-87.9699129	4.168688
004500030010	85.87516667	25.50077778	2187	90.87864912	4.120051
023900350010	87.71791667	21.26725	1999	-89.51624988	4.0075
004500320010	79.60983333	20.97652778	2193	94.66816045	4.275093

SCW	RA (Degrees)	DEC (Degrees)	GTI (Seconds)	ROLL (Degrees)	Off-axis Distance (Degrees)
023900340010	87.76666667	21.54177778	1997	-89.49663835	4.017829
004400730010	84.71258333	26.03258333	2193	91.15870551	4.181254
004400740010	82.48666667	26.01791667	2191	92.12018141	4.257287
023900330010	87.79420833	21.81994444	2001	-89.46706842	4.026063
023901000010	87.79908333	22.09041667	1760	-89.44060015	4.03069
017000910010	79.46604167	21.98958333	1787	94.21008304	4.30461
010200230010	87.80008333	21.93819444	2199	-88.20242976	4.029595
023900320010	87.801375	22.099	2017	-89.43425684	4.03327
023900630010	81.2725	18.57788889	1997	-87.85327108	4.203689
042200240010	87.71308333	22.87863889	1745	90.93971436	4.048417
023900310010	87.812875	22.05083333	282	-89.44375342	4.04338
030000260010	87.70758333	22.94775	1778	90.83259178	4.059341
023900640010	81.02541667	18.72858333	1999	-87.73272793	4.23913
023900650010	80.78954167	18.89513889	2814	-87.6122491	4.274644
023900660010	80.56608333	19.07794444	1999	-87.48840255	4.309069
023900670010	80.35529167	19.27344444	1999	-87.36533206	4.344565
023900680010	80.15941667	19.48208333	2000	-87.24186569	4.378871
004400910010	79.36325	21.47025	2500	94.6580328	4.434291
004300680010	79.32245833	21.96408333	2199	94.64289651	4.448086
004400360010	79.322	21.96413889	2194	94.57619456	4.448545
004400400010	87.946125	21.95783333	2189	91.51430536	4.175583
004400120010	87.94625	21.95813889	2161	91.51417958	4.175708
004300720010	87.94625	21.95780556	2194	91.59767322	4.175708
004300440010	87.946375	21.95816667	2158	91.60996989	4.175833
004400160010	79.31958333	21.95791667	2190	94.58183482	4.450958
004300480010	79.31941667	21.95794444	2194	94.65879846	4.451125
023900690010	79.97908333	19.70311111	1995	-87.11930174	4.411739
023900700010	79.81441667	19.93577778	1997	-86.99503193	4.443386
004400870010	87.957375	21.46019444	2160	91.69130963	4.216422
023900710010	79.66770833	20.17847222	2000	-86.87286366	4.472463
023900720010	79.53820833	20.42922222	1999	-86.75322564	4.500262
023900730010	79.427125	20.68913889	2001	-86.63647728	4.525195
030000060010	79.32095833	21.07719444	1800	93.55232228	4.536086
023900740010	79.33620833	20.95463889	1997	-86.52664268	4.546616
042200040010	79.32166667	21.00316667	1778	93.67200623	4.550361
023900750010	79.26479167	21.22561111	1998	-86.41955852	4.565019
042200170010	84.60875	26.34652778	1777	92.96333052	4.467041
036500980010	82.69104167	17.67491667	1798	-89.68752753	4.417835
017000840010	81.67179167	18.02533333	1799	93.78599056	4.458382
023900760010	79.21283333	21.50002778	2001	-86.31817412	4.580743
023900920010	79.18466667	21.78397222	1755	-86.22278366	4.589208
023900770010	79.18291667	21.77805556	2001	-86.22374324	4.591185
030000230010	86.53283333	18.62975	1772	90.341713	4.325858
010200190010	79.17408333	21.93577778	2190	-85.25775046	4.596516
017000710010	88.09291667	21.97575	1793	91.04241007	4.322408
023900870010	85.528375	26.05194444	1763	-87.83035071	4.454608
036500850010	88.00958333	22.89375	1743	-89.36434082	4.340915

SCW	RA (Degrees)	DEC (Degrees)	GTI (Seconds)	ROLL (Degrees)	Off-axis Distance (Degrees)
030000130010	82.434	17.70833333	1802	91.41340628	4.455681
010200120010	85.70675	25.985	1617	-90.20484431	4.467541
023900970010	85.750875	18.06244444	1800	-89.44404636	4.370763
035200250010	84.879	26.33083333	3511	-88.80028737	4.510329
035200320010	84.87891667	26.33138889	3517	-88.7864919	4.510847
035200460010	84.88008333	26.33122222	3469	-88.74734104	4.510972
035200390010	84.8815	26.33102778	3516	-88.76948122	4.511132
035200530010	84.879875	26.33152778	3510	-88.72215097	4.511217
035200180010	84.88016667	26.33172222	3514	-88.81061116	4.511477
035200110010	84.88104167	26.33147222	3517	-88.81531556	4.51145
010200320010	85.598875	17.97227778	2145	-84.87649841	4.385821
035200040010	84.87891667	26.33402778	3567	-88.81256989	4.513405
030100150010	85.32554167	26.17975	2170	92.77628776	4.49824
004400790010	83.65908333	17.51522222	2194	94.54032086	4.445009
017000880010	81.55925	26.014	1753	93.02832255	4.618895
030000190010	84.60825	26.42086111	1797	92.92182259	4.539983
042200210010	86.526625	18.54883333	1760	90.5212728	4.384529
035200030010	84.886625	26.35419444	617	-88.81574357	4.534847
036501060010	80.14075	19.13130556	1563	-88.13692704	4.60112
004300810010	85.73591667	18.00097222	1666	94.06341557	4.418978
004400470010	81.53020833	18.00108333	2191	95.15440668	4.547843
004400490010	85.73616667	18.00091667	2198	93.97412814	4.419139
004300350010	85.73575	18.00052778	2196	94.21695123	4.419302
004400050010	81.53004167	18.00083333	2192	95.15427513	4.548143
004400030010	85.73591667	18.00047222	2194	93.97492421	4.419425
004300790010	81.52970833	18.00083333	1956	95.23648183	4.548307
004300370010	81.53004167	18.00061111	2192	95.36954569	4.548336
042200110010	82.435625	17.63316667	1724	91.60107959	4.526963
004300590010	81.40891667	25.99305556	2177	92.43120778	4.674636
004400270010	81.40995833	25.99544444	2155	92.4538396	4.676172
036500920010	84.94120833	26.38261111	1787	-86.66885456	4.576054
004400230010	85.85804167	25.99991667	2190	90.54238747	4.548407
004400250010	81.407625	25.99955556	2187	92.45392655	4.680899
004300570010	81.40754167	25.99958333	2192	92.42370253	4.680965
004300550010	85.85820833	25.99997222	2188	90.51338042	4.548533
004300610010	85.8585	25.99986111	2190	90.51421171	4.548569
004400290010	85.85854167	25.99991667	2193	90.54121624	4.548637
004400920010	79.29804167	23.45952778	2158	94.16570528	4.717557
036501020010	80.61379167	25.44466667	1854	-85.05946411	4.702776
036501030010	80.61379167	25.44466667	1236	-85.05946411	4.702776
017000740010	85.87820833	18.02222222	1794	92.55268389	4.465329
017000920010	79.52033333	19.98402778	1794	94.31876641	4.68659
042200250010	87.255625	24.83536111	1763	91.49382381	4.518874
023900950010	81.55816667	17.90791667	1795	-88.16163073	4.615683
010200240010	87.74516667	19.93530556	2197	-86.73706813	4.460079
023900990010	87.82708333	20.09275	1795	-89.76807421	4.465176
035200300010	86.817125	25.35405556	3573	-89.65423311	4.561711

SCW	RA (Degrees)	DEC (Degrees)	GTI (Seconds)	ROLL (Degrees)	Off-axis Distance (Degrees)
035200230010	86.81704167	25.35422222	3568	-89.66213162	4.561779
035200090010	86.81708333	25.35419444	3573	-89.66218182	4.561786
035200160010	86.81708333	25.35430556	3570	-89.66464738	4.561869
035200510010	86.81783333	25.35491667	3573	-89.583152	4.562825
035200580010	86.817625	25.35533333	3572	-89.55785716	4.562996
035200370010	86.81770833	25.35530556	3572	-89.6179796	4.563031
035200440010	86.817625	25.35538889	3569	-89.60291574	4.563037
004400960010	88.02045833	23.45944444	2054	90.80369576	4.507064
010200100010	81.26033333	25.97847222	2154	-88.2862061	4.739055
010200300010	81.389375	17.97077778	2196	-83.74019638	4.64484
023900890010	81.09283333	25.89186111	1799	-85.86536743	4.758028
030000270010	87.25833333	24.90363889	1789	91.41873853	4.564709
023901010010	87.77629167	24.09555556	1631	-89.10653169	4.540002
030000250010	88.1595	20.99158333	1741	90.27622157	4.494277
017000780010	86.01116667	26.01061111	1744	91.09935752	4.630044
010200140010	87.86316667	23.94788889	2165	-89.68165717	4.550376
042200230010	88.15966667	20.92316667	1713	90.41746937	4.509659
004500280010	88.18020833	20.97108333	2146	91.74421986	4.518939
017000900010	79.40333333	23.99305556	1752	94.09843047	4.817735
036500880010	86.79508333	18.56408333	1796	-90.5655095	4.546667
036501040010	79.05066667	23.00736111	1556	-85.63280062	4.834939
036501040020	79.05066667	23.00736111	1587	-85.63280062	4.834939
004400110010	87.88904167	19.95913889	2182	92.46225133	4.578299
004300430010	87.88904167	19.95886111	2179	92.62559403	4.57842
004300730010	87.88908333	19.95883333	3012	92.60179181	4.57847
004400410010	87.889125	19.95861111	2159	92.46249918	4.578604
004300770010	79.37683333	19.95872222	2193	95.22487798	4.827537
004400450010	79.37670833	19.95877778	2192	95.16975152	4.827628
004300390010	79.378875	19.95375	2994	95.31453686	4.827742
030000050010	79.87308333	19.14111111	1788	92.70460277	4.809339
042200070010	80.29879167	25.37775	1734	94.63278581	4.87258
042200030010	79.86775	19.07366667	1725	92.86295529	4.853449
004300490010	79.25708333	23.95113889	3594	94.01467729	4.933618
004400170010	79.25495833	23.95263889	2185	93.99506961	4.936168
004300670010	79.25783333	23.96119444	2195	94.00864965	4.937002
004300630010	88.01054167	23.957	2160	90.583929	4.687245
004400310010	88.01075	23.95680556	2162	90.55656303	4.687351
004400210010	88.01075	23.95738889	2189	90.55562741	4.6876
004300530010	88.01095833	23.95738889	2193	90.58421327	4.687788
004400350010	79.25679167	23.96069444	2198	93.98878081	4.937751
030000090010	80.29358333	25.45166667	1751	94.58909411	4.9284
017000720010	88.033625	19.97725	1800	91.48813558	4.701122
023900930010	79.32654167	19.78402778	1800	-86.87734972	4.947617
036500840010	87.56975	24.85166667	1795	-88.46524855	4.775193
030800030010	87.46025	19.02577778	620	88.14601334	4.713466
010200280010	79.23408333	19.92972222	2195	-84.22546673	4.969582
030800040010	87.42904167	18.92647222	2218	88.09033872	4.751825

SCW	RA (Degrees)	DEC (Degrees)	GTI (Seconds)	ROLL (Degrees)	Off-axis Distance (Degrees)
004500580010	79.76716667	18.98580556	2198	95.04714477	4.986573
010200180010	79.107125	23.93483333	2155	-86.2945094	5.064783
023900910010	79.03575	23.77908333	1759	-85.55400885	5.072629
036500860010	88.44166667	20.93136111	1771	-90.23569677	4.782793
004400820010	79.41841667	19.45425	2196	95.20137617	5.021347
017000700010	88.16245833	23.98041667	1780	90.58391485	4.834846
042200050010	78.7535	22.93055556	1784	94.52568294	5.110279
004400800010	81.561875	17.50161111	2198	95.12281182	4.974438

Bibliography

Agostinelli, S., J. Allison, K. Amako, et al. (2003). Geant4-a simulation toolkit. Nuclear Instruments and Methods in Physics Research A. **506:** 250-303.

Akerlof, C., R. Balsano, S. Barthelemy, et al. (1999). "Observation of contemporaneous optical radiation from a gamma-ray burst." Nature **398**: 400-402.

Aloy, M. A., E. Müller, J. M. Ibáñez, et al. (2000). Relativistic Jets from Collapsars. Astrophysical Journal. **531:** L119-L122.

Amako, K. (2000). "Present status of Geant4." Nuclear Instruments and Methods in Physics Research Section A: Accelerators, Spectrometers, Detectors and Associated Equipment **453**(1-2): 455-460.

Arques, M., N. Baffert, D. Lattard, et al. (1999). "A basic component for ISGRI, the CdTe gamma camera on board the INTEGRAL satellite." Nuclear Science, IEEE Transactions on **46**(3): 181-186.

Band, D., J. Matteson, L. Ford, et al. (1993). BATSE observations of gamma-ray burst spectra. I - Spectral diversity. Astrophysical Journal. **413:** 281-292.

Barkov, M. V. and G. S. Bisnovatyi-Kogan (2005). Infrared Afterglow of the Gamma Ray Burst GRB041219 as the Result of Reradiation from Dust in a Circumstellar Cloud. Astrophysics. **48:** 369-373.

Barr, P. and E. Kuulkers (2003). IBIS Observer Manual, ESA.

Barthelmy, S., D. Burrows, J. Cummings, et al. (2004). Swift-BAT detection of the bright long burst GRB041219. GRB Coordinates Network. **2874:** 1.

Barthelmy, S. D., T. L. Cline and P. Butterworth (2001). GRB Coordinates Network (GCN): A Status Report. Gamma 2001: Gamma-Ray Astrophysics. **587:** 213.

Beardmore, A. P., P. A. Evans, K. L. Page, et al. (2006). GRB061122: Swift-XRT position. GRB Coordinates Network. **5842:** 1.

Bellazzini, R., L. Baldini, F. Bitti, et al. (2006). A photoelectric polarimeter for XEUS: a new window in x-ray sky. Space Telescopes and Instrumentation II: Ultraviolet to Gamma Ray. Edited by Turner, Martin J. L.; Hasinger, Günther. Proceedings of the SPIE, Volume 6266, pp. 62663Z (2006). **6266:** 119.

Berger, E., R. Sari, D. A. Frail, et al. (2000). A Jet Model for the Afterglow Emission from GRB 000301C. Astrophysical Journal. **545:** 56-62.

Berlin, T. H. and L. Madansky (1950). "On the Detection of gamma-Ray Polarization by Pair Production." Physical Review **78**(5): 623.

Bird, A. J., E. J. Barlow, L. Bassani, et al. (2006). "The second IBIS/ISGRI soft gamma-ray survey catalog." Astrophysical Journal **636**(2): 765-76.

Bird, A. J., A. Malizia, A. Bazzano, et al. (2007). The Third IBIS/ISGRI Soft Gamma-Ray Survey Catalog. Astrophysical Journal Supplement Series. **170:** 175-186.

Blandford, R. D. and R. L. Znajek (1977). Electromagnetic extraction of energy from Kerr black holes. Monthly Notices of the Royal Astronomical Society. **179:** 433-456.

Brown, R. H., H. P. Palmer and A. R. Thompson (1955). Polarization measurements on three intense radio sources. Monthly Notices of the Royal Astronomical Society. **115:** 487.

Castro-Tirado, A. J., M. R. Zapatero-Osorio, N. Caon, et al. (1999). Decay of the GRB 990123 Optical Afterglow: Implications for the Fireball Model. Science. **283:** 2069.

Celotti, A. and G. Ghisellini (1999). Bursts from Internal Shocks: Is it Really Synchrotron Emission? Gamma-Ray Bursts: The First Three Minutes. **190:** 189.

Cenko, S. B. (2004). GRB041219: optical afterglow detection. GRB Coordinates Network. **2885:** 1.

Chen, K., H.-K. Chang and C. Ho (1996). Optical Pulse Polarization of the Crab Pulsar. Astrophysical Journal. **471:** 967.

Cheng, K. S., C. Ho and M. Ruderman (1986). "Energetic Radiation from Rapidly Spinning Pulsars. II. VELA and Crab." Astrophysical Journal **300**: 522.

Coburn, W. and S. E. Boggs (2003). "Polarization of the prompt gamma-ray emission from the gamma-ray burst of 6 December 2002." Nature **423**: 415-417.

Connors, P. A. and R. F. Stark (1977). Observable gravitational effects on polarised radiation coming from near a black hole. Nature. **269:** 128.

Costa, E., R. Bellazzini, G. Tagliaferri, et al. (2007). An X-ray Polarimeter for HXMT Mission.

Costa, E., F. Frontera, J. Heise, et al. (1997). Discovery of an X-ray afterglow associated with the gamma-ray burst of 28 February 1997. Nature. **387:** 783-785.

Covino, S., G. Ghisellini, D. Lazzati, et al. (2004). Polarization of Gamma-Ray Burst Optical and Near-Infrared Afterglows. Astronomical Society of the Pacific Conference Series. **312:** 169.

Covino, S., D. Lazzati, G. Ghisellini, et al. (1999). GRB 990510: linearly polarized radiation from a fireball. Astronomy and Astrophysics. **348:** L1-L4.

Covino, S., D. Malesani, G. Ghisellini, et al. (2003). Polarization evolution of the GRB 020405 afterglow. Astronomy and Astrophysics. **400:** L9-L12.

Dado, S., A. Dar and A. De Rujula (2007). Implications of the Large Polarization Measured in Gamma Ray Bursts.

Dar, A. and A. de Rújula (2004). Towards a complete theory of gamma-ray bursts. Physics Reports. **405:** 203-278.

Daugherty, J. K. and A. K. Harding (1982). Electromagnetic cascades in pulsars. Astrophysical Journal. **252:** 337-347.

Daugherty, J. K. and A. K. Harding (1996). Gamma-Ray Pulsars: Emission from Extended Polar CAP Cascades. Astrophysical Journal. **458:** 278.

Davisson, C. M. and R. D. Evans (1952). Gamma-Ray Absorption Coefficients. Reviews of Modern Physics. **24:** 79-107.

Dean, A. J., A. Bazzano, A. B. Hill, et al. (2005). Global characteristics of the first IBIS/ISGRI catalogue sources: unveiling a murky episode of binary star evolution. Astronomy and Astrophysics. **443:** 485-494.

Dean, A. J., A. J. Bird, N. Diallo, et al. (2003). The Modelling of Background Noise in Astronomical Gamma Ray Telescopes. Space Science Reviews. **105:** 285-376.

Del Zanna, L., D. Volpi, E. Amato, et al. (2006). Simulated synchrotron emission from pulsar wind nebulae. Astronomy and Astrophysics. **453:** 621-633.

Dezalay, J. P., C. Barat, R. Talon, et al. (1992). Short cosmic events - A subset of classical GRBs? American Institute of Physics Conference Series. **265:** 304-309.

Dezalay, J. P., J. P. Lestrade, C. Barat, et al. (1996). The Hardness-Duration Diagram of Gamma-Ray Bursts. Astrophysical Journal. **471:** L27.

Diehl, R., N. Baby, V. Beckmann, et al. (2003). SPI-specific analysis method and software overview. Astronomy and Astrophysics. **411:** L117-L121.

Djorgovski, S. G., S. R. Kulkarni, J. S. Bloom, et al. (1999). GRB 970228: redshift and properties of the host galaxy. GRB Coordinates Network. **289:** 1.

Dolan, J. F., P. T. Boyd, R. J. Hill, et al. (1996). The Polarization of the Crab Pulsar with HST. IAU Colloq. 160: Pulsars: Problems and Progress. **105:** 301.

Dyks, J. and B. Rudak (2003). "Two-Pole Caustic Model for High-Energy Light Curves of Pulsars." The Astrophysical Journal **598**(2): 1201-1206.

Eichler, D. and A. Levinson (2003). Polarization of Gamma-Ray Bursts via Scattering off a Relativistic Sheath. Astrophysical Journal. **596:** L147-L150.

Erjushev, N. N. and L. I. Tsvetkov (1970). Variations of the intensity of circularly polarized radio emission during solar flares. Solnechnye Dann. Bull. Akad. Nauk SSSR. **1969:** 94-98.

Fan, Y. Z., B. Zhang and D. M. Wei (2005). Early Optical-Infrared Emission from GRB 041219a: Neutron-rich Internal Shocks and a Mildly Magnetized External Reverse Shock. Astrophysical Journal. **628:** L25-L28.

Fender, R. (2003). "Circularly polarised radio emission from GRS 1915+105 and other X-ray binaries." Astrophysics and Space Science **288**(1): 79-95.

Fender, R. and T. Maccarone (2004). High energy emission from microquasars. Cosmic Gamma-Ray Sources. **304:** 205.

Ferguson, C., E. J. Barlow, A. J. Bird, et al. (2003). "The INTEGRAL Mass Model - TIMM." Astronomy and Astrophysics **411**: L19-L23.

Fernandez, J. E., J. H. Hubbell, A. L. Hanson, et al. (1993). "Polarization effects on multiple scattering gamma transport." Radiation Physics and Chemistry **41**(4-5): 579-630.

Fishman, G. J. and C. A. Meegan (1995). Gamma-Ray Bursts. Annual Review of Astronomy and Astrophysics. **33:** 415-458.

Fishman, G. J., C. A. Meegan, T. A. Parnell, et al. (1985). Burst and Transient Source Experiment (BATSE) for the Gamma Ray Observatory (GRO). International Cosmic Ray Conference. **3:** 343-346.

Fishman, G. J., C. A. Meegan, R. B. Wilson, et al. (1994). The first BATSE gamma-ray burst catalog. Astrophysical Journal Supplement Series. **92:** 229-283.

Frail, D. A., S. R. Kulkarni, L. Nicastro, et al. (1997). The radio afterglow from the gamma-ray burst of 8 May 1997. Nature. **389:** 261-263.

Frail, D. A., S. R. Kulkarni, R. Sari, et al. (2001). Beaming in Gamma-Ray Bursts: Evidence for a Standard Energy Reservoir. Astrophysical Journal. **562:** L55-L58.

Frontera, F. and G. Pareschi (1995). Comparative study of hard x-ray (>10 keV) focusing techniques for space astronomy. Proc. SPIE Vol. 2515, p. 2-13, X-Ray and Extreme Ultraviolet Optics, Richard B. Hoover; Arthur B. Walker; Eds. **2515:** 2-13.

Fruchter, A. S., S. E. Thorsett, M. R. Metzger, et al. (1999). Hubble Space Telescope and Palomar Imaging of GRB 990123: Implications for the Nature of Gamma-Ray Bursts and Their Hosts. Astrophysical Journal. **519:** L13-L16.

Gaensler, B. M., J. Arons, V. M. Kaspi, et al. (2002). Chandra Imaging of the X-Ray Nebula Powered by Pulsar B1509-58. Astrophysical Journal. **569:** 878-893.

Gaensler, B. M., M. J. Pivovaroff and G. P. Garmire (2001). Chandra Observations of the Pulsar Wind Nebula in Supernova Remnant G0.9+0.1. Astrophysical Journal. **556:** L107-L111.

Gallo, E., R. P. Fender and G. G. Pooley (2003). A universal radio-X-ray correlation in low/hard state black hole binaries. Monthly Notices of the Royal Astronomical Society. **344:** 60-72.

Gehrels, N. (1992). Instrumental background in gamma-ray spectrometers flown in low Earth orbit. Nuclear Instruments and Methods in Physics Research A. **313:** 513-528.

Gehrels, N. (2004). The Swift gamma-ray burst mission. New Astronomy Review. **48:** 431-435.

Ghisellini, G. and D. Lazzati (1999). "Polarization light curves and position angle variation of beamed gamma-ray bursts." Monthly Notices of the Royal Astronomical Society **309**: L7-L11.

Ginzburg, V. L. (1979). Theoretical physics and astrophysics.

Gluckstern, R. L., M. H. Hull and G. Breit (1953). "Polarisation of Bremsstrahlung Radiation." Physical Review **90**: 1026-1029.

Golenetskii, S., R. Aptekar, E. Mazets, et al. (2006). Konus-wind observation of GRB 060901. GRB Coordinates Network. **5498:** 1.

González, M. M., B. L. Dingus, Y. Kaneko, et al. (2003). A gamma-ray burst with a high-energy spectral component inconsistent with the synchrotron shock model. Nature. **424:** 749-751.

Gorosabel, J., E. Rol, S. Covino, et al. (2004). GRB 020813: Polarization in the case of a smooth optical decay. Astronomy and Astrophysics. **422:** 113-119.

Gotthelf, E. V. and Q. D. Wang (2000). A Spatially Resolved Plerionic X-Ray Nebula around PSR B0540-69. Astrophysical Journal. **532:** L117-L120.

Gotz, D., S. Mereghetti, S. Shaw, et al. (2004). GRB 041219 - a long GRB detected by INTEGRAL. GRB Coordinates Network. **2866:** 1.

Graham-Smith, F., J. F. Dolan, P. T. Boyd, et al. (1996). The ultraviolet polarization of the Crab pulsar. Monthly Notices of the Royal Astronomical Society. **282:** 1354-1358.

Granot, J. (2003). "The Most Probable Cause for the High Gamma-Ray Polarization in GRB 021206." Astrophysical Journal Letters **596**: L17-L21.

Greiner, J., S. Klose, K. Reinsch, et al. (2003). Evolution of the polarization of the optical afterglow of the gamma-ray burst GRB030329. Nature. **426:** 157-159.

Gruzinov, A. and E. Waxman (1999). Gamma-Ray Burst Afterglow: Polarization and Analytic Light Curves. Astrophysical Journal. **511:** 852-861.

Hall, H. (1936). "The Theory of Photoelectric Absorption for X-Rays and gamma - Rays." Reviews of Modern Physics **8**(4): 358.

Halloin, H., P. von Ballmoos, J. Evrard, et al. (2004). CLAIRE gamma-ray lens: flight and long-distance test results. Proceedings of the SPIE

Halpern, J. P., R. Uglesich, N. Mirabal, et al. (2000). GRB 991216 Joins the Jet Set: Discovery and Monitoring of Its Optical Afterglow. Astrophysical Journal. **543:** 697-703.

Harrison, F. A., J. S. Bloom, D. A. Frail, et al. (1999). Optical and Radio Observations of the Afterglow from GRB 990510: Evidence for a Jet. Astrophysical Journal. **523:** L121-L124.

Helfand, D. J., B. F. Collins and E. V. Gotthelf (2003). Chandra X-Ray Imaging Spectroscopy of the Young Supernova Remnant Kesteven 75. Astrophysical Journal. **582:** 783-792.

Helfand, D. J., E. V. Gotthelf and J. P. Halpern (2001). Vela Pulsar and Its Synchrotron Nebula. Astrophysical Journal. **556:** 380-391.

Henoux, J. C. and G. Chambe (1990). H-alpha impact polarization observed in solar flares as a diagnostic of energy transport mechanisms. Journal of Quantitative Spectroscopy and Radiative Transfer. **44:** 193-201.

Henoux, J. C., G. Chambe, S. Sahal, et al. (1983). Impact linear polarization observed in a UV chromospheric line during a solar flare. Astrophysical Journal. **265:** 1066-1075.

Heristchi, D. (1986). "Hard X-ray and gamma-ray bremsstrahlung production by high-energy protons in solar flares." Astrophysical Journal **311**: 474-484.

Hester, J. J., K. Mori, D. Burrows, et al. (2002). Hubble Space Telescope and Chandra Monitoring of the Crab Synchrotron Nebula. Astrophysical Journal. **577:** L49-L52.

Hester, J. J., P. A. Scowen, R. Sankrit, et al. (1995). WFPC2 Studies of the Crab Nebula. I. HST and ROSAT Imaging of the Synchrotron Nebula. Astrophysical Journal. **448:** 240.

Hewish, A., S. J. Bell, J. D. Pilkington, et al. (1968). Observation of a Rapidly Pulsating Radio Source. Nature. **217:** 709.

Hill, A. B., R. Walter, C. Knigge, et al. (2005). The 1-50 keV spectral and timing analysis of IGR J18027-2016: an eclipsing, high mass X-ray binary. Astronomy and Astrophysics. **439:** 255-263.

Hills, G. L. (1997). The Application of Polarimetric Techniques to Gamma Ray Astronomy. Dept. of Physics and Astronomy, University of Southampton. **Ph.D. Thesis**.

Hobbs, G., A. G. Lyne and M. Kramer (2003). Jodrell Bank Timing Astrometry. Radio Pulsars. **302:** 215.

Hurley, K. and T. Cline (2004). The Past, Present, and Future of the Third Interplanetary Network. Gamma-Ray Bursts: 30 Years of Discovery. **727:** 613-617.

Hurley, K., T. Cline, I. Mitrofanov, et al. (2002). IPN triangulation of GRB021206 (exceptionally bright). GRB Coordinates Network. **1727:** 1.

Jean, P. (2005). Private Communication - SPI Thresholds. D. Clark. Southampton.

Jean, P., G. Vedrenne, J. P. Roques, et al. (2003). SPI instrumental background characteristics. Astronomy and Astrophysics. **411:** L107-L112.

Jenet, F. A., G. B. Hobbs, K. J. Lee, et al. (2005). "Detecting the Stochastic Gravitational Wave Background Using Pulsar Timing." The Astrophysical Journal **625**(2): L123-L126.

Jensen, B. L., J. U. Fynbo, J. Gorosabel, et al. (2001). The afterglow of the short/intermediate-duration gamma-ray burst <ASTROBJ>GRB 000301C</ASTROBJ>: A jet at z=2.04. Astronomy and Astrophysics. **370:** 909-922.

Jones, D. H. P., F. G. Smith and P. T. Wallace (1981). Linear polarization of optical radiation from the Crab pulsar. Monthly Notices of the Royal Astronomical Society. **196:** 943-953.

Kalemci, E., S. Boggs, C. Wunderer, et al. (2004a). Background in the Multiple Events (ME) of INTEGRAL/SPI. 5th INTEGRAL Workshop on the INTEGRAL Universe. **552:** 855.

Kalemci, E., S. Boggs, C. Wunderer, et al. (2004b). Measuring Polarization with SPI on INTEGRAL. Proceedings of the 5th INTEGRAL Workshop on the INTEGRAL Universe (ESA SP-552). , Munich, Germany. .

Kalemci, E., S. E. Boggs, C. Kouveliotou, et al. (2007). Search for Polarization from the Prompt Gamma-Ray Emission of GRB 041219a with SPI on INTEGRAL. Astrophysical Journal Supplement Series. **169:** 75-82.

Kanbach, G. (1999). Temporal and Spectral Details of Bright EGRET Pulsars. Astrophysical Letters Communications. **38:** 17.

Kanbach, G., S. Kellner, F. Z. Schrey, et al. (2003). Design and results of the fast timing photo-polarimeter OPTIMA. Instrument Design and Performance for Optical/Infrared Ground-based Telescopes. Edited by Iye, Masanori; Moorwood, Alan F. M. Proceedings of the SPIE, Volume 4841, pp. 82-93 (2003). **4841:** 82-93.

Kanbach, G., A. Slowikowska, S. Kellner, et al. (2005). New optical polarization measurements of the Crab pulsar. Astrophysical Sources of High Energy Particles and Radiation. **801:** 306-311.

Katz, J. I. (1994). Two populations and models of gamma-ray bursts. Astrophysical Journal. **422:** 248-259.

Katz, J. I. (1997). Yet Another Model of Gamma-Ray Bursts. Astrophysical Journal. **490:** 633.

Katz, J. I. and L. M. Canel (1996). The Long and the Short of Gamma-Ray Bursts. Astrophysical Journal. **471:** 915.

Katz, J. I. and T. Piran (1997). Persistent Counterparts to Gamma-Ray Bursts. Astrophysical Journal. **490:** 772.

Kirsch, M. G. F., G. Schönherr, E. Kendziorra, et al. (2006). The XMM-Newton view of the Crab. Astronomy and Astrophysics. **453:** 173-180.

Klebesadel, R. W., I. B. Strong and R. A. Olson (1973). Observations of Gamma-Ray Bursts of Cosmic Origin. Astrophysical Journal. **182:** L85.

Knödlseder, J. and The GRI Consortium (2007). GRI: Exploring the extremes ESA Cosmic Vision Proposal.

Komissarov, S. and Y. Lyubarsky (2004). MHD Simulations of Crab's Jet and Torus. Astrophysics and Space Science. **293:** 107-113.

Kouveliotou, C., C. A. Meegan, G. J. Fishman, et al. (1993). Identification of two classes of gamma-ray bursts. Astrophysical Journal. **413:** L101-L104.

Krane, K. S. (1988). Introductory Nuclear Physics, John Wiley & Sons, Inc.

Kuiper, L., W. Hermsen, G. Cusumano, et al. (2001). The Crab pulsar in the 0.75-30 MeV range as seen by CGRO COMPTEL. A coherent high-energy picture from soft X-rays up to high-energy gamma-rays. Astronomy and Astrophysics. **378:** 918-935.

Kulkarni, S. R., S. G. Djorgovski, S. C. Odewahn, et al. (1999). The afterglow, redshift and extreme energetics of the gamma-ray burst of 23 January 1999. Nature. **398:** 389-394.

Kulkarni, S. R., D. A. Frail, M. H. Wieringa, et al. (1998). Radio emission from the unusual supernova 1998bw and its association with the gamma-ray burst of 25 April 1998. Nature. **395:** 663-669.

Kundu, M. R. and T. P. McCullough (1972). Polarization Structure of a Solar Flare Region at 9.5 mm Wavelength. Solar Physics. **27:** 182.

Labanti, C., G. Di Cocco, G. Ferro, et al. (2003). "The Ibis-Picsit detector onboard Integral." Astronomy and Astrophysics **411**: L149-L152.

Laing, R. A. and A. H. Bridle (2002). Relativistic models and the jet velocity field in the radio galaxy 3C 31. Monthly Notices of the Royal Astronomical Society. **336:** 328-352.

Lampton, M., B. Margon and S. Bowyer (1976). "Parameter estimation in X-ray astronomy." Astrophysical Journal **208**: 177-190.

Lazzati, D. (2006). Polarization in the prompt emission of gamma-ray bursts and their afterglows. New Journal of Physics. **8:** 131.

Lazzati, D., E. Rossi, G. Ghisellini, et al. (2004). "Compton drag as a mechanism for very high linear polarization in gamma-ray bursts." Monthly Notices of the Royal Astronomical Society **347**: L1-L5.

Lebrun, F., A. Bazzano, V. Borrel, et al. (2003a). The Compton Cube. Nuclear Instruments and Methods in Physics Research A. **504:** 38-43.

Lebrun, F., J. P. Leray, P. Lavocat, et al. (2003b). "ISGRI: The INTEGRAL Soft Gamma-Ray Imager." Astronomy and Astrophysics **411**: L141-L148.

Lei, F., A. J. Dean and G. L. Hills (1997). "Compton Polarimetry in Gamma-Ray Astronomy." Space Science Reviews **82**: 309-388.

Levine, A. and R. Remillard (2004). GRB041219: RXTE ASM observations. GRB Coordinates Network. **2917:** 1.

Lin, R. P., B. R. Dennis, G. J. Hurford, et al. (2002). "The Ramaty High Energy Solar Spectroscopic Imager (RHESSI) Mission." Solar Physics **201**(1): 3-32.

Lingenfelter, R. E. and X.-M. Hua (1991). Compton backscattered 511 keV annihilation line emission and the 170 keV line from the Galactic center direction. Astrophysical Journal. **381:** 426-438.

Longair, M. S. (1992). High energy astrophysics. Vol.1: Particles, photons and their detection, Cambridge: Cambridge University Press, 1992, 2nd ed.

Longair, M. S. (1994). High energy astrophysics. Vol.2: Stars, the galaxy and the interstellar medium.

Lund, N. (1992). "A study of focusing telescopes for soft gamma rays." Experimental Astronomy **2**(5): 259-273.

Lynds, R., S. P. Maran and D. E. Trumbo (1969). Optical Identification and Observations of the Pulsar NP 0532. Astrophysical Journal. **155:** L121.

Lyne, A. G., M. Burgay, M. Kramer, et al. (2004). A Double-Pulsar System: A Rare Laboratory for Relativistic Gravity and Plasma Physics. Science. **303:** 1153-1157.

Lyutikov, M., V. I. Pariev and R. D. Blandford (2003). "Polarization of Prompt Gamma-Ray Burst Emission: Evidence for Electromagnetically Dominated Outflow." Astrophysical Journal **597**: 998-1009.

MacFadyen, A. I., S. E. Woosley and A. Heger (2001). Supernovae, Jets, and Collapsars. Astrophysical Journal. **550:** 410-425.

Manchester, R. N. (1971). Observations of the Crab Pulsar at 410 and 1664 MHz. Astrophysical Journal. **163:** L61.

Manchester, R. N., G. R. Huguenin and J. H. Taylor (1972). Polarization of the Crab Pulsar Radiation at Low Radio Frequencies. Astrophysical Journal. **174:** L19.

Marcinkowski, R., M. Denis, T. Bulik, et al. (2006). GRB 030406 - an extremely hard burst outside of the INTEGRAL field of view. Astronomy and Astrophysics. **452:** 113-117.

Massaro, E., R. Campana, G. Cusumano, et al. (2006). The optical to gamma-ray emission of the Crab pulsar: a multicomponent model. Astronomy and Astrophysics. **459:** 859-870.

Matz, S. M., D. J. Forrest, W. T. Vestrand, et al. (1985). High-energy emission in gamma-ray bursts. Astrophysical Journal. **288:** L37-L40.

Mazets, E. P., S. V. Golenetskii, R. L. Aptekar, et al. (1981a). Cyclotron and annihilation lines in gamma-ray burst. Nature. **290:** 378-382.

Mazets, E. P., S. V. Golenetskii, V. N. Ilinskii, et al. (1982). Cosmic gamma-ray burst spectroscopy. Astrophysics and Space Science. **82:** 261-282.

Mazets, E. P., S. V. Golenetskii, V. N. Ilinskii, et al. (1981b). Catalog of cosmic gamma-ray bursts from the KONUS experiment data. I. Astrophysics and Space Science. **80:** 3-83.

McBreen, S., L. Hanlon, S. McGlynn, et al. (2006). "Observations of the intense and ultra-long burst GRB041219a with the Germanium Spectrometer on INTEGRAL." arXiv:astro-ph/0604455.

McConnell, M. L., J. M. Ryan, D. M. Smith, et al. (2007). Rhessi Solar Flare Polarization Measurements in the 20-100 keV Energy Range. American Astronomical Society Meeting Abstracts. **210**.

McConnell, M. L., J. M. Ryan, D. M. Smith, et al. (2002). "RHESSI as a Hard X-Ray Polarimeter." Solar Physics **210**(1): 125-142.

Meegan, C. A., G. J. Fishman, R. B. Wilson, et al. (1991). Intensity Distribution of Gamma-Ray Bursts Observed by BATSE. Bulletin of the American Astronomical Society. **23:** 1470.

Meier, D. L., S. Koide and Y. Uchida (2001). Magnetohydrodynamic Production of Relativistic Jets. Science. **291:** 84-92.

Mereghetti, S. and D. Gotz (2006a). GRB 060901: further INTEGRAL results. GRB Coordinates Network. **5493:** 1.

Mereghetti, S. and D. Gotz (2006b). INTEGRAL results on GRB 061122. GRB Coordinates Network. **5836:** 1.

Mereghetti, S., D. Jennings, H. Pedersen, et al. (1999). Prospects for Rapid Gamma-Ray Burst Localization with Integral. Astrophysical Letters Communications. **39:** 301.

Mereghetti, S., A. Paizis, D. Gotz, et al. (2006a). "GRB 061122A: a long GRB detected by INTEGRAL." GRB Coordinates Network **5834**: 1.

Mereghetti, S., A. Paizis, D. Gotz, et al. (2006b). "GRB 060901: a long GRB detected by INTEGRAL." GRB Coordinates Network **5491**: 1.

Meszaros, P. (2006). Gamma-ray bursts. Reports of Progress in Physics. **69:** 2259-2322.

Mészáros, P. (2001). Gamma-Ray Bursts: Accumulating Afterglow Implications, Progenitor Clues, and Prospects. Science. **291:** 79-84.

Meszaros, P., P. Laguna and M. J. Rees (1993). Gasdynamics of relativistically expanding gamma-ray burst sources - Kinematics, energetics, magnetic fields, and efficiency. Astrophysical Journal. **415:** 181-190.

Meszaros, P. and M. J. Rees (1997a). Optical and Long-Wavelength Afterglow from Gamma-Ray Bursts. Astrophysical Journal. **476:** 232.

Meszaros, P. and M. J. Rees (1997b). Poynting Jets from Black Holes and Cosmological Gamma-Ray Bursts. Astrophysical Journal. **482:** L29.

Meszaros, P., M. J. Rees and H. Papathanassiou (1994). Spectral properties of blast-wave models of gamma-ray burst sources. Astrophysical Journal. **432:** 181-193.

Metzger, M. R., S. G. Djorgovski, S. R. Kulkarni, et al. (1997). Spectral constraints on the redshift of the optical counterpart to the gamma-ray burst of 8 May 1997. Nature. **387:** 878-880.

Mirabel, I. F., L. F. Rodriguez, B. Cordier, et al. (1992). A double-sided radio jet from the compact Galactic Centre annihilator 1E140.7 - 2942. Nature. **358:** 215-217.

Mizuno, T., T. Kamae, J. S. T. Ng, et al. (2005). Beam test of a prototype detector array for the PoGO astronomical hard X-ray/soft gamma-ray polarimeter. Nuclear Instruments and Methods in Physics Research A. **540:** 158-168.

Moffett, D. A. and T. H. Hankins (1999). Polarimetric Properties of the Crab Pulsar between 1.4 and 8.4 GHZ. Astrophysical Journal. **522:** 1046-1052.

Moon, D. S., S. B. Cenko and J. Adams (2004). GRB041219: confirmed NIR afterglow. GRB Coordinates Network. **2876:** 1.

Mori, K., D. N. Burrows, J. J. Hester, et al. (2004). Spatial Variation of the X-Ray Spectrum of the Crab Nebula. Astrophysical Journal. **609:** 186-193.

Nakar, E., T. Piran and E. Waxman (2003). Implications of the bold gamma-ray polarization of GRB 021206. Journal of Cosmology and Astro-Particle Physics. **10:** 005.

Narayan, R., B. Paczynski and T. Piran (1992). Gamma-ray bursts as the death throes of massive binary stars. Astrophysical Journal. **395:** L83-L86.

Neal, V., G. Fishman and D. Kniffen (1990). Gamma-Ray Observatory - The next great observatory in space. Mercury. **19:** 98-111.

Negueruela, I., D. M. Smith, P. Reig, et al. (2006). Supergiant Fast X-ray Transients: a new class of high mass X-ray binaries unveiled by INTEGRAL. ESA SP-604: The X-ray Universe 2005**:** 165-170.

Norris, J. P., R. J. Nemiroff, J. D. Scargle, et al. (1994). Detection of signature consistent with cosmological time dilation in gamma-ray bursts. Astrophysical Journal. **424:** 540-545.

Novick, R., M. C. Weisskopf, R. Berthelsdorf, et al. (1972). Detection of X-Ray Polarization of the Crab Nebula. Astrophysical Journal. **174:** L1.

Oates, S. R. and S. McBreen (2006). GRB061122: Swift/UVOT optical observations. GRB Coordinates Network. **5846:** 1.

Paczynski, B. (1991). Cosmological gamma-ray bursts. Acta Astronomica. **41:** 257-267.

Paczynski, B. (1998). Are Gamma-Ray Bursts in Star-Forming Regions? Astrophysical Journal. **494:** L45.

Paczynski, B. and J. E. Rhoads (1993). Radio Transients from Gamma-Ray Bursters. Astrophysical Journal. **418:** L5.

Pavlov, G. G., O. Y. Kargaltsev, D. Sanwal, et al. (2001). Variability of the Vela Pulsar Wind Nebula Observed with Chandra. Astrophysical Journal. **554:** L189-L192.

Pavlov, G. G., M. A. Teter, O. Kargaltsev, et al. (2003). The Variable Jet of the Vela Pulsar. Astrophysical Journal. **591:** 1157-1171.

Peacock, A., B. G. Taylor and J. Ellwood (1990). The high throughput X-ray spectroscopy mission - XMM. Advances in Space Research. **10:** 273-285.

Perlman, E. S., C. A. Padgett, M. Georganopoulos, et al. (2006). Optical Polarimetry of the Jets of Nearby Radio Galaxies. I. The Data. Astrophysical Journal. **651:** 735-748.

Petrosian, V., J. M. McTiernan and H. Marschhauser (1994). "Gamma-ray emission and electron acceleration in solar flares." Astrophysical Journal **434**(2): 747-755.

Piran, T. (1999). Gamma-ray bursts and the fireball model. Physics Reports. **314:** 575-667.

Popham, R., S. E. Woosley and C. Fryer (1999). "Hyperaccreting Black Holes and Gamma-Ray Bursts." The Astrophysical Journal **518**: 356-374.

Price, P. A., F. A. Harrison, T. J. Galama, et al. (2001). Multicolor Observations of the GRB 000926 Afterglow. Astrophysical Journal. **549:** L7-L10.

Rees, M. J. (1999). Some comments on triggers, energetics and beaming. Astronomy and Astrophysics Supplement Series. **138:** 491-497.

Rees, M. J. and P. Meszaros (1994). Unsteady outflow models for cosmological gamma-ray bursts. Astrophysical Journal. **430:** L93-L96.

Rees, M. J. and P. Mészáros (2005). Dissipative Photosphere Models of Gamma-Ray Bursts and X-Ray Flashes. Astrophysical Journal. **628:** 847-852.

Rhoads, J. E. (1997). How to Tell a Jet from a Balloon: A Proposed Test for Beaming in Gamma-Ray Bursts. Astrophysical Journal. **487:** L1.

Rhoads, J. E. (1999). The Dynamics and Light Curves of Beamed Gamma-Ray Burst Afterglows. Astrophysical Journal. **525:** 737-749.

Roberts, M. S. E., C. R. Tam, V. M. Kaspi, et al. (2003). The Pulsar Wind Nebula in G11.2-0.3. Astrophysical Journal. **588:** 992-1002.

Romani, R. W. and I. A. Yadigaroglu (1995). Gamma-ray pulsars: Emission zones and viewing geometries. Astrophysical Journal. **438:** 314-321.

Roques, J. P., S. Schanne, A. von Kienlin, et al. (2003). SPI/INTEGRAL in-flight performance. Astronomy and Astrophysics. **411:** L91-L100.

Ruderman, M. A. and P. G. Sutherland (1975). Theory of pulsars - Polar caps, sparks, and coherent microwave radiation. Astrophysical Journal. **196:** 51-72.

Ruffert, M., H.-T. Janka, K. Takahashi, et al. (1997). "Coalescing neutron stars - a step towards physical models. II. Neutrino emission, neutron tori, and gamma-ray bursts." Astronomy and Astrophysics **319**: 122-153.

Rutledge, R. E. and D. B. Fox (2004). Re-analysis of polarization in the gamma-ray flux of GRB 021206. Monthly Notices of the Royal Astronomical Society. **350:** 1288-1300.

Rybicki, G. B. and A. P. Lightman (1986). Radiative Processes in Astrophysics.

Ryde, F. (2005). Is Thermal Emission in Gamma-Ray Bursts Ubiquitous? Astrophysical Journal. **625:** L95-L98.

Rykoff, E., U. Michigan and R. Quimby (2004). GRB041219: prompt optical observations from ROTSE-IIIb. GRB Coordinates Network. **2868:** 1.

Sagar, R., S. B. Pandey, V. Mohan, et al. (2001). GRB 000926 and its optical afterglow : Another possible evidence for non-isotropic emission. Bulletin of the Astronomical Society of India. **29:** 1-13.

Sari, R. e. (1999). Linear Polarization and Proper Motion in the Afterglow of Beamed Gamma-Ray Bursts. Astrophysical Journal. **524:** L43-L46.

Scarsi, L. (1993). SAX overview. Astronomy and Astrophysics Supplement Series. **97:** 371-383.

Schaefer, B. E. (1981). Probable optical counterpart of a Gamma-ray burster. Nature. **294:** 722-724.

Schaefer, B. E. (1992). Severe new limits on extragalactic models of gamma-ray bursts. Gamma-Ray Bursts - Observations, Analyses and Theories**:** 107-112.

Schoenfelder, V., H. Aarts, K. Bennett, et al. (1993). "Instrument description and performance of the Imaging Gamma-Ray Telescope COMPTEL aboard the Compton Gamma-Ray Observatory." Astrophysical Journal Supplement Series **86**(2): 657-692.

Segreto, A., C. Labanti, A. Bazzano, et al. (2003). Cosmic rays tracks on the PICsIT detector. Astronomy and Astrophysics. **411:** L215-L222.

Seward, F. D., W. H. Tucker and R. A. Fesen (2006). Faint X-Ray Structure in the Crab Pulsar Wind Nebula. Astrophysical Journal. **652:** 1277-1287.

Sguera, V., E. J. Barlow, A. J. Bird, et al. (2005). INTEGRAL observations of recurrent fast X-ray transient sources. Astronomy and Astrophysics. **444:** 221-231.

Shaviv, N. J. and A. Dar (1995). Gamma-Ray Bursts from Minijets. Astrophysical Journal. **447:** 863.

Shaw, S. E., M. J. Westmore, A. J. Bird, et al. (2003). A mass model for estimating the gamma ray background of the Burst and Transient Source Experiment. Astronomy and Astrophysics. **398:** 391-402.

Shaw, S. E., M. J. Westmore, A. B. Hill, et al. (2004). Gamma-ray all-sky imaging with the Burst and Transient Source Experiment. Astronomy and Astrophysics. **418:** 1187-1200.

Silver, E. H., H. L. Kestenbaum, K. S. Long, et al. (1978). "Search for X-ray polarization in the Crab pulsar." Astrophysical Journal **225**: 221-225.

Skibo, J. B., C. D. Dermer and R. L. Kinzer (1994). "Is the high-energy emission from Centaurus A compton-scattered jet radiation?" Astrophysical Journal **426**(1): 23-26.

Slowikowska, A., G. Kanbach and A. Stefanescu (2007). Fully Resolved Optical Polarization of the Crab Pulsar. American Institute of Physics Conference Series. **921:** 419-420.

Smith, F. G., M. J. Disney, K. F. Hartley, et al. (1978). Resolution of the peak of the Crab Pulsar optical pulse. Monthly Notices of the Royal Astronomical Society. **184:** 39P-43P.

Smith, F. G., D. H. P. Jones, J. S. B. Dick, et al. (1988). The optical polarization of the Crab Pulsar. Monthly Notices of the Royal Astronomical Society. **233:** 305-319.

Smither, R. K., P. B. Fernandez, T. Graber, et al. (1995). "Review of Crystal Diffraction and Its Application to Focusing Energetic Gamma Rays." Experimental Astronomy **6**: 47-56.

Stanek, K. Z., P. M. Garnavich, S. Jha, et al. (2001). Rapid UBVRI Follow-up of the Highly Collimated Optical Afterglow of GRB 010222. Astrophysical Journal. **563:** 592-596.

Stanek, K. Z., P. M. Garnavich, J. Kaluzny, et al. (1999). BVRI Observations of the Optical Afterglow of GRB 990510. Astrophysical Journal. **522:** L39-L42.

Stephen, J. B., E. Caroli, R. C. da Silva, et al. (2001). Gamma-Ray Polarization Measurements with INTEGRAL/IBIS. Gamma 2001: Gamma-Ray Astrophysics. **587:** 816.

Sturner, S. J., C. D. Dermer and F. C. Michel (1995). Magnetic Compton-induced pair cascade model for gamma-ray pulsars. Astrophysical Journal. **445:** 736-755.

Sturrock, P. A. (1971). A Model of Pulsars. Astrophysical Journal. **164:** 529.

Suffert, M., P. M. Endt and A. M. Hoogenboom (1959). Polarization measurements of proton capture gamma rays. Physica. **25:** 659-670.

Sunyaev, R. A. and L. G. Titarchuk (1985). Comptonization of low-frequency radiation in accretion disks Angular distribution and polarization of hard radiation. Astronomy and Astrophysics. **143:** 374-388.

T'o-t'o (1313-1355). Sung-Shih [Annals of the Sung dynasty, astronomical treatise]: 25a.

Takata, J., H. K. Chang and K. S. Cheng (2007). Polarization of High-Energy Emission from the Crab Pulsar. Astrophysical Journal. **656:** 1044-1055.

Tindo, I. P., V. D. Ivanov, S. L. Mandel'Stam, et al. (1970). On the Polarization of the Emission of X-Ray Solar Flares. Solar Physics. **14:** 204.

Ubertini, P., F. Lebrun, G. Di Cocco, et al. (2003). "IBIS: The Imager on-board INTEGRAL." Astronomy and Astrophysics **411**: L131-L139.

Urry, C. M. and P. Padovani (1995). Unified Schemes for Radio-Loud Active Galactic Nuclei. Publications of the Astronomical Society of the Pacific. **107:** 803.

van Paradijs, J., P. J. Groot, T. Galama, et al. (1997). Transient optical emission from the error box of the gamma-ray burst of 28 February 1997. Nature. **386:** 686-689.

van Paradijs, J., C. Kouveliotou and R. A. M. J. Wijers (2000). Gamma-Ray Burst Afterglows. Annual Review of Astronomy and Astrophysics. **38:** 379-425.

Vedrenne, G., J.-P. Roques, V. Schönfelder, et al. (2003). "SPI: The Spectrometer Aboard INTEGRAL." Astronomy and Astrophysics **411**: L63-L70.

Viironen, K. and J. Poutanen (2004). Light curves and polarization of accretion- and nuclear-powered millisecond pulsars. Astronomy and Astrophysics. **426:** 985-997.

von Ballmoos, P., H. Halloin, J. Evrard, et al. (2004). "CLAIRE's first light." New Astronomy Reviews **48**(1-4): 243-249.

Walter, R. and The Integral Survey Team (2004). Highly Absorbed Galactic Sources Revealed by INTEGRAL. Bulletin of the American Astronomical Society. **8:** 970.

Wampler, E. J., J. D. Scargle and J. S. Miller (1969). Optical Observations of the Crab Nebula Pulsar. Astrophysical Journal. **157:** L1.

Waxman, E. (2003). Astronomy: New direction for gamma-rays. Nature. **423:** 388-389.

Webber, W. R. and J. A. Lezniak (1974). The comparative spectra of cosmic-ray protons and helium nuclei. Astrophysics and Space Science. **30:** 361-380.

Weidenspointner, G., J. Kiener, M. Gros, et al. (2003). First identification and modelling of SPI background lines. Astronomy and Astrophysics. **411:** L113-L116.

Weidenspointner, G., C. B. Wunderer, N. Barrière, et al. (2005). Monte Carlo study of detector concepts for the MAX Laue lens gamma-ray telescope. Experimental Astronomy. **20:** 375-386.

Weisskopf, M. C., G. G. Cohen, H. L. Kestenbaum, et al. (1976). Measurement of the X-ray polarization of the Crab Nebula. Astrophysical Journal. **208:** L125-L128.

Weisskopf, M. C., R. F. Elsner, D. Hanna, et al. (2006). The prospects for X-ray polarimetry and its potential use for understanding neutron stars. 363-rd Heraeus Seminar in Bad Honef, Germany.

Weisskopf, M. C., J. J. Hester, A. F. Tennant, et al. (2000). Discovery of Spatial and Spectral Structure in the X-Ray Emission from the Crab Nebula. Astrophysical Journal. **536:** L81-L84.

Weisskopf, M. C., E. H. Silver, H. L. Kestenbaum, et al. (1978). A precision measurement of the X-ray polarization of the Crab Nebula without pulsar contamination. Astrophysical Journal. **220:** L117-L121.

Westmore, M. J. (2002). Dept. of Physics and Astronomy, University of Southampton. **Ph.D. Thesis**.

Wiersema, K. and C. C. Thoene (2006). GRB060901: optical observations. GRB Coordinates Network. **5501:** 1.

Wigger, C., W. Hajdas, K. Arzner, et al. (2004). "Gamma-Ray Burst Polarization: Limits from RHESSI Measurements." The Astrophysical Journal **613**: 1088-1100.

Wijers, R. A. M. J., P. M. Vreeswijk, T. J. Galama, et al. (1999). Detection of Polarization in the Afterglow of GRB 990510 with the ESO Very Large Telescope. Astrophysical Journal. **523:** L33-L36.

Willingale, R., B. Aschenbach, R. G. Griffiths, et al. (2001). New light on the X-ray spectrum of the Crab Nebula. Astronomy and Astrophysics. **365:** L212-L217.

Willis, D. R. (2002). Mass Modelling Techniques for Gamma ray Burst Missions. Dept. of Physics and Astronomy, University of Southampton.

Willis, D. R., E. J. Barlow, A. J. Bird, et al. (2005). "Evidence of polarisation in the prompt gamma-ray emission from GRB 930131 and GRB 960924." Accepted, A&A **astro-ph/0505097**.

Wilson, R. R. (1952). Monte Carlo Study of Shower Production. Physical Review. **86:** 261-269.

Winkler, C., K. Bennett, H. Bloemen, et al. (1992). The gamma-ray burst of 3 May 1991 observed by COMPTEL on board GRO. Astronomy and Astrophysics. **255:** L9-L12.

Winkler, c., T. J.-L. Courvoisier, G. Di Cocco, et al. (2003). "The INTEGRAL Mission." Astronomy and Astrophysics **411**: L1-L6.

Winkler, C., R. M. Kippen, K. Bennett, et al. (1995). COMPTEL observations of the strong gamma-ray burst GRB 940217. Astronomy and Astrophysics. **302:** 765.

Xu, Z., J. C. Hénoux, G. Chambe, et al. (2005). Multiwavelength Analysis of the Impact Polarization of 2001 June 15 Solar Flare. Astrophysical Journal. **631:** 618-627.

Yonetoku, D., T. Murakami, T. Nakamura, et al. (2004). Gamma-Ray Burst Formation Rate Inferred from the Spectral Peak Energy-Peak Luminosity Relation. Astrophysical Journal. **609:** 935-951.

Zhang, B. and P. Mészáros (2004). "Gamma-Ray Bursts: progress, problems & prospects." International Journal of Modern Physics A **19**(15): 2385-2472.

Zhang, L. and K. S. Cheng (1997). High-Energy Radiation from Rapidly Spinning Pulsars with Thick Outer Gaps. Astrophysical Journal. **487:** 370.